Novel Applications of Atomic Force Microscopy to the Analysis of Barrier Film Defects

Joseph Anthony Bottomley

May 2012

A thesis submitted to the University of Birmingham for the degree of Doctor of Engineering

UNIVERSITY OF
BIRMINGHAM

University of Birmingham Research Archive

e-theses repository

This unpublished thesis/dissertation is copyright of the author and/or third parties. The intellectual property rights of the author or third parties in respect of this work are as defined by The Copyright Designs and Patents Act 1988 or as modified by any successor legislation.

Any use made of information contained in this thesis/dissertation must be in accordance with that legislation and must be properly acknowledged. Further distribution or reproduction in any format is prohibited without the permission of the copyright holder.

i. Abstract

As a result of numerous advantages over glass based devices, flexible displays continue to gather momentum. Many problems associated with fabrication of devices on polymers have been overcome, but the detrimental effect of water permeation through these substrates due to defects is still prevalent despite attempts to block pinholes with thin film barrier materials. A rigorous study of film defects using atomic force microscopy (AFM) plus novel application of the calcium test, with additional scanning electron microscopy and white light interferometry data has been undertaken. While pursuing this study, new methods of displaying defect data were discovered, allowing the problem to be visualised better. In addition, the results demonstrated that the major cause of device failure was point defects in the barrier films caused by airborne dust which adheres to the film surface before application of the barrier. The calcium test was applied in new ways to demonstrate the damaging influence of these film defects. To explain the results, a new model of permeation was devised through quantative analysis of the defects present on industrially produced films and confirmed using model substrates and a synthetic model, to explain the behaviour observed in the literature, but never previously explained. The conclusion was that the combination of AFM study, calcium testing and theoretical modelling gave improved understanding of the defect problems in flexible display devices. It is expected that the findings of this work will help DuPont Teijin Films to eliminate such flaws from their manufacturing process, ultimately allowing the films to be applied to commercial applications.

ii. Acknowledgements

The writing of this thesis has been a long but worthwhile process, assisted by many collaborators, especially from my sponsoring company, DuPont Teijin Films.

There are several people who, throughout the research process, have been of great help and I would like to acknowledge these people here.

Firstly, I would like to thank Karl Rakos, my industrial supervisor who has not only been a great supervisor, but also a good friend. His assistance and support during the entirety of this work, throughout all the high and low points has had a great impact. I would like to thank the staff of DuPont Teijin Films. Whilst there are too many to mention individually, it is because of these people and their assistance that I found myself in such a supportive and enjoyable working environment.

I would also like to thank Dr Richard Greenwood for his support and direction throughout this work plus Professor Kevin Kendall and Dr Paul Mills for their guidance and thesis reading which has helped bring this document to the present standard.

I would also like to thank my family, always supporting my endeavours and continuing to do so, with particular thanks to my sister, Lizzie for her great support when times got particularly hard.

Finally, a special thankyou is deserved to my partner, Amalia Tsanaka. Quite possibly she is the only person who fully understands my personality quirks and she has been a continued source of energy and inspiration throughout this work.

iii. Table of Contents

iv. Lists of Figures, Tables and Equations

List of Figures

Figure 8.22: SEM-EDX data taken at different areas around a barrier coated silica particle

Figure 8.23: Schematic to show the permeation of through particles set at 25% of their total diameter and the light barrier coating which prevents this in those set to 75%

List of Tables

List of Equations

v. List of Acronyms

Å	Angstrom
AFM	Atomic Force Microscope/Microscopy
CRT	Cathode Ray Tube
DTF	DuPont Teijin Films
EngD	Doctor of Engineering
HTO	Hydrogen Tritium Oxygen
LCD	Liquid Crystal Display
mbar	Milibar
mm	Millimetre
MP	Megapixel
nm	Nanometre
OLED	Organic Light Emitting Diode
PAR	Polyarylates
PC	Polycarbonate
PCO	Polycyclic olefin
PECVD	Plasma Enhanced Chemical Vapour Deposition
PEN	Polyethylene naphthalate
PET	Polyethylene terephthalate
PES	Polyethersulphone
PhD	Doctor of Philosophy
PI	Polyimide
ppm	Parts Per Million
PSI	Phase Shifting Interferometry
SEM	Scanning Electron Microscope/Microscopy
SPM	Scanning Probe Microscope/Microscopy
STM	Scanning Tunneling Microscope/Microscopy
T_g	Glass transition
TTM	Through Transmissive Media
VSI	Vertical Scanning Interferometry
WLI	White Light Interferometer/Interferometry
WVTR	Water Vapour Transmission Rate
µm	Micrometre

1. Introduction

1.1 Project Overview & Objectives

The field of flexible electronics continues to gather momentum through increasing interest from manufacturers. Flexible displays in particular are predicted to show rapid growth (Jakhanwal, 2011; Forge, 2009) comparable to the explosion in popularity of Liquid Crystal Displays (LCDs) in the last 10 years (Hairston, 2009; Forge, 2009). Flexible flat panel display technologies offer many advantages over their rigid glass counterparts including very thin profiles, vastly reduced weight, improved robustness, extreme portability, high throughput manufacturing and ultimate engineering freedom (MacDonald, 2004). The range of requirements for substrates in these devices has resulted in transparent polymers becoming an attractive candidate for both front and back planes. Whilst polymers can meet most of the requirements as substrates in flexible displays, the application of Organic Light Emitting Diodes (OLEDs) to such systems and the reactive nature of these has resulted in one of the key demands being a maximum water and O_2 permeability (10^{-6} g/m² per day and 10^{-4} g/m² respectively) (Burrows, 2001; Erlat, 2004; Park, 2005, Choi, 2008). However the permeability of many candidate plastic substrates to both water and oxygen is much greater than materials currently used in flat panel display technology (Hanika, 2003). The barrier property of polymer substrates for use in flexible electronics and display applications is therefore one of the most demanding requirements and hence a highly active area of research. Glass is currently the most commonplace and demonstrates barrier properties around 10^{-12} g/m² per day against water. Hence, it is utilised in existing commercialised OLED devices such as the Sony XEL-1 (Sony, 2008) (Figure 1.1) and some smartphones (Samsung, 2012a).

Figure 1.1: The Sony XEL-1 'Ultra Slim OLED TV' (Sony, 2011)

To improve the barrier properties of polymeric materials, additional coating layers such as metal oxides must be deposited across the surface to suppress permeability (Hanika, 2003). Highly sensitive methods have been developed to measure the performance of such barriers, one of which is the so called 'Calcium test' (MOCON Pres. 2010). One procedure involves the deposition of a thin layer of calcium metal on to a flexible plastic substrate which is then laminated to a glass slide to protect the calcium against airborne moisture. Any water which subsequently permeates through the polymer film reacts on contact with the encapsulated calcium, creating areas of localised transparency known as 'pinholes' (Adam, 2007).

The application of this calcium test has been extended beyond a simple technique to measure permeation, primarily using an atomic force microscope (AFM). The origin of these pinholes has been studied here for the first time in recorded literature in an attempt to establish the fundamental factors which cause barrier failures. Such AFM has been complimented with other techniques including white light interferometry (WLI) and scanning electron microscopy (SEM). A model system has also been developed to recreate these defects and determine the fundamental factors which cause barrier breaks. The ultimate goal of the work reported in this thesis was to bring knowledge about these flaws to the sponsor company, DuPont Teijin Films (DTF) to allow

barrier properties to be improved to meet the stringent requirements necessary for long device lifetimes.

1.2 Thesis Aims

The aim of this thesis is to determine the cause of pinhole defects on barrier films, establish their composition, attempt to locate their source and ultimately investigate methods of both removing and preventing their occurrence. As a result of time constraints and the sheer amount of work involved, some aspects of the research remain uncompleted, but a great deal of knowledge has been obtained not only to determine the causes of failures observed, but also on the mechanisms and conditions which determine whether a surface defect will result in barrier failure. The AFM was utilised for the majority of the work, supplemented by white light interferometry, scanning electron microscopy and other techniques.

1.3 Academic Impact

This thesis confirms for the first time the source of device failures by direct analysis, confirmed using comparisons against known surface textures and a synthetic model. As a result, a new theory of permeation of moisture through thin film barriers has been devised capable of explaining observations reported in the literature, a problem which no other theory has been able to resolve. Furthermore, a novel application of the calcium test has been devised utilising it better than the simple permeation test. Also an original application of AFM to create a new technique for the capture of large area, high resolution images has been devised.

1.4 Commercial Impact

The production of polyester films forms the core business of DTF with polyethylene napthalate film as the preferred choice for a flexible display substrate. The biggest problem with using this film, or indeed any polymeric film, is the low barrier performance. If DTF can produce a product which meets the required specification of displays manufacturers, this would not only provide a large market share but a head start in this sector, with potential large returns.

This thesis is considered by many within DTF to have generated a large amount of knowledge in the area of thin film barriers and flaws, the calcium test, and barrier deposition. Other work unreported in this thesis includes analysis of a very large number of industrial samples to resolve customer complains, enhance product development and participate with general research activities.

A large number of surface topography images were generated whilst carrying out work for both the company and this thesis, this data been used to assist research and provide crucial knowledge which directly impacted commercial research. Furthermore, the capture of this data has served to create a library of images to which researchers will be able to refer. The AFM has proved to be indispensible compared to other available techniques for research, it has effectively extended and complimented metrology performed with white light interferometry. In addition it has provided information which could not be obtained by SEM, including quantative measurements of features and surface density changes. During the course of the work carried out for this thesis, DTF has increased its market share in areas such as flexible photovoltaics. The work carried out on barriers for flexible displays has direct relevance to this relatively new field.

1.5 Thesis Layout

The thesis is divided into eight chapters, with each one grouping a particular area of research;

Chapter 1 is a brief introduction to the area in which the thesis is based with some general information into the area and its relevance to DuPont Teijin Films. Chapter 2 outlines the evolution of the technology from which the need to research this area has arisen including a discussion of the materials used in these devices and industrially relevant information. Chapter 3 describes the existing literature in this area and demonstrates where there are holes in the current knowledge to define where this work fits into that which already exists. This is followed by Chapter 4, a brief summary of all the equipment, materials and processes used throughout this thesis. Chapter 5 contains the first results, including a description of a novel method to analyse large areas of film using the AFM. This is followed by Chapter 6 which describes a method developed for detecting barrier defects and preliminary analysis of these. Chapter 7 extends this work by testing the effects of well characterised systems on barrier films. This leads into Chapter 8, in which a model system is created to test conclusions from the preceding work on permeation theories. Finally, Chapter 9 presents the major conclusions of the thesis, examining the finding of the work and suggesting further potential avenues of research, followed by the references and appendix.

2. Project Background

2.1 The Evolution of Displays

It is impossible to ignore the explosion in popularity of flat screen displays since the late 90's (Merck, 2007), because their slim profiles, decreasing prices and ever improving performance has made them accessible to an increasing segment of the consumer market. Whilst it is still disputed by some that Cathode Ray Tube (CRT) displays outperform flat panel devices in certain aspects (Hollands, 2002), ongoing advances in LCDs have brought improvements to the point that such differences are no longer a concern to the mass market. In fact, it can now be argued that when considering certain features, the latest LCDs now outperform CRTs. Perhaps the biggest drive for the uptake of flat screen displays is that consumers are now able to have very large screens enabling a cinema-like experience in the home, without sacrificing the vast amounts of space a similar sized CRT would require (Hairston, 2009). Furthermore the proliferation of high definition media has further driven the market for displays capable of displaying such content (Ferns, 2007).

2.1.1 A Brief History of Flat Panel Displays

Liquid crystals were first observed in 1888 by the Austrian botanist Friedrich Reinitzer (Reinitzer, 1888), but remained a scientific curiosity for the next 80 years. It wasn't until 1963 that a display based on these materials was proposed by Richard Williams of the Radio Corporation of America, although it took several more years to be developed (Williams, 1963a; Williams, 1963b). Whilst impressive, this early device required operating temperatures in excess of 100 °C, resulting in high power consumption, poor image quality and short lifetimes (Hoogboom, 2006). Soon after, the Twisted Nematic device was developed to address these issue by James Fergason of Kent State University, patented in 1969 and applied two years later (Fergason, 1969).

It was in Japan that the potential of the technology was realised, first in calculators and small screen display devices but ultimately working its way into more complex appliances (Kawamoto, 2002). The first true flat screen television emerged in 1988 as a result of the determination by Sharp's general manager of the newly formed liquid crystals division, Isamu Washizuka, who was adamant that the next evolution in LCDs should be a quantum leap. His vision gave rise to the first 14 inch Thin Film Transistor colour LCD (Figure 2.1) which Sharp's CEO initially thought was a clever trick, believing such a device was not possible (Kawamoto, 2002). It was this device that demonstrated to the world that a flat, wall hangable television was not only possible, but commercially viable, giving birth to the LCD industry.

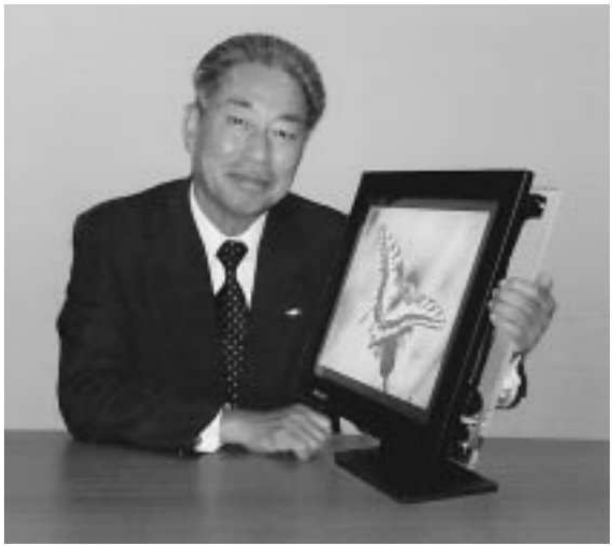

Figure 2.1: Washizuka pictured with the first 14 inch full colour LCD

By the turn of the millennium sales of LCDs were rapidly catching up to those of CRTs and the explosion in popularity of flat panel displays further increased with reducing device costs through improving production methods. Flat displays were now available to the mass market and the resulting sales brought ever decreasing prices and improved technology; bringing us to the large, high definition, rapid refresh rate screens that many people now have in their homes. The majority of major manufacturers phased out production of CRTs over the last 10 years, with sales of most

high end devices ending by 2010 (Hairston, 2009). Although a few smaller companies still make CRTs for specialist applications, LCDs have become the universal displays medium.

It took many years for the LCD revolution to come about and truly challenge the dominance of CRTs which had been the mainstay for so many years. Organic light emitting diode devices have experienced a similarly difficult development cycle, as is often the case with many original technologies. However, the success story which was the development of LCDs should show that despite many setbacks and seemingly impossible obstacles, goals which appear unattainable can still be realised. Hence the expectation that despite many technical hurdles OLEDs will be the displays medium which will supersede liquid crystals (Crawford, 2005).

2.1.2 The Development of OLED Displays

Following on from the success of LCD technology, a new chapter in displays was opened by the innovation that is the Organic Light Emitting Diode (OLED) with potential that many manufacturers envisage for utilising this technology in flexible devices (Crawford, 2005).

The first OLED to be successfully fabricated was by Ching Tang and Stephen VanSlyke at Eastman Kodak's research facility (Tang, 1987). Their device utilised both hole and electron transporting layers whereby recombination of the two at the layer interfaces resulted in light emission, much like a semi-conductor LED (Bergh, 1972). A breakthrough was reached in 1990 by Burroughes, fabricating the first electroluminescent device based on 100 nm thick layers of poly(p-phenylene vinylene) (Figure 2.2), reporting a high efficiency emission of green light (Burroughes, 1990).

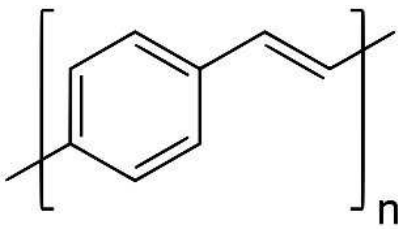

Figure 2.2: Chemical structure of poly(p-phenylene vinylene)

Whilst previous OLEDs were comprised of small molecule systems, these new polymers could be suspended in a liquid, theoretically allowing application via printing techniques, with the potential to greatly reduce production costs (DuPont, 2010). These discoveries encouraged other groups to initiate their own research into OLEDs for application to flat panel displays. Although the materials are still relatively expensive, large scale commercial production has become viable. OLED materials can be purchased ready synthesised from suppliers, including coloured emitters, dopants and electon/hole transport materials (OLED-Info, 2012).

2.1.3 Working Principle of OLEDs

OLEDs work in a similar way to semi-conductor LEDs but differ in their construction; a conducting thin film polymer is sandwiched between a cathode and anode, one of which is usually a noble- and the other a base-metal. Applying a voltage to these creates positive electron 'holes' and negatively charged electrons from the emissive layer which migrate into the conductive polymer. The recombination of these creates a decay state and the the emission of electromagnetic radiation which can be tuned to the frequency of visible light (Figure 2.3). Producing an alternating array of pixels, for red, green and blue can then form the basis of a display device (Dodabalapur, 1997).

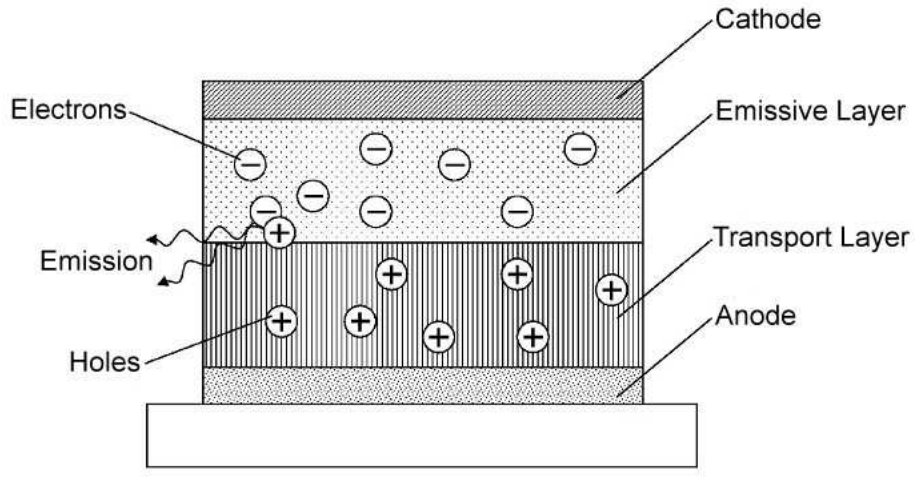

Figure 2.3: The working principle of OLEDs, showing the recombination of electrons and holes between the conductive polymer layers, generating light (Modified from; Mao, 2007)

2.2 Flexible Displays

Flexible displays extend the advantages of flat panels screens to a greater extent; they can be applied to a broader range of applications and are much more robust, not to mention much thinner and lighter than even LCD displays. Although a liquid crystal panel is often just millimetres thick, the total thickness of the completed device is a result of many components for light production, management and polarisation, all of which make the device bulkier (Figure 2.4).

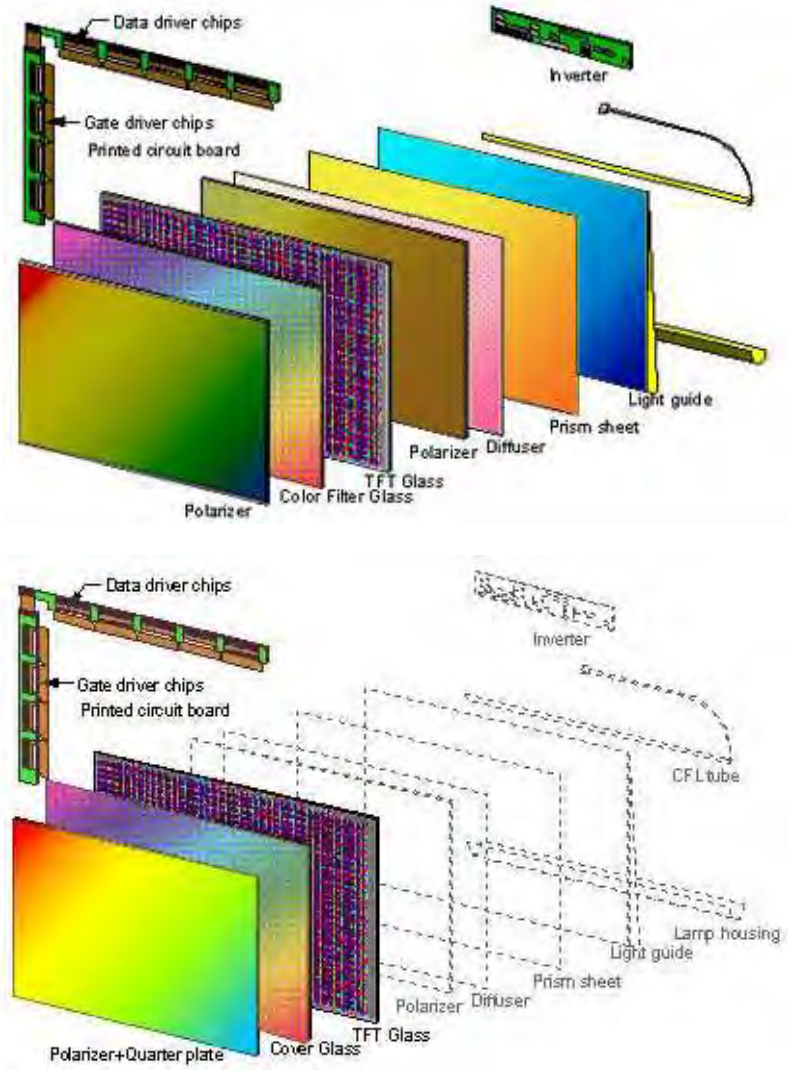

Figure 2.4: Components within a typical LCD (top) compared to those within a typical OLED display (bottom) highlighting the difference in thickness (Glyn, 2012)

The successful application of OLEDs is beneficial for the realisation of flexible displays because making a flexible LCD is a non-trivial matter for a number of reasons (Crawford, 2005);

Production: The lithography steps used for producing the active matrix on the substrates take place at very high temperatures, at which many potential polymers would degrade or warp.

Materials issues: Within an LCD panel there are many inflexible components required to make the display function which would crack under bending stress. Furthermore, effecitve light management in LCD displays relies on thick Perspex sheets which are also inflexible.

Fundamental problems: The internal cell spacing between the front and back planes in an LCD must remain constant, if the device is flexed this spacing changes, causing the liquid crystals to flow and disrupting the light guiding properties of the crystalline structure.

Although LCDs do not require the same high levels of barrier as OLED displays (Charton 2005), the latter do not suffer from the problems outlined above. In addition, overcoming existing challenges associated with OLEDs seems more achievable than those facing the development of flexible LCDs.

2.2.1 Commercialisation of OLED displays

It was only a matter of time before flexible electronics evolved from areas such as wiring and automotive heating elements to higher technology applications. As with many new technologies the potential is not fully realized until the initial idea has been launched and designers find novel ways of exploiting it. Whilst the use of OLEDs in lighting is widely discussed, OLED displays are attractive to manufacturers as a higher value proposition (Sheats, 2007). As stated previously, there are already screens on the market which utilise OLEDs, with other major manufacturers including Samsung and LG close to releasing their own devices (Samsung, 2012b; Telegraph, 2012). Much like

the first 14 inch LCD from Sharp, the technology will become more popular as manufacturers develop the technology, production becomes cheaper and market penetration increases.

2.2.2 Advantages of Flexible Displays

Glass based OLED displays have already reached commercial application, however a great deal of interest surrounds the development of flexible displays for numerous reasons;

2.2.2.1 Reduced Cost Manufacturing

Perhaps the largest drive for the development of flexible displays is the potential to carry out 'roll-to-roll' manufacturing. Continuous production methods tend to be more cost effective than batch processing (Plumb, 2005; McKenzie, 2006) and displays are no exception. The fabrication of LCD panels has required collaboration between major electronics manufacturers to reduce costs and make production viable (Reuters, 2011). Production is a stepwise batch process, each stage of which is wasteful due to the lithography techniques used. In contrast OLEDs can be printed on to a substrate using a printing technique, decreasing waste, production costs and increasing throughput (Choi, 2008). This technique also allows displays to be created in succession on a continuous sheet of polymer (Figure 2.5).

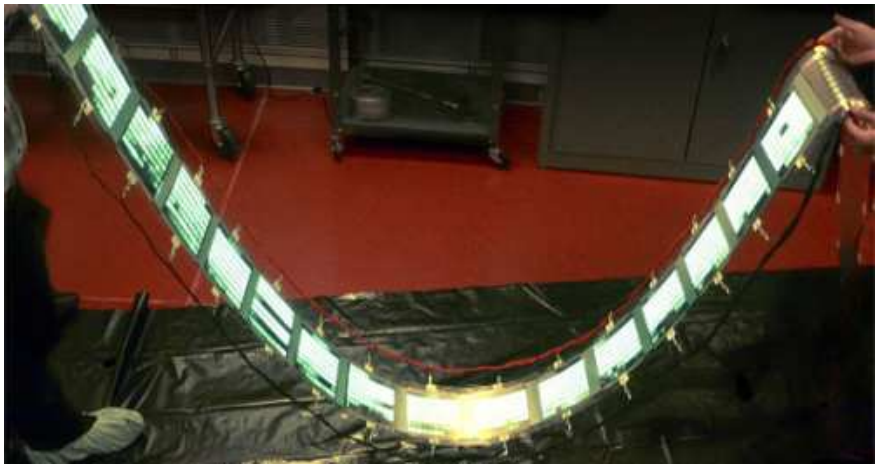

Figure 2.5: OLED roll-to-roll printing technique demonstration by General Electric (CNET, 2008)

2.2.2.2 Durability

Polymers often have a much greater shock resistance than silicon or glass (Crawford, 2005) since their flexible nature means they are more capable of absorbing and dampening impacts. Furthermore, with the increase in popularity of portable devices incorporating large screens a polymer based display has a reduced risk of breaking if dropped.

2.2.2.3 Thin Profile

OLED displays are emissive, meaning that they require no backlight, hence the main reason that such devices can be so incredibly thin. Sony's glass based XEL-1 display features a 3 mm depth profile, however production on polymer substrates will allow displays to be produced which are even thinner (Crawford, 2005). An extreme example was demonstrated by Samsung at FPD International in 2008 showcasing a 0.05 mm thick screen so thin that it was caught by air currents (Figure 2.6).

Figure 2.6: Samsung's 0.05 mm thick display panel (Engadget, 2008)

2.2.2.4 Portability

For an equivalent volume, polymers are typically lighter than glass, plastic based devices can be much lighter than equivalent glass based displays. The nature of flexible, lightweight electronics

will ultimately lead to applications which are not possible with existing technology; one example is the integration of a screen into the sleeve of a jacket, with the capability of live mapping and GPS information, an application currently under test by the U.S. Army (Figure 2.7). Eventually it could be possible to have a TV which one can roll into a tube and easily transport throughout the home or to another house as simply as transporting a newspaper or poster.

Figure 2.7: 4.3 inch flexible OLED display currently undergoing field testing by the U.S. Army (Engadget, 2010)

2.2.3.5 Engineering Freedom

One may suspect that some of the original application ideas of flexible displays were attempts by manufacturers to invent new markets to justify research into the area. A wrist mounted screen may have limited practical use for many people and marketing OLED TVs as LCD replacements would be difficult on the merits of decreased profile and weight alone. It is inevitable that many unexpected and innovative applications will emerge as the technology matures. 'OLED wallpaper' is a good example; as production becomes cheaper, massive OLED screens which can be applied to the internal walls of a room in a way similar to wallpaper may be achievable. These could be used as light sources to simulate daylight during winter months, or potentially as highly immersive

displays, allowing the room occupier to be surrounded by different landscapes at the touch of a button. This author predicted such an idea some years ago and in recent times Toshiba engineers have envisaged similar applications (Telegraph, 2009).

2.2.3 Disadvantages with OLED displays

Reading up to this point OLEDs may appear to be the next logical progression in display technology and one may even question why they have not yet become more commonplace. Problems have existed through the development of OLEDs and whilst many have been overcome, others are still prevalent;

2.2.3.1 Uneven Pixel Lifetimes

In an OLED display, red, green and blue pixels are normally created using a number of organic compounds (Millard, 2000), each of which emits light at different wavelengths. If all pixels were the same size and operated at a uniform driving power for the same length of time, the brightness of each primary colour would decrease unequally, with the highest energy blue emitters degrading quickest; this is a consequence of using an organic system. It was stated in 2007 that red and green emitters had been produced which lasted some 10^6 hours, whereas the best blues lasted around 10^4 hours (Aldrich, 2007). The lifetime issues have since been overcome with both the development of increasingly stable blue-emitters and through the use of novel device designs such as different sized pixels (Figure 2.8) or novel pixel arrangements (Park, 2009). Applying a lower driving current over a larger area means these domains can output the equivalent brightness as smaller pixels running at higher power. Another approach is to use white-emitting OLEDs for each pixel but with the addition of a colour filter, such as those used in LCD displays (CNET, 2012). Careful tuning of the size and operating parameters of pixels has resulted in even degradation of all pixels during the lifetime of a device.

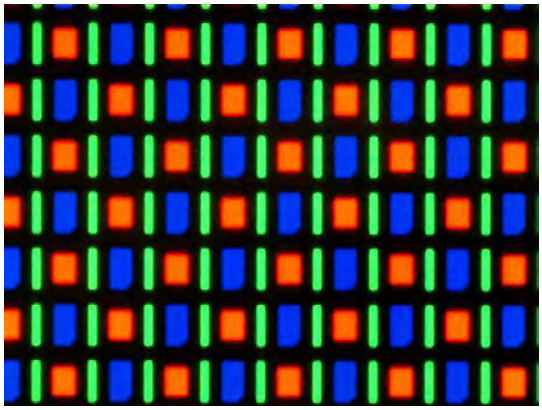

Figure 2.8: Example OLED screen at 200x zoom showing differences in pixel sizes (Rollings, 2010)

2.2.3.2 Image Persistence

OLED based displays can suffer from an effect known as 'screen burn', an artefact which can also be observed on old CRT displays and early plasma screens, in OLED displays it is the result of uneven pixel aging (Mori, 2006). As the brightness of each colour decays over time, the uneven lifespan of each colour can cause discrepancies between red, green and blue intensities between pixels. This results in screen 'burn-in', with the effect of creating areas of uneven brightness which can be seen on the screen regardless of the information displayed thereafter. It is commonly a result of showing static images for long periods of time such as channel logos or information found in video games. Due to techniques developed from past generations of displays to eliminate this effect, it is likely that similar preventative methods can be applied to OLED based displays. Furthermore, since their inception, more advanced OLED materials have been developed which have longer lifetimes than the first generation, reducing the effect that this problem would have during the lifetime of a product.

2.2.3.3 Manufacturing Costs

Perhaps the largest obstacle holding back OLED displays from the mass market are the production economics, one of the biggest drives for the development of flexible displays is the potential cost

saving rather than potential applications. Existing OLED products are manufactured using a shadow mask vacuum deposition technique (Millard, 2000), although this is an effective, well understood process, it is also wasteful. Combined with the current cost of OLED polymers, displays produced with this technique are relatively expensive. The collaborations between different companies which have resulted in city-sized factories being built for the sole purpose of manufacturing LCD panels has done a great deal to drive down the cost of manufacturing. It is likely that given time, similar partnerships will emerge for OLED screen production. The ability to employ a roll-to-roll manufacturing process is also expected to greatly reduce manufacturing costs, however a suitable flexible substrate is required.

2.2.3.4 Damage from Water and Oxygen

Many polymers exist which could be used as roll-to-roll production substrates, but none of these meet the range of requirements required for use in flexible displays. However, plastics are often blended, functionalised, coated and filled to impart additional properties and by doing so it is possible to modify a basic polymer to work in exceptional circumstances (Hanika, 2003). The problem of polymer permeability still remains prohibitive. In the food packaging industry, one common method to improve the barrier properties of plastics is the application of an impermeable coating such as aluminium oxide or silicon nitride to prevent the passage of water and oxygen (Hanika, 2003). Such barriers are comparatively low-tech and while they are effective for the shelf life of food, OLED barriers must last for many years, making the issue an even greater challenge (Hanika, 2003).

2.3 Material Requirements for Flexible OLED Displays

It has been established that the material requirements for flexible screens are very demanding. High quality glass already meets the needs for existing displays including surface smoothness, optical clarity, mechanical stability, chemical resistance, cost and barrier performance. Polymers are viewed as an alternative, but any material expected to be used as a replacement must perform comparably in these areas, either as a basic substrate or through the means of added functionality.

2.3.1 Comparison of Polymers

With such a large range of polymers in existence the most likely candidates have been defined as; polyethylene terephthalate (PET), polyethylene naphthalate (PEN), polycarbonate (PC), polyethersulphone (PES), polycyclic olefin (PCO), polyimide (PI) and polyarylates (PAR) (Crawford, 2005). It is important to note that this list only includes transparent polymeric films as a direct glass replacement. Materials such as super-thin glass and stainless steel have been considered by other groups, but as the former can only be used in a fixed position and the latter is not transparent hence is only suitable as a backplane, neither have been considered in this thesis (Crawford, 2005). Comparing a range of key materials properties it is possible to assess the suitability of these polymers (Tables 2.1 & 2.2).

Table 2.1: Comparison of key materials properties of preferred transparent polymer candidates for flexible OLED displays (Crawford, 2005)

	PET	PEN	PC	PES	PCO	PI	PAR
Coefficient of Thermal Expansion (-55 to 85 °C) ppm/ °C	15	13	60-70	54	74	17	53
Transmission at 400-700nm (%)	> 85	> 85	> 90	90	91.6	Yellow	90
Water absoption (weight %)	0.14	0.14	0.2-0.4	1.4	0.03	1.8	0.4
Young's modulus (GPa)	5.3	6.1	1.7	2.2	1.9	2.5	2.9
Tensile strength (MPa)	225	275	NA	83	50	231	100

Table 2.2: Properties of base films for polymer substrates (Choi, 2008)

	PET	PEN	PC	PES	PCO	PI
Thickness (mm)	0.1	0.1	0.1	0.1	0.1	0.1
Total light transmittance (%)	90.4	87	92	89	94.5	30 - 60
Retardation (nm)	Large	Large	20	< 10	7	Large
Refractive index	1.66	1.75	1.56	1.6	1.51	-
Glass Transition Temp. (°C)	80	150	145	223	164	< 300
Coefficient of Thermal Expansion (ppm/ °C)	33	20	75	54	70	8 - 20
Water absorption ratio (%)	0.5	0.4	0.2	1.4	< 0.2	2.0-3.0
H_2O barrier ($g/m^2/day$)	9	2	50	80	-	-

Examining the differences across Table 2.1; PET and PEN can be seen to have a low coefficient of thermal expansion, furthermore values of Young's Modulus show that polyesters are stiffer than the other polymers tested and the higher Tensile Strength shows that they are capable of withstanding greater stretching forces, a very useful property for a portable, flexible device. The two polyesters do however, have a lower visible light transmission compared to the other films and it can be seen that their intrinsic barrier properties are somewhat worse, but this final difference is insignificant given that no polymer is able to provide a barrier even close to that which is required.

2.3.2 Choice of Polyesters

DuPont Teijin Films, produce both PET and PEN polyester films, both of which are potential candidates as substrates in flexible displays. The information in Tables 2.1 & 2.2 suggests that polyesters would be the ideal material for use as a flexible displays medium, despite the higher price of PEN over PET, although it still remains cheaper than the other polymers considered; PEN would be the better choice given its all round improved properties (Figure 2.9). It has high optical clarity to at least the level required to meet the specification, a very high resistance to solvents, low

water uptake and is resistant against flexing forces. While it can be said that PEN films may have dimensional stability issues at elevated temperatures, thermal cycling processes can almost eliminate this (MacDonald, 2004).

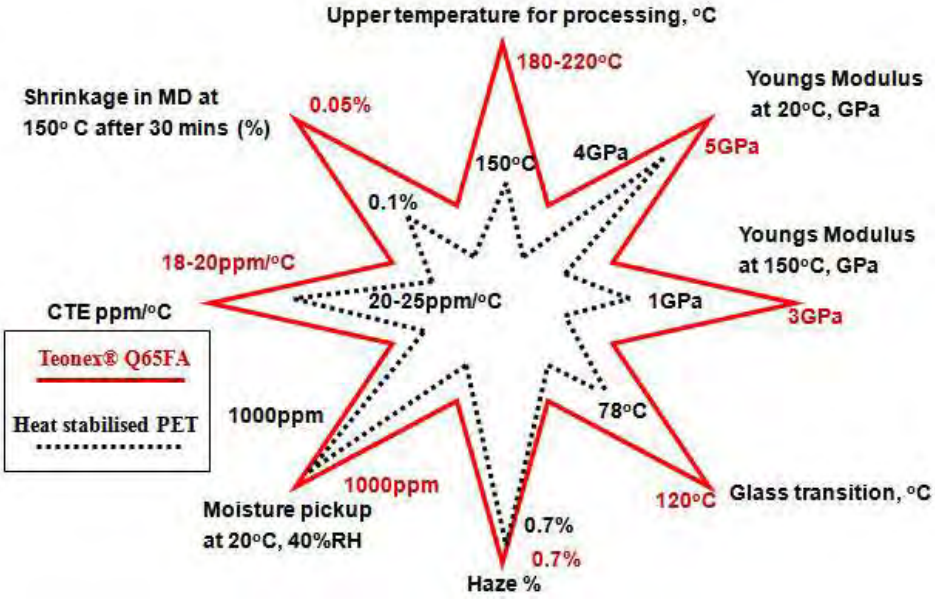

Figure 2.9: Comparison of properties for heat stabilised PET and 'Teonex' PEN (DTF, 2008)

Analysing particular requirements in detail allows us to compare the suitability of polyesters for application in flexible displays. All references in the text of Section 2.3.2 have been obtained from (MacDonald, 2004; Crawford, 2005; Choi, 2008; MacDonald, 2008a).

2.3.2.1 Optical Clarity

The clarity of polymeric substrates is important for emissive displays, particularly when the generated image has to pass though the material in question. Indeed, it is much more important for the front plane of a device to be as transparent as possible whereas the back plane can be made of a material such as stainless steel. A total light transmission of greater than 85 % of the visible spectrum and a haze of less than 0.7 % are nominal requirements for display substrates. All polymers presented in Table 2.1 & 2.2 meet these demands other than polyimide, which despite

being a very versatile polymer, has a yellow-brown colour, however it could still be utilised as a back plane.

2.3.2.2 Birefringence

Film birefringence is a major consideration when one considers devices which utilise polarised light, such as LCDs. Biaxially oriented polyester films exhibit birefringence and as a result are of limited applicability for such applications, however as OLED displays do not operate using polarised light so that they can be considered as suitable candidates.

2.3.2.3 Thermal Stability

Thermal and dimensional stability are highly important factors for materials on to which electronics or thin layers will be deposited. Until production techniques can be refined to allow ambient temperature printing, existing lithography steps must be used to manufacture devices. Such layer deposition may involve high temperature processing or thermal cycling, both of which can cause films with low glass transition temperatures (T_g) to change shape; a result of relaxation in the polymer structure. Polyester films are often biaxially oriented to impart improved material properties which can result in shrinkage and expansion when heated to T_g, which for PET and PEN is 78 °C and 120 °C respectively. Thermal stability can be improved using a heat stabilisation process, in which the film is exposed to high temperatures under low tension. Performing this results in a PEN film which exhibits shrinkage typically below 0.05 % when exposed to temperatures up to 180 °C for 30 minutes and 0.1 % for PET (Figure 2.10). In fact PEN demonstrates good dimensional stability up to 200 °C, which is within the requirements of a substrate for use in flexible displays.

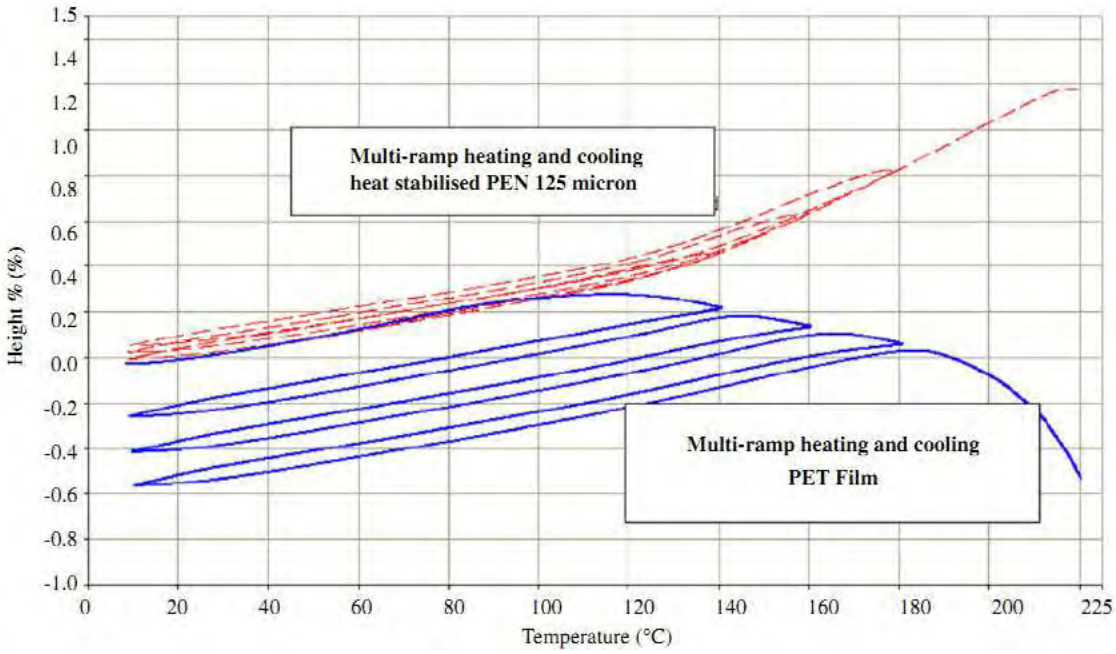

Figure 2.10: Comparison of shrinkage of standard PET and heat-stabilised PEN by thermal mechanical analysis (MacDonald, 2004)

2.3.2.4 Solvent resistance

During device layer deposition and especially as OLED printing techniques become more widespread, polymer films will be exposed to a wide variety of solvents. Amorphous polymers tend to have lower solvent resistance compared to those which are semi-crystalline. PET and PEN are known for their high solvent resistance and do not require additional coatings to achieve this.

2.3.2.5 Surface Smoothness

The components in a display device make up an active layer approximately 50 nm thick, the protective barrier coating utilised by DTF is of a similar depth. Consequently, any sufficiently large surface features have the potential to disrupt these thin layer structures (Figure 2.11). DTF utilises planarisers which have the ability to greatly increase surface smoothness, these are explained further in Chapter 7.

Figure 2.11: Light microscopy image of a short circuit caused in micro-circuitry by a film defect

2.3.2.6 Barrier Properties

Regardless of flexibility, a key characteristic for any substrate used in OLED based displays is a need for incredibly high barrier properties. The generally accepted permeability requirement for substrates is no more than 10^{-6} g/m²/day for water and 10^{-4} g/m²/day for oxygen, much higher than any other commercial application (Figure 2.12).

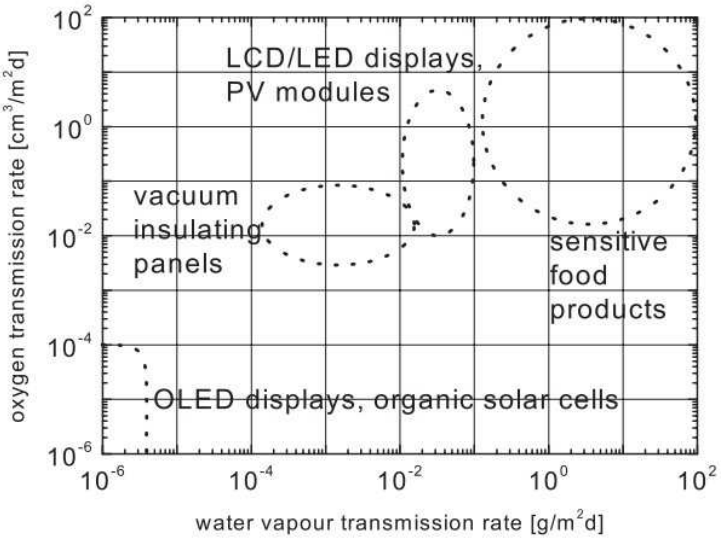

Figure 2.12: Barrier requirements of different polymer applications (Charton 2005)

The barrier properties of glass are around 10^{-12} g/m^2/day whereas the barrier of standard PEN is around 2 g/m^2/day (Figure 2.13). It is possible to improve this figure using various coatings, but reaching the required barrier performance is still very difficult. Resolving this issue is the key goal of this thesis.

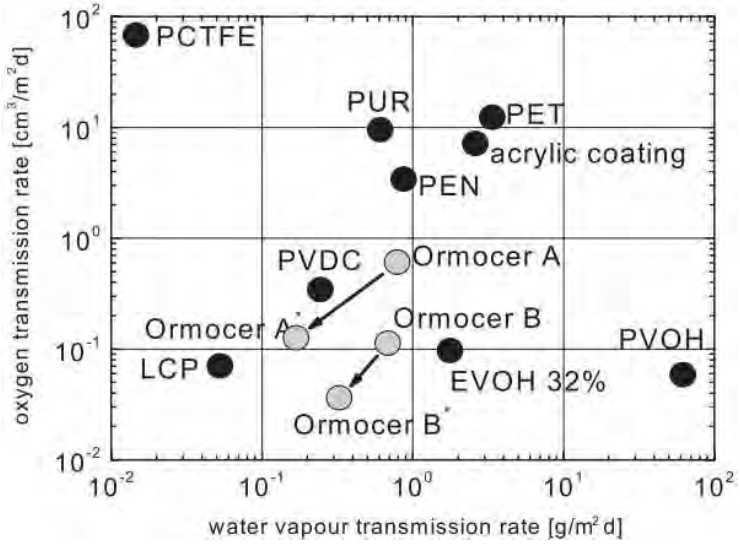

Figure 2.13: Barrier properties of uncoated polymers, including Polychlorotrifluoroethylene (PCTFE), Polyurethane (PUR), Polyvinylidene chloride (PVDC), Liquid crystal polymer (LCP), Inorganic-organic hybrid polymer (Ormocer), Ethylene Vinyl Alcohol (EVOH) and Polyvinyl alcohol (PVOH) (Charton 2005)

2.3.3 Requirements of Barrier Layers

Polyesters appear to be the best candidates for flexible display substrates. Any shortcomings they have can be overcome by post-processing steps such as the addition of planarisers or fillers, but the one deficiency they still suffer is that of their barrier properties, but this is one which effects all polymers (Figure 2.13). Table 2.3 shows typical values of oxygen and water transmission through PET and how they change with the application of different barriers using various techniques. While it can be seen that utilising a thin barrier film significantly increases the barrier performance of PET, the transmission of oxygen and water is still far too high to be useful in an OLED system.

Table 2.3: Comparison of the oxygen and water barrier properties of PET with different layers using a variety of deposition techniques (Decker, 2002)

Barrier Material	Coating Thickness (nm)	Oxygen Transmission ($ccm/m^2/day$)	Water Vapour Transmission ($g/m^2/day$)	Deposition Process
12 µm PET Film (No barrier)	N/A	100	64.64	
Aluminised PET (Single layer)	~30	0.31 - 1.55	0.31 - 1.55	Evaporation
Aluminised PET (Double layer)	2 x ~ 30	0.03	(No data)	Evaporation
SiO_x on PET	10 ~ 80	0.35 - 10	0.46 - 1.24	Evaporation
SiO_x on PET	10 ~ 80	0.08 - 1.55	0.5 - 5.0	PECVD
Al_2O_3 on PET	20	1.5	5	Evaporation
Al_2O_3/SiO_x on PET	50	2.0 - 3.0	1	Evaporation
Diamond-like carbon on PET	20	2	1.5	PECVD

Regardless of the choice of substrate, no material has yet displayed sufficiently high barrier properties and hence, this issue is still one of the largest hurdles still to be overcome before flexible OLED displays can be commercialised.

2.4 Industrial Relevance

One of the main differences between a typical PhD and an EngD is the industrial aspect of the latter, the research goal is directly relevant to the sponsoring company and is expected to have an impact on the business. The research presented in this thesis was carried out at DTF's Global Research Centre in Wilton, near Middlesbrough, England; using DTF's laboratories, with access to cleanroom facilities maintained by the Centre for Process Innovation. This section aims to put the findings in this thesis into the context of the company's research activities and highlight its relevance. All information in Section 2.4 was obtained internally from DuPont Teijin Films Ltd. with the exception of information presented in Section 2.4.3.

2.4.1 Company Background and Markets

DuPont Teijin Films is a 50:50 joint venture between DuPont and Teijin Limited, the company is "the world's leading producer of differentiated polyester films", including the Melinex® and Mylar® brand PET polyester and Teonex® brand PEN polyester. Specialising in products for specialty, industrial, packaging, advanced magnetic media and electrical & electronics markets, the company employs about 3000 people globally with dedicated marketing, technical and operations staff in every region of the world.

2.4.2 Market Spaces

DTF's broad product portfolio has allowed the company to operate in multiple industrial sectors, this section includes an outline of the market spaces of DTF's product range;

2.4.2.1 Electronics and Electrical Components

In the ever changing world of electronics, DTF has products for both existing and emerging developments. Current products include films for displays such as polarizing and diffuser films, flexible circuits, membrane touch switches, capacitors and cable products. More novel applications include flexible displays and both front and back sheets for low cost photovoltaic devices.

2.4.2.2 Construction

Polyester films are used during many construction processes, such as casting & release and the production of steel for both commercial and domestic appliances. DTF polyesters are also used in the manufacture of laminated glass and reinforced plastics for roofing and structural panels.

2.4.2.3 Health Care

With the increase in worldwide population, global healthcare markets continue to grow, the requirements of this sector will become more demanding and diverse over time. DTF products are utilised in a number of medical areas including; medical test strips, labelling and health cards.

2.4.2.4 Identification and Security

DTF products can also be found in the form of I.D. cards, security cards, driving licences and solvent resistant labels for safety warnings, healthcare dosage instructions and pressure sensitive labels. Polyester films are also finding use in existing and emerging Radio Frequency Identification (RFID) applications.

2.4.2.5 Image Printing and Recording Media

DTF films are used in the preparation stages of traditional printing processes, flexographic printing plates and as the final imaging media for a range of printing processes. Furthermore, the polymers are utilised for high density magnetic recording media, microfilms and engineering drawings.

2.4.2.6 Industrial Applications

DTF polyester films are used in many industrial applications, capitalising on polyester's inherent properties, films can be tailored for industry in a number of ways, including multiple thicknesses, a range of visual clarity and multiple surface enhancements giving improved adhesion or printability.

2.4.2.7 Packaging

DTFs packaging films are applied to a huge range of products; geography, climate and consumer needs differ due to regional variations, as a result so must the specification of the packaging.

Products are used in many areas including; sealant films, fresh foods, food on the go, shelf stable, cook in pack, liquid packaging and non-food products which require high chemical resistance.

2.4.2.8 Post Consumer Recycle (PCR) Films

A current area of great interest in all walks of life is the reduction in usage of raw materials and energy. DTF have introduced the world's first heat-stable polyester film that used 30% post consumer recyclate.

2.4.3 The Market for Flexible Displays

The focus of DTF has shifted over time to stay competitive, 20 years ago films for video cassettes and printed photography were large areas for the business. Whilst the move of media to an increasingly digital format has resulted in a sharp decline of these markets, new opportunities such as flexible electronics and photovoltaics have emerged. Commodity markets such as those for packaging materials have also seen threats from companies in developing markets which can manufacture these materials at a lower cost, but continual development of these basic products has ensured that the company has retained a significant market share.

The work in this thesis concentrates on the emerging flexible displays market which is still in the development phase. The main applications for OLEDs are expected to be in both displays and lighting applications, the markets for these are growing and predicted to see continued increases over the coming years.

2.4.3.1 OLED Lighting Market Forecasts

The market for OLED lighting is expected to see growth from 2011, reaching 1.5 Billion USD by 2015 and growing to 6.3 Billion by 2018 (Figure 2.14). Over 100 companies and universities are currently researching OLED lighting, primarily in the EU, US, Japan and Korea. There are approximately 20 OLED lighting organisations worldwide, Europe is currently the leading participant in OLED

lighting in terms of projects numbers, government funding, and participating companies (Forge, 2009).

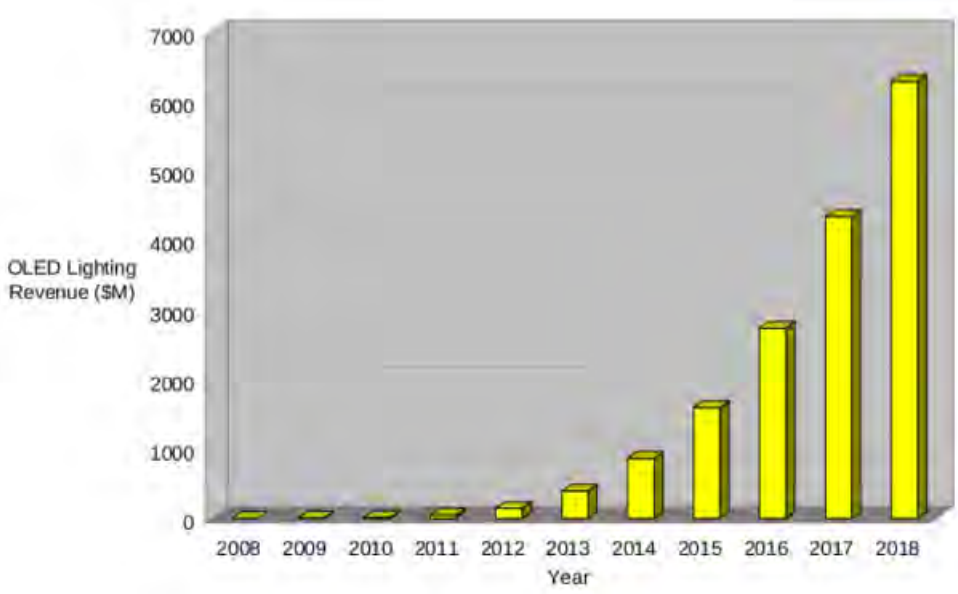

Figure 2.14: Projected market growth of OLED lighting from 2008 until 2018 (Forge, 2009)

2.4.3.2 OLED TV Market Forecasts

It is predicted that OLED based displays will account for half of all global OLED sales in 2012, increasing from 150 Million USD in 2011 to around 1.5 billion in 2013. (Figure 2.15) The global TV market is expected to reach 2.8 million units by 2013 up from just 3000 units in 2007 *(Forge, 2009).*

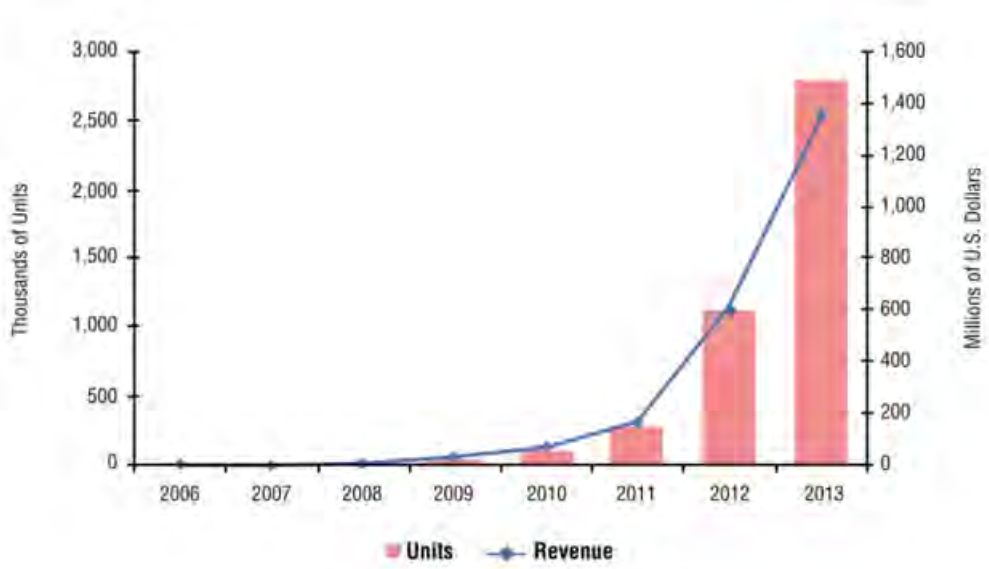

Figure 2.15: Sales forecast for OLED displays from 2006 until 2013 (Forge, 2009)

2.4.3.2 OLED Displays Market Forecasts

The OLED displays market is expected to grow to 7.3 billion USD by 2014, driven primarily by the adoption of active matrix displays found in mobiles phones and other portable devices (Zhu, 2009) (Figure 2.16).

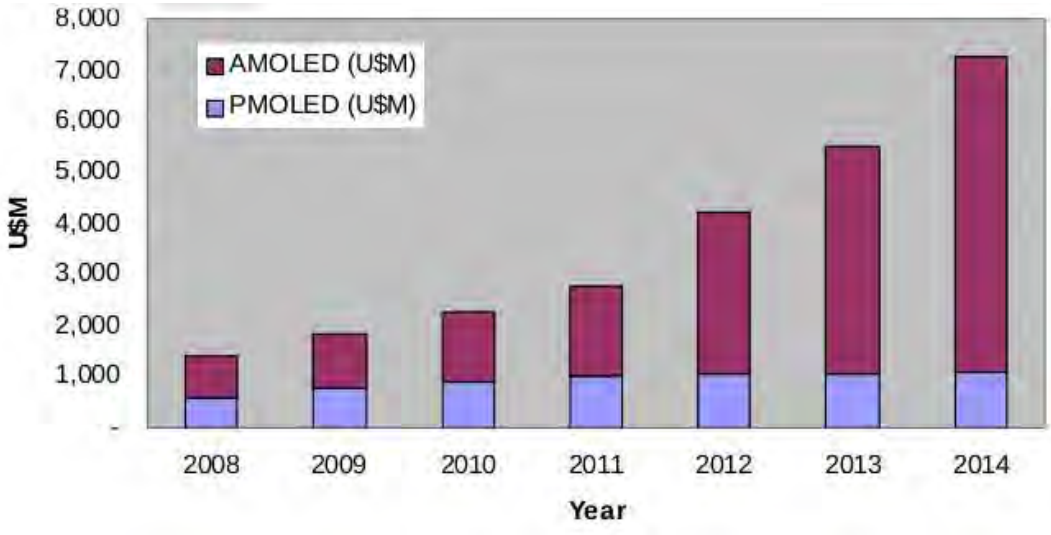

Figure 2.16: Predicted sales of OLED devices from 2008 until 2014 (Zhu, 2009)

It is clear from these forecasts that OLED displays and lighting are predicted to be huge growth areas in the near future. Any company involved in the supply of materials to this market will see a portion of this success, hence it is crucial from an industrial point of view to bring DTFs polymer films to a standard which would allow them to be used for flexible displays.

2.4.4 DuPont Teijin Films UK Ltd. Accounts Information

Table 2.4 shows both the turnover and post tax profit of DTF UK Ltd. from 2007 to 2010. Restructuring costs and movement away from traditional markets affected profits at the beginning of this period, however the interest generated by recent novel product lines has brought a large profit for the company more recently.

Table 2.4: DuPont Teijin Films UK Ltd.
Turnover and Gross Profit from 2007 – 2010 (Companies house, 2012)

	2007	2008	2009	2010
Turnover (£M)	85.3	97.2	82.4	129.6
Post Tax Profit (£M)	0.6	8.2	7.7	25.1

2.5 Chapter Conclusions

The advance of technology continues to improve our living standards. Although CRT displays worked sufficiently as display devices for TVs and computers, LCDs brought huge size reductions and allowed the deployment of screens in devices such as mobile phones. Without which mobile devices would have had to rely on screens utilised in early devices such as simple LED displays which would not have been capable of delivering the user experience to which we have become accustomed. The advent of flexible displays will bring forth another revolution in portability and

cost, with which the evolution of applications which have yet to be imagined will appear, however as briefly discussed in this chapter, the technology has a great deal of potential. Whilst some may question whether such technology is required, the progression of science and research will continue to reveal surprising developments.

It has also been demonstrated that polyesters are the most suitable material for this application through a combination of their properties and price. The market forecast for OLED based devices is set to be very large and if DTF manufactured films can meet the required specifications, the company would be in a very attractive position commercially, hence the requirement to perform this research.

3. Literature Review

3.1 Introduction

In Chapter 2 the requirement for high barrier performance of flexible OLED substrates was summarised. Now this chapter reviews the existing published work in the field of barrier films and their defects. It starts with an evaluation of literature in the area of OLED degradation to establish existing theories as to why OLEDs fail, before moving on to examine why permeation through thin films occurs and by which mechanisms in an attempt to determine the level of current understanding. This chapter then proceeds to assess current methods of measuring permeation to gauge the effectiveness of each to establish the most suitable technique for this study.

3.2 Causes of OLED Device Failure

Many publications exist which examine the reasons for OLED failure, and from these come a number of different conclusions. Typically, Sheats gave a summary of degradation theories in 1998 (Sheats, 1998);

- Reactions between the cathode and OLED polymer due to moisture entering the device through defects in the cathode created during fabrication.
- Reactions between the anode and OLED polymer, a result of using indium tin oxide (ITO) believed to release oxygen during operating, oxidising the OLED material.
- The susceptibility of OLED chemicals to photo-bleaching, due to their highly reactive nature.
- Short circuits created through topographic defects in the electrodes, promoting ion migration and overloading the OLED.
- Loss of efficiency, believed to be a cumulative effect of the above.

The same publication stated that through development of more stable compounds, the issues of photo-bleaching and loss of efficiency had been somewhat overcome. Furthermore it was surmised that indium tin oxide was unlikely to be a source of oxygen and the development of other anode materials would circumvent this. The only major problem which remained was said to be the growth of dark spots due to issues at either the cathode or the anode. Work has continued in both areas since the mid-nineties giving evidence supporting both theories.

3.2.1 Reactions at the Electrodes

As early as 1996 it was suggested that dark spots observed within OLED devices were the result of short circuits, caused by either moisture or impurities present in fabrication materials. These spots had the capability to affect either electrode (Aziz, 1996), as verified in the following year (Zou, 1997). Also in 1996, it was found that dark spots could be caused by localised electrical shorts; while the origin of these was not identified, the cause was thought to be a result of either impurities in the OLED polymer introduced during fabrication or roughness in the anode layer (Scott, 1996). However, it was also demonstrated that dark spots could result from delamination of the cathode from the OLED polymer (McElvain, 1996). The suggestion that cathode pinholes were responsible was restated the following year, it is remarkable to note that the same paper concluded that failure could not be due to the ingress of atmospheric contaminants because dark spots were still observed when the device was operated under vacuum. It was admitted that inhomogeneities in the underlying layers were likely to be responsible for cathode pinhole creation but a relationship could not be proved (Ettedgui, 1997). During the same year similar results were published, and it was found that dark spots were indeed the result of cathode delamination resulting from fabrication defects; however it was noted that when devices were operated under vacuum, although dark spots still appeared, the operating lifetimes were greatly extended. The same effect was observed when the device was encapsulated, hence it was suggested that the mechanism for failure when operated in an inert atmosphere was different from that seen when

operated in ambient conditions. Despite these findings the author stated that encapsulation was far too costly for such applications! (Savvate'ev, 1997) The theory that two degradation mechanisms were likely at work was supported by Philips in 1998; when operating the devices either at ambient conditions or under nitrogen, degradation reactions were found to be occurring at the cathode and anode respectively (Berntsen, 1998). In the same year, two publications observed that degradation was accelerated in humid atmospheres. Despite this, it was surmised that the formation of dark spots in encapsulated devices was a result of residual moisture within the device (Aziz, 1998a; Aziz, 1998b).

Although work to this point suggested two degradation mechanisms, some groups still maintained that only one was responsible, stating that dark spots were only initiated by pinholes in the cathode (Do, 1999). In contrast there were others who still argued that the anode was the problem; finding the OLED polymer material was unaffected by dark spots and the formation being due to a high concentration of oxygen in the anode; with dark areas containing no traces to suggest ITO decomposition (Nguyen, 1999). The following year it was acknowledged in one paper that "device degradation mechanisms remain elusive", stating that mobile ions from the electrodes or contaminants introduced during fabrication were responsible for device degradation, but concluding that they could affect either electrode (Shen, 2000). Also in 2000, it was observed once again that exposing devices to ambient conditions led to the formation of dark spots. The cause was claimed to be cathode delamination as a result of surface defects created during layer deposition. This paper also studied different OLED polymers and a range of cathode materials, finding the same results (Liew, 2000). The idea that topographical changes could affect the cathode was also investigated by another group. While they concluded that these affected the anode only, they disagreed that it was as a result of impurities introduced during fabrication (Do, 2000).

Novel work was published in 2001 attempting to identify the cathode pinholes responsible for device failure; an atomic force microscope was used to examine the cathode layer at the site of a developing dark spot during operation, however no perturbations were discovered, furthermore the

delamination effects described previously were also not observed. Once again it was noted that the dark spots grew when exposed to an ambient atmosphere and was assumed that aerobic oxidation was responsible for failure (Kolosov, 2001). It is quite possible that failures in this case occurred at the anode, assuming two degradation mechanisms are in operation. In 2002 it was stated again that metal migration leads to short circuits and that this was the main cause for device failure; during operation roughening occurs at the ITO/OLED polymer interface intensifying the current and overloading the OLED, forming dark spots (Ke, 2002). Yet papers were still being published claiming cathode pinholes were the reasons for dark spots (Kim, 2002). Whilst layer roughness was acknowledged as a problem, one publication stated that irregularities responsible for failures were present in the OLED polymer rather than the anode (Jin, 2003).

The following year it was said that the reaction of water with the OLED polymer caused failure at the anode layer interface rather than a reaction with the electrode itself, however the source of this water was not questioned, neither were the implications of eliminating its source (Xu, 2004). In the same year it was stated once again that darks spots can happen due to degradation at either electrode from various environmental phenomena (Aziz, 2004).

Later in 2007, the idea of uncontrollable imperfections from low materials quality or non-optimised fabrication conditions as the major cause of dark spots was reiterated, with ambient reactants acting only as promoters (Gardonio, 2007). Even as recently as 2009 the idea that surface roughness is responsible for dark spot occurrence was restated, said to be due to the intrinsic roughness of ITO and reporting an improvement with smoothing layers (Hsu, 2009).

3.2.2 Summary of dark spot theories

It is apparent that the cause of dark spots is still in dispute with evidence to support the many theories published over the years. Despite numerous observations that dark spot growth is promoted when operating under ambient conditions or improvements seen with encapsulation, no work exists which attempts to prevent the ingress of atmospheric contaminants to observe the

effect this has on device lifetime. Furthermore, no attempts to study the quality and permeability of the barrier layers has been carried out. It seems likely that black spots are caused by the ingress of moisture through pinholes in the protective barrier layers which then reacts with the electrodes, rather than the OLED material. With the move from glass to polymers as the base substrate for OLEDs, the increased risk of moisture ingress has mostly been ignored. It is suspected that as dark spots have been observed since devices were first fabricated on glass, the same mechanisms are believed to be responsible for the formation of these as on polymer based devices.

3.3 Encapsulation

Encapsulating OLED devices has been demonstrated to improve device lifetime with better protection lowering the occurrence of dark spot formation, even as early as 1994 large improvements were found when using encapsulation (Burrows, 1994). A number of groups observed extended operating lifetimes through encapsulation, along with operating under inert atmospheres (Savvate'ev, 1997; Berntsen, 1998; Aziz, 1998a; H. Aziz, 1998b; Liew, 2000; Schaer, 2001; Aziz, 2004; Park, 2005a). Application of a barrier coating is a simple way of providing encapsulation, early glass based devices typically used a thin layer of silver whereas polymer based devices typically use thin inorganic coatings.

3.3.1 Pinholes in OLED Encapsulation Layers

Despite the majority of papers failing to determine the upstream causes for device failure, a small number of publications have attempted to identify whether pinholes in OLED encapsulation layers could be caused by extrinsic particles.

When working with glass based OLEDs (Lim, 2001a; S. F. Lim, 2001b; Lim, 2002) it was stated that dark spot formation is a result of cathode corrosion due to water and oxygen, introduced through pinhole defects in the covering protective layer. This was demonstrated by intentionally creating

flaws in the barrier by depositing silica particles on the substrate before production. The theory was that the real-world occurrence of pinholes is caused by dust and dark spot growth rate is determined by the size of the pinhole. The first consideration of pinholes on a polymer base substrate was also in 2001; device failures on aluminium coated polymers were studied, finding OLED degradation to be caused by three external causes; dust particles introduced during the fabrication process, contamination by water vapour and pollution by oxygen. It was explained that for a given distribution of dust particles, water was three orders of magnitude more destructive than oxygen at room temperature. It was also believed that degradation was confined to pinholes created by the dust as the aluminium provided an excellent barrier elsewhere, however no further analysis was carried out to confirm this (Schaer, 2001).

3.3.2 Permeation through Thin Film Barriers on Polymeric Substrates

The application of thin film barrier layers to polymeric films has existed for much longer than OLED devices, permeation mechanisms through such layers have been the subject of interest for many years. Much of the original research in this field came from the packaging industry but tackles areas which have become relevant to OLED devices with the introduction of polymers as substrates. As far back as 1941 it was concluded that bulk oxides are effectively impermeable to moisture and oxygen permeation (Barrer, 1941), but as detection methods became more sensitive it was found that permeants were still capable of passing through barrier coatings (Prins, 1959). In 1983, the permeation of oxygen through thin aluminium films (10-50 nm) deposited on polyester was examined; using both SEM and light microscopy it was found that the density of pinholes on the surface determined the overall permeability of the film. This study concluded that the largest flaws were a result of particles which were already present on the surface, or were introduced during metallization. The smallest pinholes (<5 μm) had a size distribution comparable to that of airborne dust of a comparable size (Jamieson, 1983). Some years later it was stated that above a threshold thickness an aluminium barrier layer showed no improvement as the overall permeation

of oxygen and water was determined by the presence of pinholes. Contrary to previous work it was concluded that dust could be dismissed as the cause in 99% of cases as pinhole formation was more likely due to crystallisation of the condensed aluminium, film roughness or the vaporisation of any remaining solvents (Weiss, 1989). However, the suggestion that overall permeation is dominated by flaws in the barrier layers was repeated in 1993, with the additional discovery that many smaller defects are more destructive than a few large ones of the same total area (Rossi, 1993).

Three years later, the relationship between the surface morphology of barrier coated PET and its diffusivity to water was considered; it was found that for small regions of around 0.5 μm^2, smoother surfaces were found to offer better barrier coatings, however over large areas there was no correlation due to the presence of pinholes and surface deformations which dominated the permeation profile. It was concluded that pinholes were not the only source of permeation and another diffusion mechanism operates through the bulk oxide than that through pinholes (Garcia-Ayuso, 1996). In the same year it was also shown that although increasing barrier thickness slowed diffusion, the expected improvement is limited by defects such as pinholes, grain boundaries and micro cracks (Chatham, 1996). The following year it was found that the free energy of activation for transport through barrier coated films was the same as that for uncoated PET, suggesting that the barrier coatings were imperfect and permeation was relatively unrestricted (Tropsha, 1997), suggesting pinhole related diffusion was the main driving factor. This was backed up in 1999; where it was stated that the relationship of thermal activation energy for water vapour relies on barrier performance, which is determined by barrier morphology and defects (Erlat, 1999). In the same year, it was proposed that the interaction of water with the barrier coating plays a significant part in determining the barrier performance (Henry, 1999).

However, one year later a computer model of a thin film barrier was produced using the assumption that permeation only occurred through pinholes, the results compared very well to real world data, giving further evidence to support defect dominated transport for both oxygen and water (da Silva Sobrinho, 2000). Yet in 2001, it was found by one group that permeation through

barrier layers is dominated by nano-scale defects (< 1 nm diameter) created during layer deposition rather than from pinholes. Whilst the existence of pinholes was acknowledged it was said that these could not account for the entire transmission rate alone (Erlat, 2001).

A complete consideration of all the causes of permeation was considered in 2002, it was stated that barrier layers were more like nano-porous solids. A model was made which accounted for diffusion through the oxide lattice (<0.3 nm spaces), nano-defects (0.3-0.4 nm) and so called 'macro-defects' (>1 nm). Although no defects could be detected with microscopy on a real-world sample, permeation data indicated all of these contribute to the total permeation (Roberts, 2002).

By 2003, the requirement of high barriers for OLEDs on flexible substrates was being accepted as an application for ultrabarrier films, whilst not solely written about such devices one publication discussed the need of high barriers for such applications. Once again, it was concluded that permeation through barrier layers is indeed dominated by defects caused by dust and surface imperfections which lead to uncoated or damaged areas of polymer (Hanika, 2003). The following year a review of the existing knowledge was published which considered all applications of thin film barriers. It was stated that whilst evidence had been given for defect driven permeation there were also arguments to suggest morphological effects were quite influential. Furthermore if pinholes are completely eliminated barrier performance is only increased by less than three orders of magnitude, less than expected if pinholes were the sole cause (Lewis, 2004). The same year, it was identified that permeation predominantly occurs through tortuous nanoscale pathways through the structure of the barrier layer. This hinted that changing the barrier material would affect the chemical interaction between water and the barrier layer, changing the speed at which the water would travel (Erlat, 2004). Even as late as 2010 it was stated that surface perturbations in barrier films are caused by intrinsic flaws in the underlying polymer, rather than pinholes resulting from extrinsic defects (Tamagaki, 2010).

3.3.3 Summary of Theories on Permeation through Thin Film Barriers

Once again it can be seen that many theories exist for one observation, all of which offer supporting evidence. Whilst it has been stated that permeation is directly related to grain boundaries and micro-defects or large pinholes, it seems quite possible that all of these are in fact responsible, but with different severities. The large pinholes are likely to be the greatest contributor to thin film permeation, if these were to be eliminated the nano-pores would then be responsible for the majority until they were eliminated, whereby diffusion through grain boundaries would then dominate. Evidence that different barrier materials can slow permeation suggests that water must interact with the layer in some way, it is unlikely that this effect could occur through large pinholes due to their size relative to the water molecules, suggesting more than one permeation mechanism must be in operation. Smooth surfaces have also been shown to give better performance, this suggests that rough topography causes a thinning of the barrier during deposition, the problem of surface roughness is well understood in DTF and is tackled with the application of planarisers, discussed in detail in Chapter 7. It seems likely that if surface topography can cause barrier disruptions, extrinsic dust particles are also capable for the same reasons, whilst dust is believed to be the cause for pinholes this has yet to be conclusively proved.

3.3.4 Multilayer Films

Evidence to support the theory of pinhole driven permeation was found during research of multilayer barrier films, in 2002 an OLED device fabricated on a 175 μm PET polyester substrate was demonstrated, featuring an alternating organic-inorganic multilayer barrier film. It was claimed that WVTR vales of 2×10^{-6} were observed using this technique (Weaver, 2002). Despite this initial success, the following year multilayer barrier systems on flexible substrates were demonstrated to be at high risk of damage resulting from flexing stress through handling, causing cracks to form in the multilayer barrier stack (Chwang, 2003). Furthermore it was determined in 2004 that the apparent high barrier performance reported two years previously was not valid; the

barrier stack is essentially a series of many single layer barriers, permeation through each is controlled by the presence of defects. Permeants still progress through the film but the multiple layers create a 'tortuous path' through which they must traverse, in fact there is no change to the steady state permeation flux which still occurs at the same rate as with single layer barriers (Graff, 2004). Some agreed that whilst previous work with multilayer barrier shows much potential, they still require a great deal of work (Charton 2005). In 2007 an in depth modelling study into multilayer barrier films was undertaken which found two distinct permeation regimes; the first being when the organic layer thickness is less than the average size of the defects in the organic layers and the second when the thickness is larger. In the former the "tortuous path" mechanism operates, however, a simple diffusive mechanism operates in the latter. This suggests that the biggest gain in barrier performance can be obtained when operating in the first regime, however each layer must be incredibly thin, to a level which is "approaching the limit of conventional coating process capabilities". Furthermore these layers must be deposited in ultra-clean conditions where particles larger than the barrier thickness must be excluded, but such tight control of manufacturing hygiene would be difficult to implement in a roll-to-roll production method. As it is believed that the presence of dust is the same problem which affects single layer in a barrier stack, if such contaminants can be excluded from the multilayer process it would be a more attractive proposition to then use single layer barrier layers (Greener, 2007). As recent as 2010, cracking effects in multilayer barriers were investigated and their effects on permeation documented, showing that such systems are still far from usable (Jia, 2010).

3.3.5 Evaluation of Existing Literature

It is apparent that the cause of failure in OLED devices has not yet been identified, it seems very likely that the cause of dark spots in devices is in fact due to a number of different failure mechanisms. With improvements in fabrication and construction materials the causes which were cited for failure in the mid-nineties are unlikely to be the reason for which they now fail. Evidence

showing that the growth of these dark spots is promoted in ambient conditions suggests that airborne species have a detrimental effect, however very little work considered the 'upstream' causes of eventual failures. In some cases it was identified that cathode failure was due to a reaction with airborne water, but it seems unusual that no attempts to determine the source of this were carried out. Use of the calcium test also demonstrates that degradation can still occur in the absence of active components, this is discussed in more detail in Chapter 6. As it has been shown that increasing surface smoothness improves barrier properties, one can conclude that the most extreme surface disruption would be caused by the addition of extrinsic particles. Failures are likely to be a combination of a number of permeation mechanisms which have decreasing levels of severity, whilst some evidence for these exists in the literature, there has been no attempt to quantify the direct relationship between individual defects and their contribution to the ingress of permeants. Very little work exists on barriers coated on to polymeric materials used for OLED devices, a number of conclusions have been made but have a great deal of assumptions and tend to be based on other work rather than direct measurement. Finally, whilst multilayer films show high apparent barrier properties, it has been found that these more expensive structures that are difficult to fabricate, do not offer a greater performance increase.

3.4 Techniques for Measuring Barrier Film Performance

It seems likely that pinholes in the protective barrier layers are the major cause of OLED failure offering low resistance pathways for moisture to enter the device. As high barrier films are required for OLED applications, powerful techniques to measure their performance to ensure they are acceptable for use in devices have been developed. It has been stated that direct observation of surface defects by techniques such as AFM and SEM are very inefficient (Zhang, 2009) due to the low frequency of defects and the small field of views afforded by such analysis at the required resolutions. Furthermore it has been concluded that searching for pinholes using a technique such

as SEM is "very difficult, if not impossible" (da Silva Sobrinho, 1999). Moreover, barrier layers are very thin, to the degree that they appear transparent using large area optical inspection methods. As the continuity of a barrier film cannot be directly measured it is much more simple to test their barrier properties to gauge the quality of the coating, whilst this does not give information about specific defects it does reveal how well the film would perform in a real world system. A number of techniques are now available allowing the detection of very low values of water permeation through thin films;

3.4.1 MOdern CONtrols (MOCON) Aquatran

Analysis tools manufactured by MOCON, Inc. are some of the most common for measuring the barrier properties of thin films (Dunkel, 2005; Nisato, 2002), the most sensitive of which is the 'Aquatran Model 1' (Table 3.1).

Instrument Name	Detection Level ($g/m^2/day$)	Year
Cup Method	5	1950
IRD (Infra red)	0.5	1968
Permatran® W	0.05	1975
Permatran-W® 3/31	0.005	1994
Aquatran®	0.0005	2002

Table 3.1: Table charting progress of WVTR sensitivity measurements (Maixner, 2002)

The equipment is described in detail by the manufacturer (Stevens, 2009; Aquatran 2006; MOCON Pres. 2010). A film sample is sealed in a diffusion cell, on one side of which a highly saturated wet environment is maintained at a constant temperature, whilst on the other a dry nitrogen carrier gas is passed to a coulometric phosphorous pentoxide sensor where is it claimed that all water vapour which enters is converted to a measurable charge (Figure 3.1).

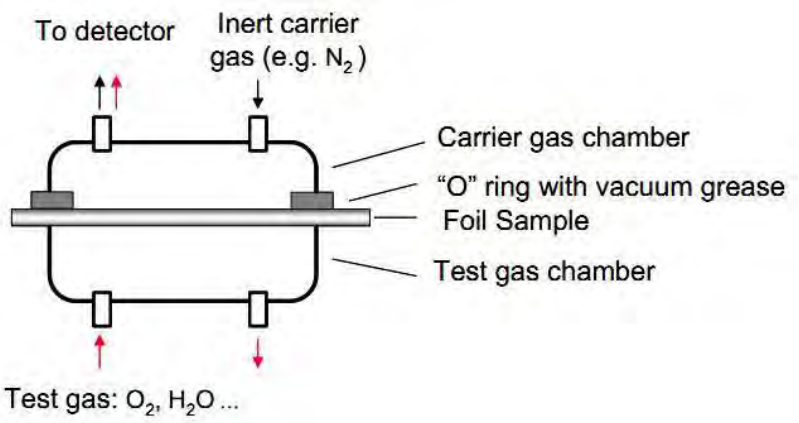

Figure 3.1: Schematic representation of a standard test cell in a typical permeation testing machine (Nisato, 2002)

The current detection limit of this technology is around 5 x 10^{-4} g/m^2/day for water vapour. As OLED substrates are required to have water vapour barrier properties of at least 1 x 10^{-6} g/m^2/day, it is inadequate for existing requirements.

The Aquatran is a straightforward, non-destructive method of monitoring barrier performance of thin films, however as it is only capable of measuring bulk permeation for a sample and cannot meet the demands of high performance barrier materials, hence it is unsuitable for this work.

3.4.2 Tritium Permeation

One highly sensitive method of measuring the water vapour transmission rate (WVTR) involves the application of a radioactive tracer (Dunkel, 2005; Groner, 2006; Dameron, 2008; Stevens, 2009; MOCON Pres. 2010). Tritiated water contains one hydrogen tritium oxygen (HTO) molecule for every 1667 water molecules. A 1 cm^3 droplet of this is placed on one side of a test cell creating an environment at 100% relative humidity, the test substrate is then clamped between two o-rings within a chamber (Figure 3.2).

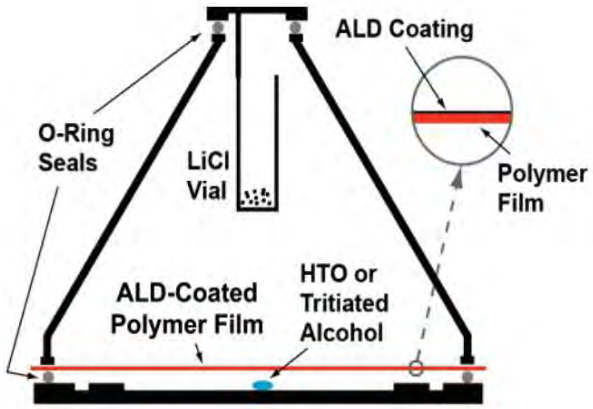

Figure 3.2: Schematic of typical HTO barrier testing apparatus (Dameron, 2008)

Water vapour which travels through the substrate can be detected by one of two methods; either passing a carrier through the downstream side of the cell to transport any permeant to an ionization chamber where it can be detected, or via a hydroscopic salt which absorbs any permeant and the levels of HTO can be calculated be measuring radioactive decay. Tritium detection is very sensitive, it is reported to be capable of a theoretical detection limit of 2.4 x 10^{-7} g/m^2/day and has been demonstrated to 1 x 10^{-6} g/m^2/day when tested with aluminium foil, making it more than 1000 times more sensitive than the detection abilities of the MOCON Aquatran. Despite its sensitivity there is very little evidence of it seeing widespread use, it is believed that the main reason for this is due to the radioactive nature and toxicity of tritium. Not only is HTO hazardous to handle, but its use generates highly dangerous contaminated waste (Bryan, 2005).

As a tool for measuring WVTR, tritium detection is very powerful in that it is both highly sensitive and non-destructive, meaning the test substrate can be subsequently examined using other analysis techniques. However, as HTO detection is only capable of measuring bulk permeation across a sample, combined with the serious health risks, it is not suitable for use in this thesis.

3.4.3 Mass Spectrometry

There are alternative analysis methods which are capable of very high levels of sensitivity, one of which is mass spectrometry detection (Norenberg, 1999; Nisato, 2002). A volume of a gas is placed into a stainless steel cell, which is subsequently sealed with the test polymer and placed into an ultrahigh vacuum (~10^{-8} Pa). After a few hours it is transferred into a test chamber, in which the side sealed with the polymer is positioned to face a quadrupole mass spectrometer; this monitors the partial pressures of numerous mass / charge ratios of any gasses escaping from the cell which can then be plotted as a function of time. As a fixed volume of gas is placed into the test cell at the start of the experiment, the drop in partial pressure can be measured, the techniques have been reported to achieve sensitivity figures of around 1 x 10^{-6} g/m^2/day.

Mass spectrometry detection is very sensitive, and is able to reach the requirements for testing OLED substrates when carried out using very small samples. It can also be considered to be a non-destructive method as other analysis techniques can be applied to the test substrate after detection. Despite its strengths, this is another procedure which is only capable of measuring bulk permeation and requires very specialist equipment which may not be readily available, hence its rarity in the literature and why it is not suitable for work in this thesis.

3.4.4 X-ray and Neutron Reflectivity

This is an unusual technique which has been applied to multilayer barrier films to determine the permeation rate of water and observe structural changes (Bryan, 2005). Swelling of individual polymer layers can be observed as water progresses through the film by plotting specular X-ray reflectivity as a function of time under elevated humidity and temperature. Neutron reflectivity is used to monitor water distribution throughout multilayer stacks using a deuterated tracer under ambient conditions. It is claimed that using the X-ray technique the density of neutron scattering can be measured over material depths of several thousand Angstoms with a single digit resolution, layer swelling of around 7 ±5 Angstroms has been demonstrated.

This is a very sensitive technique capable of detecting slight differences in polymer thickness as a direct result of water permeation and its distribution throughout the system. However, despite this it can only measure the progression of water through film but not the location of defects, or the volume of water that diffuses through, hence it is unsuitable for this study.

3.4.5 Reactive Oxygen Etching

Although the majority of permeation techniques discussed up to this point can achieve WVTR sensitivities of the required 10^{-6} g/m²/day, they only provide bulk permeation data and cannot provide information about the pinhole locations through which it is believed that moisture permeates. Reactive oxygen etching is different, it allows optical inspection of defect sites by highlighting the 'cavity' under any barrier flaws (da Silva Sobrinho, 1998; da Silva Sobrinho, 1999; Dennler, 2001). By exposing the inorganic barrier coated side of a polymer to an oxygen plasma, any flaws present in the barrier film allow the plasma to etch the underlying organic layer, whereas the inorganic barrier is resistant to this effect (Figure 3.3).

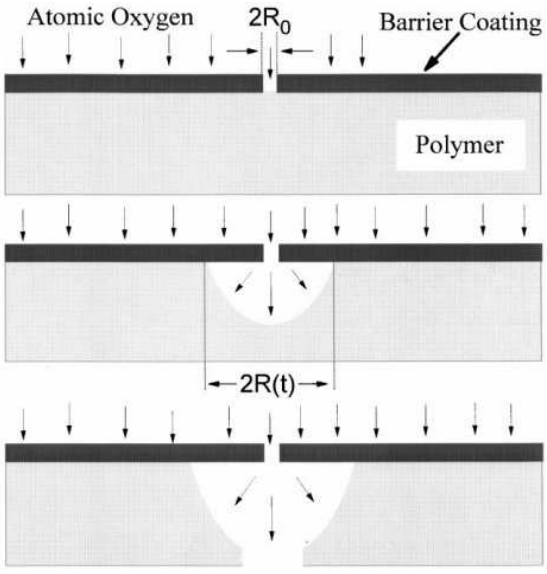

Figure 3.3: Schematic representation of the undercutting effect of an oxygen plasma on a barrier coated polymer (da Silva Sobrinho, 1999)

These sites can then be labelled by coating the bare polymer side of the film with a corn starch solution and exposing the barrier side to an iodine vapour; as this diffuses through holes in the barrier layer it encounters the starch in the newly formed cavities and turns into a dark blue colour (Figure 3.4). Using this method the locations of barrier breaks are made visible to the naked eye, allowing rapid inspection of large areas of film.

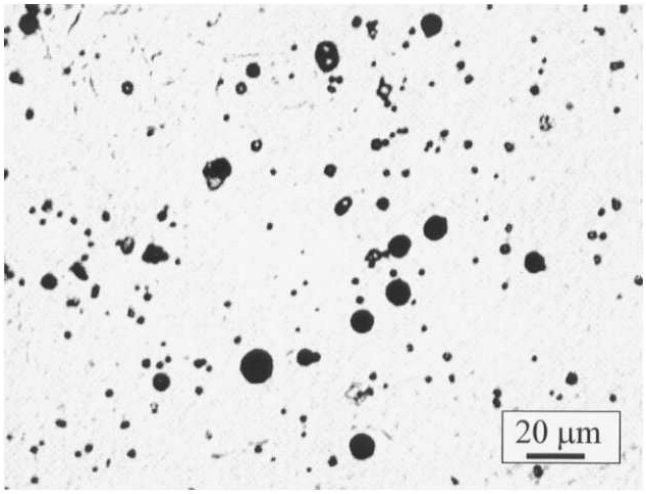

Figure 3.4: Optical microscopy of a labelled, 25 nm SiO_2 coated PET sample after oxygen plasma etching for 2 hours (da Silva Sobrinho, 1999)

This technique can also be used to provide an estimation of moisture permeation; the growth of the undercut regions is nearly linear with respect to exposure time, this relationship allows extrapolation back to time = 0 and hence the size of the barrier defect can be calculated.

Reactive oxygen etching allows exact pinpointing of the defect sites which are directly responsible for water permeation, it is also possible to estimate with reasonable accuracy the permeation values of the test substrate. This technique allows very large areas of film to be rapidly analysed on a scale not possible using any other technique. However, this method is destructive and whilst permeation rates can be calculated, these are still theoretical rather than directly measured values, as such it is better suited to rapid, large area defect counts.

3.4.6 The Calcium Test

3.4.6.1 Optical Inspection

The final technique for measuring WVTR across barrier films is the so called 'Calcium test'. Like reactive oxygen etching it allows defect sites to be pinpointed but in addition is capable of measuring the permeation rate of water vapour through the barrier layer (Nisato, 2002; Nisato, 2003; Adam, 2007; MOCON Pres. 2010; Bouten, 2002; Carcia, 2006; Carcia, 2009). There are two versions of the calcium test; the most common relies upon the visual difference observed during the corrosion of calcium metal into transparent calcium oxide. A thin film of calcium is deposited on to the surface of a barrier coated test substrate which is then encapsulated on to a glass plate using an epoxy resin (Figure 3.5) this is then subjected to elevated humidity and temperature to accelerate the aging process.

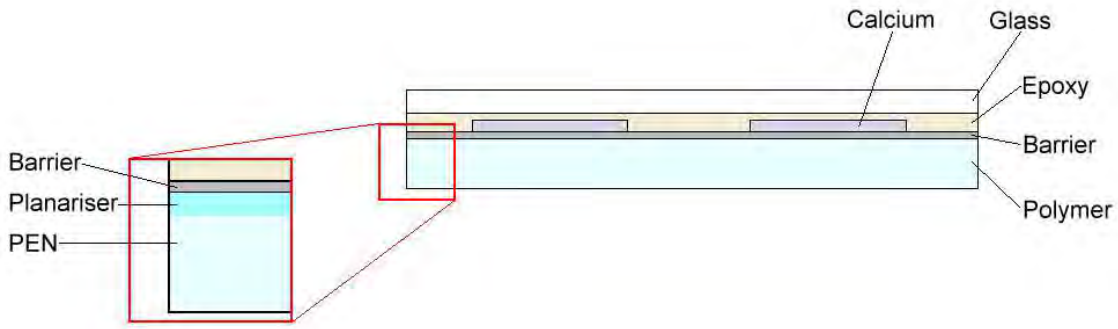

Figure 3.5: Typical calcium test cross section

As water permeates through barrier flaws it encounters the metallic calcium, whereupon a reaction takes place turning it into transparent $Ca(OH)_2$. The test cell is monitored using a video camera or transmission light microscope with which images are intermittently captured; the progression of water into the cell is observed as light regions which grow in size over time (Figure 3.6).

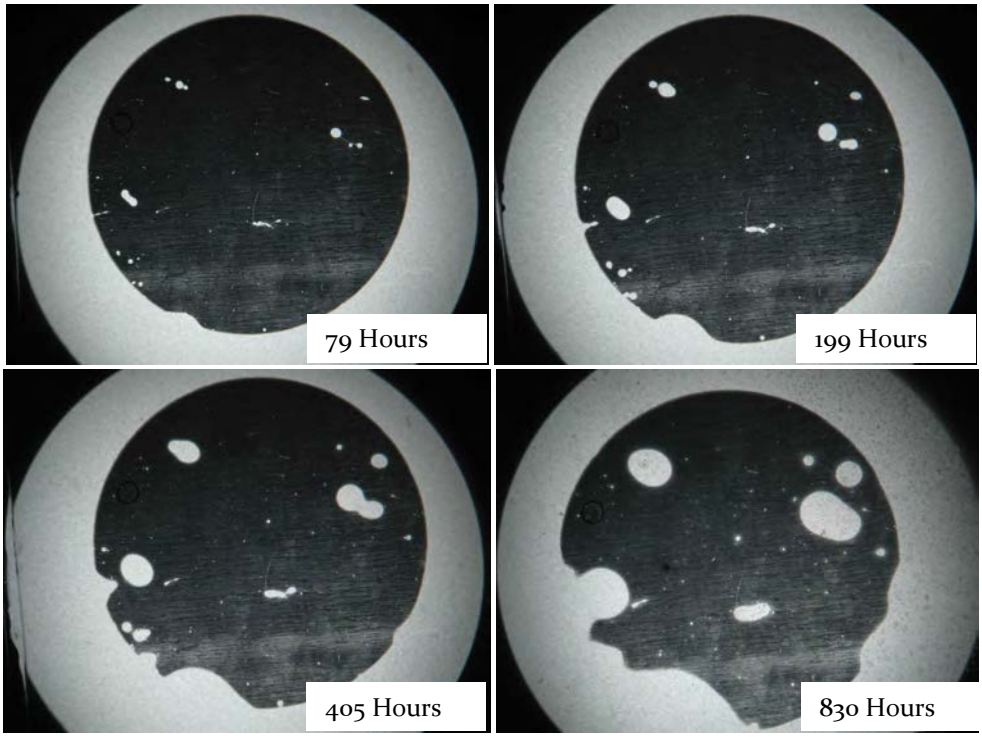

Figure 3.6: Top-down transmission light microscopy images of moisture progression through a calcium test cell, elapsed test time inset in each image

As the calcium thickness can be controlled with great precision, the total area of calcium oxide can be measured, thus the volume of calcium which reacts can be calculated and hence the quantity of permeant deduced. With multiple image captures, this can be plotted as a function of time to allow the permeation rate to be calculated. Water vapour transmission rates down to 10^{-6} g/m²/day have been reported with this technique.

3.4.6.2 Electrical Resistance

An alternative but less common approach to using the calcium test involves monitoring the conductivity of the metal across the cell rather than light transmission through it (Paetzold, 2003; Choi, 2007; MOCON Pres. 2010). This allows for continuous online measurements to be taken, furthermore there is no risk of sampling fluctuations which may arise using optical methods, such as variations in the light output. The electrical test cell is constructed in a method similar to the

normal calcium test, but with the addition of silver metal pads which contact either side of the calcium. As water vapour permeates through the barrier layer it will react with the calcium metal, as calcium oxide is an insulator the cross section of the conductive material decreases, increasing the overall resistance. WVTRs of 10^{-6} g/m²/day have also been reported using this technique.

The calcium test allows sites of water ingress to be determined with high precision with the addition of permeation data, it can also be considered to be non-destructive technique as post-calcium test samples remain undamaged allowing other analyses to be performed. It is stated that the test cannot distinguish between oxygen and water permeation (Stevens, 2009), however it has been demonstrated that below 200 °C oxygen does not participate in the reaction and acts only as a carrier gas (Adam, 2007) only reacting at temperatures above 300 °C (Cubicciotti, 1952). It has also been determined that in ambient conditions, water is 1000 times more destructive than oxygen (Kolosov, 2001), hence the suspicion that water is the damaging species. With the combination of both permeation data and the non-destructive nature of this technique, it was chosen as the most suitable for work within this thesis.

3.4.7 Evaluation of Permeation Techniques

An appraisal of publications since 1990 revealed that the calcium test is the second most common technique for measuring WVTR (Figure 3.7); as the calcium test is a relatively new method it is likely that this division will decrease as the calcium test becomes more widespread.

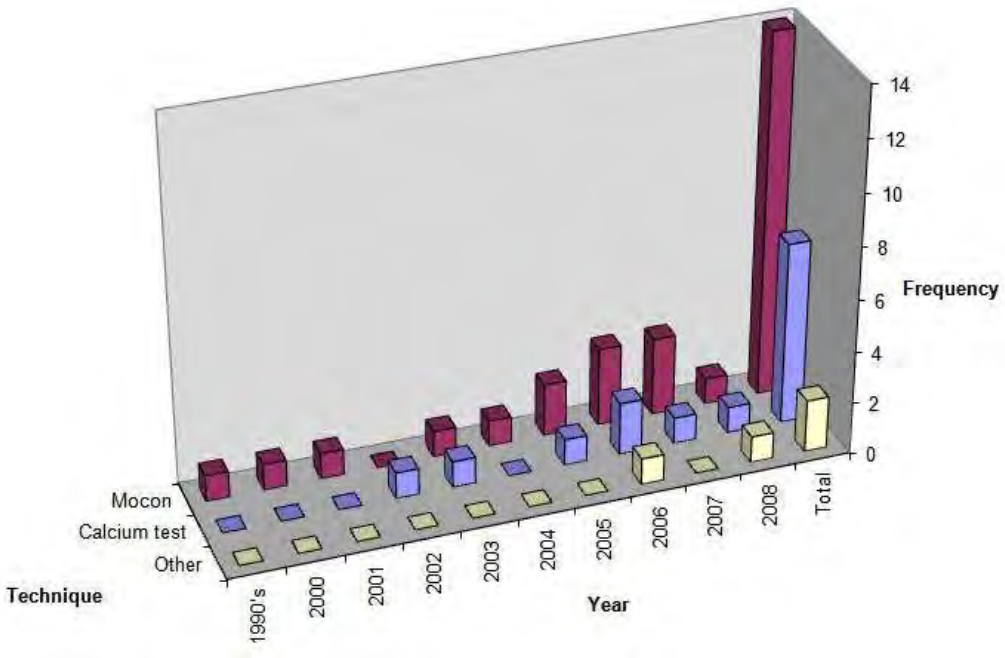

Figure 3.7: Frequency of techniques used to measure the WVTR of barrier films since the 1990's (Cullen, 2007)

Comparing all the techniques which have the required sensitivity, the simple methodology afforded by the calcium test is very likely to be the reason that it is gaining popularity in permeability studies. Even so, it remains under development with constant improvements and redesigns occurring through use (Edge, 2009). The increased popularity however and the ability to monitor not just the average, but the localised permeation rate through barrier defects make this a very useful procedure. An overview of the techniques compared in Section 3.4 demonstrates the strengths of the calcium test compared to other techniques (Table 3.2)

	MOCON	Tritium	Mass Spec.	X-ray	Reactive Oxygen	Calcium Test
Sensitivity ($g/m^2/day$)	5×10^{-4}	2.4×10^{-7}	1×10^{-6}	-	-	1×10^{-6}
Permeation Measured	Bulk	Bulk	Bulk	Progress	Pinhole	Pinhole
Detection Capability	Water Oxygen	Water	Multiple Species	Water	None	Water
Permeation Determination	Direct	Direct	Direct	None	Estimated	Calculated
Destructive technique	No	No	No	No	Yes	No

Table 3.2: An overview of the most common permeation measurement techniques

A number of techniques for measuring permeation have been discussed, from these it has been demonstrated that only two are capable of highlighting pinhole sites through which water appears to pass. The calcium test is the preferred analysis method, its appearance in the literature has only demonstrated its application as a permeation technique with no evidence of it being employed otherwise. In this thesis the ability of the calcium test to emphasize defect sites will be fully exploited.

3.5 Conclusions

Very little work exists which specifically examines barriers applied to polymers for use in OLED devices. It is apparent that the cause of failure in OLED devices has not yet been identified. Failures in early examples were probably caused by problems which were correctly identified in research of the time, but were not a result of permeation and have since been eradicated. Evidence of the promotion of these failures in ambient conditions, coupled with theories that permeation is primarily caused by large pinhole defects in the protective barrier layers supports theories that moisture ingress is the main cause for the failure of devices. There have been no attempts to

quantify the direct relationship between individual defects and their contribution to the ingress of water, or to determine the 'upstream' causes of eventual failures. Whilst dust is said to be a problem there is no definitive evidence to confirm this. Finally, whilst multilayer films show high apparent barrier properties, it has been found that these expensive, more challenging to fabricate structures, do not offer a performance increase, hence work to improve single layer barriers is still the core focus of this work.

A number of techniques now exist which allow the detection of water at the required sensitivity, but many of these can only monitor bulk permeation figures. There are only two which can be used to highlight specific defect areas and of these, the calcium test is the only one which can be considered to be non-destructive. Its mechanism of action also demonstrates there are major areas of moisture ingress in thin film barriers which are not caused by the active components present in an OLED device, providing compelling evidence that large pinholes are the most significant contributor. It is believed that whilst these are not the only cause of thin film permeation, such defects are the most destructive and their eradication will be a major step towards the commercialisation of flexible displays.

The work in this thesis aims to address the gaps in existing knowledge by using the calcium test to monitor permeation levels of specific defects with subsequent analysis using AFM and SEM to allow compositional and structural data to be compared to permeation. Such information will assist in identifying the causes of barrier failure and the critical features which result in barrier film disruption. This will confirm whether the suspected larger pinhole defects are responsible for the greatest permeation and determine their source. It is also expected that a model system can then be produced using artificial defects to replicate these flaws, confirming the fundamental factors which determine whether a defect will cause a barrier break. Such a detailed, direct analysis of the defects in thin barrier films had never been performed before the work described here.

4. Methods and Materials

4.1 Introduction

This Chapter describes the main methods employed used to investigate film defects: microscopy and the calcium test. The experimental techniques used to create samples is also presented, including a comparison of surfactants for the synthetic defect particles system.

4.2 Microscopy Techniques

4.2.1 Atomic Force Microscopy

All references for this section were obtained from (Phillips, 1994; Veeco, 2000; Magonov, 2000; Zhdan, 2009; Qi, 2011).

4.2.1.1 Overview

The atomic force microscope (AFM) is one of a family of microscopes where a sharp probe is scanned across a surface and interactions between this and the surface are monitored to produce meaningful data about the sample. The AFM is an evolution of the scanning tunnelling microscope (STM) which was developed in 1982 at IBM, with the AFM developed as a collaboration between IBM and Stanford University in 1986. The invention of scanning tunnelling microscopy (STM) allowed visualisation of surface structures with true atomic resolution, when first demonstrated it revolutionised microscopy. It works on the principle of placing a sharp metallic probe in the immediate vicinity of a conducting or semiconducting sample and applying an electric potential between the two, it is then possible to detect a tunnelling current which can be used to generate an atomic-scale image. The invention of AFM was a result of a natural desire to extend STM applications to the imaging of non-conducting materials. Instead of a tunnelling current,

measurement of tip-sample force interaction is employed. The success of STM and AFM applications led to the development of a number of related SPM techniques including the ability to measure specific nanoscale forces.

The AFM at DTF's Wilton Site is a Bruker Dimension 3100 Scanning Probe Microscope, featuring a closed loop X-Y head, Nanoscope IV controller with Nanoscope 6.13 r1 software. All scans were carried out in so called 'tapping mode', using NT-MDT supplied probes with a guaranteed radius of curvature less than 10 nm and at speeds of 1 Hz or less using a typical resolution of 512 x 512 pixels, unless otherwise stated.

4.2.1.2 Operating principles

A microscale cantilever commonly made from silicon or silicon nitride, with a sharp tip (Fig. 2.13) is rastered across a sample surface. When this is brought close to the sample surface, interatomic forces such as Van der Waals between the tip and the sample lead to a deflection of the cantilever according to Hooke's law. Typically, the deflection is measured using a laser spot reflected from the top surface of the cantilever on to an array of photodiodes (Figure 4.1).

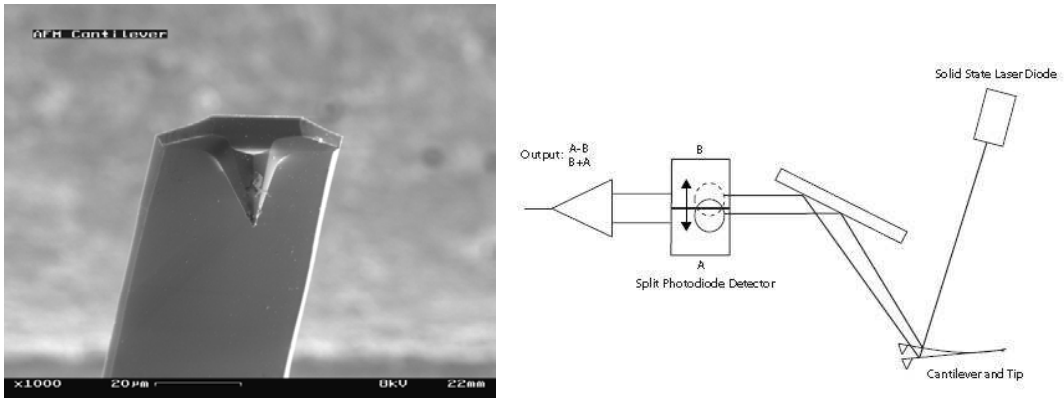

Figure 4.1: SEM Image of a typical silicon AFM cantilever (left) and the laser path in an AFM (right)

The tip controlling scanner is mounted at the end of a tube containing two polycrystalline piezoceramic material cylinders, one assigned for vertical z-travel and another for lateral x, y motion. A feedback mechanism is further employed to adjust the tip-sample distance allowing a constant force to be maintained between the tip and the sample in real-time. The resulting map of the area can be recorded and translated into sample topography. The AFM can be operated in a number of modes depending on the application. In general, possible imaging modes are divided into contact and non- or semi-contact where the cantilever is oscillated above the sample. In contact imaging, the tip of the probe is in constant physical contact with the surface of the sample, as the probe is rastered along the surface, changes in topography cause the tip of the cantilever to deflect. Through prior calibration, this movement is detected and can be used to calculate the height of the peak that caused the deflection with Angstrom vertical resolution. The principle of tapping imaging is similar to contact, except that the tip is not in constant contact with the surface and is an order of magnitude further away at the closest point of the cantilever oscillation. This is accomplished by vibrating the cantilever close to its resonant frequency and as the tip is rastered over the sample, multiple intermolecular attractions to the surface cause the amplitude of the sweep to be reduced, the size of this reduction is a function of the separation of the tip from the sample and again, can be used to generate an image.

In practice, the main difference between the two methods is that contact is more precise as the cantilever tip is closer to the surface and so can follow the topography much more accurately, however, soft surfaces can be damaged by a tip in constant contact giving false readings, hence tapping is preferred for soft substrates such as polymers.

4.2.1.3 Resolution

The resolution of an AFM image depends mostly upon how sharp the tip apex is and during use tips do become blunt. In principle AFM can provide higher resolution than SEM and has been shown to give true atomic resolution in ultra-high vacuum and liquid environments (Figure 4.2).

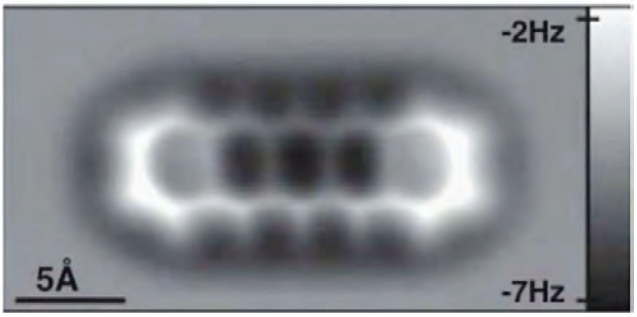

Figure 4.2: Frequency modulated AFM image of pentacene performed under vacuum (Gross, 2009)

4.2.1.4 Advantages/Disadvantages

The AFM can provide very accurate vertical and lateral resolution information, furthermore each scan can provide additional data such as morphology, density and particle shapes, this is even before considering functionalised tips or liquid imaging. Many forces can be measured using AFM including Van der Waals, capillary, chemical bonding, electrostatic and magnetic. The contact nature of AFM brings both pros and cons; whilst it can impart additional information to an analysis there are possible risks of surface damage in addition to tip wear and contamination, all of which can create artefacts and false data. However, the nature of AFM operation does provide a true three-dimensional surface profile of samples with absolute dimensional data (Figure 4.3); additionally, samples viewed by AFM do not require any special treatments, such as metal coating, which would irreversibly change the sample. Most AFM modes can operate very well in ambient conditions or even in liquid environments, making it possible to study biological macromolecules such as DNA, and even living organisms.

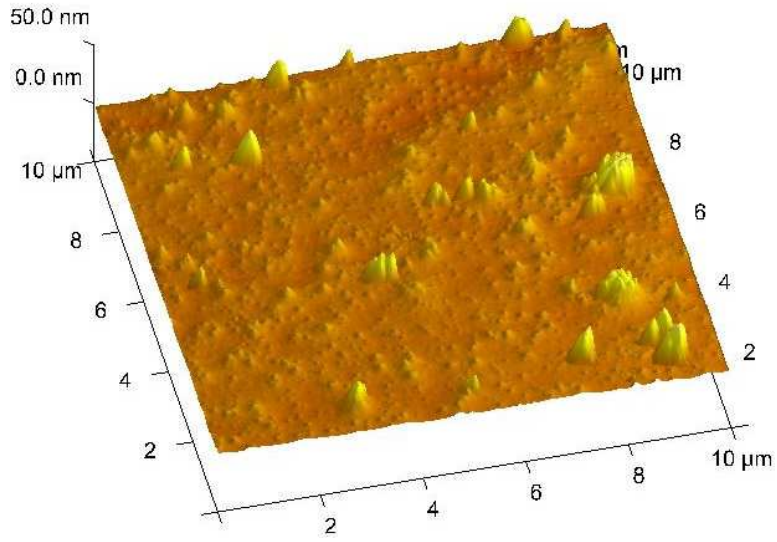

Figure 4.3: 3D image of a filled polymer surface generated with AFM scan data

Problems with AFM include the potential creation of image artefacts caused by worn tips and scanning speed. Traditionally an AFM could not produce images as fast as an SEM, requiring several minutes for a typical scan, however with the advent of modes such as video-rate AFM (which utilises smaller probes to increase cantilever oscillation speed), images can now be captured quicker than the equivalent SEM at reasonable quality. In the past AFM images could also be affected by hysteresis of the piezoelectric controllers and cross-talk between axes which required software filtering; such post-processing could flatten out or generate topographical features. Newer AFMs use real-time correction software or closed-loop scanners eliminating these problems, some also use separated orthogonal scanners which serve to eliminate cross-talk. Furthermore in recent times some manufacturers are moving away from piezo controllers choosing to use voice coil actuators instead, which eliminate these problems entirely. Another problem can be due to the nature of AFM probes due to the fact that they cannot normally measure steep walls or overhangs. Specially made cantilevers do exist which can be modulated sideways as well as up and down to measure such sidewalls, which although possible, is not trivial.

4.2.1.5 Application in the Literature to Barrier Films

Many examples have been found in the literature where the AFM has been applied, however it has typically only found use comparing differences in surface micro-roughness, measuring the surface roughness of barriers or substrates (Ghosh, 2005; Park, 2005b; Carcia, 2009; Hsu, 2009; Burrows, 2001; Yonekura, 2010), or to show microscale surface structures (Garcia-Ayuso, 1996; Henry, 1999; Erlat, 1999; Henry, 2001; Roberts, 2002; Erlat, 2004). It has also been used to provide very high magnification images of surfaces (Tropsha, 1997; Erlat, 2001; Kotova, 2004; Park, 2005a; Hanika, 2003). Only one paper has been found which used AFM in a more novel way, which attempted to identify the pinholes believed to exist on cathodes and study their evolution (Kolosov, 2001), apart from this, the ability of the tool to measure the exact sizes of flaws has been completely overlooked.

4.2.2 White Light Interferometry

All references in this section were obtained from the same sources (Hariharan,1995; Veeco, 1999; Minoni, 2000; Wyant, 2002; Veeco, 2009).

4.2.2.1 Overview

White light interferometry (WLI) is a technique for non-contact measurement of surface topography with high vertical and moderate lateral resolution. Interferometry makes use of superposition to combine separate light waves to reveal changes occurring to either one. DTF own three white light interferometers, a Veeco NT3300, NT9800 and prototype Large Area Metrology scanner, all can operate in phase-shifting, vertical-scanning and intensity modes.

4.2.2.2 Operating principles

A light ray is split into two identical beams by a grating or partial mirror, each of these travels a different route before being recombined at the detector, the path difference results in a phase change. Any phase differences can be interpreted as physical changes in the path length or a change in the refractive index (Fig. 4.4). Phase-shifting interferometry (PSI) allows measurements of smooth surfaces and small steps, whilst vertical scanning interferometry (VSI) was developed to allow measurements of rough surfaces and steps up to several millimetres high (at slightly reduced sensitivity). The range of a profiler is the greatest vertical distance they can accurately measure, the limit for PSI is about 160 nm whereas VSI is 2 mm; a huge distance in the scale of the nano-world.

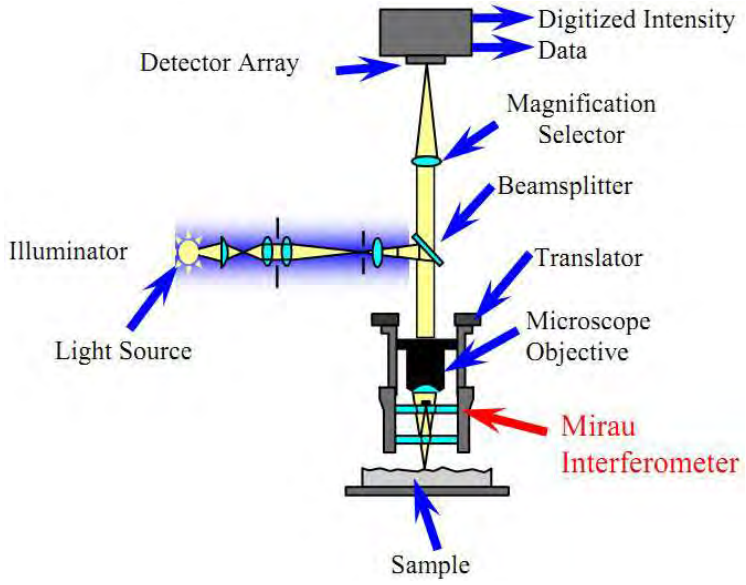

Figure 4.4: Schematic of an interference microscope (Wyant, 2002)

4.2.2.2i PSI Mode

In PSI mode a white-light beam is filtered and passed through a beamsplitter reflecting half of the incident beam to a reference and half towards the sample, these two beams are reflected and recombine to form interference fringes on the detector. This additive effect manifests as

interference fringes which can be observed as alternating light and dark bands when in focus (Fig. 4.5).

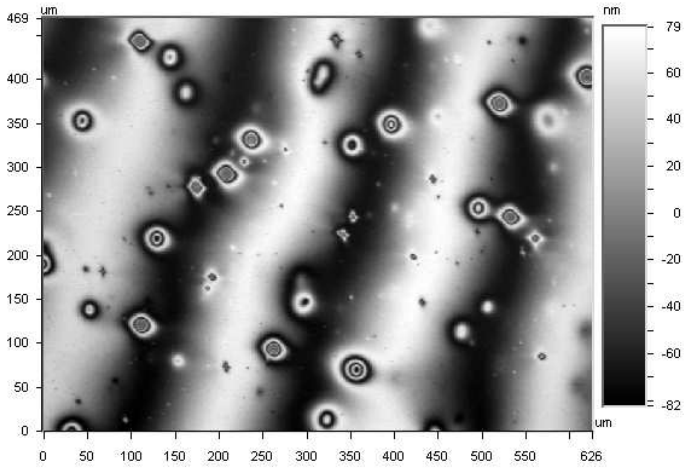

Figure 4.5: Typical interference fringes observed on a focused sample surface

During a measurement, the reference surface is moved a known distance to cause a phase shift between the two beams. The system records the resulting interference pattern at different relative phase shifts, then converts the intensity values to phase data by integration. The result is then processed to remove ambiguities between adjacent pixels and the relative surface height can be calculated. When the surface-height difference between adjacent features becomes larger, height errors may be introduced and the wavefront cannot be reliably reconstructed. As a result, PSI is limited to fairly smooth surfaces.

4.2.2.2ii VSI Mode

Vertical scanning interferometry is a newer technique than PSI but the basic principles are similar. Light reflected from a reference mirror combines with light reflected from a sample to produce interference fringes, which can be reconstructed to produce data about the sample surface. In VSI mode the white light source is filtered with a neutral density filter preserving the short coherence length of the white light, but most importantly instead of measuring the phase shift, the system

now measures the degree of coherence between fringes. The signal is once again sampled at fixed intervals whilst the optical path is varied by moving the objective through a fixed distance. The system scans through the maximum focus point in every measurement and the camera captures frames of interference data at evenly spaced intervals, as the system scans downward a signal for each point on the surface is recorded. Low-frequency components are removed from each signal, rectified by square-law detection and then filtered. Finally, the peak of the low-pass output is located and the corresponding vertical position is calculated.

4.2.2.3 Resolution

The resolution of a surface profiler refers to the smallest distance it can accurately measure, this can refer to either lateral or vertical resolution.

4.2.2.3i Lateral resolution

Lateral resolution is a function of the magnification objective and the detector array size; each magnification objective has its own optical resolution based on its magnification and numerical aperture. If the chosen configuration is much smaller than the optical resolution it causes oversampling, in this case the resolution is optically limited, ideally the detector sampling interval should be larger than the optical resolution and hence limited by the detector. If however, the detector sampling interval is somewhat larger than the optical resolution, it causes undersampling and can result in undetected surface features. The NT9800 is capable of detecting particles down to a diameter of 0.5 μm on a flat surface; advances in lenses and software processing is said to improve this further.

4.2.2.3ii Vertical Resolution

Both modes of operation have different resolution limits, for a single phase shifting interferometry measurement the resolution is about 3 Angstroms, decreasing to 1 when multiple measurements are taken. For a single vertical shifting interferometry measurement the resolution is about 3 nm decreasing to less than 1 nm with multiple measurements. Resolution data is essentially the noise limit of the system, or the lowest vertical resolution which can be obtained at that time. Surface profilers have been demonstrated to be accurate to sub-nm levels.

4.2.2.4 Advantages/Disadvantages

White light interferometry is well suited to measuring large surface areas rapidly with high precision and very high vertical resolution, with the ability to gather data for surfaces too rough to be examined by techniques such as AFM or SEM. Being a non-contact method it avoids the risk of substrate damage and the large field of view gives more representative data, especially for coated surfaces which tend to exhibit variations in surface quality. A non-contact mode of operation also allows for further functionality over methods such as AFM and SEM, one example being the Through Transmissive Media (TTM) module, which allows the WLI to look through one material at a surface which lies underneath and is discussed further in Chapter 6.

The obvious disadvantage of this technique is that it still uses a form of light for illumination and hence the lateral resolving power is still limited by the wavelength of light, whilst improvements in lenses, software and novel tools utilising ultraviolet light will further improve this, the interferometer available for work in this thesis is limited by its application of white light (Figure 4.6).

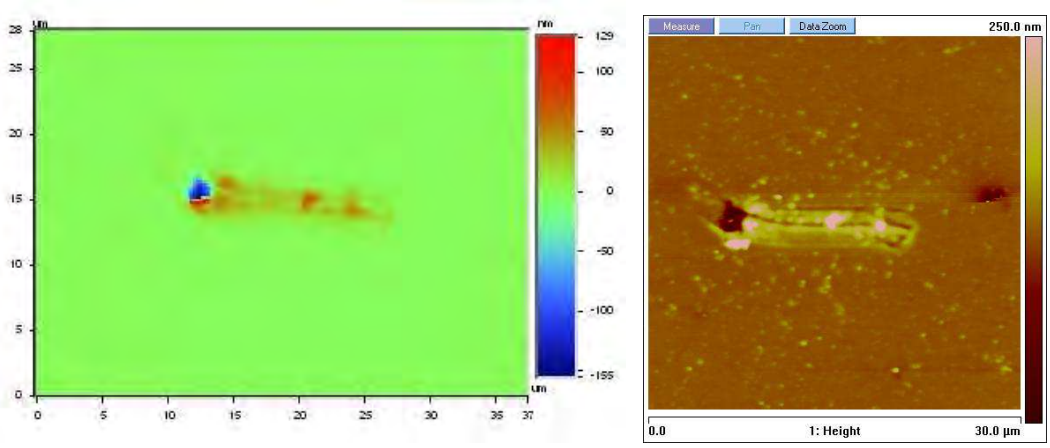

Figure 4.6: Surface defect imaged by WLI at high-magnification (left) and AFM (right), note; the majority of extreme height topography is detected by WLI, however surface micro-texture is not

4.2.2.5 Application in the Literature to Barrier Films

Interferometry has seen little application to the study of defects on barrier films. Only two papers have been found in which it has been applied, in one it is utilised to provide a cross section over a large lateral area with small height differences (Do, 2000). The other makes much better use of WLI (MacDonald, 2004), in which the instrument is used to demonstrate the difference in surface quality between low and high grade polyester films over many square millimetres.

4.2.3 Scanning Electron Microscopy

All references for this section were obtained from (Sarkar, 2001; Chiu, 2009; Jones, 2009; Tse, 2009; Zhdan, 2009, Marsh, 2011).

4.2.3.1 Overview

The scanning electron microscope (SEM) is a type of microscope that, instead of using a traditional light source, makes use of a beam of high-energy electrons raster-scanned across a surface to produce images. The wave nature of particle streams demonstrated by de Broglie and the ability to focus electrons using a magnetic field by Busch, were the two major breakthroughs needed for the

development of the electron microscope. Whilst these produced the first transmission electron microscopes in the 1930's, the first commercial SEM became available in the 1960's. Due to the shorter wavelength of an electron beam, electron microscopes are capable of producing much higher resolution images than optical microscopes.

The SEM used to acquire data in this thesis is a FEI Quanta FEG 250 environmental SEM with a Bruker AXS Quantax 200 Microanalysis EDX system. Operating conditions utilised an accelerating voltage of 15 kV, a 4.5 spot size (arbitrary, dependant on instrument) with an aperture of 3 and a working distance of 10mm.

4.2.3.2 Operating principles

When a beam of electrons hits a solid, the electrons are either back scattered or absorbed, these incident electrons disperse through the material (Figure 4.7), producing numerous signals including secondary electrons, back scattered electrons, x-rays, Auger electrons and light. Using multiple types of detector it is possible to record emissions to produce topographical and compositional data. It is the size of the diffusion cloud rather than the diameter of the electron beam which determines SEM resolution, (hence why higher beam power can sometime produce lower resolution images) this effect is most apparent on step edges where white outlines are created.

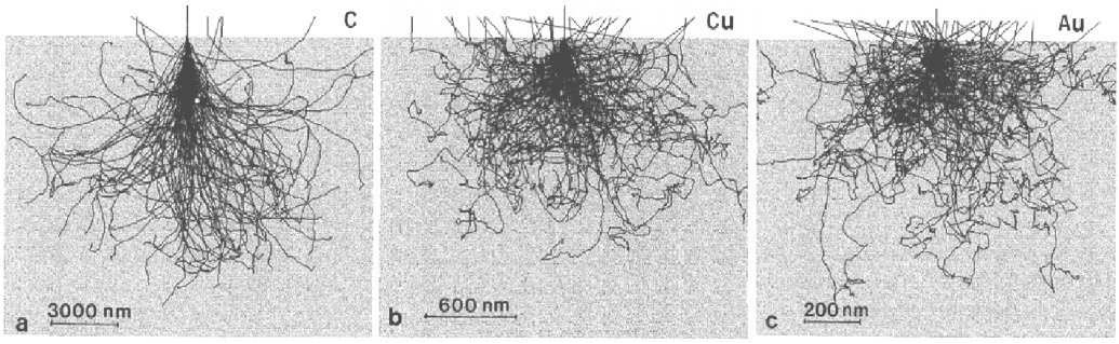

Figure 4.7: Monte Carlo simulation of 100 electron trajectories in three materials using a 25 kV accelerating voltage, note difference in scale bars with increasing material density (Jones, 2009)

The principle behind SEM construction is very simple; an electron beam is formed by an electron gun which is focused by both condenser and objective lenses to a spot, nanometres in diameter on to a sample, the entire system is sealed under hard vacuum to prevent attenuation of the electron beam. The emitted secondary electrons and x-rays are collected by a photomultiplier to form an image and provide chemical compositional data.

Many SEMs are set to observe secondary (SE) and backscattered electrons (BSE), with x-ray detection (EDX) being the most common integrated spectral analytical technique, most modern SEMs are equipped with such a detector. The images produced by an SEM depend on the detection mode employed, whilst both SE and BSE imaging is possible, SE mode images are dominated by topographic content whereas BSE mode is more capable of detecting atomic mass, useful for determining atomic number and material density.

4.2.3.3 Resolution

Magnification in an SEM can be controlled over a range of about x 25 to x 250,000 with extreme examples of x 2,000,000 demonstrated with very specialist equipment, imaging a specimen area about 60 nm wide with resolution up to 0.4 nm. Unlike TEM and optical microscopes, image magnification in the SEM is not related to the power of the objective lens. The function of the condenser and objective lenses in an SEM is to focus the beam to a spot rather than to image the specimen. In principle an SEM could work without either condenser or objective lenses provided the electron gun could produce a beam with a sufficiently small diameter although it would be unlikely to achieve particularly high resolutions.

4.2.3.4 Sample Preparation

Any object can be examined using an SEM as long as it is electrically conductive on the surface, conductivity allows a sample to be earthed and prevents build up of static charge. As a need to

analyse non-conductive samples has arisen, so have ways to get around this problem; it is possible to coat samples with materials such as gold, platinum or graphite to impart conductivity and hence allow SEM analysis. Under SEM analysis, a specimen is normally required to be completely dry, as the chamber is at high vacuum. Hard, dry materials such as wood, bone, feathers, dried insects or shells can be examined with little further treatment (such as metallisation), but living cells and tissues and whole, soft-bodied organisms usually require chemical fixation and drying to preserve the structure or cryo-fixation employed.

4.2.3.5 Advantages/Disadvantages

The scanning electron microscope has many advantages over those which utilise visible light, the most obvious is the much greater resolving power of the former. Typically, SEMs also have very large depths of field allowing more of a specimen to be in focus at any one time, meaning closely spaced specimens can be magnified at much higher levels (Figure 4.8).

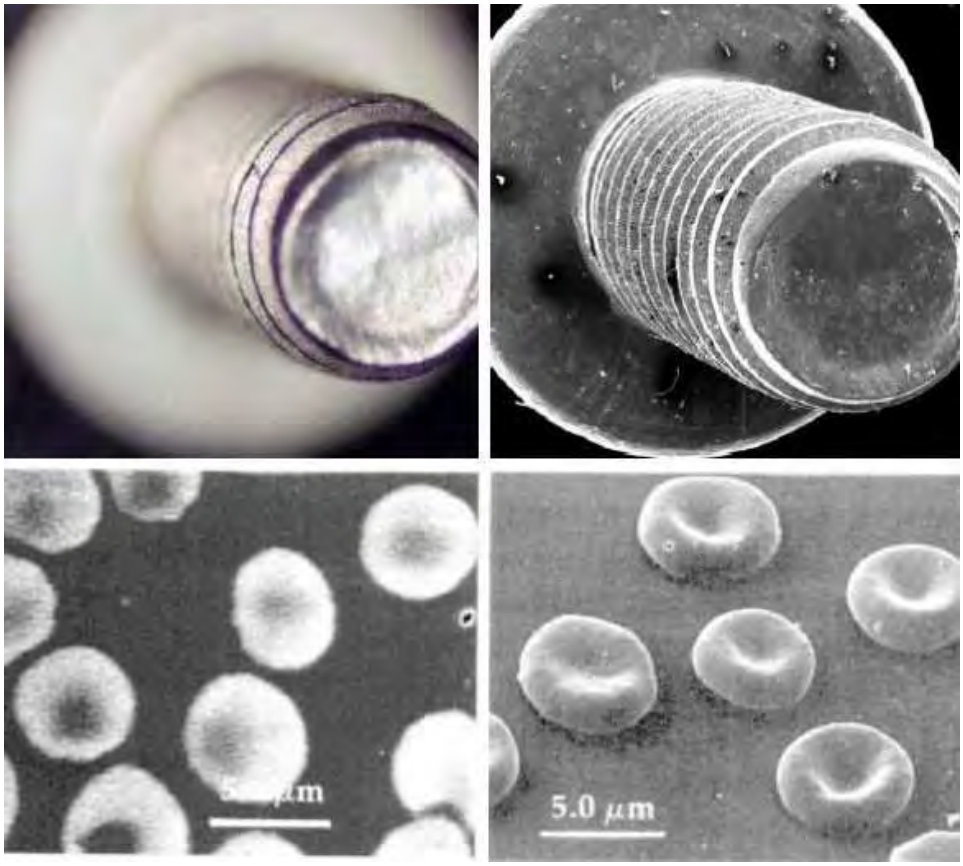

Figure 4.8: Images taken using light microscopy (left) and SEM (right) imaging a bolt to demonstrate differences in depth of field (top) and blood cells to demonstrate differences in resolution (bottom) (Tse, 2009)

Whilst video-rate AFM is now possible, SEM remains the most common way to rapidly acquire images once it has reached vacuum. Furthermore, analysis by SEM can be supplemented with its ability to gather information about material composition.

Despite these positives SEM still requires a great deal of sample preparation such as the deposition of a conductive coating or cryo-fixing, moreover SEM imaging must be carried out under vacuum, it is not possible to image samples under liquids and even so called environmental SEMs have a limited range of samples to which they can be applied. Non-conducting samples still remain particularly challenging to analyse with SEM due to their tendency to charge, furthermore particularly small specimens can be moved around by the electron beam or damaged with high voltages. Furthermore, whilst SEM images may appear three dimensional this is only apparent and

a common mistake of inexperienced users is to misinterpret features and bright spots to give a false impression of peaks and valleys. Finally, due to the secondary electron capturing method of imaging, an SEM may not display a true representation of the surface under examination, sometimes generating an image which actually corresponds to lower layers.

4.2.3.6 Application in the Literature to Barrier Films

The SEM is the most common technique applied in scientific literature to produce high magnification images, its application to the field of thin film barriers and OLEDs highlights this. The majority of papers utilising this tool concentrate on showing the condition of the electrodes (Scott, 1996; Aziz,1996; Aziz, 1998 b; Schaer, 2001), specific defects found on the electrodes (Nguyen, 1999; Do, 1999; Ke, 2002) or the overall quality of the electrodes, barrier coatings or film (Jamieson, 1983; Ettedgui, 1997; Henry, 1999; Erlat, 2001; Yonekura, 2010). Some papers have used the SEM to image cross sections of defects or layer thicknesses (Tropsha, 1997; Nagai, 2007; Tamagaki, 2010), however only one paper has been found which included an example of a dust particle discovered at the centre of a pinhole (Lim, 2001 a).

SEM has been extensively used throughout published literature to show interesting features but only as an imaging tool, no attempts to use the instrument to identify the root cause of pinholes has been attempted. The example which shows a dust particle is the only one which provides any evidence for the long held theory that dust does indeed cause these problems but is the exception.

4.3 Barrier Deposition

DTF's aluminium oxide barrier is applied using a sputtering process, it allows the application of thin inorganic films on to temperature sensitive materials such as polymeric substrates. A General Vacuum Optilab roll-to-roll vacuum sputter coater featuring three AC powered magnetrons in as many individually pumped zones (Bobst, 2012) is used for this. Deposition is carried out using a 6

kW potential, 3 x 10^{-3} mbar vacuum with a 1:9 ratio of Oxygen in Argon at a web speed of 0.3 m/s. Aluminium targets were supplied from Heraeus.

4.4 Calcium test

In addition to the description in Chapter 2, the method for creating calcium test samples is relatively straightforward; samples of film are cut into 90 mm^2 sections and placed in a vacuum oven at 5x10-1 bar, then held at 120 °C for 60 minutes to remove residual moisture, these are then transferred directly to an adjoined dry nitrogen glove box where all subsequent preparative work takes place. The polymer film is covered with a shadow mask in a vacuum deposition chamber where calcium deposition takes place. A set thickness of 100 nm, measured using a quartz crystal oscillator, is deposited on to the barrier side of the film. The polymer is then removed and adhered on to a section of cleaned, dried glass using an epoxy resin with the calcium sealed on the internal side. The epoxy is then cured by subjecting the cell to 360 nm ultraviolet light at for 3 minutes on both sides, followed by heating to 85 °C for 30 minutes to ensure it has fully set, it is now ready for testing (Figure 4.9).

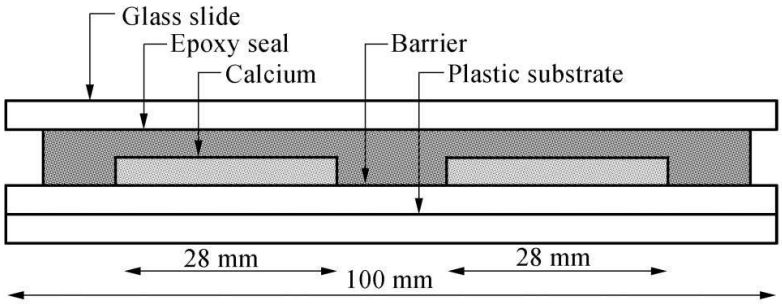

Figure 4.9: Calcium test cell structure and dimensions (figure not to scale) (Adam, 2007)

Procedures were carried out within a Siemens Mbraun Series MB200B glovebox with a MB VOH-300 Vacuum oven and MB20G vacuum controller.

A nitrogen atmosphere was created using liquid nitrogen evaporation creating glovebox conditions of 0.3 ppm H_2O and < 0.1 ppm O_2, at a pressure of 1.1 mbar. Calcium metal was supplied through Sigma Aldrich (product no. 44187-2) and deposited using a Sigma Instruments SQC-222 co-deposition controller, monitored using gold plated oscillator crystals (product no. 934000). Encapsulation carried out using UQG optics Float glass, cleaned using deionised water and AIS countdown neutral detergent general, final cleaning was carried out using Fisher isopropyl alcohol. The epoxy sealant used for sealing test cells was Electrolite Corporation ELC 2500 Clear and cured using Electrolite Corporation ELC4001 light curing unit, with an ELC-2542 power supply.

4.5 Wet-Coat Silica Deposition

The creation of a model system is described in detail in Chapter 8, utilising de-ionised water prepared at DTF and a number 0 Mayer bar (4 g/m^2). Silica particles were supplied by Nippon Shokubai, Seahostar KE-P grade.

4.5.1 Comparison of surfactants

Surfactants are regularly used in DTF production processes to allow wet coating of particles onto film surfaces whilst minimising agglomeration. Numerous surfactants were trialed to determine the most suitable for the model, whilst the surfactants are designed to vaporise from the surface under heating, at the reduced temperature of this study it was suspected that residues may remain on the film surface. The first tests were carried out using 'Caflon', an effective commercial surfactant which although well understood and used extensively within DTF, is being phased out of regular use for more environmentally friendly alternatives. Tween 20 is expected to replace Caflon, it is not as effective but fulfils the environmental safety requirements, however when used for these tests it was found to leave a residue on the surface. Synperonic 91/6 performed very well, a small volume was required to achieve the equivalent wetting of Caflon, no residues remained on the

surface and hence it was chosen for all subsequent work. Both Synperonic 13/10 and Synperonic 13/it performed well, however larger volumes were required compared to Synperonic 91/6. Nuosperse was found to leave large amounts of residue on the film surface and so it was deemed unsuitable for this study (Figure 4.10).

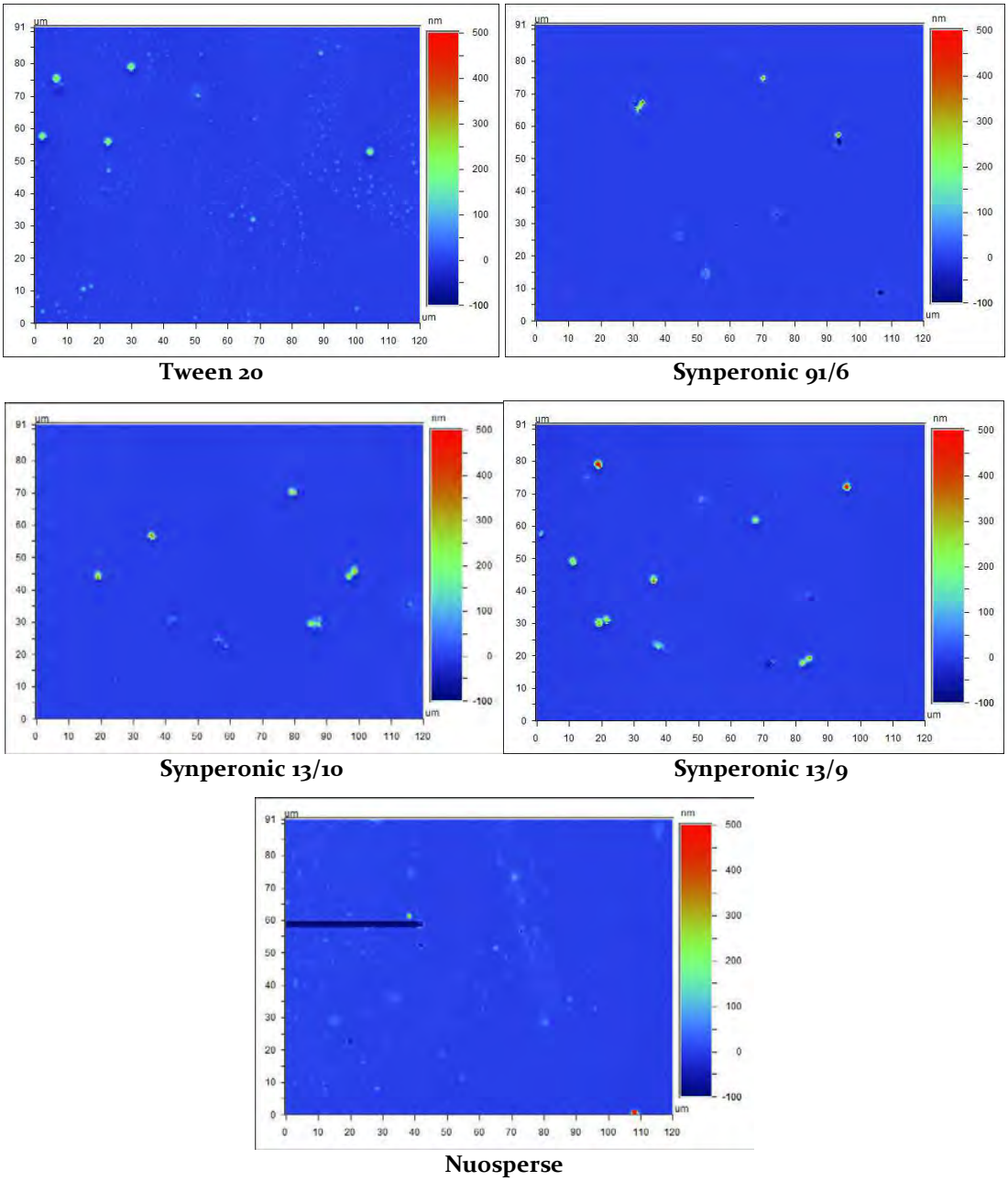

Figure 4.10: WLI image of planarised PEN, wet coated with 2.5 µm silica particles using different surfactants exposed to 100 °C for 30 seconds

4.6 Conclusions

In this study AFM has been chosen to complete the majority of the analysis work because it is not affected by the optical diffraction limit and has the ability to resolve features with absolute dimensional data requiring little sample preparation. This was supported by SEM for elemental analysis and production of high magnification images. However, the problems of applying it to polymers made it unsuitable for the majority of samples in this study. WLI was utilised for large area appraisals and the analysis of macro-defects.

In the literature, defects have been visualised using SEM but only for representative illustration. No applications of SPM techniques have been found for the characterisation and measurement of these flaws aside from some high resolution polymer and barrier surface images.

5. Large Area AFM Stitching

5.1 Introduction

This chapter follows the development and application of a novel atomic force microscopy technique to enable the tool to analyse a much larger area than normal. The idea behind such a method is to allow large fields of view, normally associated with scanning electron microscopy and white light interferometry, but with the absolute topographical detail one can only obtain using AFM (Magonov, 1997).

A thorough analysis of the variables associated with AFM analysis has been carried out to allow comparisons of the effects these have on the resulting images produced, including analyses of quantative roughness values for each dataset. All work in this chapter has been carried out on a well defined development film, chosen for the large number of surface features to assist the stitching process.

The AFM stitching technique was subsequently developed into a method, which was deemed to have direct application to industrial research. AFM stitching is an original technique made possible due to the unique array of metrology equipment within DTF; it is believed that the data presented in this chapter demonstrates some of the largest AFM images ever recorded with a conventional AFM (Armstrong, 2011).

5.2 Existing Capability

The AFM is capable of resolving details beyond the micron scale and in theory could be applied to characterise barrier pinholes once they have been located. Whilst the frequency of these is relatively high over the comparatively large areas covered by the calcium test, searching for these using any high powered microscopy technique alone is unfeasible.

'Stitching' is a process routinely carried out within DTF on the white light interferometers; the technique involves digitally joining multiple high resolution images to produce a large area, high resolution dataset, the likes of which cannot be obtained with a single scan. This increase in detail can improve the accuracy of data collection.

The DTF AFM is a Veeco Dimension 3100 atomic force microscope with a NanoScope IV controller. It has a maximum field of view of approximately 100 x 100 µm (Veeco, 2001) and a typical tapping mode probe has a radius of curvature of < 10 nm; a maximum resolution image of 1024x1024 pixels over a 100 x 100 µm FOV can take upto 3 hours to capture at a scan speed of 0.1 Hz. This extreme figure is required for surfaces with sudden Z differences to prevent 'smearing' of features, discussed later in Section 5.5.4.

Using these parameters and with the inclusion of post processing, scanning an area approaching the millimetre scale could take weeks, but an AFM user can only realistically operate the machine for a limited number of hours throughout each day. The ability to apply a WLI like stitch capability to the AFM would have major implications for high quality, large area analysis, allowing large field of view images at previously unseen levels of detail.

5.3 Initial Trials

It was realised that files captured using the AFM can be processed with the WLI controller software opening the possibility of carrying out stitching. A development film filled with a binary particle system consisting of 300 and 120 nm diameter particles at 15 ppm and 1000 ppm respectively was chosen as a test substrate. This was ideal because the smaller particles cannot be resolved using WLI, yet such information is required for product development.

5.3.1 Mathematical Roughness Terms

Throughout this chapter a number of common mathematical roughness terms are utilised to allow quantative comparisons of the different datasets defined as;

R_a – Average Roughness; calculated over the entire measured array, using the ANSI B46.1 standard, defined by Equation 5.1.

$$R_a = \frac{1}{n}\sum_{i=1}^{n}\left|Z_i - \bar{Z}\right|$$

Equation 5.1

R_q – RMS roughness; calculated over the entire measured array, defined by Equation 5.2.

$$R_q = \sqrt{\frac{1}{n}\sum_{i=1}^{n}\left(Z_i - \bar{Z}\right)^2}$$

Equation 5.2

R_{sk} – Skewness; a measure of the symmetry of the profile about the mean line. Negative skew indicates a predominance of valleys, while positive skew is seen on surfaces with peaks, defined by Equation 5.3.

$$R_{sk} = \frac{1}{nR_q^{\,3}}\sum_{i=1}^{n}\left(Z_i - \bar{Z}\right)^3$$

Equation 5.3

R_{ku} – Kurtosis; a measure of the sharpness of the profile about the mean line. Spiky surfaces have a high kurtosis value (Rku > 3); bumpy surfaces have a low kurtosis (Rku < 3); and perfectly random surfaces have a kurtosis of 3, defined by Equation 5.4.

$$R_{ku} = \frac{1}{nR_q^{\,4}} \sum_{i=1}^{n} \left(Z_i - \bar{Z}\right)^4$$

Equation 5.4

R_{pm} – Average maximum profile peak height; the average of the ten highest-to-mean points, defined by Equation 5.5, this is classed as an extreme measurement.

$$R_{pm} = \frac{1}{N} \sum_{i=1}^{N} R_{pi}$$

Equation 5.5

R_p – Maximum profile peak height; the difference between the mean line and the highest peak, this is also classed as an extreme measurement.

5.3.2 The capabilities of AFM compared to WLI

A 100 x 100 µm area of a section of development film was chosen and analysed by both AFM and WLI, a statistical analysis of the area was performed and subsequent comparison of the results showed a clear difference between both sets of data (Table 5.1).

Table 5.1: Comparison of statistical data for the same area of film analysed by both WLI and AFM

	WLI	AFM
R_a (nm)	26.66	16.88
R_q (nm)	35.81	25.86
R_{sk}	0.52	4.21
R_{ku}	5.34	70.82
R_{pm} (nm)	258.05	520.96
R_p (nm)	429.15	695.91
Resolution (MP)	0.35	1.02
Pixel Size (nm)	163.10^2	97.66^2

This comparison shows a remarkable difference between the two techniques. Values of R_a and R_q values are comparable between the two techniques however all the other parameters are larger when applying AFM analysis; the higher skewness and kurtosis values signify a larger dominance of peaks, likely due to the ability of the AFM to detect the apex of any peaks which cannot be resolved using WLI; this is further supported by values for both R_{pm} and R_q, presenting the average peak height to be higher with AFM. It appears that measured surface roughness is a function of resolution.

5.3.3 Comparison of AFM to Stitched AFM

For the first stitch, nine images were captured from within a 100 x 100 µm area, simply by changing the scanning area within the movement limits of the AFM head piezos; each image was then converted to a format compatible with the Vision software and manually stitched with a 10 µm overlap (Figure 5.1). Ultimately a 100 x 100 µm 7.6 megapixel image was produced with a 39^2 nm pixel resolution.

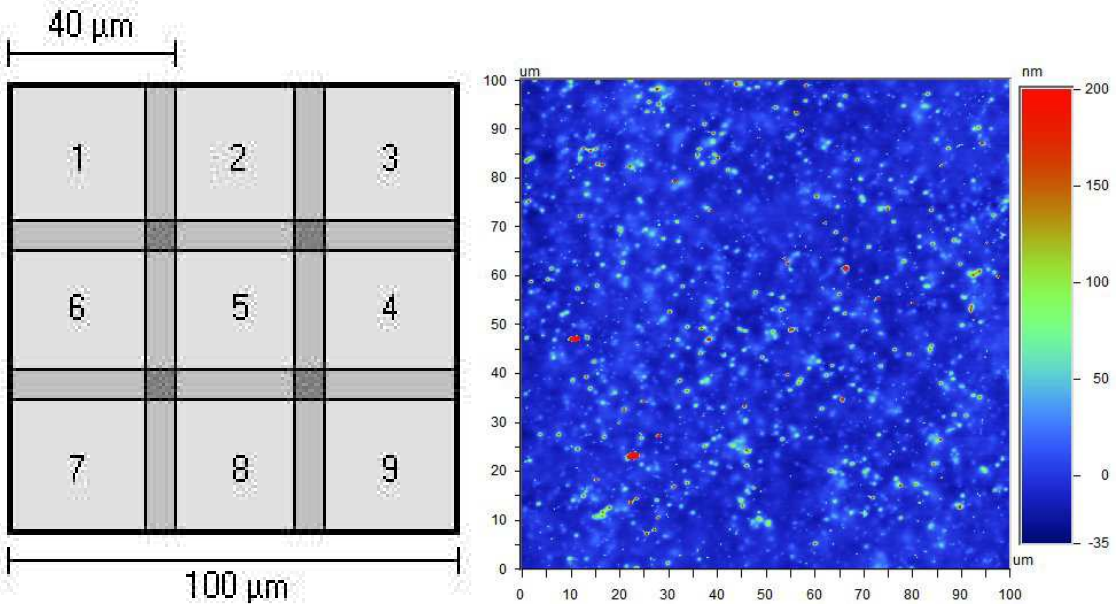

Figure 5.1: Initial scan pattern with darker areas representing scan overlap (left) required to align images during stitch, and the 3x3 AFM topography image produced using this scan pattern (right)

A single frame image was then captured of the same area using the AFM, producing a 100 x 100 µm 1.04 megapixel image with a 98^2 nm pixel resolution. Comparing the two revealed results similar to those in Section 5.3.2, whereby the higher resolution data produced results indicating a peakier surface (Table 5.2).

Table 5.2: Comparison of statistical analysis data of the same area of film analysed by both AFM and Stitched AFM

	AFM	Stitched AFM
R_a (nm)	9.87	9.09
R_q (nm)	19.88	18.48
R_{sk}	9.84	10.12
R_{ku}	203.95	222.46
R_{pm} (nm)	521.57	672.95
R_p (nm)	706.08	724.90
Resolution (MP)	1.02	7.59
Pixel Size (nm)	97.66^2	39.10^2

The rationalisation for this result is the same as previously. Increasing the resolution over the same array size means the actual shape of the surface is better represented using stitching, with the maximum and minimum features being more accurately represented. If the two sets of figures were very similar then the additional information gathered when stitching would simply mean the technique is oversampling the surface. The difference between the AFM and WLI was expected, but the differences between the AFM numbers prompted study to develop the technique further.

5.4 Development of the AFM Stitching Technique

Development of AFM stitching required continuous adjustment, primarily because the AFM and its controller software were never expected to implement such procedures. Many problems were encountered but were ultimately overcome, the most significant of which are explained below.

5.4.1 Image Alignment

When using an interferometer to carry out a stitch, the machine keeps a record of the coordinates at which each frame is captured allowing the controller software to automatically align features between images and accurately connect them. Importing multiple frames captured using the AFM to perform the same operation is not possible as no such record is created, so all stitching must be carried out manually. Furthermore, the WLI software will only allow two images to be stitched at once using a non-automated method, so to create large areas stitches two images must be joined, saved as one file, then re-opened to allow a third to be attached and so on.

With such a large number of images, a range of stitching techniques were trialled to find which was the most reliable. Using the default method, the software attempts to overlap and align the images automatically, but when applied to AFM files it struggled with the task. The next option allows the user to manually perform the overlap, whereby both images are presented and can be superimposed by means of a click and drag system until features present on both images are aligned (Figure 5.2).

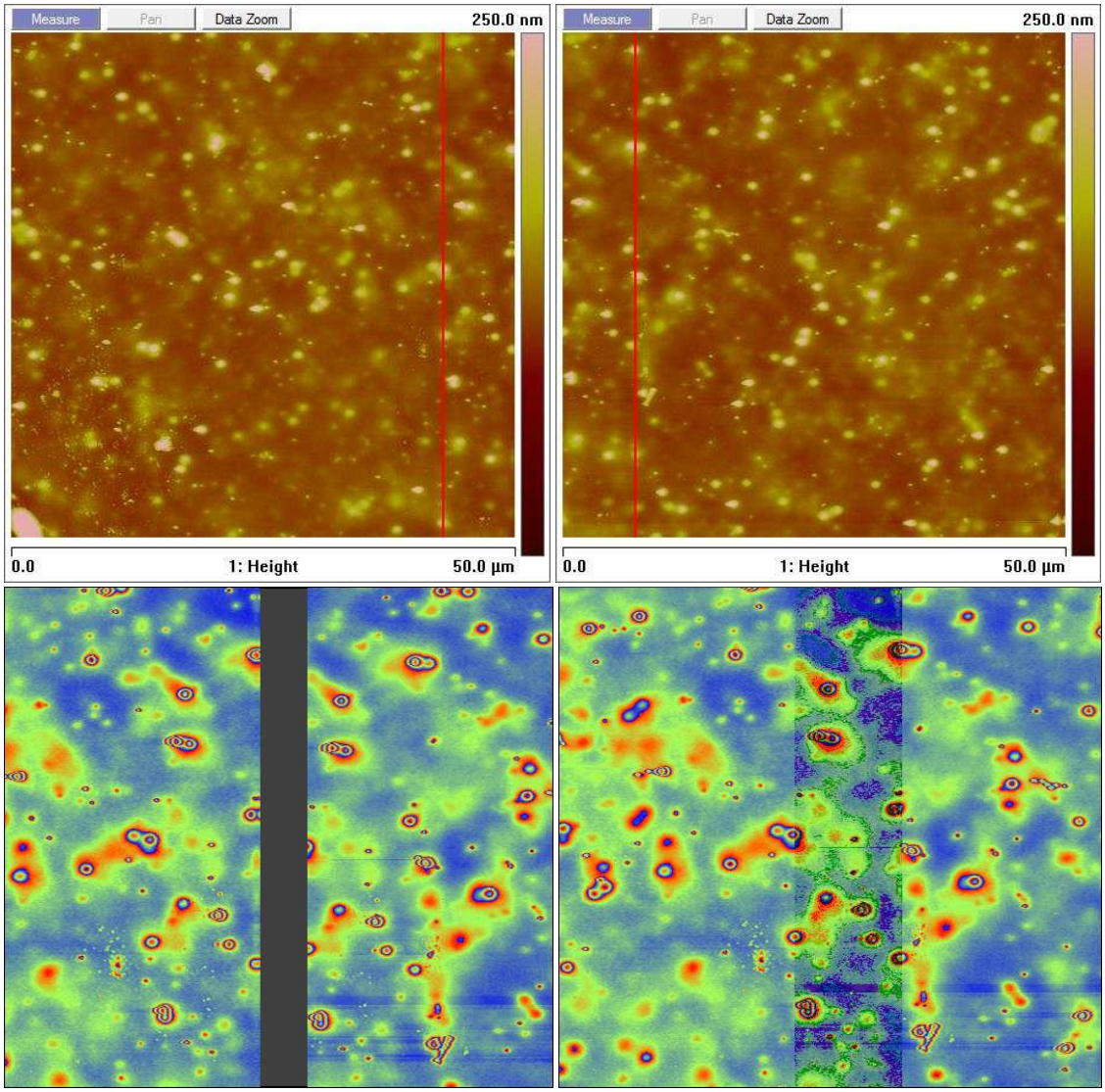

Figure 5.2: AFM Topography data taken from a set of sequential images, overlap indicated by red line (top) and the view of these two images in the WLI software before (bottom left) and after (bottom right) manual positioning

Despite the promising start of this technique, it was quickly realised that due to a combination of piezo creep, thermal drift and stage repeatability, image sequences could not be aligned over larger lengths using this manual method. Exploring the features of the software it was found that image pairs could be stitched manually using a pair of user defined coordinates, known as 'fiducials';

whilst more time intensive and somewhat difficult to use, it allows accurate alignment of features between images and also corrects for drift and rotation between frames (Figure 5.3).

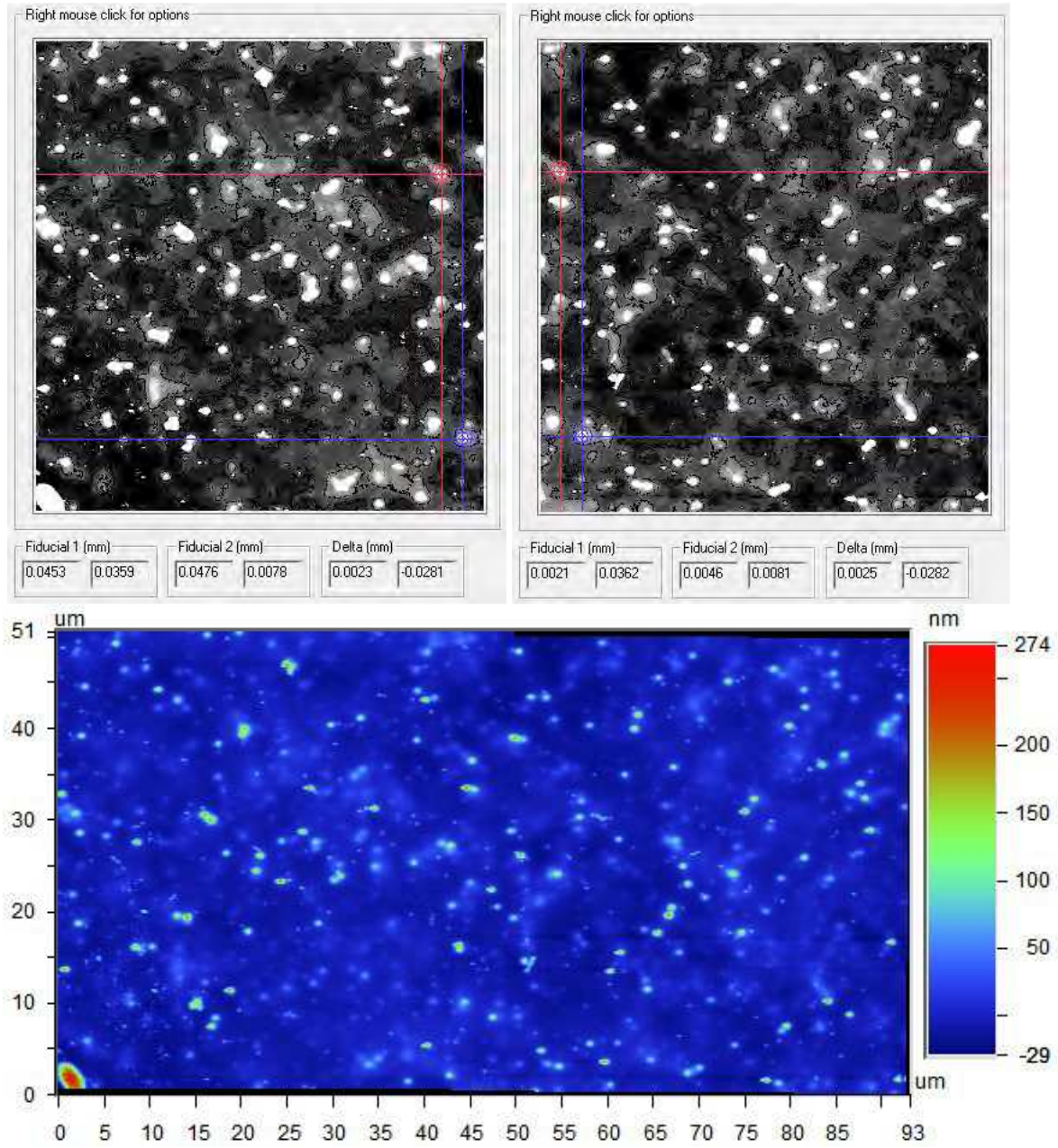

Figure 5.3: AFM topography images presented in the WLI software with manually placed alignment fiducials (top) and the resulting stitched image (bottom)

5.4.2 Stitching Patterns

Fiducial stitching ensured that each image pair was correctly orientated, however it was then found that slight inaccuracies inherent to the movement of the stage started to become apparent. These were most obvious using a line-by-line method; when applied to datasets with large aspect ratios they became impossible to align (Figure 5.4).

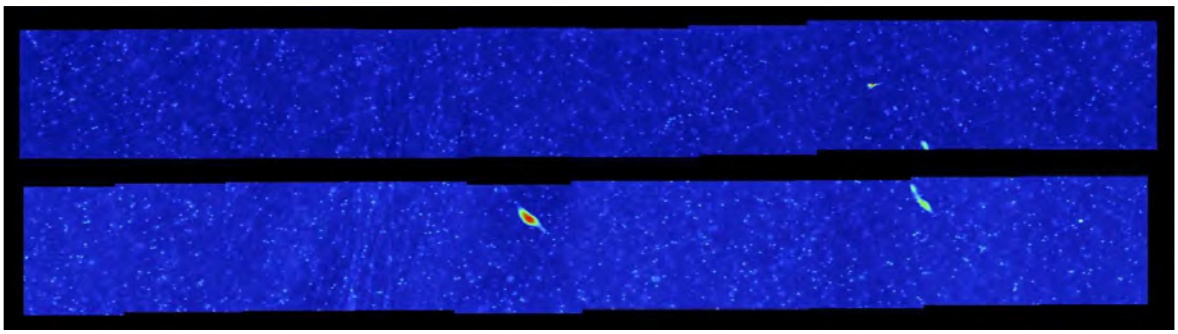

Figure 5.4: AFM topography data for two parallel stitched lines, note uneven spacing between images making accurate combination of the two impossible

Numerous techniques were trialled, however a quadratic method was ultimately chosen. A square image is produced in a stepwise fashion from each corner of the array and stitched together into increasingly larger segments (Figure 5.5). Using these square sections, the software correction algorithms are able to negate the effects of piezo drift in the Y direction and stage errors in the X direction more easily, adjusting each frame as they are added.

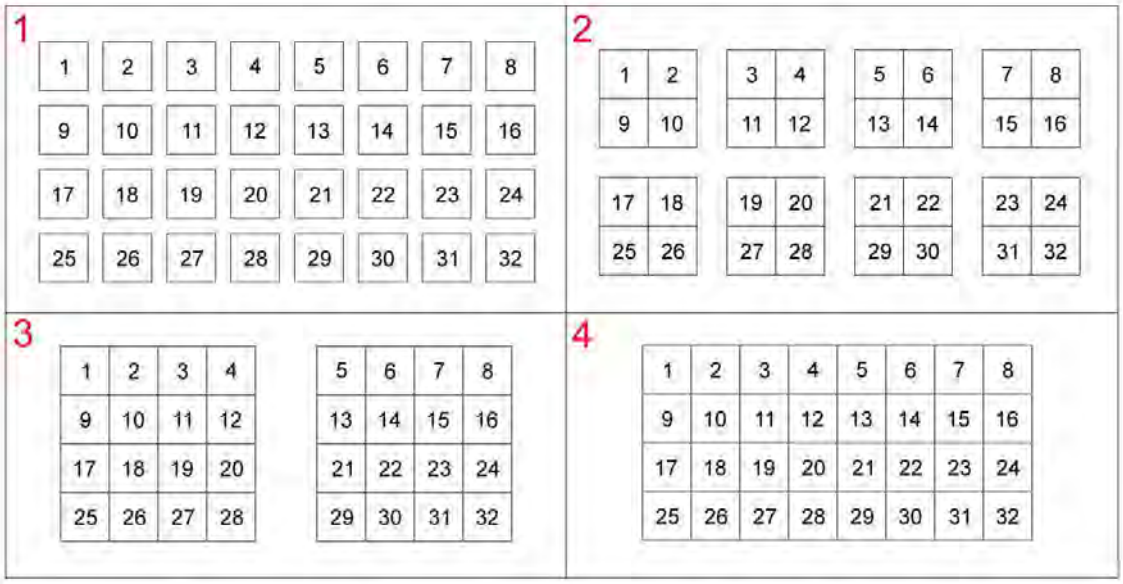

Figure 5.5: Typical stepwise stitching pattern

The quadratic method also made placing fiducials much easier; with large datasets one must magnify each image to ensure that the features chosen are the same on both frames (Figure 5.6).

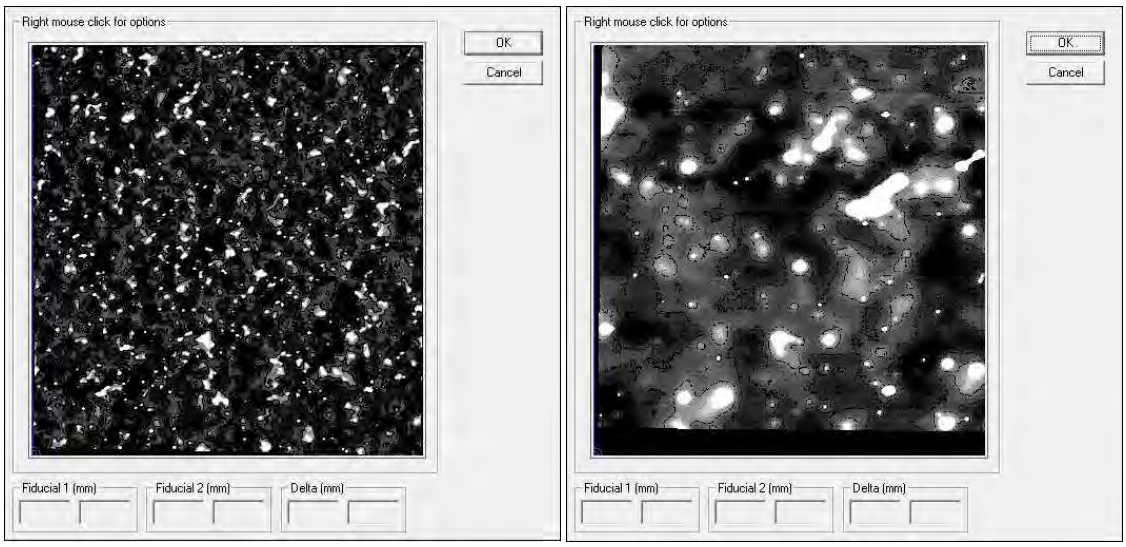

Figure 5.6: 108 x 108 µm topography image (left) and a 25 x 25 µm zoomed region on the same image (right) allowing accurate positioning of fiducials

When using a line by line method, the aspect ratio of the image is maintained after zooming, as a result selecting appropriate reference points becomes very difficult (Figure 5.7), however this problem was eliminated after employing the quadratic stitching method (Figure 5.6).

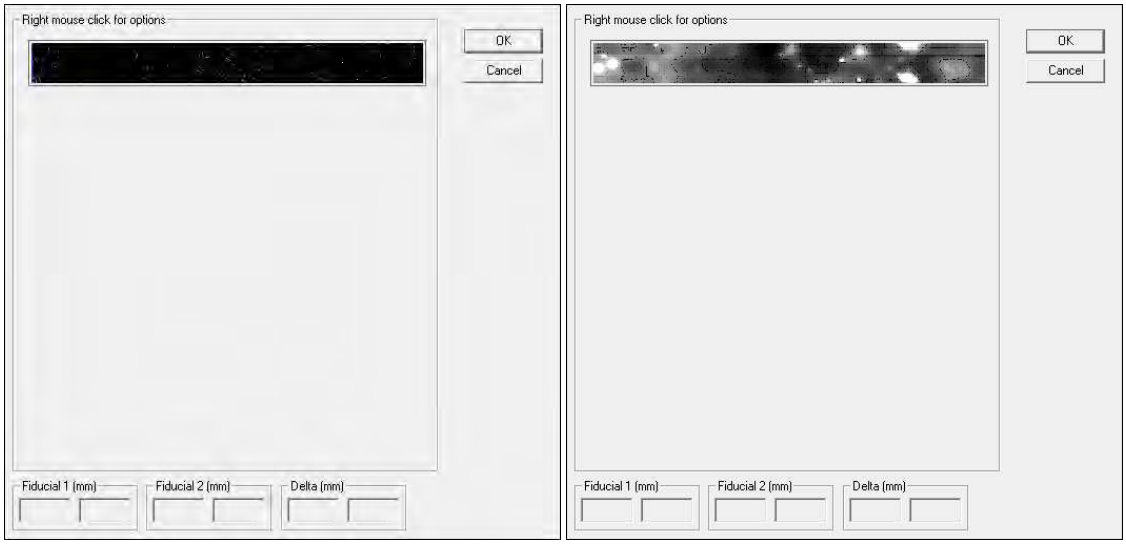

Figure 5.7: A 546 x 45 µm image (left) and a 35 x 2.9 µm zoomed region, demonstrating the maintained aspect ratio of the software

5.4.3 AFM Automation

Capturing a large number of frames using the AFM is very time intensive considering both the requirement of the operator to supervise the machine and image acquisition time. This was greatly reduced however, by means of novel AFM automation; it is possible to create a so called 'programmed move' with the software, the purpose of which is to allow a user to mark locations on a sample so they can be revisited later. Using this feature a number of sequential data points were recorded in a serpentine pattern, to minimise piezo drift and hysteresis effects. The controller software was then made to follow this programme, engaging at each point before moving again, normally this feature is used to allow the AFM to engage in the same point over a time to allow multiple images to be captured, but forcing it to move between engaging results in a chain of images to be captured.

The AFM was now capable of capturing numerous images over a large area automatically but still required user intervention. When the AFM engages in tapping mode the free amplitude modulation of the probe is monitored by the controller, when this decreases to a pre-determined level, such as 95% of the set point, the machine interprets this decrease to be the result of the probe encountering the sample surface thus reducing the distance the probe can oscillate (Figure 5.8).

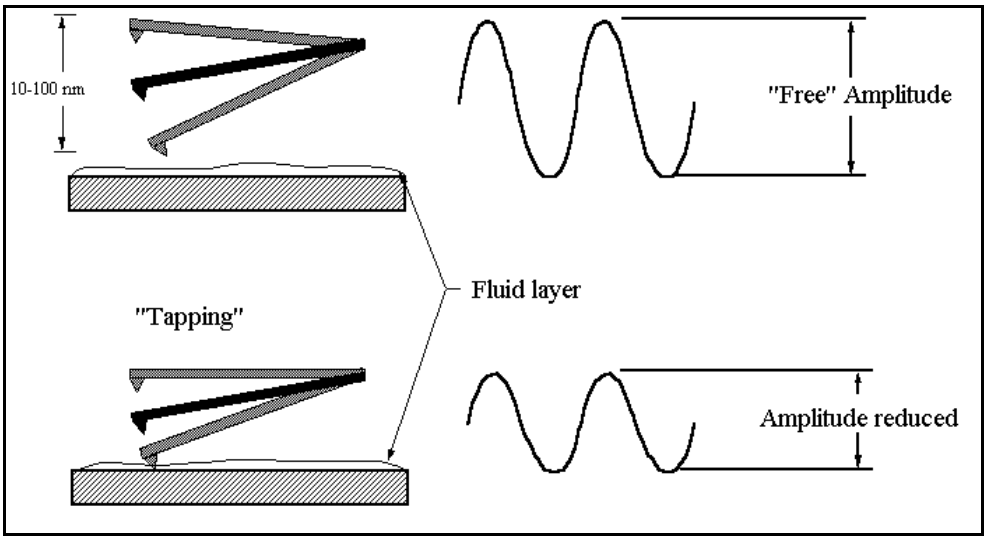

Figure 5.8: Schematic to represent the RMS Amplitude of the AFM cantilever (Magonov, 2000)

At this point the tapping force exerted by the tip on the sample is very light and as it rasters across the surface the probe is unable to respond to sharp topographical features rapidly enough. Hence whenever the AFM engages the operator is expected to lower the amplitude set point sufficiently to allow the tip to track the surface. Differences in both surface topography and composition require the settings to be tuned per scan, allowing accurate data capture whilst reducing tip wear.

As all scans would be taken from the same sample with comparable topography, it was stipulated that the safety set point could be set lower, so the AFM would automatically engage using parameters sufficient for acceptable image capture. Exploring the software again allowed the parameters to be successfully adjusted to the point where this was possible. The AFM was now capable of capturing multiple image sets, suitable for stitching, without constant intervention.

5.4.4 Image processing

A raw AFM image requires post-processing to remove artefacts such as tilt, bow and scanning errors; such processing is a very time intensive process, a number of steps must be performed to correct scanning artefacts inherent to AFM (Figure 5.9).

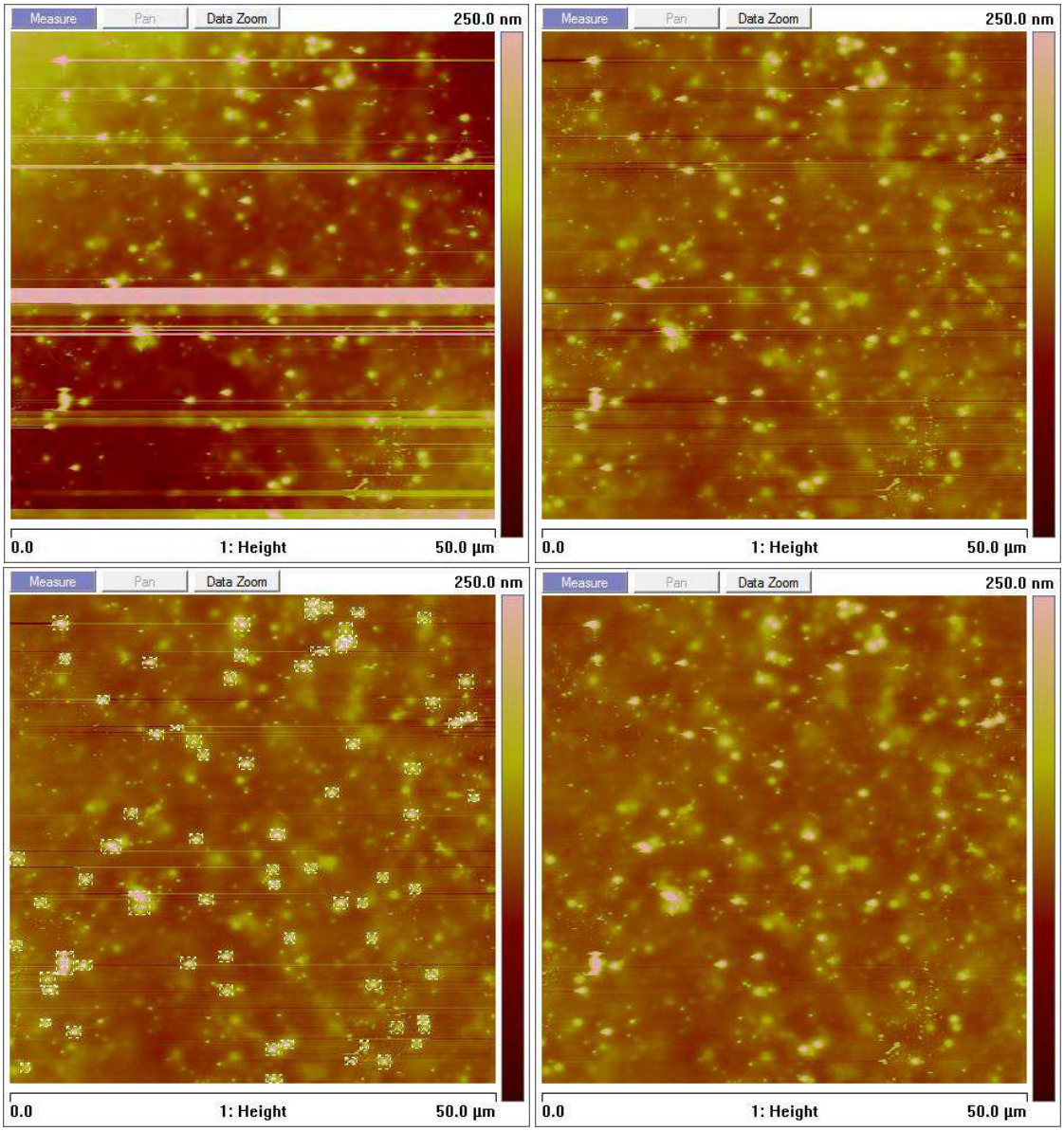

Figure 5.9: Example AFM image processing steps, showing raw image (top left), first order flattening (top right) user defined peak removal (bottom left) and final image with all errors removed (bottom right)

When processing images, a user has to instruct the AFM software to ignore any particularly large peaks when 'flattening' an image; surfaces with a large amount of topography require much more correction. An operator has to take great care that false data is not accidentally produced, either with the addition or removal of terms. When processing large numbers of images for stitching, it is possible to unintentionally remove low frequency, long range features which may not be observed in individual frames. In addition when correcting for particularly large peaks, the software may adjust the image baseline to an incorrect value, this manifests as an area of particularly low or high average topography on the final stitched image. Both of these problems can be negated with careful image processing, ensuring that the image stays true to the actual sample.

Discussions with Bruker provided more advanced analysis software which could be used to perform batch image processing and included more advanced correction tools to reduce the workload. Whilst still very time consuming, images could be processed much quicker than previously, reducing user fatigue and the number of man hours required.

5.4.5 Tip Wear

Tip wear was also considered as a potential problem, however scans taken before and after 100 automated scans demonstrated that the tips were still in very good condition (Figure 5.10). Roughness vales for both of these surfaces were comparable, suggesting that if tip wear is occurring it is not sufficient to affect these results, it is likely that this is due to the surface under analysis being a soft polymer.

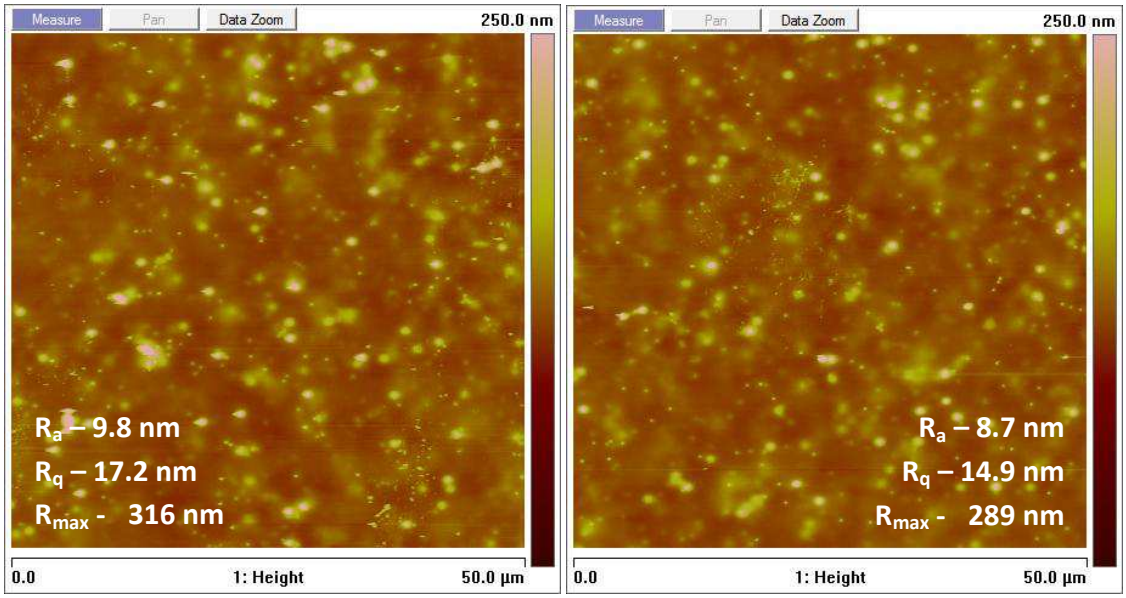

Figure 5.10: Scans of development film before (left) and after (right) 100 consecutive scans, roughness values for each image displayed in white

5.5 Scanning Optimisation for AFM Stitching

Whilst the AFM stitching technique was now reliable enough for use, the minimum requirements for data capture had yet to be determined. Using very high resolution scans would provide the best quality data, but would likely result in oversampling and take more time, whereas the opposite would result in data loss, negating the benefits of performing the stitch in the first place.

5.5.1 Minimum scan requirements

The primary advantage of AFM stitching is its ability to capture topographical data with the high resolution of the AFM over large areas which normally require WLI. However, the trade-off to this benefit is the capture time, determined by both field of view, resolution and scan speed.

DTFs AFM can record a maximum of 1.05 megapixels (1024 x 1024) per image at a 1:1 ratio, regardless of the field of view. Larger fields of view tend to require slower scan speeds to maintain image quality but cover a larger area; smaller scan sizes tend to be quicker but cover smaller fields

of view. Whilst the speed of smaller scans increases greatly when pixel size is the equivalent to a larger field of view, maintaining the one megapixel resolution per frame means that the eventual image will be a more accurate representation of the surface.

The quality of stitches depends on how many frames were used to make up the final image and the resolution at which each was taken. For instance, if a 0% overlap could be used it would be possible to make a 200 x 200 µm stitch using 4 x 100^2 µm frames, 16 x 50^2 µm frames, 64 x 25^2 µm frames and so on, for each case the maximum resolution would be 4.2, 16.8 and 67.1 megapixels respectively. The amount of time it takes to capture such data, regardless of processing and stitching time is approximately 4.5 hours, 9 hours and 18 hours. The processing and stitching steps can easily quadruple these figures and hence whilst it is desirable to have the highest quality data possible, the acquisition times become prohibitively high. Increasing the number of data points gives diminishing returns as the number of pixels increases linearly over a square area (Figure 5.11).

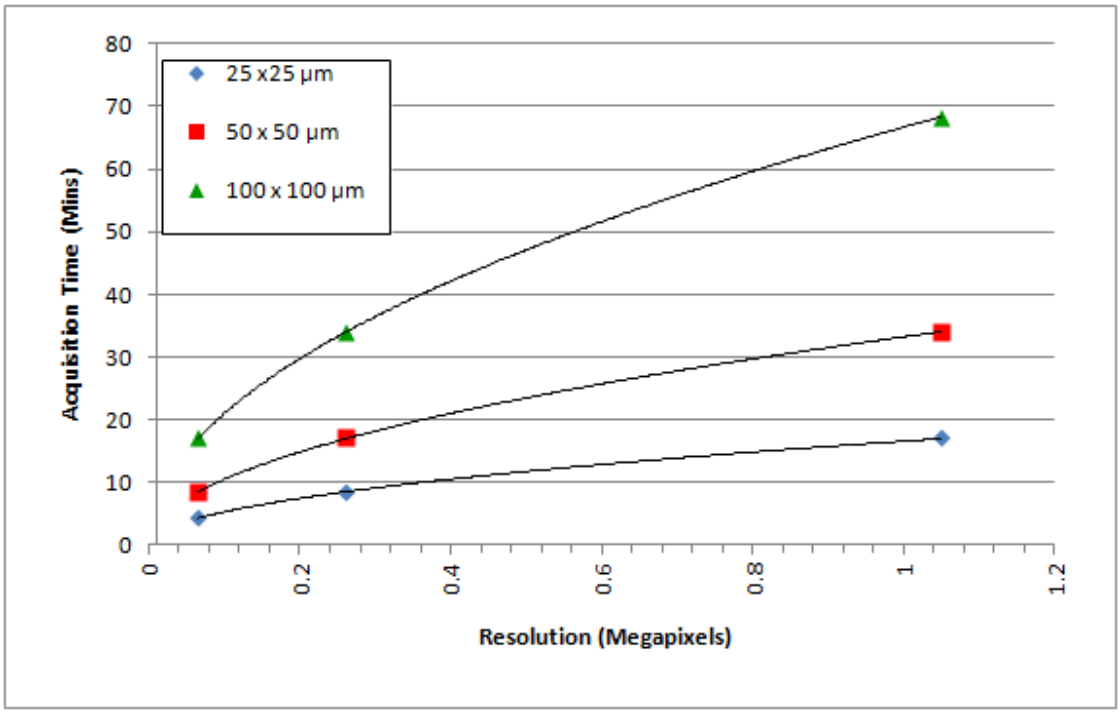

Graph to show the trade off between acquisition times and resolution for individual fields of view

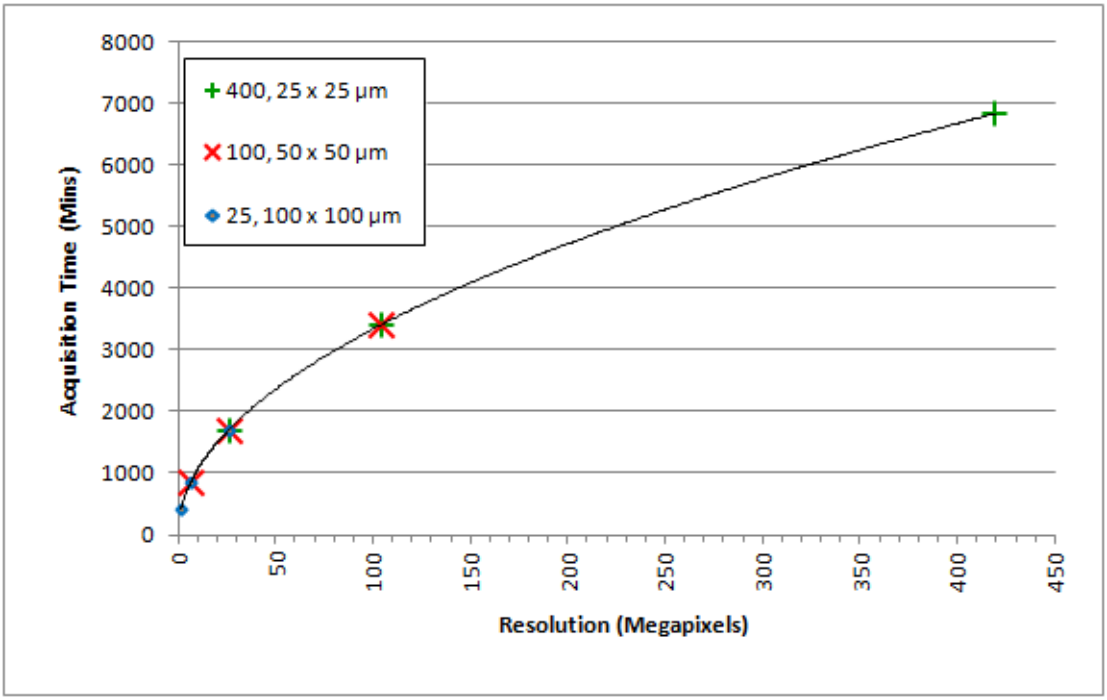

Graph to show acquisition times required to acquire images for a 500 µm² stitched array using different frame sizes

Figure 5.11: Graphs to demonstrate the increasing amounts of time required to capture diminishing amounts of data

It was decided to perform a range of scans to determine how significantly the resolution affects data quality and the requirement to create an accurate representation of the surface.

5.5.2 Resolution Requirements of Individual Frames

Generally, the higher the resolution of an image, the better the quality, this is true of any digitally stored data; from a surface metrology aspect capturing AFM or WLI images with higher resolutions means a more accurate representation of the surface under analysis. When using these metrology tools to analyse new or unknown surfaces higher resolutions are desired, however when analysing known surfaces for statistical analysis or quality control, such extreme detail is not required. With the development film the size of the particles was known so analysis of this material concentrates on roughness, peak size distributions and bearing ratios; all of which only require peak counts. As

AFM stitching is a time intensive process, any possibility to reduce capture time is of interest, as higher resolution imaging takes more time a minimum sampling interval is desired to avoid oversampling whilst still acquiring relevant data. An area of the film was scanned at four different resolutions to allow such comparisons (Figure 5.12).

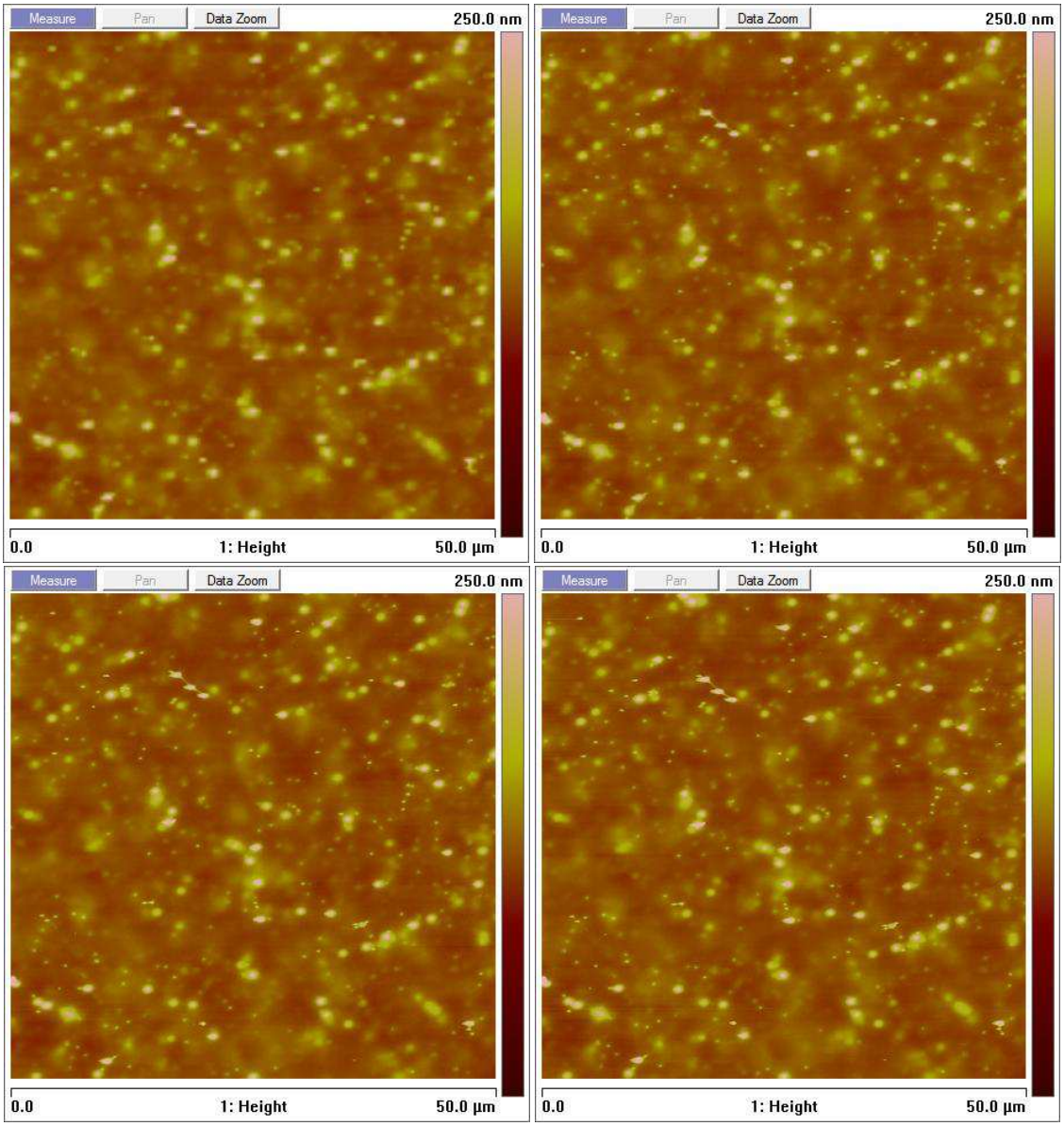

Figure 5.12: Four 50² µm AFM topography scans of the same area of film, comprised of 0.02 (top left), 0.066 (top right), 0.26 (bottom left) and 1.05 (bottom right) megapixels

Examining the four images at a 50 x 50 µm field of view they appear to be very similar, however upon zooming into a 9.8 x 9.8 µm area the differences become apparent (Figure 5.13).

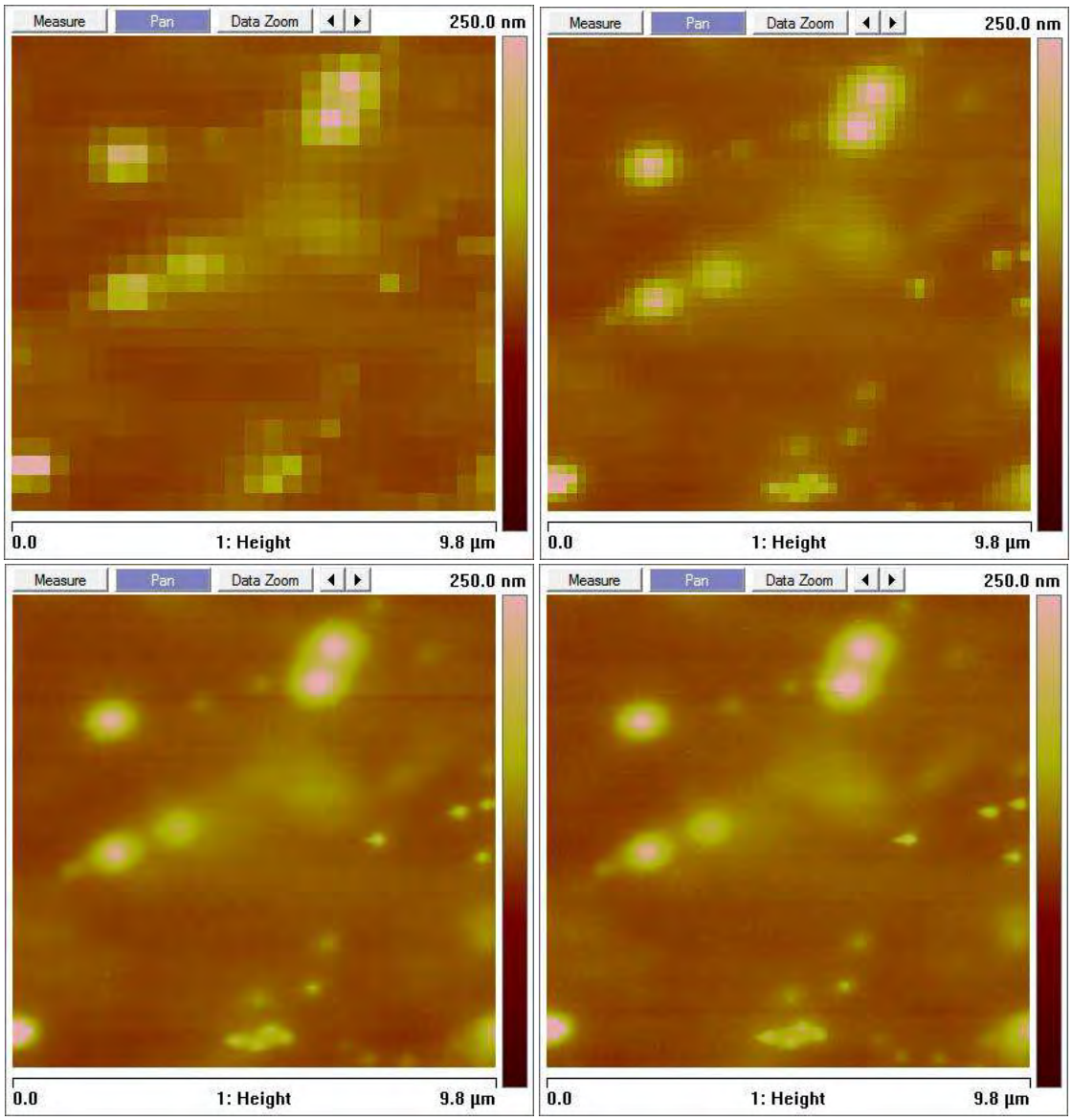

Figure 5.13: Four 9.8 x 9.8 µm zoomed areas from each image in Figure 5.12, full size image of 0.02 (top left), 0.066 (top right), 0.26 (bottom left) and 1.05 (bottom right) megapixels

Comparing the highest and lowest resolution images, the risks of undersampling become clear (Figure 5.14).

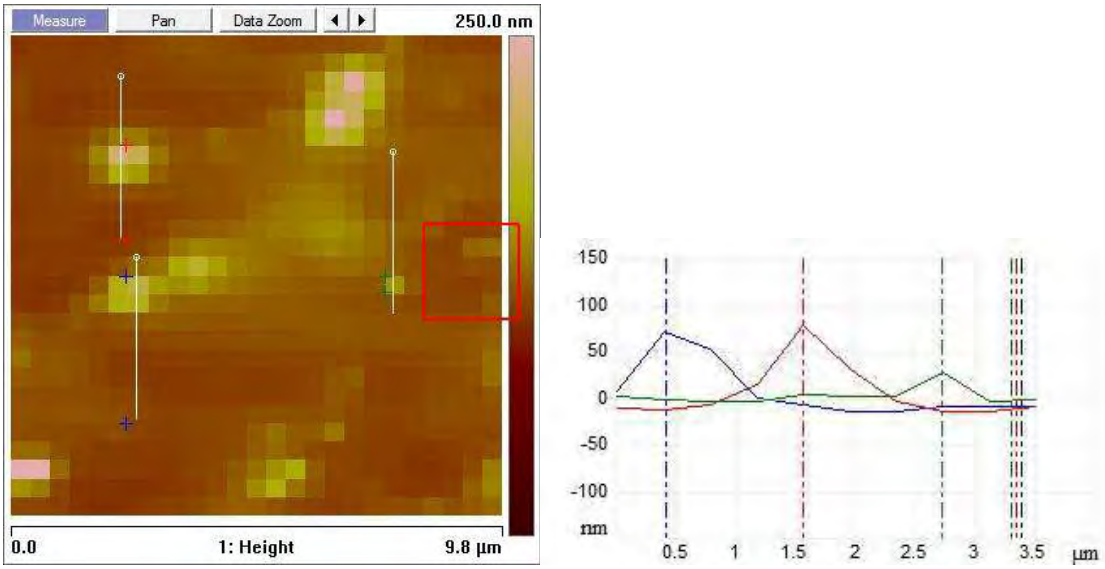

Lowest resolution scan from Figure 5.13, cross sections of 80.77 nm, 87.11 nm and 31.94 nm

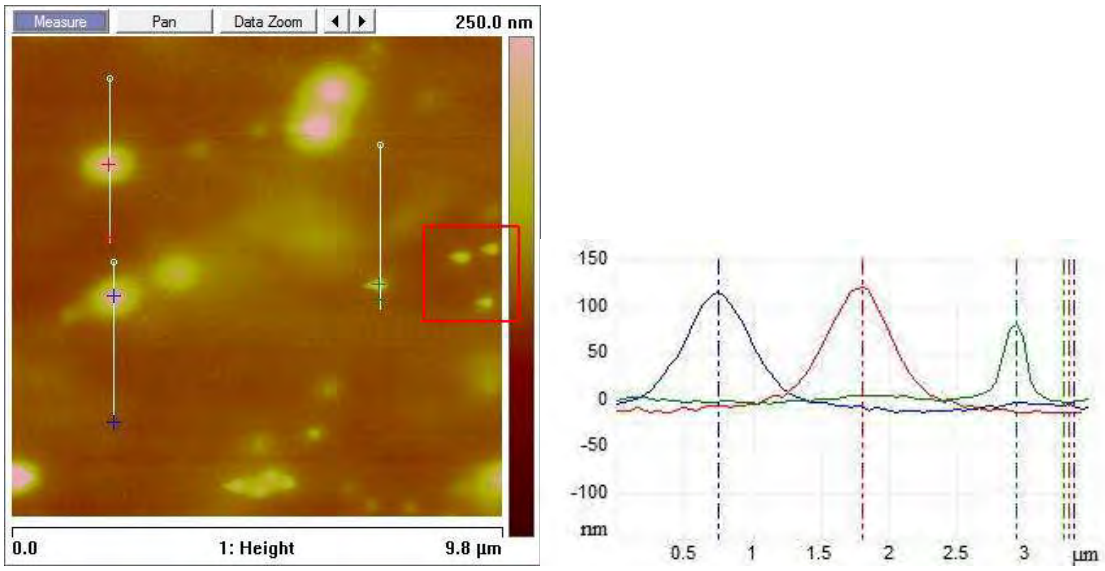

Highest resolution scan from Figure 5.13, cross sections of 112.70 nm, 135.32 nm and 82.80 nm

Figure 5.14: Cross sections of AFM topological features from highest and lowest resolution scans from Figure 5.13

Using this extreme example it can be seen that not only does the low resolution AFM image give incorrect height measurements for individual peaks, it does not capture the correct shape of the features either. Although the AFM will measure the heights at the centre of each of these pixels correctly, it is unlikely that the probe encountered the apex of each feature. In some areas the tip

completely misses data, highlighted by the red squares in both scans in Figure 5.14, where the cluster of three small particles present in the high resolution scan cannot be observed at low resolution. It is interesting to note that whilst the WLI pixels are smaller than those in the lowest resolution scans (Table 5.3), the inability of the tool to measure the fine details of particularly sharp features presents a different problem; it will be capable of measuring the surface roughness with reasonable accuracy, however the extreme heights of small peaks and the overall skewness of the surface is likely to be determined to be less than it actually is. Comparing stitched data over an area of 50 x 500 μm using low resolution AFM, high resolution AFM and WLI, we see predictable results (Table 5.3).

Table 5.3: Statistical comparison of low resolution AFM, high resolution AFM and while light interferometry

	AFM Low	AFM High	WLI
R_a (nm)	8.78	10.67	7.25
R_q (nm)	14.37	18.12	10.10
R_{sk}	4.33	4.84	1.83
R_{ku}	44.31	56.12	8.80
R_{pm} (nm)	313.45	503.08	89.22
R_p (nm)	406.26	661.79	103.47
Resolution (MP)	0.18	6.99	0.78
Pixel Size (nm)	390.63^2	65.10^2	196.82^2

The high resolution AFM is capable of resolving the surface with great accuracy, with the highest R_a and R_q values. Low resolution AFM does detect many of the peaks but not all, hence lower values of R_a, R_q, skewness and kurtosis. It also appears that the issue highlighted in Figure 5.13 can be observed in that the highest points of many peaks are not resolved, evidenced by the lower R_{pm} and R_p values. It is interesting to note the large differences between the WLI and AFM data, whilst the

WLI has better lateral resolution than the low resolution AFM, it is unable to resolve the tops of sharp peaks, however the low resolution AFM is still capable of finding these features, but does not always encounter the apex. Due to WLI operating with visible light, the resolving power of the tool would in fact be less than the pixel size stated in Table 5.3, however the machine does employ a multisampling technique to improve this detection. An example frame from each technique demonstrates this; more large peaks are visible in the high resolution AFM compared to that recorded at low resolution, however no particularly high peaks can be observed on the WLI image, however features on this appear 'cleaner' than those on the low resolution AFM image (Figure 5.15).

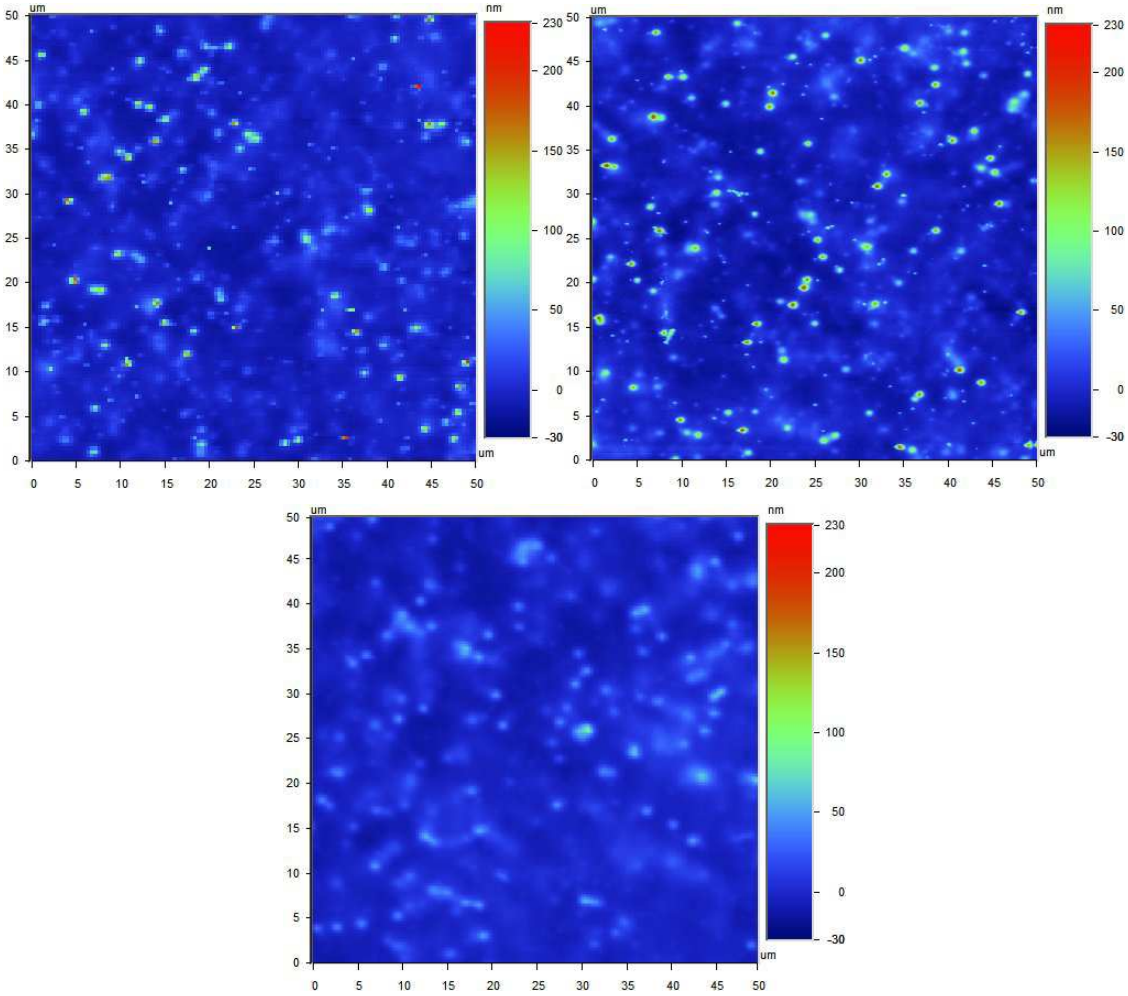

Figure 5.15: Comparison of low resolution AFM (top left), high resolution AFM (top right) and WLI (bottom)

It is worth noting that lateral dimensions of surface features affect the average roughness values more than single sharp peaks (Rakos, 2012), WLI essentially averages down the true heights but still accounts for overall roughness.

5.5.3 Array Size Requirements

The array size is the combined size of all captured images and is ultimately the size of the final stitched image, increasing the size of the array produces a result which is a more accurate representation of the surface. Work on barrier PEN exemplifies this well; if one were to continuously take sequential AFM scans of the barrier layer almost all images would exhibit a very smooth flat surface, however given enough time one would encounter an area which included a barrier discontinuity. It is these outlying features which greatly affect the performance of films and so it is important to include these rare but significant areas. With the desire to reduce the amount of time AFM stitching takes, the capture of a minimum number of frames is essential to avoid wasting time and oversampling, hence a balance must be found which still allows a true representation of the surface. The ideal situation would be to have topographical information for the entire sample but this is impractical, whereas capturing too few images will not give an accurate description.

Three sets of data using the same 50 x 500 μm stitch area have been compared; acquired using low resolution AFM (0.07 MP per frame) (Table 5.4), high resolution AFM (0.60 MP per frame) (Table 5.5) and white light interferometry (0.31 MP per frame) (Table 5.6), to determine how each technique is affected with increasing array size.

Table 5.4: Low resolution AFM, with results for arrays comprised of 1, 2, 6 and 12 frames

Area (μm^2)	2500	3535	6125	8660

R_a (nm)	9.21	9.01	8.98	8.84
R_q (nm)	14.86	14.64	14.42	14.44
R_{sk}	3.97	4.21	3.84	4.36
R_{ku}	33.87	40.47	34.04	45.92
R_{pm} (nm)	160.99	203.37	232.25	310.76
R_p (nm)	275.52	311.89	311.89	405.74

The average roughness values of the low resolution AFM stitch are not greatly affected by the array size (Table 5.4), increasing the area over which the data is obtained values of R_a and R_q remain relatively constant. Similarly skewness remains unaffected as the AFM can still detect peaks at low resolution regardless of the heights; the difference in kurtosis suggests a peaky surface but the fluctuations suggest the array is not being represented accurately. The increasing values for R_{pm} and R_p are to be expected; as the AFM collects data over a larger area the probability of encountering the less common but larger peaks increases, demonstrating the requirement to capture such outlying features.

Table 5.5: High resolution AFM, with results of arrays comprised of 1, 2,6 and 12 frames

Area (μm^2)	2500	3535	6125	8660
R_a (nm)	10.88	9.98	10.87	10.67
R_q (nm)	17.89	16.57	17.77	18.12
R_{sk}	3.66	4.04	3.69	4.84
R_{ku}	24.68	30.84	25.95	56.12
R_{pm} (nm)	205.38	230.32	253.84	503.08
R_p (nm)	224.74	274.13	334.18	661.79

High resolution AFM is affected in much the same way as the low resolution scans with increasing the array size (Table 5.5), R_a and R_q remain comparable throughout but their larger values suggest increased accuracy. The skewness also remains constant as the AFM still detects large numbers of peaks in all datasets, the increase in kurtosis is somewhat more striking however, more data points

mean that the probability of the probe encountering a high peak will be increased, hence the shift in data. Again, the increases in both R_{pm} and R_p are expected for the same reasons as with low resolution AFM.

Table 5.6: White light interferometry stitch, topography of arrays comprised of 1, 2, 3 and 7 frames

Area (μm^2)	2500	3535	6125	8660
R_a (nm)	7.03	7.06	7.15	7.20
R_q (nm)	9.92	10.07	10.14	10.13
R_{sk}	2.00	2.23	2.13	1.99
R_{ku}	9.18	12.03	10.90	9.83
R_{pm} (nm)	82.42	99.51	99.01	106.25
R_p (nm)	99.85	129.77	130.26	130.66

The results of WLI were perhaps the most surprising (Table 5.6), as the area under analysis increases there appears to be no significant change across all datasets on this scale. It is believed that this is because white light interferometry cannot detect the small particles or the tops of the sharpest peaks, meaning there is very little change to the any of the roughness factors unless a particularly large defect were to be encountered.

5.5.4 Capture Time

The drive to speed up the image acquisition process when performing an AFM stitch is one that has been highlighted many times in this chapter, one of the most simple ways to speed up AFM image acquisition is by increasing the raster speed of the probe. The downside of this is that the quality of images will decrease, mainly as a result of tracking errors demonstrated by a 9.8 x 9.8 µm zoomed regions from a 50 x 50 µm scan at 0.25, 0.5 & 1 Hz (Figure 5.16), these images demonstrate typical artefacts caused by scanning too quickly.

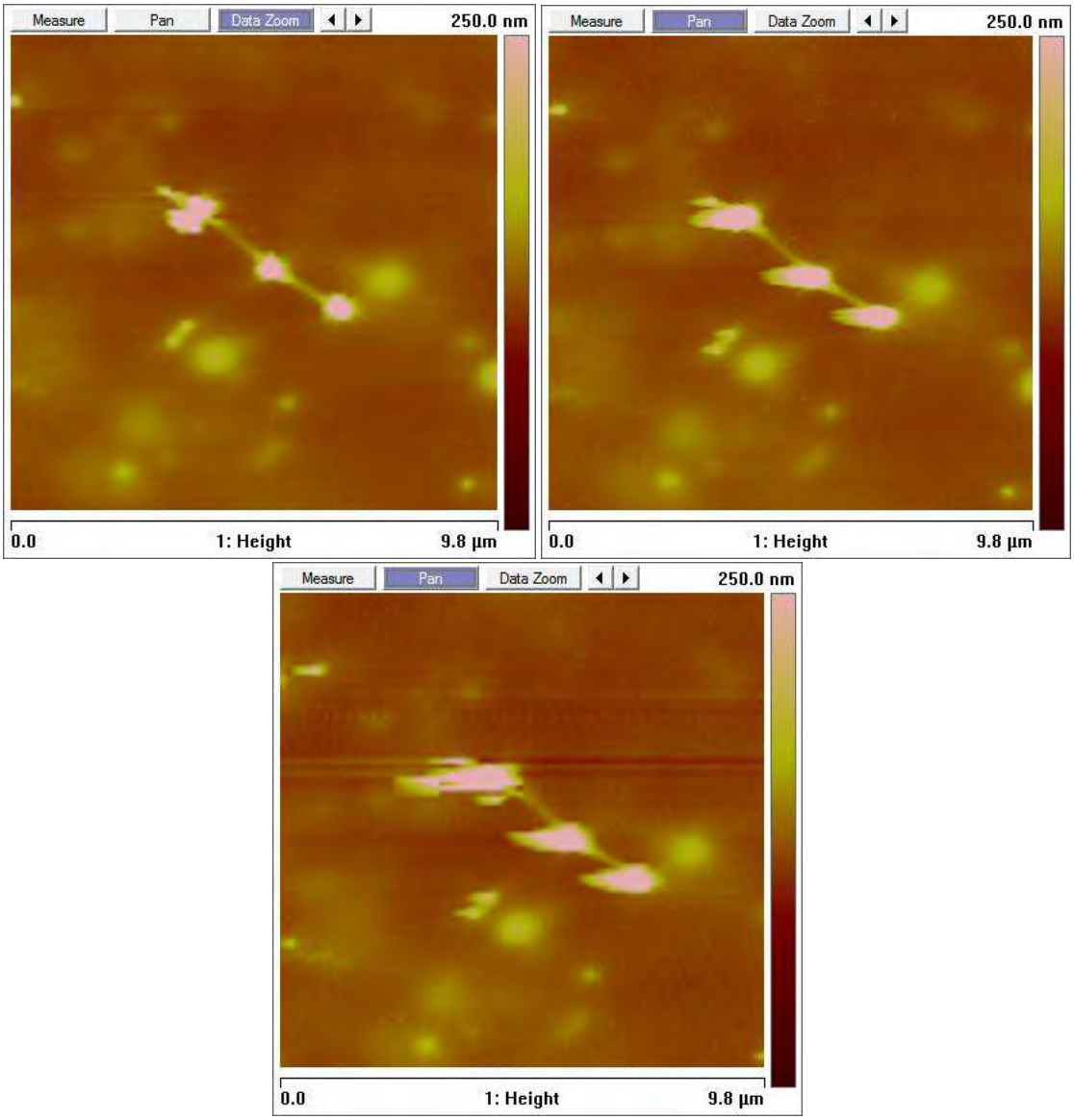

Figure 5.16: Regions from 50 µm² scans showing examples of reduced surface tracking as a result of increasing tip raster speed at 0.25 Hz (top left), 0.5 Hz (top right) and 1 Hz (bottom)

Measuring the roughness parameters from the three full size images, the results are something of a surprise (Table 5.7).

Table 5.7: Comparison of roughness parameters of an AFM topography scan with increasing probe raster speed for a 50 x 50 μm area

Raster Speed (Hz)	0.25	0.5	1
R_a (nm)	9.25	9.36	9.97
R_q (nm)	16.20	16.74	18.18
R_{sk}	5.01	5.00	5.15
R_{ku}	45.88	42.37	44.20
R_{pm} (nm)	241.72	233.13	256.17
R_p (nm)	335.32	260.81	349.38

Over a 50 x 50 μm area, the differences in scanning speed appear to make little difference to the roughness parameters despite the obvious decrease in image quality, this was a very positive result as higher speeds meant faster data capture. The same tests were performed over a 100 μm^2 area using low (Table 5.8) and high resolution (Table 5.9) AFM, the results were comparable to those for 50 μm^2.

Table 5.8: Comparison of roughness parameters of a low resolution AFM topography scan with increasing probe raster speed for a 100x100 μm area

Raster Speed (Hz)	0.25	0.5
Pixel Size (nm)	390.63^2	390.63^2
Resolution (MP)	0.07	0.07
Capture Time (min)	17	8.5
R_a (nm)	9.49	9.94
R_q (nm)	16.12	17.69
R_{sk}	4.37	4.63
R_{ku}	35.32	36.07
R_{pm} (nm)	229.71	226.72
R_p (nm)	267.16	254.54

Table 5.9: Comparison of roughness parameters of a high resolution AFM topography scan with increasing probe raster speed for a 50x50 μm area

Scan Speed (Hz)	0.25	0.5
Pixel Size (nm)	97.66^2	97.66^2
Resolution (MP)	1.05	1.05
Capture Time (min)	68.3	34
R_a (nm)	9.63	9.96
R_q (nm)	16.62	17.83
R_{sk}	4.60	4.80
R_{ku}	38.66	39.14
R_{pm} (nm)	282.30	279.73
R_p (nm)	345.32	378.88

Whilst slower raster rates give more accurate images and less chance of line errors, it would appear that a more rapid scan speed can be applied for AFM stitching without a negative effect on roughness measurements. However, rough surfaces such as the development film enforce an upper limit due to post processing requirements; it would be possible to drive the tip faster but images feature many more artefacts and scanning errors, whilst many could be removed the quality of the data would suffer.

5.6 Large Area AFM Stitch

With everything considered thus far, an ambitious attempt at a large area stitch was attempted, the aim was to generate an array that was approximately 250 x 500 μm at a very high resolution. In total, sixty images were captured in a 12 x 5 grid pattern, each at 768 x 768 pixel resolution with a 50 x 50 μm field of view using a scanning speed of 1 Hz. A 10% overlap was allowed for image alignment, accounting for piezo and thermal drift; image capture, processing and stitching took a total time of approximately one week of continuous work during office hours (Figure 5.17).

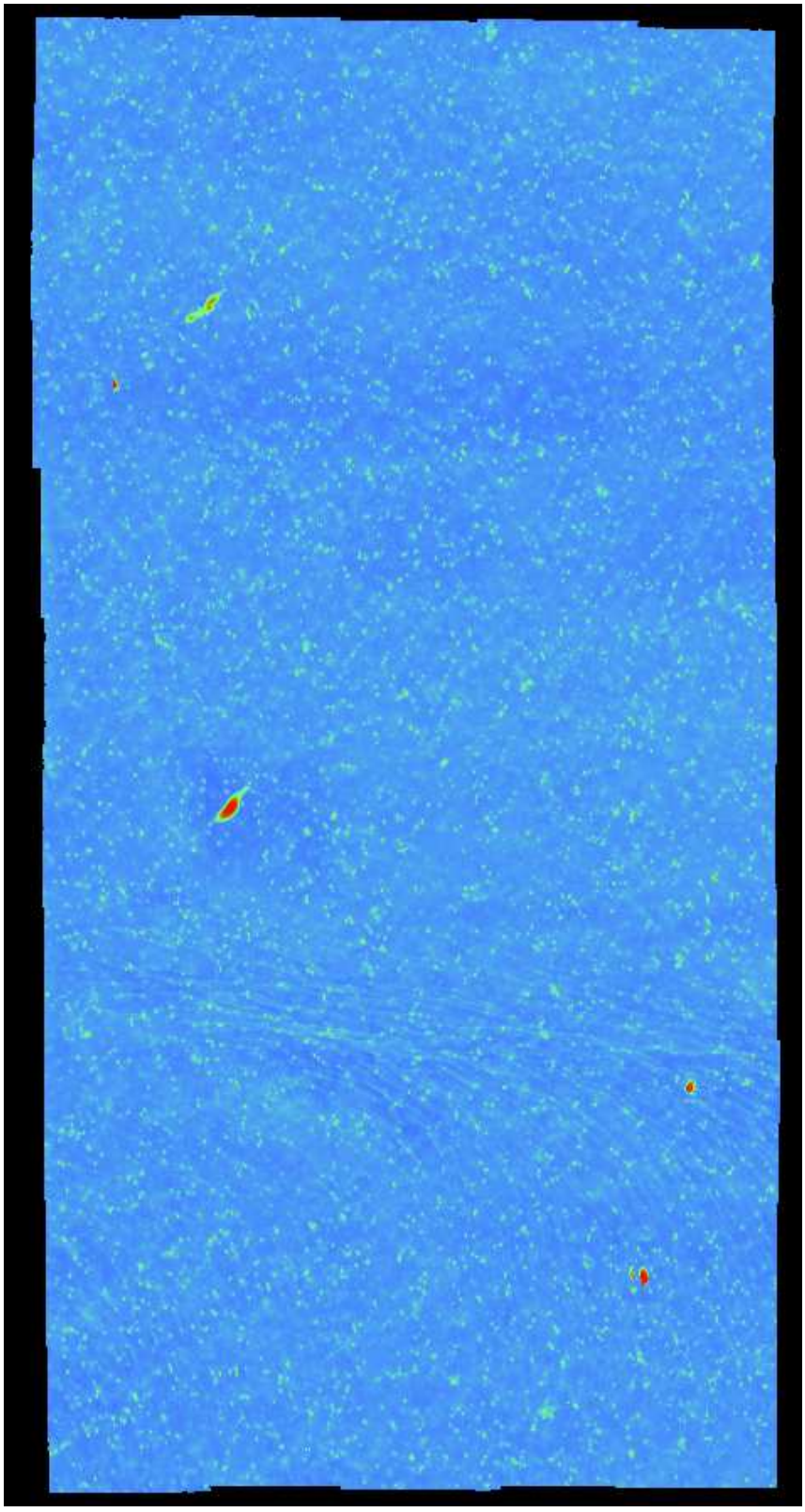

Figure 5.17: 455 x 228 µm, 65nm resolution of a highly textured DTF development film

The result is an image of incredible clarity; a 465 μm x 247 μm array with a 65.1^2 nm pixel size and 27.1 megapixel resolution. This stitch was possible due to the highly textured surface of the film, performing a similar function on a section of planarised PEN is much more difficult due to the lack of features to allow accurate edge alignment. Carrying out the process on a particularly featureless film could be performed by depositing a very sparse coating of small particles on the surface which could be used as alignment markers and subtracted from the final image.

Zooming into areas of Figure 5.17 reveals the clarity afforded by the technique, unexpected features were detected, including a long range low special frequency element which was only noticed during Baring ratio analysis. There are also areas that appear to be micro cracks on the lower half of Figure 5.17, this texture was of great interest as no features like these had been captured previously using WLI (Figure 5.18). It is unlikely that either of these features would have been detected if the roughness parameters determined in this chapter were produced by the summation of data from each individual frame.

The observation of this texture required the detail afforded by AFM imaging but the large area capability of the WLI. Stitching reduces this problem by incorporating a greater amount of detail into each scan allowing a more accurate representation of a sample surface.

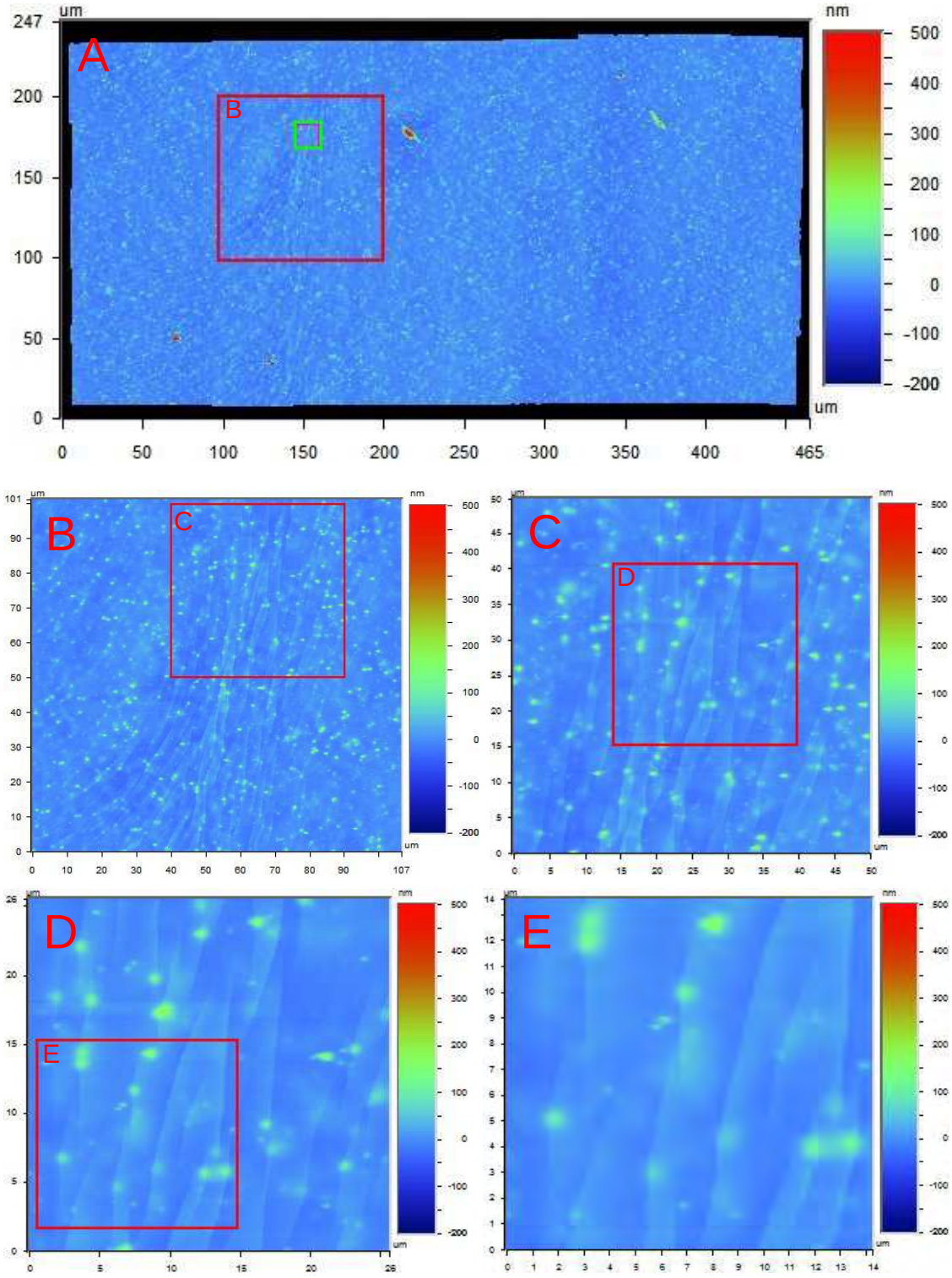

Figure 5.18: Zooming in to regions of Figure 5.17, red square highlights area represented in each subsequent image, green box in the first figure represents area in final image

Comparing the roughness parameters for this large AFM scan and a large WLI image reflect some of the findings discussed in this chapter and provide some interesting results (Table 5.10).

Table 5.10: Comparison of large area AFM and WLI stitches

	AFM	WLI
Array (μm)	247 x 465	1800 x 1300
R_a (nm)	10.77	7.36
R_q (nm)	19.78	10.23
R_{sk}	8.15	1.89
R_{ku}	175.00	10.55
R_{pm} (nm)	910.74	193.49
R_p (nm)	968.61	213.09

As one may predict, the AFM data detects the surface to be much more peaky as a result of its ability to accurately detect sharp peaks and smaller particles. Surprisingly, despite the WLI stitch covering a much larger area the results are comparable to those given in Table 5.6 for just one frame. Despite this, it is important to highlight the major advantage of these stitches with their ability to measure the continuity of the surfaces over long distances including rare but large defects which may go undiscovered using typical analysis fields of view. As discussed above, the strengths of the AFM stitch revealed information about a film which had previously gone unseen.

5.7 Future Developments

Since this work was completed, Bruker have taken a great interest in applying the work as an industrial technique, but their preliminary work has met with limited success thus far.

A third party stage replacement has been suggested by Bruker to assist in this work, available to increase the scanning area to 400 or 800 μm^2. However the stage has been demonstrated to have limited reproducibility and it is suspected that these modified stages will further sacrifice accuracy

for area. The hardware also has a limited number of pixels over the detector. If these stages were applied to the Dimension 3100 the 800 μm area would still only have 1024 x 1024 pixels over it, severely reducing the resolving power of the tool and negating the reason for carrying out the large area scan.

The new Bruker Dimension ICON has been demonstrated with a so called 'fast scan' attachment capable of producing one AFM image per second (Bruker, 2011), the acquisition of images this quickly would be very useful for the stitching technique. However, the maximum image size capable by the fast scan is 30 μm^2 and at this maximum field of view cannot capture at the highest rate. Furthermore the acquisition of a larger number of images, each requiring post-processing and individual stitching makes the fast scan impractical for use with stitching.

The best way forward for the technique would be use of the improved scanner resolution of the Dimension ICON (3000 x 3000 pixels) over its maximum field of view of 90 μm, reducing the number of images required for large area, high resolution stitches whilst maintaining the same quality. Since Bruker has taken a great interest in the technique it is also believed that the company will introduce programmed automation to the process, likely using some of the techniques applied to white light interferometry stitching.

5.8 Conclusions

This chapter has described a new method for measuring defects over large areas using the AFM. The method is akin to WLI stitching of datasets from small areas to give a large dataset over several mm^2.

It was demonstrated in Chapter 3 that AFM is typically used to measure the roughness of surfaces over very small areas and it is capable of providing more detailed surface analysis than WLI. However the latter can measure much larger areas. Therefore stitching AFM images was carried out to give both roughness resolution and large area capability. Throughout this chapter, numerous

issues were tackled to make the method capable of reproducible and reliable results, with the requirements of speed, resolution and quality considered, culminating in the production of a large area AFM stitch.

To summarise the findings it can be said that WLI can typically measure surface topography very rapidly and with reasonable detail but misses the fine detail of small particles and sharp peaks; hence extreme figures, kurtosis and skewness are all measured as being lower than they actually are. Low resolution AFM tends to give more accurate information, it is slower than WLI but quicker than high resolution AFM and is more likely to capture the high peaks and low valleys. Although it has a lower image quality compared to WLI and samples at less frequent intervals, whilst it was expected to give very poor results those obtained with this technique were much better than expected. Finally, high resolution AFM gives the best, most representative data of surface topography but takes the longest amount of time to capture, the inclusion of larger areas ensures that the statistical data is more accurate and the rare but more significant peaks found across the surface which may normally be missed can also be included in the data.

The large area stitch demonstrates the power of the technique, and has been very useful for DTF product development, furthermore interest from Bruker confirms its value, the final stitch image was revealed to the Application Director of the company who described the image as 'beautiful'.

The technique gives very detailed, high resolution images, but it is still a lengthy process and is only capable of analysing small areas compared to the large scale on which barrier failures are observed, as such is unsuitable for attempting to locate defects across barrier films. As a result, alternative methods of detection were sought and are discussed in Chapter 6.

6. Detection and Compositional Analysis of Barrier Film Defects

6.1 Introduction

Despite the initial promise of the AFM stitching technique it was decided that a more rapid and efficient method was required for this study. This chapter describes the processes which were involved in developing the calcium test from a simple permeation test into a technique to enable detection of individual flaws in thin film barrier layers. This was subsequently used to locate and perform a preliminary analysis of the defects in a DTF aluminium oxide barrier film using both AFM and SEM to obtain structural and compositional information.

6.2 High Magnification Analysis

The manufacture of semi-conductors requires stringent cleanliness throughout all stages of the production process. The same can be said for the production of displays grade films for flexible electronics. This is a result of the incredibly fine features utilised in such systems which are predicted to reach 11 nm by 2019 (IRTS-Lithography, 2011). As miniaturisation is set to continue, high levels of hygiene must be upheld to prevent contamination and intrusion of extraneous defects. Analysis of flaws on these scales requires equipment capable of very high magnification to allow detection and characterisation of individual contaminants. Atomic Force Microscopy is routinely used in the semi-conductor industry for quality control purposes (IRTS-Test, 2011), with SEM the most common choice for high magnification analysis beyond the optical diffraction limit (Phillips, 1994). The purpose of this research project was to test Atomic Force Microscopy (AFM) as the defect analysis method, backed up by SEM for supporting data. The reasons for this decision are outlined in the following sections.

6.2.1 Advantages of Atomic Force Microscopy

The AFM is an excellent high magnification analysis tool with the capability to analyse minute details at the sub-micron level on most surfaces, even in liquid environments. Unlike many high resolution imaging methods, it also has the ability to provide information on density differences, electrical conductivity, magnetic imaging and nano-manipulation, further extending its abilities (Veeco, 2008). The AFM is easily capable of inspecting specific thin film barrier flaws, but without a technique to direct the macro scale movements of the tool, searching for these is incredibly time intensive, making such non-targeted analyses unfeasible, as discussed in Chapter 5.

6.2.2 AFM vs. SEM

With the shortcomings of the AFM highlighted one might ask why scanning electron microscopy was not chosen. Whilst the object targeting and the image acquisition can be more rapid using an SEM, polymers are difficult to examine as they have a tendency to rapidly charge, even with a conductive coating, resulting in beam divergence and image degradation (Phillips, 1994). In comparison AFM can analyse insulating materials with minimal sample preparation, thus preserving surface textures and allowing repeat analyses without the risk of charging. Furthermore, an AFM can produce an equal or higher resolution image of an equivalent area but with the addition of absolute X, Y and Z data for any features (Phillips, 1994). Capturing this was considered to be of high importance in this study as it was believed that the dimensions of any surface defects, whether intrinsic or extrinsic, are the key determining factor as to whether such flaws will disrupt the barrier layer; hence a way to measure the absolute size and shape of defects is critical. It has even been stated that the examination of pinholes using SEM is 'impossible' due to their infrequency and the inability of such instruments to resolve such flaws at low magnification (da Silva Sobrinho, 2000). Regardless of the analysis technique, the size and frequency of defects are such that a large surface assay would be time consuming and somewhat inefficient. Given the requirement for both SEM and AFM to have a technique to allow macro-scale direction, it was felt

that the ability of AFM to measure polymeric surfaces without preparation and the generation of absolute dimensional data with every scan, made it the preferred choice. SEM was still utilised as a complimentary technique to extend the abilities of the AFM and provide structural data, as shown in Section 6.4.2.

6.3 The Calcium Test

Upon commencement of this project, the calcium test was utilised only as a way of evaluating the performance of thin film barriers, its application in many publications discussed in Chapter 3, inspection beyond the scope of optical microscopy having never been considered. The calcium test was subsequently developed in this thesis from a simple method for measuring permeation into a technique facilitating the locating of surface flaws to allow detailed AFM analysis.

6.3.1 OLED Device Failure

Typically, OLED based displays make use of low work function metals such as calcium, as cathodes (Dodabalapur, 1997); the oxidising effect of water on these materials has been determined to be a major cause of device failure, even more so than the reaction of water with the active OLED polymeric materials (Nisato, 2003). As a result, the calcium test can be considered to be the most representative system of an OLED device from all the available permeation tests. A visual comparison of the progression of black spot formation in OLED pixels (Figure 6.1) to that of so-called 'pinholes' on calcium test cells (Figure 6.2) further supports the comparison.

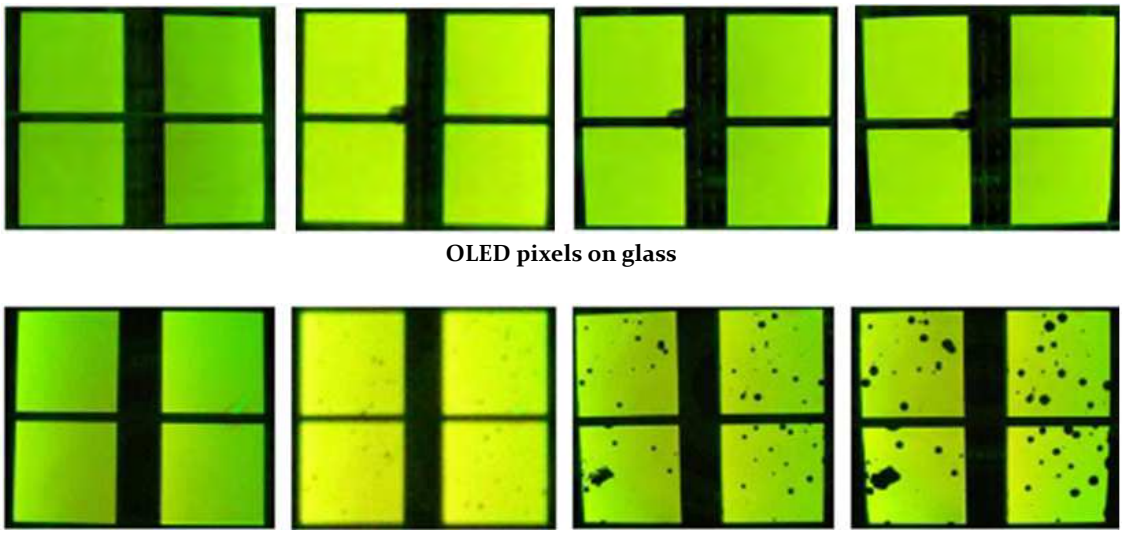

Figure 6.1: Progression of defects in OLED test cells on glass and PEN; start of test (far left) after one week (centre left), two weeks (centre right) and four weeks (far right). Each pixel is 10 mm² (DTF, 2007)

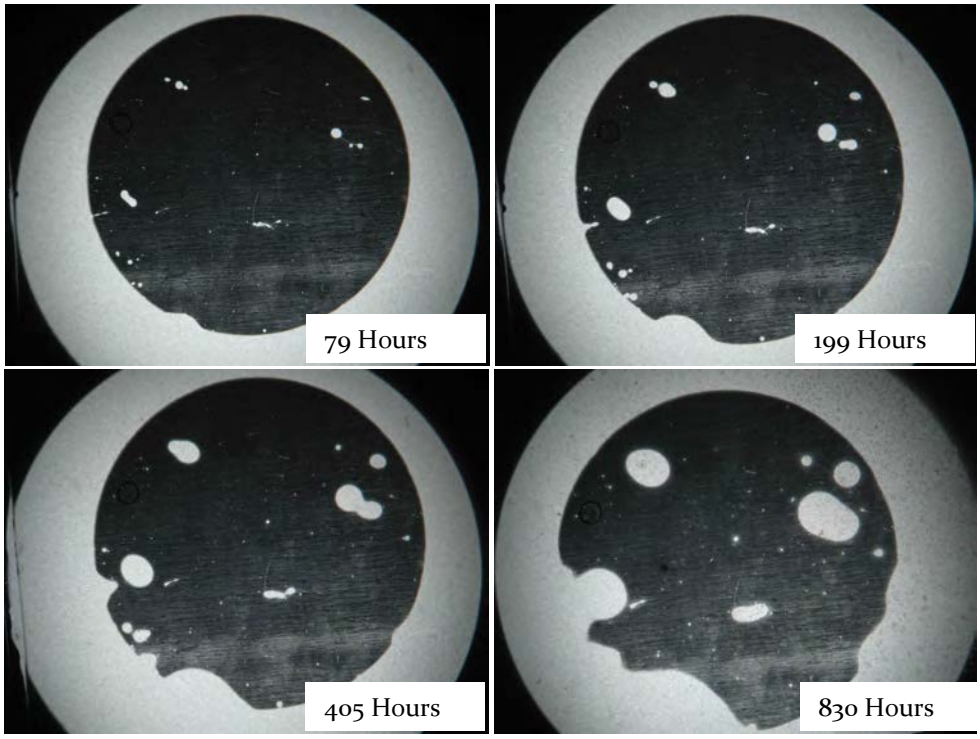

Figure 6.2: Top-down view of pinhole evolution in a calcium test cell, observed using transmission light microscopy, elapsed test time inset in each image

Pinholes appear to develop from single points of origin as transparent circular spots which increase in diameter over time; the nature of this growth suggests moisture enters from one defect site through which it diffuses at a uniform rate in all directions.

Whilst there are many methods of testing barrier performance, few can identify individual defect sites as the calcium test does. The calcium test is also somewhat cheaper to perform than permeation tests using OLED pixels, hence it was the optimal choice for this study. Moreover, using the calcium test to locate surface flaws allowed the volume of permeating water to be determined and hence the severity of each barrier break, an important piece of data which would be missed using a purely microscopy based analysis technique.

6.4 Development of the Calcium Test to Direct AFM Analysis

This section aims to outline the steps which were carried out to develop the calcium test from a simple permeation test into a powerful technique for directing the AFM towards barrier defects.

6.4.1 Mechanism of the Calcium Test

A calcium test cell is made by laminating a section of barrier coated polyester to a glass slide, the two are held together by means of an epoxy resin. The action of the calcium test is quite simple; flaws in the aluminium oxide layer act as low resistance paths for the passage of moisture. As water progresses through these flaws into the cell, it encounters the encapsulated calcium metal and reacts to form transparent calcium oxide (Adam, 2007).

$$2Ca + H_2O \rightarrow CaO + CaH_2$$
$$CaH_2 + 2H_2O \rightarrow Ca(OH)_2 + H_2$$
$$CaO + H_2O \rightarrow Ca(OH)_2$$

Via optical inspection, these areas appear as clear, circular regions in the calcium (Figure 6.2) which increase in diameter over time. As the thickness of the calcium metal is known, the mass of calcium which has reacted can be calculated and hence the volume of water which has diffused into the cell for a given period of time can be determined (Carcia, 2009).

As described previously, the mode of pinhole growth suggested single points of entry for moisture. This led to the assumption that a barrier disruption must exist wherever calcium pinholes developed, most likely originating from a central point. If this were the case, examination of the centre of the pinhole with a sufficiently powerful microscopy technique should reveal the cause of the water ingress. A technique to retain these pinholes to allow the application of AFM was now required.

6.4.2 Registration of Pinhole Locations

Inspecting the barrier surface at the centre of each pinhole requires their locations to be preserved, these will only remain visible as long as the calcium inside the cell remains protected from airborne moisture. However, delaminating the polymer from the glass and hence exposing the metal to water in the atmosphere, is essential to allow the application of any microscopy technique.

6.4.2.1 TTM Module

One attempt to circumvent this problem was through the use of a Through Transmissive Media (TTM) Module for the NT9800 white light interferometer; this accessory allows a user to study surfaces through dispersive materials up to 5mm thick (Veeco, 2009). The module has two cells, one for the sample and a compensator for the covering medium, the instrument effectively subtracts the covering surface from the scan allowing inspection of the surface underneath (Figure 6.3). In practice however, the application was less than perfect; attempting to use the epoxy in the compensator was not feasible as the thickness has to be near identical to that of the sample. The depth of epoxy in both cases could not be controlled to the required degree of accuracy. Attempts

to analyse through the glass underside proved more encouraging, however the results were still poor. Had the module been applied successfully to the calcium test samples, given that the resolution of the Wyko is insufficient to study the smallest defects in the barrier layers, use of the TTM module reduces the resolving power of the instrument, meaning it would compound this problem further.

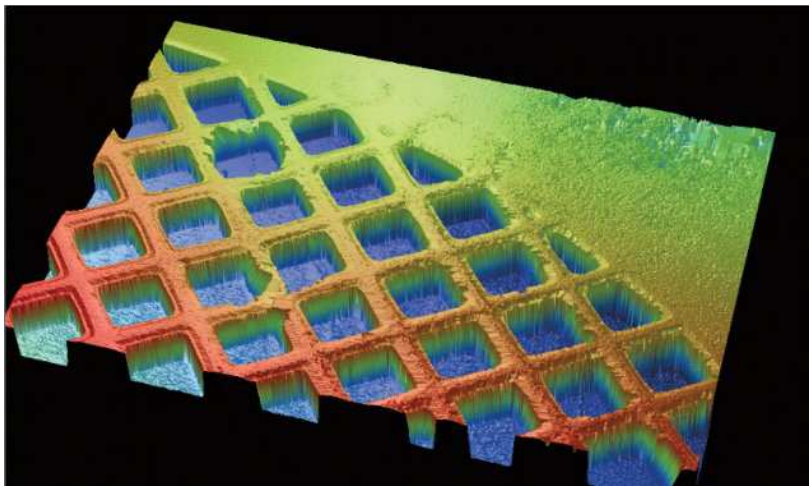

Figure 6.3: Grating imaged through 5 mm of water using TTM module (Veeco, 2009)

6.4.2.2 AFM based solutions

The possibility to purchase a gas chamber to allow AFM samples to be analysed under inert gases was considered, however no suitable accessory existed to allow substrate delamination in-situ, hence a different approach was required.

Initial attempts to locate pinholes after delamination involved securing the sample on the AFM stage as a complete cell within a custom jig; the location of each defect could then be recorded as a set of coordinates whilst they were still visible. Once the cell was removed and the polymer delaminated, it could then be returned to the jig and the locations of each pinhole could be recalled and scanned without the visual direction. In practice however, problems resulted through a lack of repeatability with the movement of the AFM stage, stated to be repeatable to 4 µm for the x-axis and 6 µm in the y-axis (Veeco, 2001), resulting in discrepancies between the recorded coordinates

and the actual locations to which the AFM stage moved. Whist in some cases it was possible to scan these areas using a large field of view and subsequently zoom in on the area of interest, this added an unnecessary, time consuming step, reducing the efficiency of the process; in some cases flaws could even not be relocated.

The solution was to take an aged calcium test cell and highlight the pinholes on the outside surface of the polymer film using a fine tipped marker pen, a light box and a light microscope. A sharp knife was then used to score an area around the calcium button in the polymer, which was subsequently delaminated from the glass (Figure 6.4).

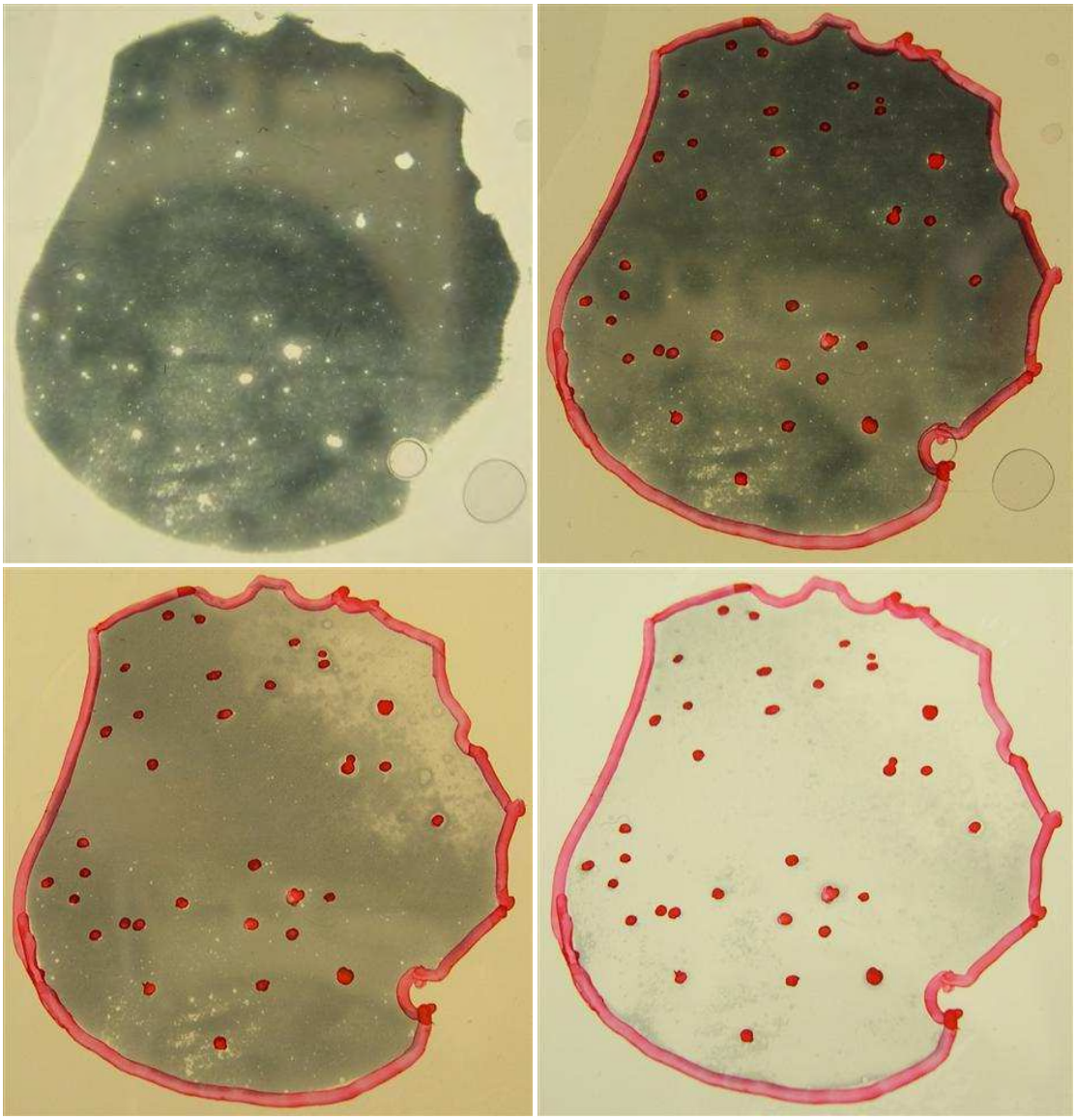

Figure 6.4: Calcium spot labelling and subsequent degradation; calcium button in test cell (top left), with added labels (top right), delaminated with partial oxidation (bottom left) and complete oxidation (bottom right)

After delamination, the approximate location of the pinholes was preserved with enough accuracy to align the AFM optics and scan the centre of these locations.

6.4.3 Barrier Delamination Issues

Although a rough technique to preserve the pinholes had been found, more problems were encountered as a result of the delamination step. It was noted that certain calcium test cells were more difficult to separate than others; investigations revealed that in some cases the barrier was actually peeling away from the test substrate and preferentially adhering to the calcium metal (Figure 6.5). Whilst the internal areas of pinholes will be devoid of metallic calcium and hence at no immediate risk, it transpired that adhesion between the barrier-calcium-epoxy interfaces were sufficient to interfere with smaller sites of interest.

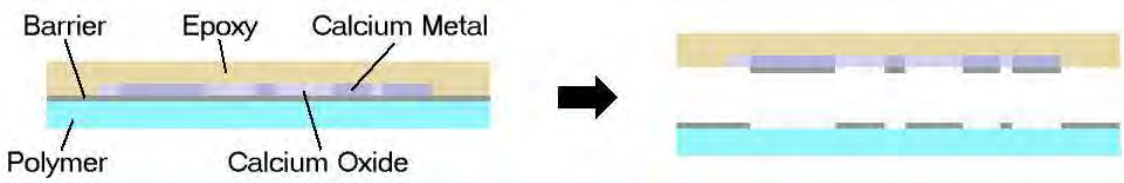

Figure 6.5: Schematic cross section of a calcium test cell before and after delamination, showing areas of barrier preferentially adhering to the remaining calcium metal

The original assumption was that the area of polymer on to which the calcium was deposited would not come into direct contact with the epoxy, acting as a buffer zone and allowing the layers to delaminate. However, optical (Figure 6.6) and AFM (Figure 6.7) inspection of delaminated calcium test buttons supported concerns that the barrier layer has a greater affinity for the calcium metal than the polymer.

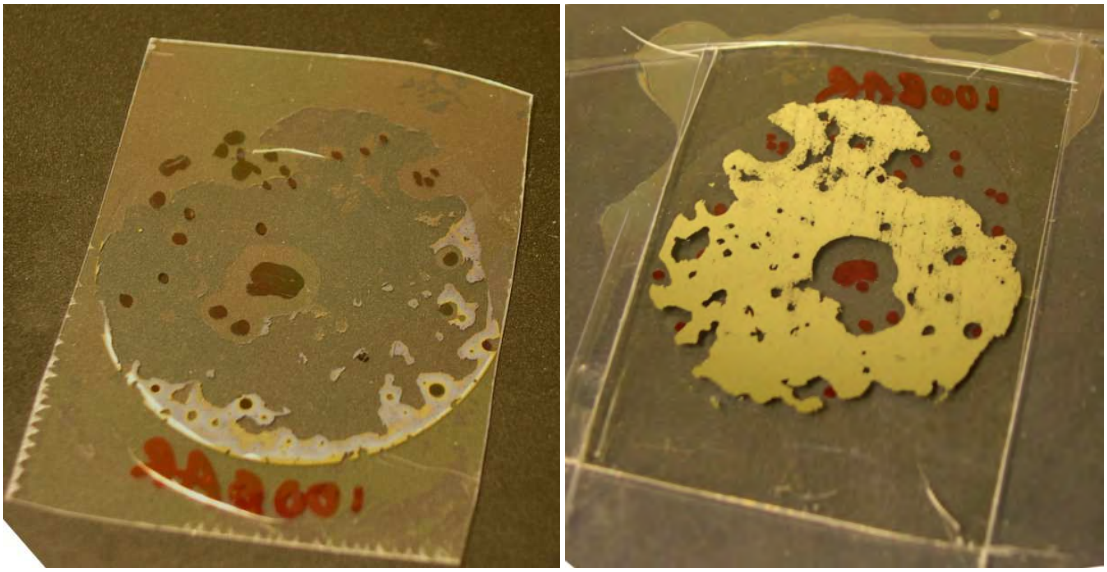

Figure 6.6: Photos of delaminated calcium buttons showing preferential barrier adhesion; discontinuous aluminium oxide on the polyester can be recognised by its yellow hue (left) and opposing glass/epoxy surface showing areas of persistent calcium after 24 hours (right)

The colour of the layer certainly matched that of aluminium oxide coated on to PEN film and the persistence of the calcium metal attached to the opposing epoxy side many hours after delamination suggested that there was indeed some form of protective coating covering the metal. AFM measurements showed the step difference of this layer to be consistently within the specification of the barrier depth (Figure 6.7).

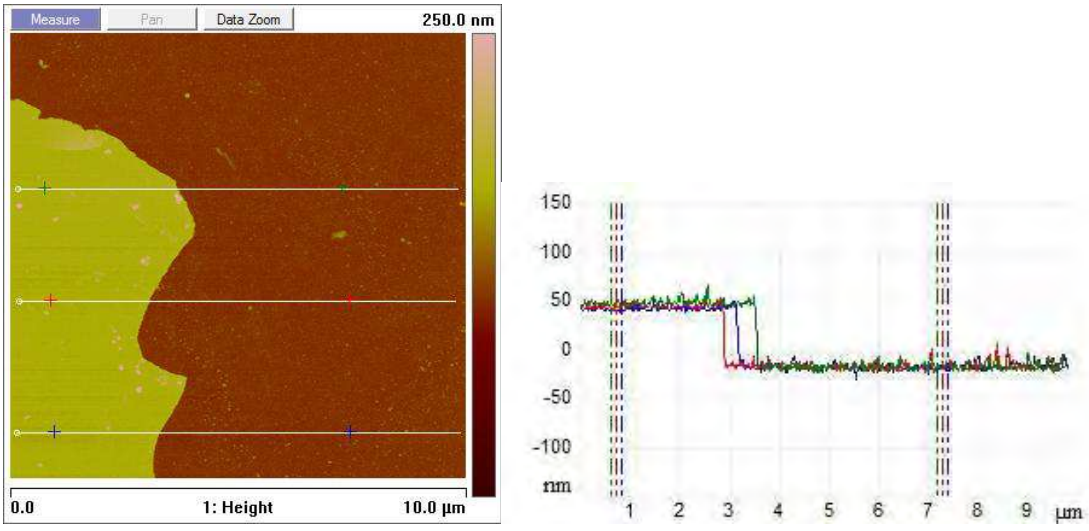

Figure 6.7: Measurement of suspected barrier edge; AFM topography image showing cross sectional sample areas (left) displayed graphically with absolute height measurements; blue; 61.4 nm , red; 62.3 nm, green; 65.4 nm (Right)

SEM EDX analysis further confirmed that these raised areas contained large amounts of aluminium, whereas the uncovered regions did not (Figures 6.8 & 6.9).

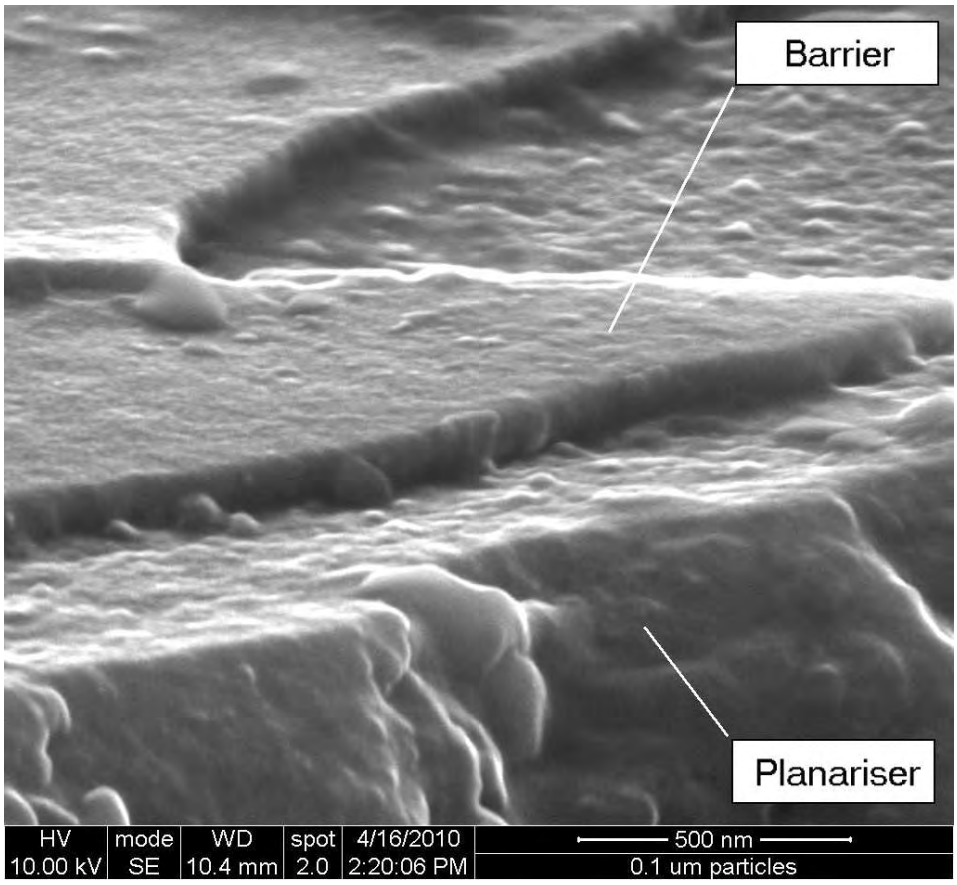

Figure 6.8: Secondary electron SEM image of the barrier layer coating on planariser at the edge of a cut film, the fine, granular structure of the aluminium oxide layer is apparent

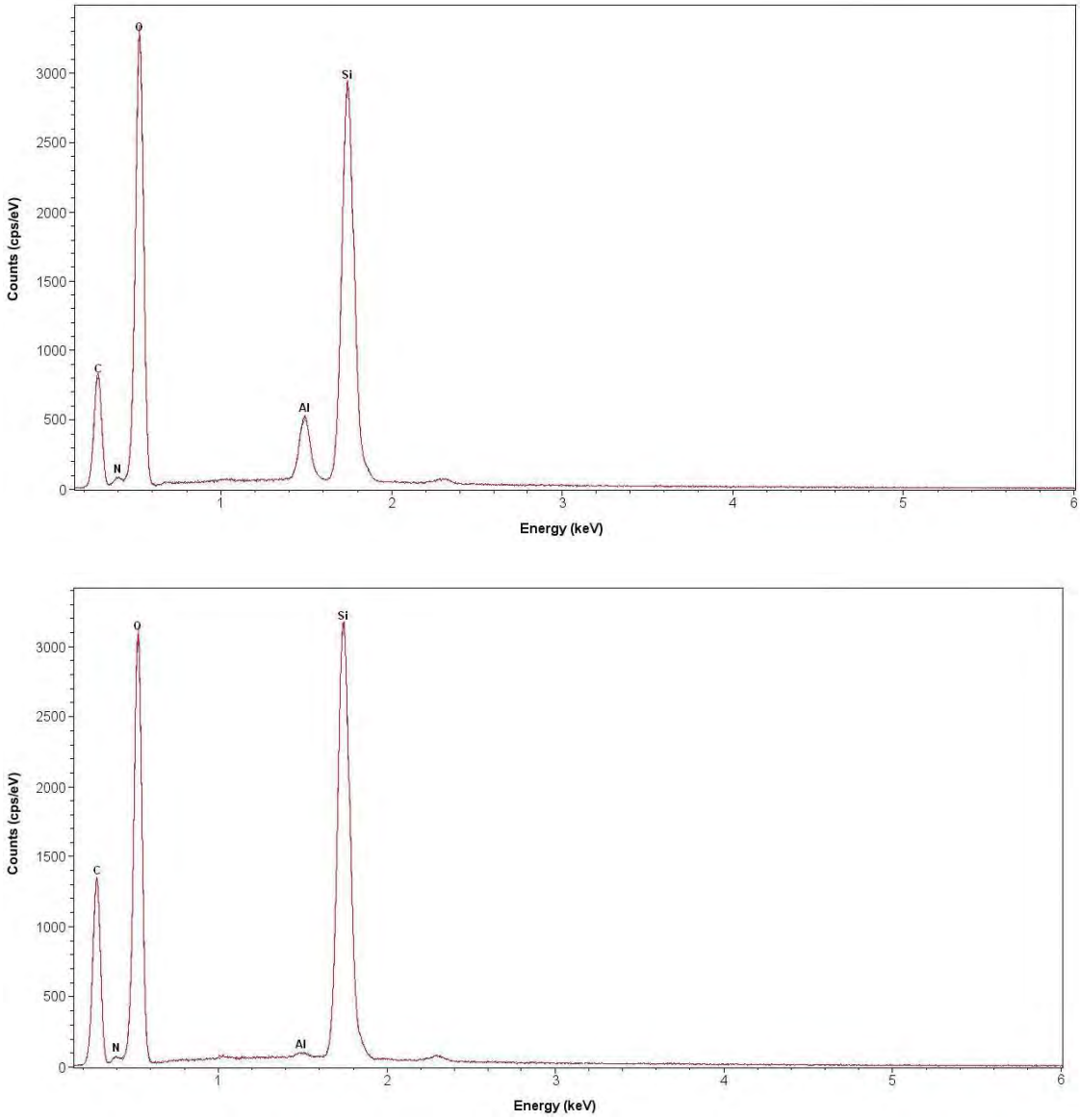

Figure 6.9: Corresponding EDX data for barrier(top) and planariser (bottom)

6.4.4 Delamination Techniques

Multiple delamination techniques were tested at varying pressures, speeds and over a range of areas, however the most effective solution proved to be slow separation underwater. Carrying out the process in an aqueous environment caused any remaining calcium metal to rapidly react as it is exposed to the water, freeing the glass and polymer surfaces. Furthermore, using a more gentle separation technique such as this, meant that any sufficiently large contaminants remained adhered in the epoxy, allowing direct inspection of the particulates responsible for barrier perturbations (See Section 6.4).

6.4.4.1 Discovery of Water Contaminants

It was noted during SEM-EDX analysis of post calcium test polymer that the calcium oxide contained significant levels of fluorine, it is suspected that this was liberated from fluoride in the water in which the calcium test cell was delaminated; the original delamination took place in demineralised water, not deionised, however, SEM-EDX of these still showed traces of fluorine. Analysis of a sample which had not been delaminated in water also showed that fluorine was present (Figure 6.10). Due to the presence of a fluorine peak only when calcium was present, it was suspected that it was a contaminant within the calcium metal.

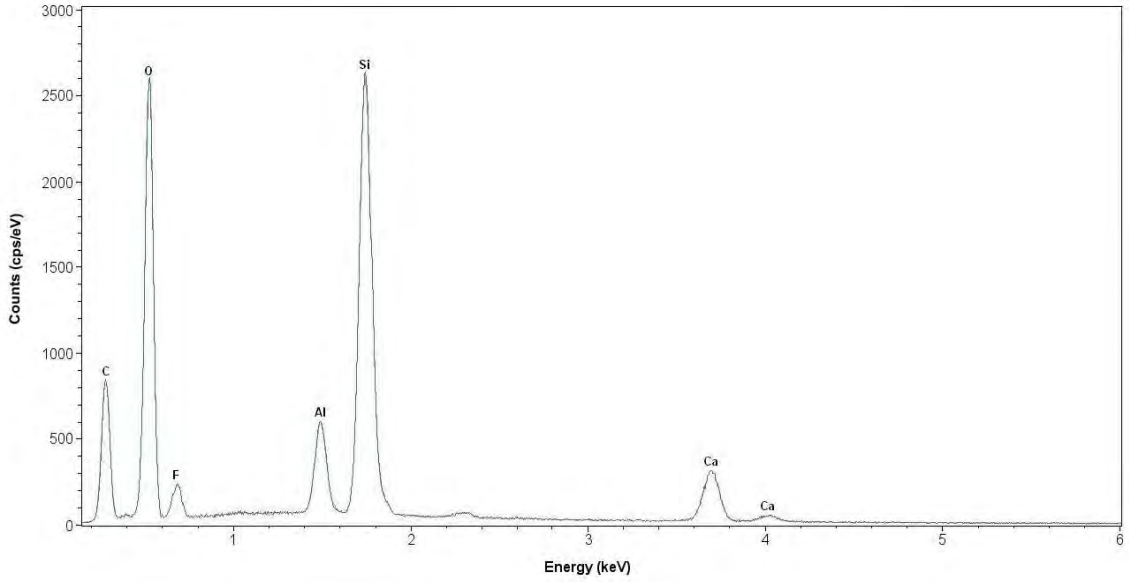

Figure 6.10: EDX plot to demonstrate the presence of fluorine in a test sample delaminated in air

6.4.4.2 Calcium Oxide Removal

Once a polymer sample has been delaminated, traces of calcium oxide remain on the surface, whilst this tends to diffuse towards the edges of pinholes and does not greatly interfere with AFM analysis, the effect of its removal was investigated. Surface cleaning had the potential to improve the quality of AFM scans, however there was an increased risk of surface disruption; hence a number of solution based cleaning techniques were investigated in an attempt to discover one which could be used without causing damaging. Whilst it was found that a brief ultrasonic clean using deionised water was very effective, it also removed the markers required for AFM direction; attempts at utilising physical markers were trialled, however the accuracy of these was insufficient. The ink labels on the non-barrier side are sufficient to align the AFM optics and permit scanning areas of interest, it is crucial that the defects are not only centred correctly, but the whole system including the optics and probe are aligned exactly otherwise scanning will commence off centre. The calcium oxide boundary regions can help in locating defects in (Figure 6.11), however once the delamination step was performed underwater these were somewhat less obvious.

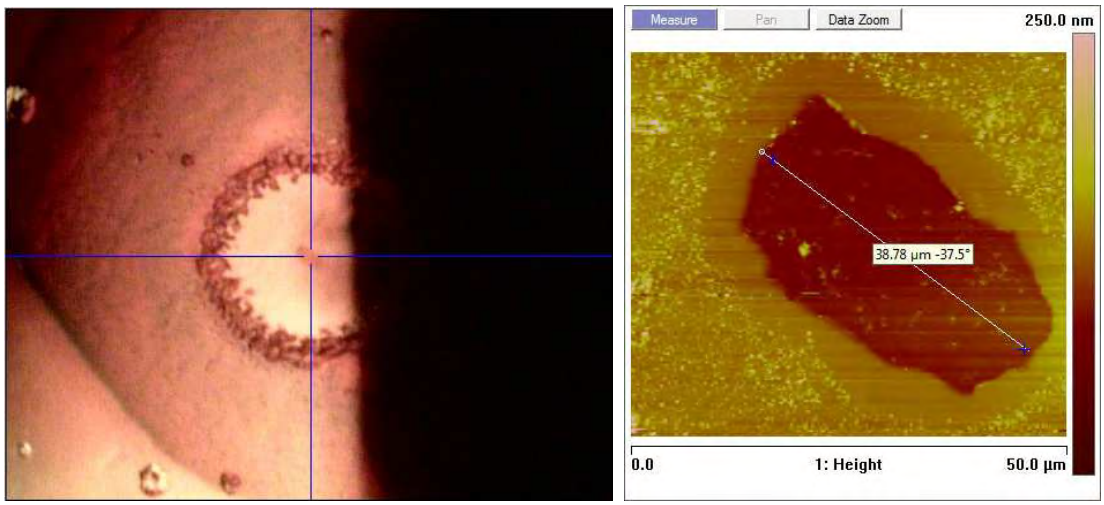

Figure 6.11: Alignment of scan area from original test cells with calcium boundary (left) and an AFM scan of the centre of this area (right)

After the introduction of aqueous delamination, it was determined that image quality was high enough to remove the cleaning step, which was not only capable of effecting surface features but in some cases was also responsible for generating surface texture. The results of which are discussed in greater detail in Appendix A.

6.4.5 The Effect of Calcium Metal on PEN and Epoxy Resin

It was decided that for the calcium test to become a routine analysis technique its reliability should be confirmed as it still remains in development (Edge, 2009). The calcium test has been shown as an effective, highly sensitive way of testing ultra barrier films within DTF and as demonstrated in the literature in Chapter 3. However, surprisingly little attention has been given to the consequences of using such a reactive metal in contact with organic materials. The possibility that the reactivity of the calcium could be an issue was first encountered during attempts to confirm the depth of the metal.

When calcium is deposited, the thickness is monitored by means of a crystal oscillator, a well documented technique which monitors the known oscillation of a quartz crystal to detect mass

increases on an acoustic resonator, caused by the accumulation of calcium on the surface. This change is then interpreted through pre-calibration to an increase in layer thickness (Sauerbrey, 1959). The high precision of the AFM in the Z direction was viewed as an excellent way of confirming the accuracy of the crystal oscillator. A 100 nm step change should be easily detected but the reactivity of the calcium made direct measurement impossible; instead AFM analysis was directed to the imprint left by the calcium button in a covering layer of epoxy resin (Figure 6.12).

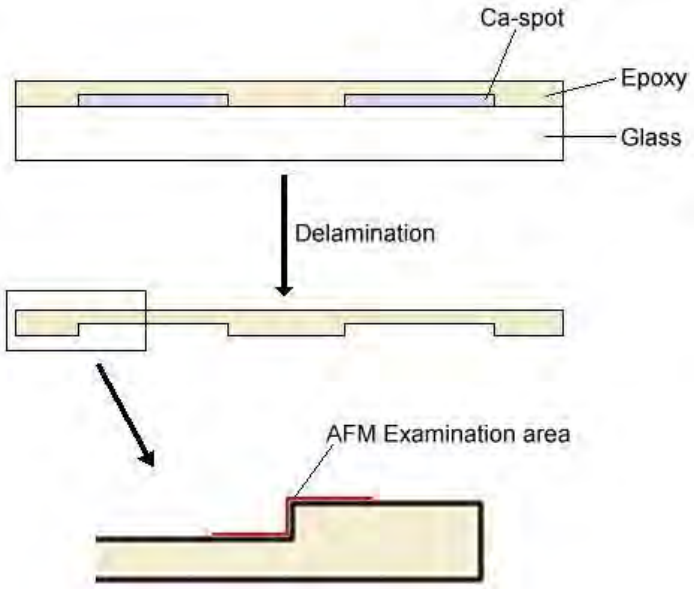

Figure 6.12: Schematic representation of the epoxy imprint where the AFM was applied in an attempt to confirm step height

6.4.5.1 Reaction of the Calcium with Epoxy

Upon analysis of the epoxy step it rapidly became clear that the surface featured a great deal more topography than was expected; areas of the sample which had been in contact with the calcium exhibited highly pitted and uneven features (Figure 6.13).

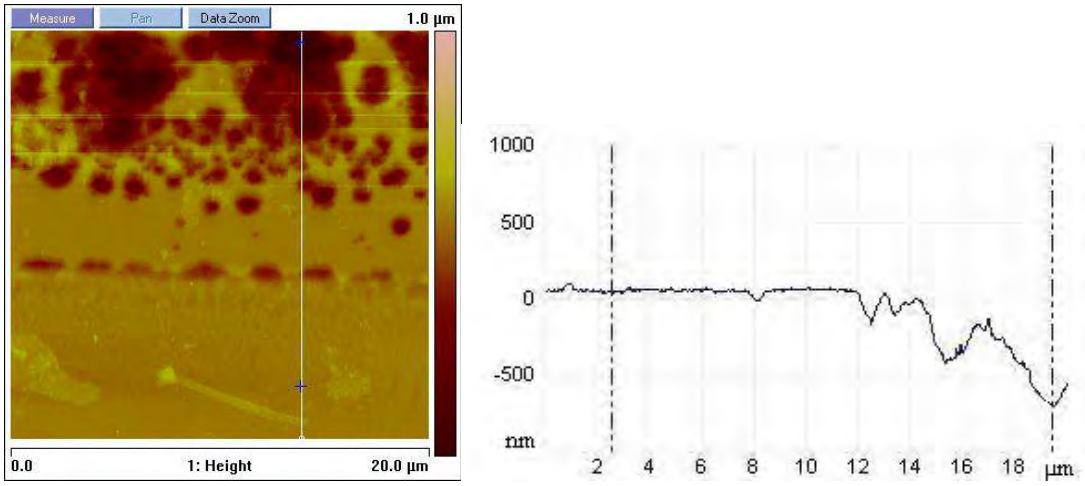

Figure 6.13: AFM topography scan of the area highlighted in Figure 6.12 (left) and a cross section through this area showing pit depths up to 737nm (right)

The experiment was repeated but the calcium was substituted with aluminium to see if a clean step could be produced using a less reactive metal, these results did give a much cleaner result (Figure 6.14).

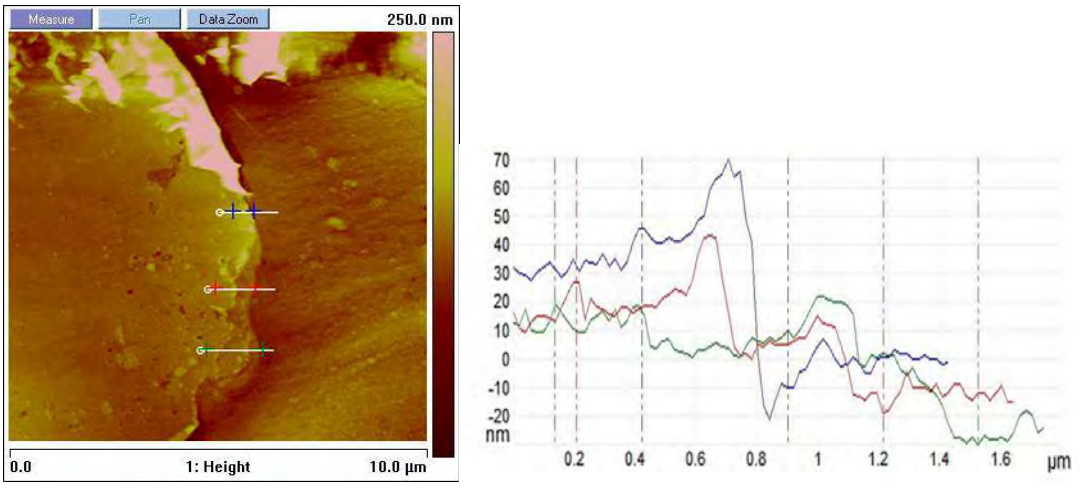

Figure 6.14:AFM topography scan of the step edge created in epoxy by an aluminium step on glass (left) and corresponding cross sections measured as 55.56 nm, 45.62 nm and 49.22 nm (right). Note differences in textures from glass and aluminium in topography scan

This suggests that a reaction does occur between the calcium and epoxy; given the reactive nature of the metal and varied composition of the adhesive, this seemed to be a reasonable assumption.

Further analysis of the epoxy found that after one month of exposure to ambient conditions, the epoxy was very stable showing development of texture, however after just one week exposed to the calcium, additional texture was detected (Figure 6.15).

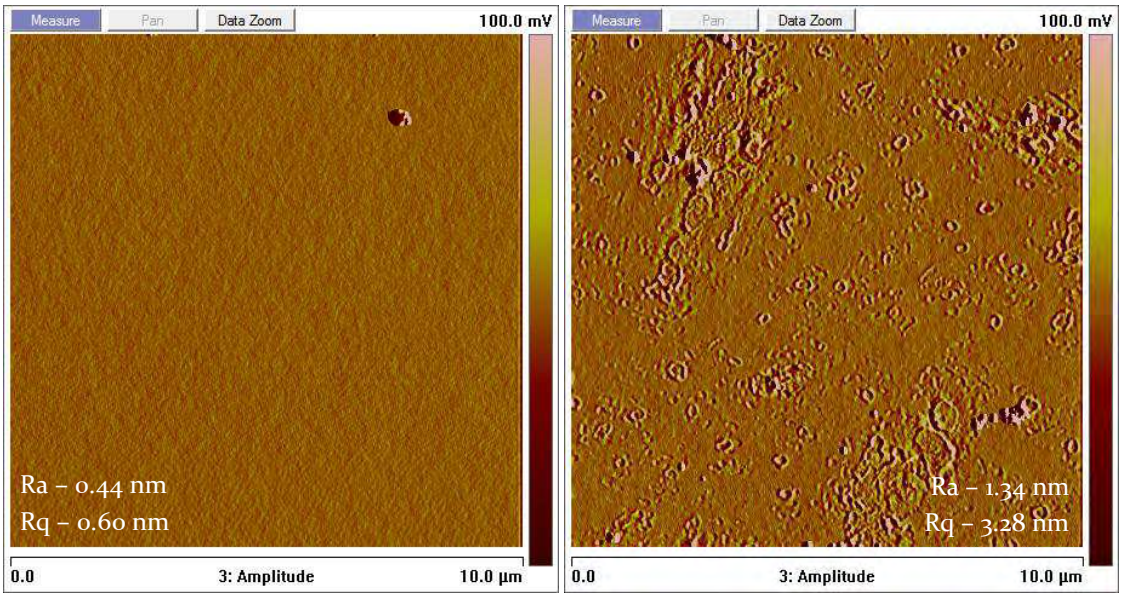

Figure 6.15: AFM amplitude images of the original epoxy resin exposed to ambient conditions for one month (left), and after 1 week of exposure to calcium metal (right), roughness values quantify increase in topography

A new epoxy was sourced, comparable to those commonly used in OLED devices and tests were repeated. Results showed that a roughening of the new epoxy, whilst still present, was much less significant, particularly over the relatively short time frame of the calcium test (Figure 6.16).

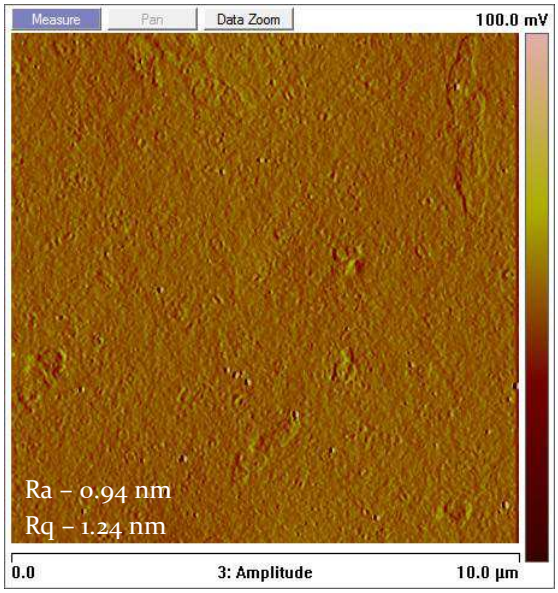

Figure 6.16: AFM amplitude image of the new epoxy resin exposed to calcium metal for one month, only small changes in roughness were detected

Exposure tests were extended to consider the effects of calcium on the polymer, PEN is known for its chemical resistance and was indeed found to be quite robust exhibiting no significant changes following extended exposure to calcium metal (Figure 6.17).

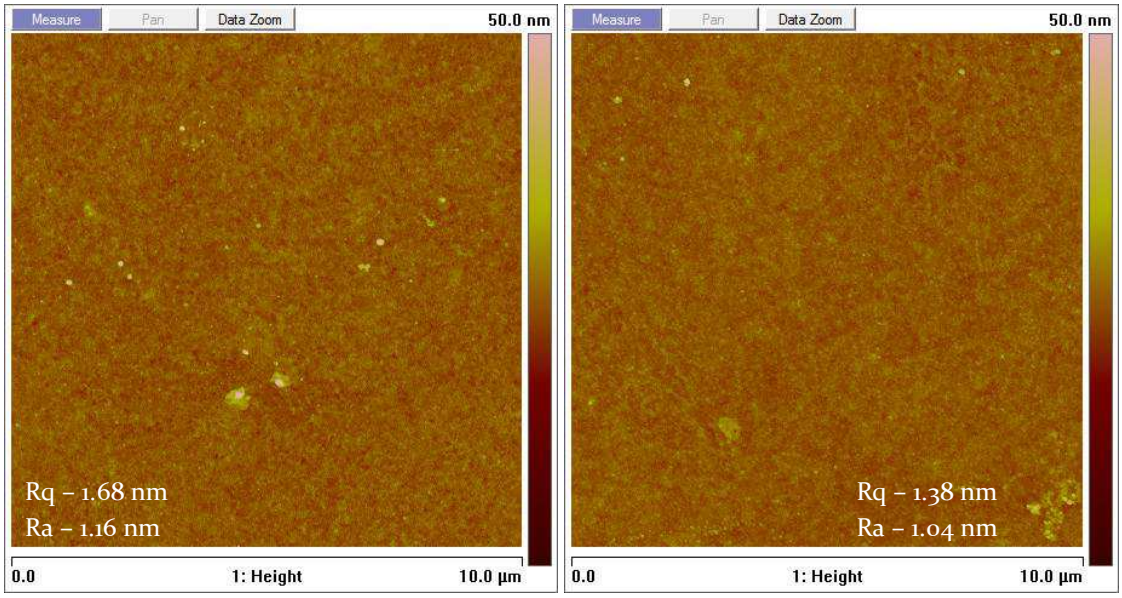

Figure 6.17: AFM surface topography images for displays grade PEN after calcium coating and rapid removal (left), compared to the same sample after exposure for 4 weeks (right), comparable roughness values confirm no significant changes occurred

6.4.5.2 Epoxy Reactivity Development

Despite the slight changes in topography observed with the new epoxy, no detrimental effects to the calcium test have been recorded, any roughening of the epoxy can be considered to have negligible effects within the timescale of the test.

As a result of this work, the epoxy resin used for the calcium test was permanently replaced. Furthermore, the long term plans of a consortium of companies developing the calcium test have considered these findings and as a result, future developments of the calcium test will feature a void area around the calcium containing a desiccant, to ensure there are no chances for future contact reactivity issues.

Detailed information on the chemical composition of the epoxy resins was sought in an attempt to look at the differences between the two epoxies at a chemical level and determine the cause of the roughening effect, however all requests for information from manufacturers were returned with outright refusals. Although application of analysis methods such as secondary ion mass

spectrometry were considered, it was decided that as this effect had been recorded and its impact on the test results considered as negligible, sufficient information had been gathered from this line of research within the scope of this thesis.

6.5 Defect analysis

At this point the calcium test had been refined and tested to a level at which it could be considered to be a robust, stable technique for pinpointing defects to allow subsequent AFM analysis. Firstly, the internal areas of the pinholes are measured though the glass of the test cell using white light interferometry to accurately measure the level of degradation (Figure 6.18).

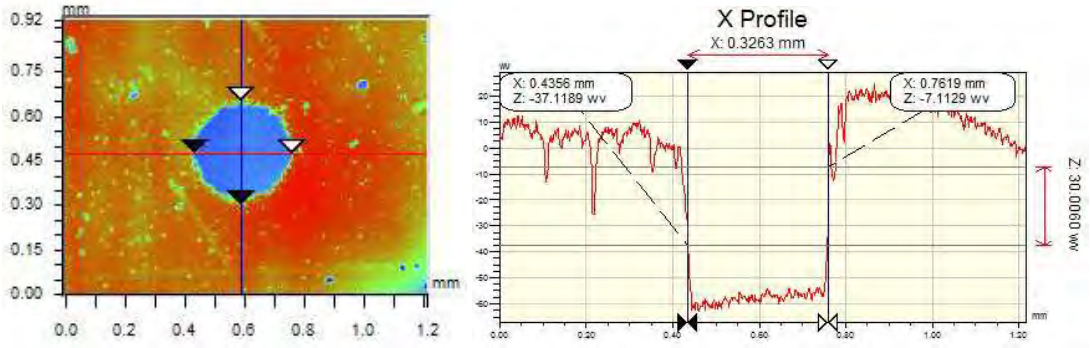

Figure 6.18: White light interferometry intensity image of a pinhole (left) and an X Profile of this feature, measured at 326.3 µm (right)

This information allows comparisons to be made between the levels of permeation resulting from individual defects, rather than using approximate measurements from optical microscopy or a total measurement for the bulk sample. Following this, the calcium pinholes are then labelled and the film is delaminated; upon separation of the polymer and glass, any remaining calcium rapidly reacts with the water in which the cell is submerged, however pinhole locations can still be identified by the previously placed ink markers. These locations are then scanned using AFM in a systematic pattern to reduce the magnitude of discrepancies in the stage movement (Figure 6.19)

and the resulting information obtained on features can be catalogued and correlated, this is discussed further in Chapter 7.

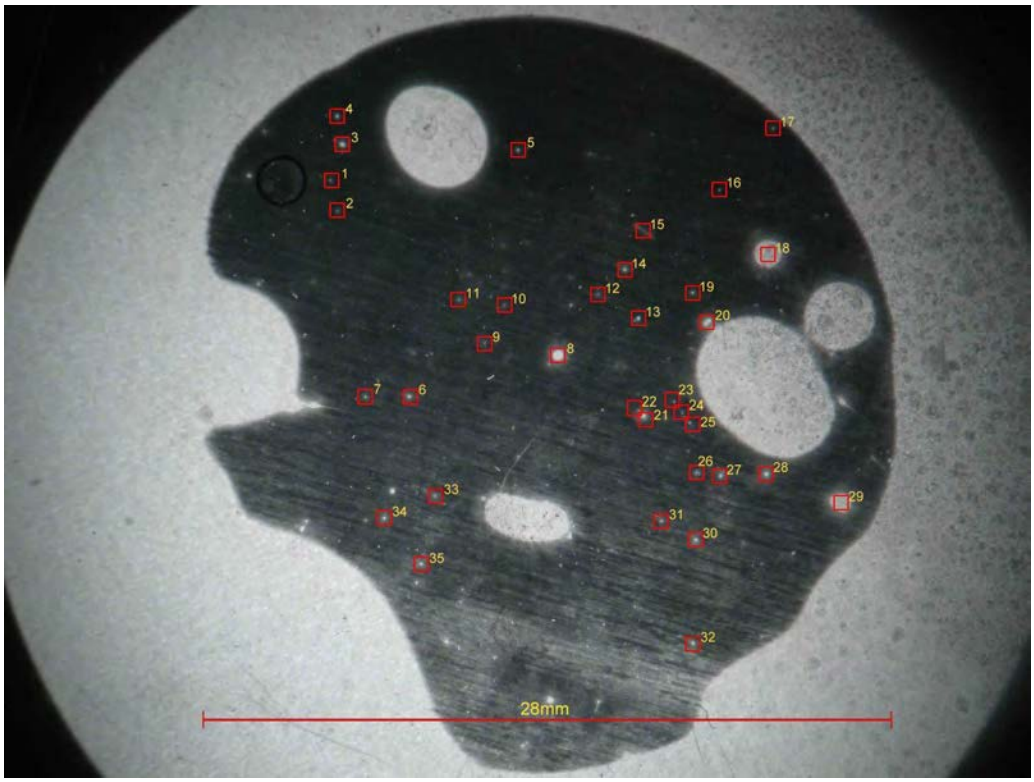

Figure 6.19: Typical calcium test AFM scanning sequence

6.5.1 Discovery of Particulates Held in Epoxy

It was speculated that if barrier disruptions could be located using this labelling technique on the polymer film, it could also be applied to the internal side of the covering epoxy. If the breaks had been caused by extrinsic contaminants it may be possible that they remained adhered in the epoxy resin during delamination. The labelling technique was applied to the glass and these areas were analysed with both AFM and SEM, doing so revealed features which did not appear to be part of the original film (Figure 6.20).

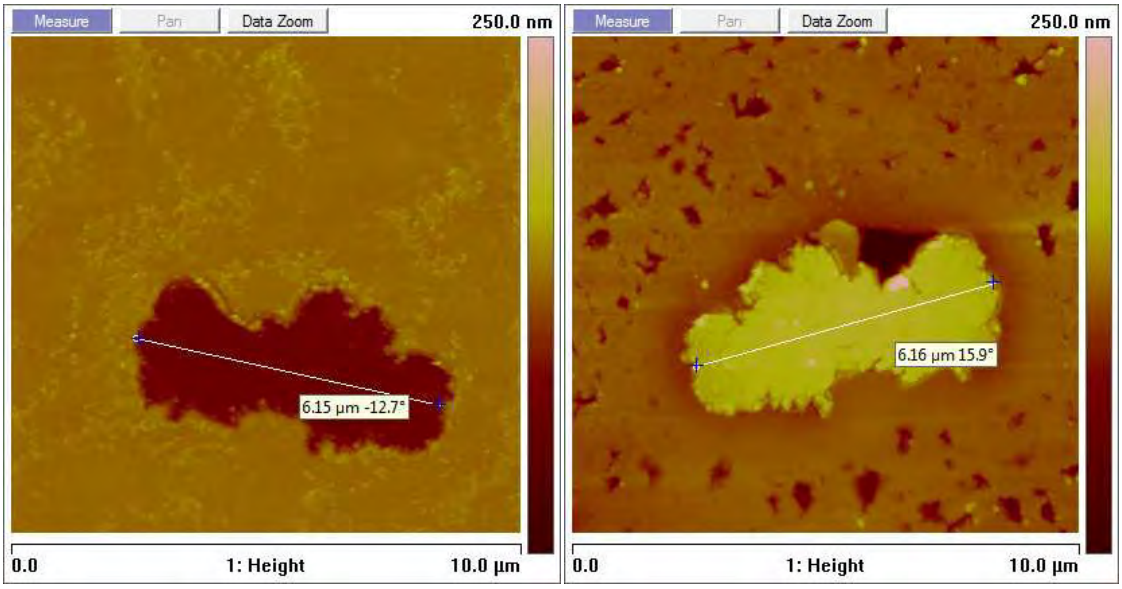

Figure 6.20; Example AFM topography image of a barrier hole (left) with the responsible contaminant captured in the opposing epoxy layer (right)

The depth of the hole in the barrier surface is on the order of the barrier thickness, SEM-EDX analyses also confirm a lack of aluminium in this region. Analysing the contaminant, it was found that by increasing the accelerating voltage of the EDX beam, aluminium could be detected on the underside of the particulate embedded in the epoxy; as this would have been the exposed side when on the film surface, the presence of aluminium suggests that it was situated on the polymer before aluminium deposition and is discussed in more in Section 6.5.2.5. A detailed study to examine the composition of these defects was undertaken and is explained in the following section.

6.5.2 Scanning Electron Microscopy Analysis

Whilst the size and shape of defects can be easily determined using the AFM, SEM analysis compliments this by providing elemental compositional data, which can help determine their source. Multiple defect sites inspected located using the calcium test were analysed using SEM and the defect locations on both the film and epoxy were analysed. The same locations were then examined using the AFM to allow quantative measurements to be taken. The following examples

are a sample of typical flaws, particularly large defects were selected for SEM analysis for the ease of defect relocation when moving between analysis instrumentation.

6.5.2.1 Elemental Mapping of 'Defect 1'

This contaminant measured 36.8 µm across its maximum chord length (Yellow line in Figure 6.21 – top left) and was responsible for a 582 µm pinhole. The appearance is typical of a flake of skin, the twisted fibrous structure is characteristic of epidermal tissue (Marsh, 2011), the elemental map of the same area shows that the defect contains a large amount of carbon, supporting the theory of its organic source. A clear imprint is shown which the contaminant left in the epoxy, it is quite surprising that such a large contaminant remained anchored to the polymer during delamination and suggests strong interactions between the contaminant and film surface (Figure 6.21).

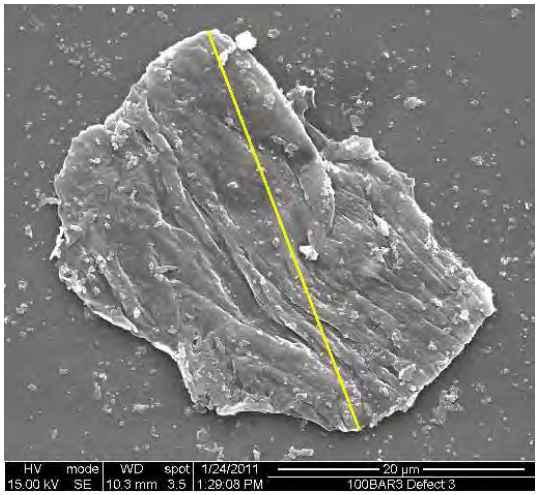

SE image of 'Defect 1' on film surface

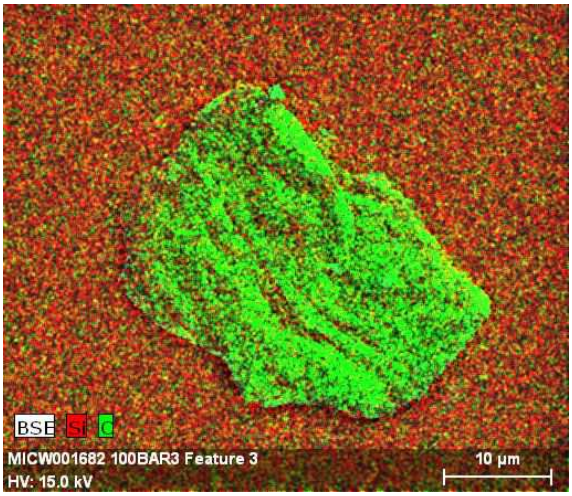

Elemental map of 'Defect 1' on film surface

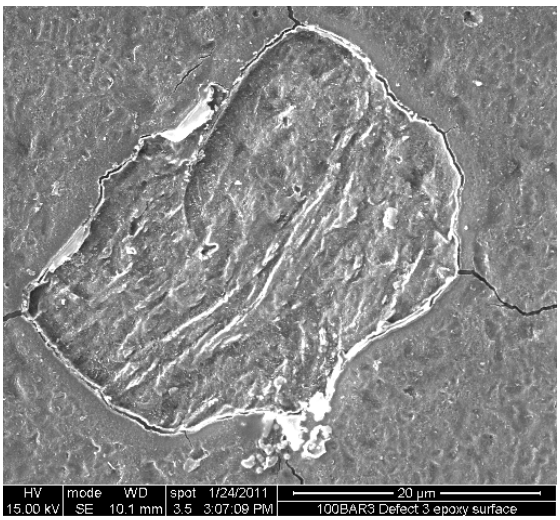

SE image of 'Defect 1' location in epoxy

Figure 6.21: Scanning electron microscopy images of 'Defect 1'

Further elemental analysis of the contaminant confirms the presence of both aluminium and silica, which can be attributed to the barrier and planariser, respectively. The other constituents include oxygen and carbon, the lack of other inorganic elements support the theory that this contaminant is epidermal tissue (Figure 6.22).

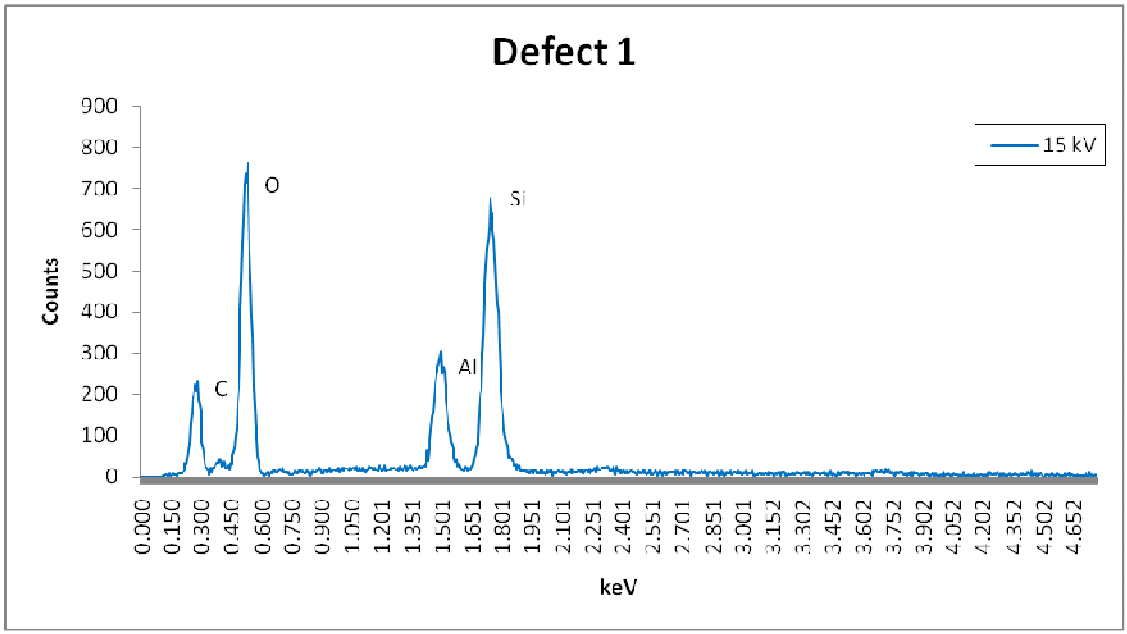

Figure 6.22: Elemental analysis data for Figure 6.21 (top left)

6.5.2.2 Elemental Mapping of 'Defect 2'

This contaminant measured 16.4 µm across its maximum chord length (Yellow line in Figure 6.23 – bottom left) and was responsible for a 241 µm pinhole. It was removed with the epoxy during delamination leaving a hole in the barrier layer, this is confirmed by an elemental analysis of the area which shows a void in the aluminium coating. The appearance of the contaminant is typical of an inorganic building material such as cement or plaster (Marsh, 2011) (Figure 6.23), EDX mapping further supports this association showing a high aluminium and silica content.

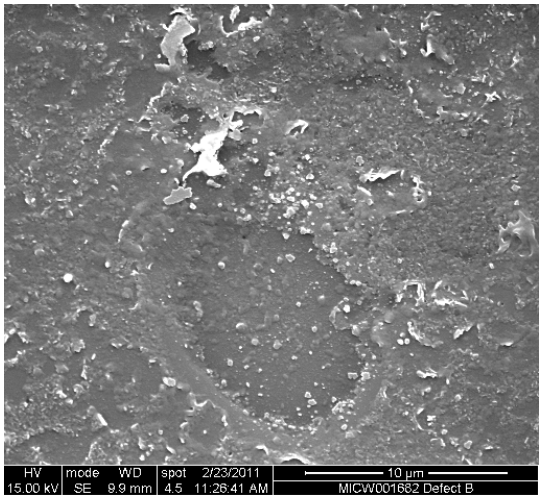

SE image of 'Defect 2' on film surface

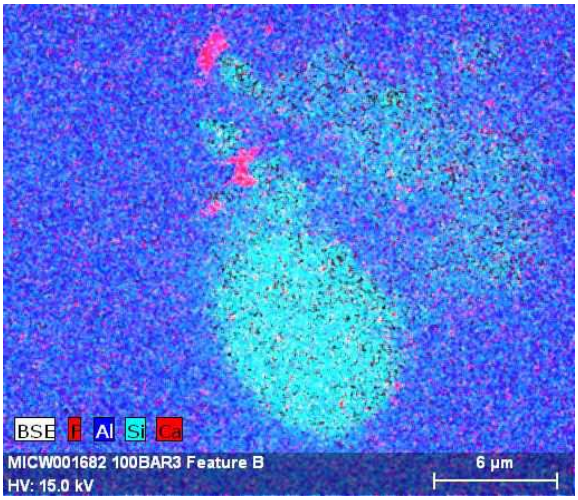

Elemental map of 'Defect 2' on film surface

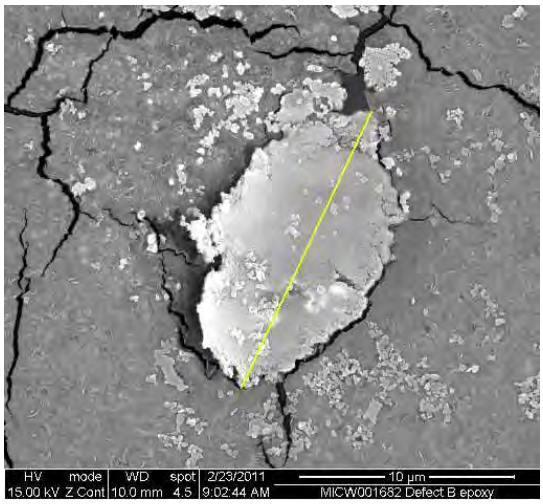

SE image of 'Defect 2' in epoxy

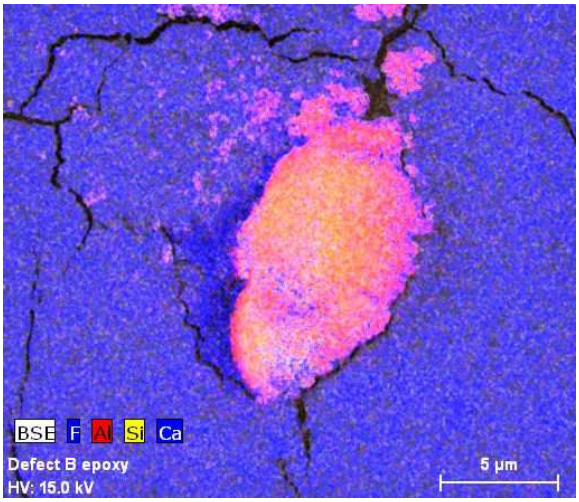

Elemental map of 'Defect 2' in epoxy

Figure 6.23: Scanning electron microscopy images of 'Defect 2'

6.5.2.3 Elemental Mapping of 'Defect 3'

These contaminants measured 15.5 µm and 9.8 µm across their maximum chord lengths (Yellow lines in Figure 6.24 – bottom left) and were responsible for a 236 µm pinhole. Similar to 'Defect 5', both structurally and compositionally, again they are likely to be building materials (Marsh, 2011). The contaminants have created a void in the aluminium layer which is confirmed once again by

elemental mapping. Elemental composition of the contaminant also shows an inorganic mix of silica and aluminium oxides (Figure 6.24).

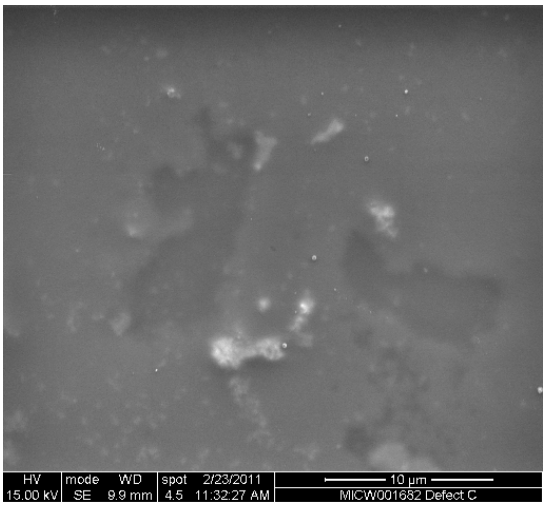

SE image of 'Defect 3' on film surface

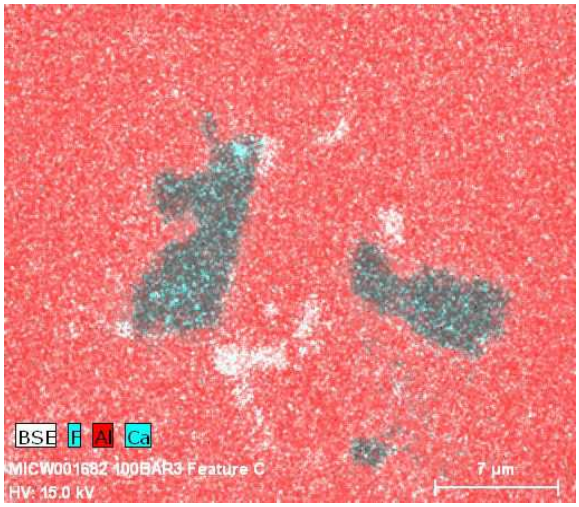

Elemental map of 'Defect 3' on film surface

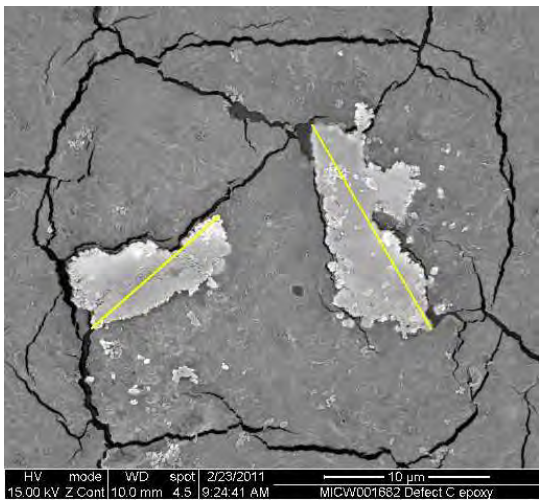

SE image of 'Defect 3' location in epoxy

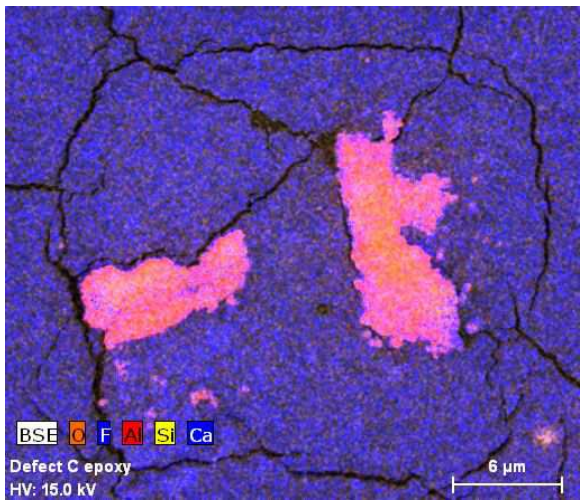

Elemental map of 'Defect 3' location in epoxy

Figure 6.24: Scanning electron microscopy images of 'Defect 3'

6.5.2.4 Elemental Mapping of 'Defect 4'

This contaminant measured 8.7 µm across its maximum chord length (Yellow line in Figure 6.25 – bottom left) and was responsible for a 697 µm pinhole. This is an unusual defect which remained held in the epoxy layer during delamination, however it appears that a remnant piece of calcium

oxide has been held in the defect area; this is confirmed via elemental analysis which also shows a lack of barrier metal in the same location. The physical appearance suggests that this contaminant is an inorganic based material, its composition contains a large amount of aluminium and calcium, confirming its inorganic nature (Figure 6.25).

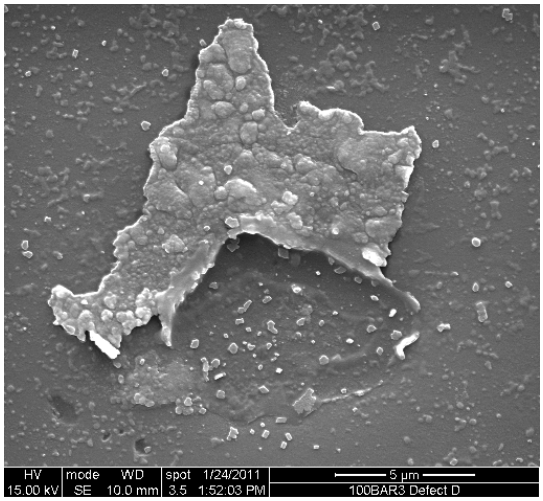

SE image of 'Defect 4' on film surface

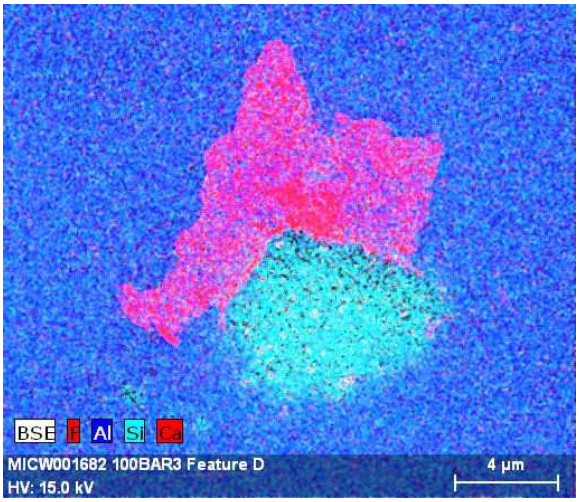

Elemental map of 'Defect 4' on film surface

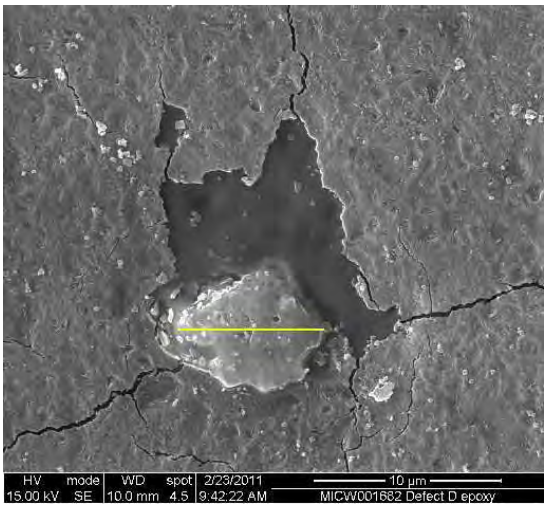

SE image of 'Defect 4' location in epoxy

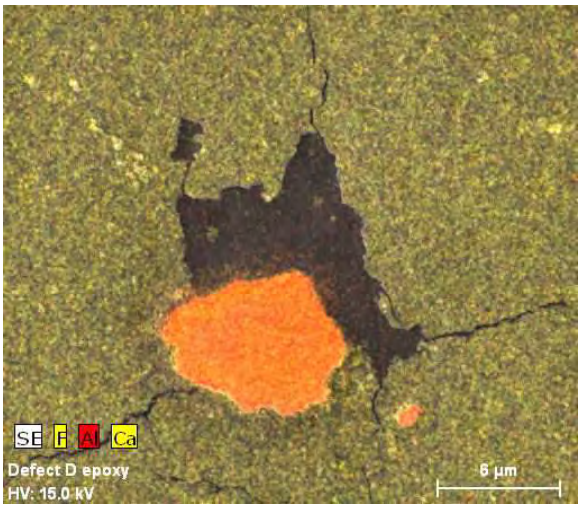

Elemental map of 'Defect 4' location in epoxy

Figure 6.25: Scanning electron microscopy images of 'Defect 4'

6.5.2.5 Elemental Mapping of 'Defect 5'

This contaminant measured 26.6 µm across its maximum chord length (Yellow line in Figure 6.26 – bottom left) and was responsible for a 376 µm pinhole. It was removed with the epoxy during delamination leaving a hole in the barrier layer. Elemental mapping shows this region is devoid of aluminium, with the presence of silicon in this area attributed to the underlying planariser visible though the hole. Both the physical and chemical structure of Defect 19 are similar to Defect 3; it is likely that this is also epidermal tissue (Marsh, 2011) (Figure 6.26).

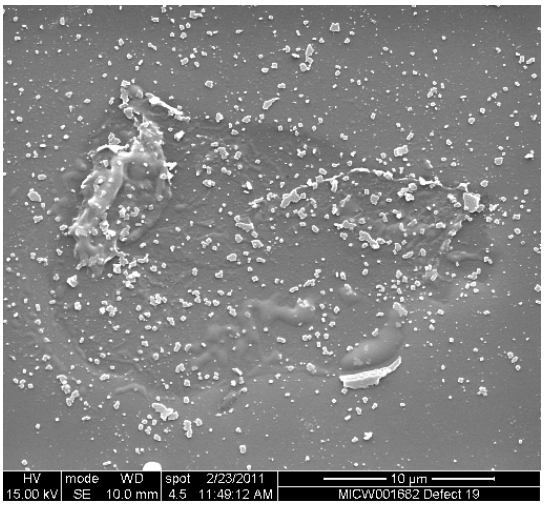

SE image of 'Defect 5' on film surface

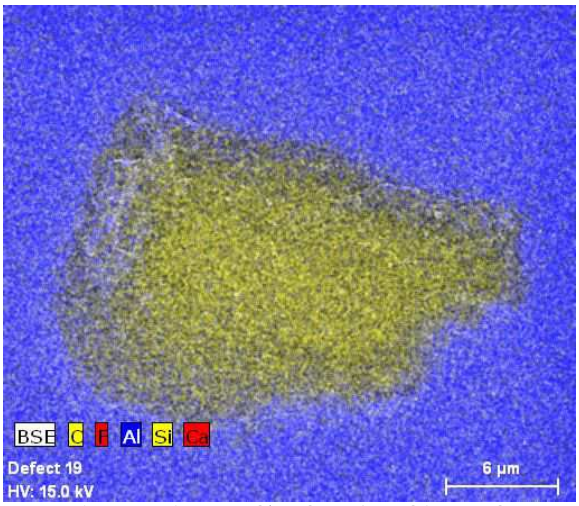

Elemental map of 'Defect 5' on film surface

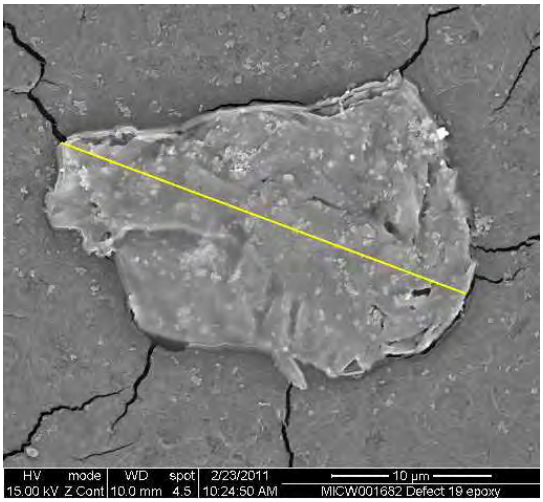

SE image of 'Defect 5' location in epoxy

Figure 6.26: Scanning electron microscopy images of 'Defect 5'

Extended EDX analysis of the defect demonstrates the presence of the contaminant on the film surface before barrier coating (Figure 6.27). When a low EDX accelerating voltage is applied (5 kV) large amounts of carbon with traces of oxygen and nitrogen are observed; the presence of gold can be attributed to the thin coating deposited for SEM imaging of polymers. Increasing the accelerating voltage (15 kV) allows the EDX to probe deeper into the sample, whereupon the presence of aluminium increases greatly, suggesting that the beam is interacting with an aluminium layer on the underside of the contaminant. This would have been the upper surface before delamination. A rise in the calcium peak also lends evidence that data from the underside of the defect is now obtained, performing EDX on any other area of the epoxy does not reveal aluminium.

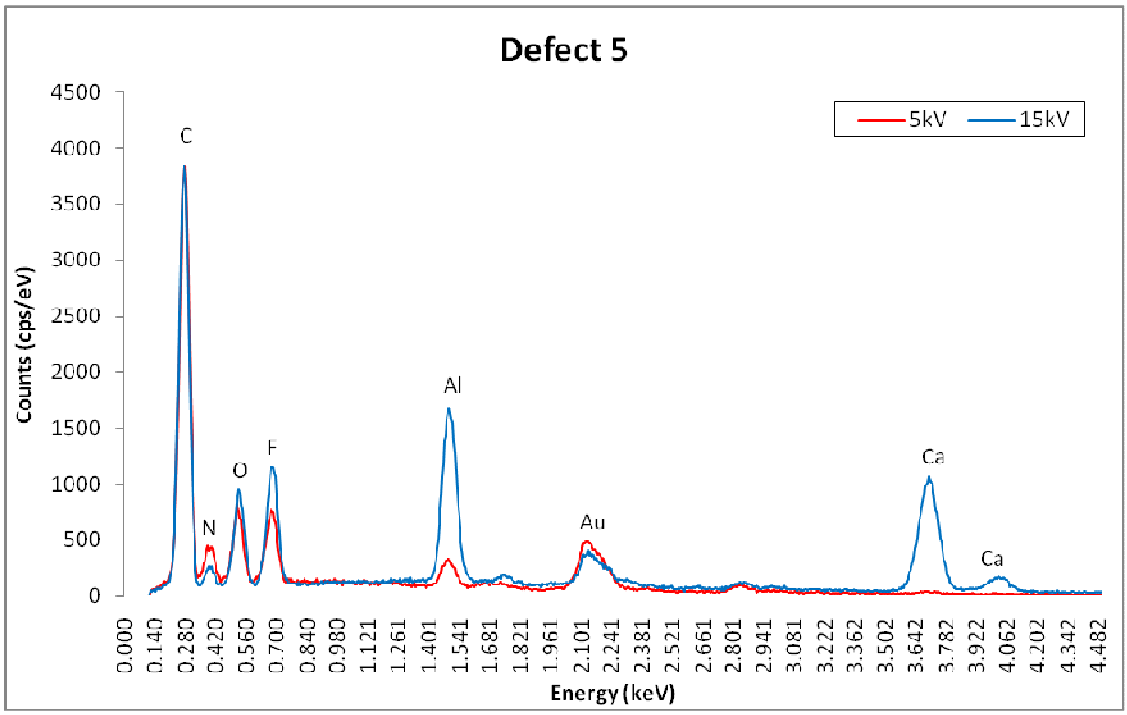

Figure 6.27: Elemental analysis data for Figure 6.26 - bottom

6.5.2.6 Elemental Mapping of 'Defect 6'

This contaminant measured 28.2 µm across its maximum chord length (Yellow line in Figure 6.28 – bottom) and was responsible for a 333 µm pinhole. This was a large defect which remained in the epoxy throughout delamination, evidenced by the apparent gap in the barrier layer. This is further supported by elemental mapping; showing a region devoid of aluminium with the underlying silicon-containing planariser apparent. This appearance is typical of an inorganic contaminant, the shape of which can be associated with building materials such as plaster (Marsh, 2011) (Figure 6.28).

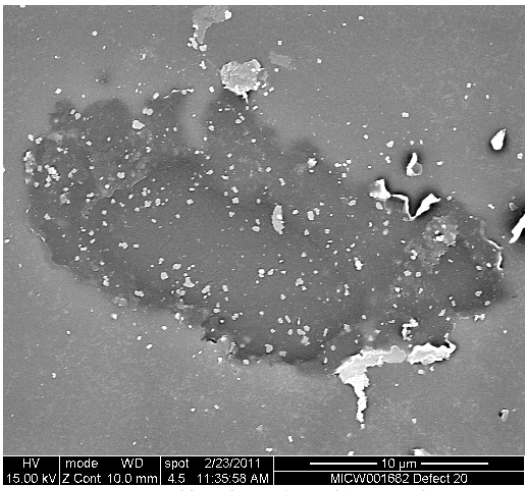

SE image of 'Defect 6' on film surface

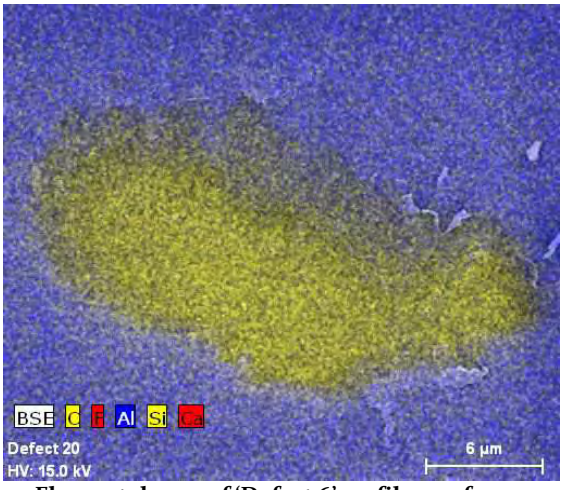

Elemental map of 'Defect 6' on film surface

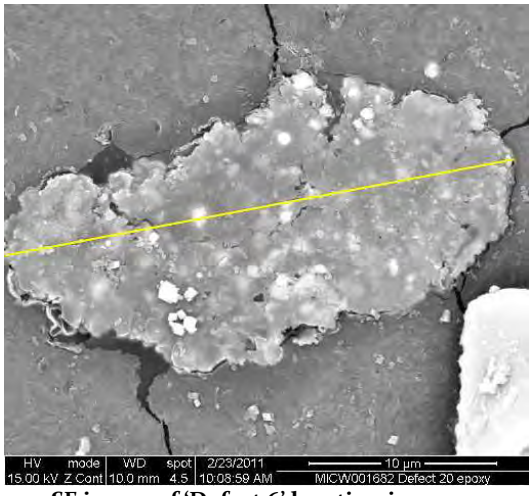

SE image of 'Defect 6' location in epoxy

Figure 6.28: Scanning electron microscopy images of 'Defect 6'

6.5.2.7 Elemental Mapping of 'Defect 7'

This unusually shaped contaminant measured 24.5 µm across its maximum chord length (Yellow line in Figure 6.29 - bottom) and was responsible for a 301 µm pinhole. This is another defect which remained held in the epoxy layer throughout delamination, creating an apparent void visible in the barrier layer and further evidenced by the elemental map, showing a lack of aluminium in this area but with the silica containing planariser detected through the void (Figure 6.29).

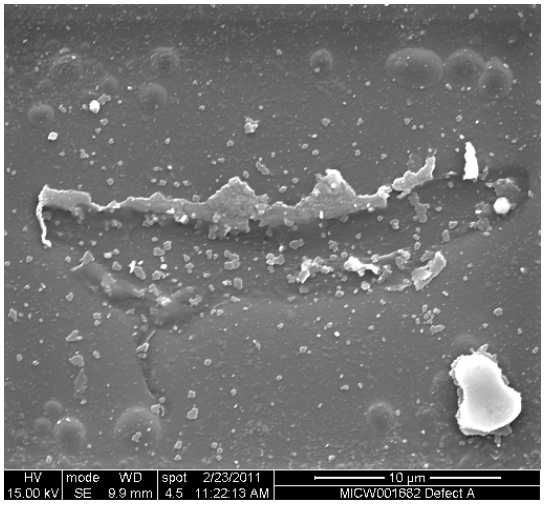

SE image of 'defect 7' on film surface

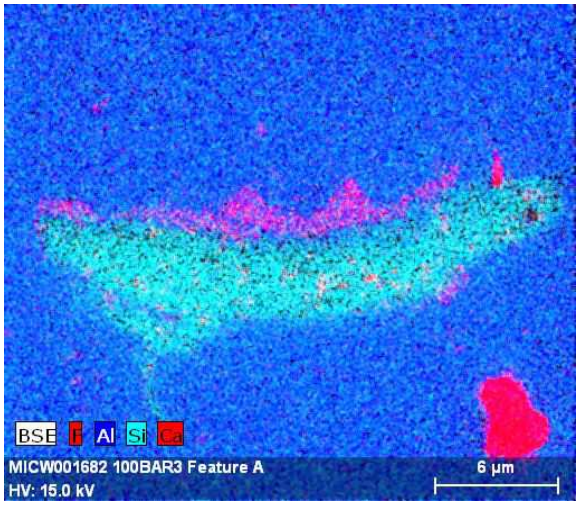

Elemental map of 'defect 7' on film surface

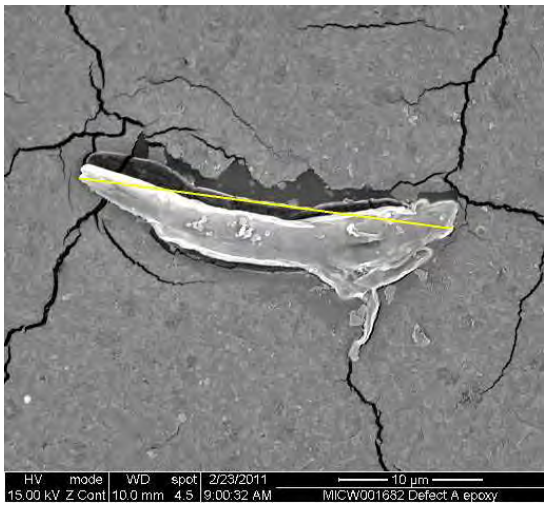

SE image of 'Defect 7' location in epoxy

Figure 6.29: Scanning electron microscopy images of 'Defect A'

EDX analysis of the defect is less revealing compared to elemental analysis of other contaminants (Figure 6.30). The shape is indicative of a small section of planariser, the likes of which can be generated during film slitting, however the lack of silica discounts this. It is possible that the contaminant is an aluminium alloy originating from the barrier coating process. Using a low accelerating voltage of 5kV, a strong aluminium peak is detected, the lack of calcium detection demonstrates that the data does not result from an aluminium coating on the underside of the particulate, evidenced when a higher accelerating voltage of 15kV is applied, increasing the aluminium peak size and introducing a calcium peak. EDX analysis of the epoxy demonstrates that the adhesive does not contain traces of the aluminium metal. It is worth noting that there is a very small palladium peak, however this appears to be present in all scans so is unlikely to be the composition of the defect.

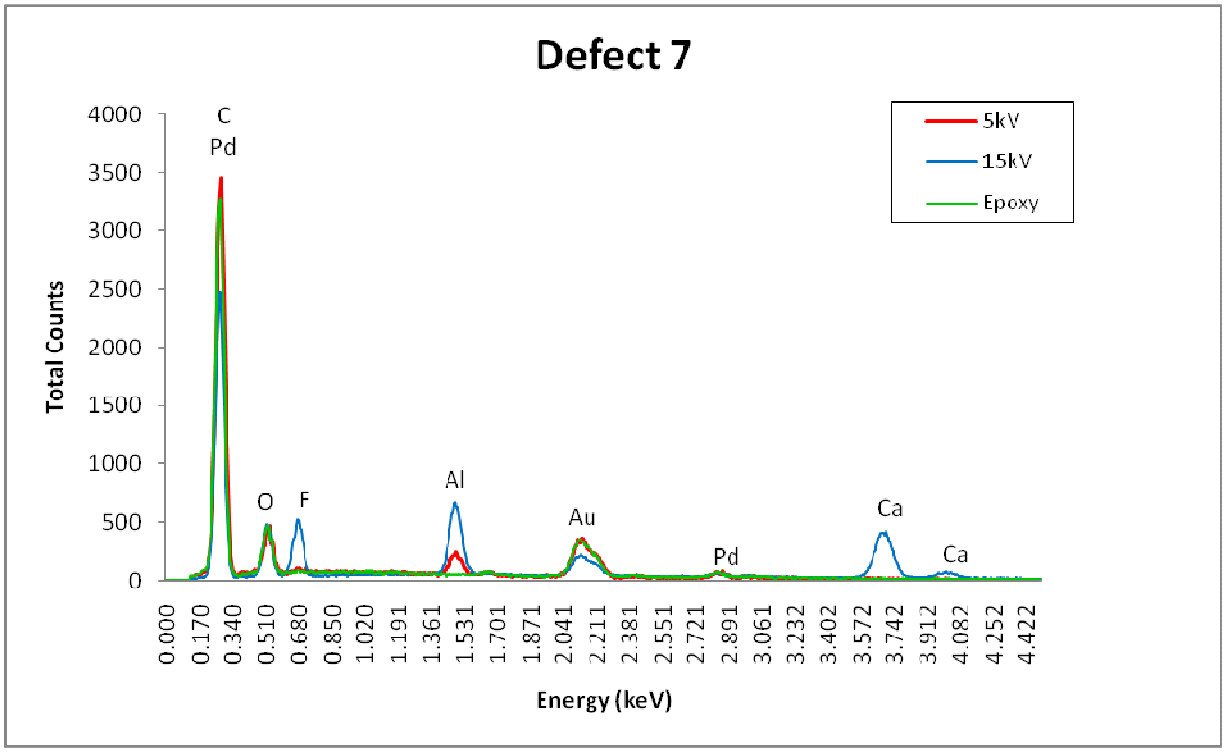

Figure 6.30: Elemental analysis data for Figure 6.29 (top right)

6.5.3 SEM Summary

Evidence thus far suggests that the majority of barrier flaws are the result of extrinsic contaminants, the majority of which appear to be comprised of typical airborne dust which most likely settles on the film surface before the barrier coating process. This raises questions regarding film hygiene during coating as all of these films are produced, handled and coated in clean room environments.

It was suggested that some of the debris may be present in the epoxy before the test starts, however the epoxy is both dried and filtered before use to assure its purity, furthermore the EDX data which demonstrates that the aluminium barrier was deposited over the defect would mean they had to be present on the film surface before the barrier layer was deposited.

It is worth noting that despite previous work suggesting a linear relationship between contaminant size and permeation (Lim, 2001a; Lim, 2001), the defects found in Section 6.4.2 do not exhibit this same correlation. For instance, 'Defect B' is 16.4 μm and is responsible for a pinhole of 241 μm, in contrast to 'Defect 7' measuring 8.7 μm yet responsible for a 697 μm pinhole. It is likely that the differences between the defect shape is a factor in these differences and not simply the size, if this is the case then this raises the question of what are the fundamental factors which determine how significant a barrier break will be.

6.6 Conclusions

Drawing together the findings presented within this chapter there are a number of conclusions which can be made.

Detection of features responsible for barrier flaws requires high power magnification beyond the diffraction limit of techniques based on visible light. SEM is unsatisfactory because it is not good with polymers and cannot provide absolute measurements of features. WLI is limited with its resolving power.

Using the calcium test combined with AFM is the solution because the severity of each defect is visualised, and the shape and size of the flaw is measured. The calcium test mirrors degradation in OLED cells very well. Pinhole locations can now be highlighted and subsequently analysed using the AFM. Pinholes are indeed the largest contributor to the diffusion of water through a number of ingress points in the barrier layer.

The main conclusion is that pinholes result from large surface disruptions in the barrier film surface, the adhesion sites of previously airborne extrinsic particles such as dust. The presence of these raises questions about their source and the hygiene of the cleanrooms used in production. SEM EDX analysis strongly supports this conclusion. This could then be tested with known defects in standard films to confirm the key parameters which cause contaminants to disrupt a barrier layer, as described in Chapter 7.

7 Film Defects Analysis

7.1 Introduction

As discussed in Chapter 3, there is an assumption in the literature that barrier imperfections are caused by dust with only one paper offering a more detailed theory, stating a linear relationship exists between contaminant size and barrier permeation (Lim, 2001a; Lim, 2001b). The analysis in Chapter 6 however, proposed that there is no such correlation. In this chapter, the calcium test detection method was applied with AFM to allow a large number of defects to be catalogued from a range of samples in an attempt to determine the fundamental factors which caused the most significant barrier breaks. Model surfaces were also examined to determine whether the barrier breaks were the result of extrinsic flaws or whether intrinsic flaws were important, as claimed by some.

7.2 Barrier Film Defects

Throughout Chapter 6, the dominance of pinholes has been discussed along with preliminary SEM data in an attempt to determine the origins of these flaws. It seemed likely that those present resulted from extrinsic debris which had settled on the film before barrier coating; hence it was felt that quantification of their dimensions and contribution to permeation should be examined to determine any correlation. It has been demonstrated by one group that a linear relationship exists between contaminant size and permeation using a model system (Figure 7.1) whereby larger particles allow greater diffusion (Lim, 2001a; Lim, 2001b).

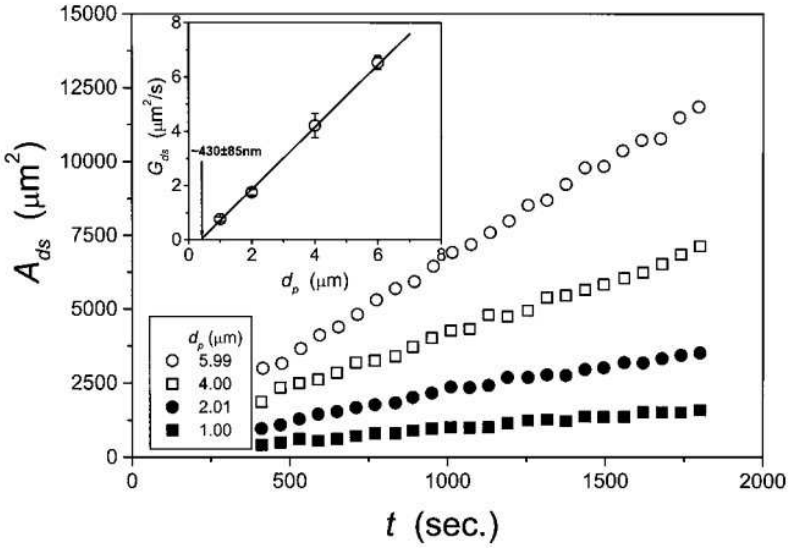

Figure 7.1: Graph showing the linear growth of pinhole growth (A_{ds}) with different particle sizes, inset shows the linear relationship between growth rate (G_{ds}) and particle diameter (d_p) (Lim, 2001a; Lim, 2001b)

It was stated that a critical point exists, whereby when the diameter of a particle is equal or less than double the barrier layer thickness, no pinhole can be formed, although the reasons for this were not explored in any depth in the publication.

7.2.1 Barrier Model

A model exists within Dupont Teijin Films for predicting the permeation of water through a barrier over a given time and how long it would take to reach steady state. It works on a number of assumptions, defined as;

- There are no interactions between water vapour and the barrier layer
- There are no reactions between the water vapour and polymer
- The concentration of the water vapour is low enough that the diffusion coefficient can be considered constant throughout the film
- The barrier layer is completely impermeable to the water vapour

- Diffusion occurs through defects greater than 10 nm in diameter in the barrier layer
- Diffusion is unhindered through the diffusion path, in that there is no resistance of the defects in the barrier layer to the water vapour. However this is only the case in the amorphous phase. The crystalline polymer is considered completely impermeable to water vapour.

As a result of the first and second assumptions Fick's second law is can be applied. In the model, the defect is considered to be a two dimensional circular hole in the surface of an otherwise perfect barrier (Looney, 2010).

7.2.1.1 Fickian Diffusion

Fick's second law (Equation 7.1) describes the concentration of a diffusion species over time, it is therefore appropriate for the modelling of the transient conditions encountered here.

$$\frac{\partial C}{\partial t} = D.\nabla^2.C(x, y, z)$$

Equation 7.1

Where;

C	-	Concentration [ppm] or [g/m^3]
T	-	Time [s]
D	-	Diffusivity [m^2/s]
x, y, z	-	Direction in three dimensions

7.2.1.2 Solution of Fick's Second Law

There is no analytical solution of this equation in more than one dimension so a suitable numerical method has to be applied. A cylindrical coordinate system geometry is used to reduce the computational demand of the solving method, this allows the solution of a two dimensional problem which represents a three dimensional system using an assumption of axial symmetry,

therefore from the origin of the cylinder to the edge, the radial flux is the same through all angles. For the model, Fick's second law is applied using two dimensional cylindrical coordinates (Equation 7.2).

$$\frac{\partial C(r,z)}{\partial t} = \frac{D}{r}\frac{\partial C}{\partial r} + D\frac{\partial}{\partial r}\left(\frac{\partial C}{\partial r}\right) + D\left(\frac{\partial C}{\partial z}\right)$$

Equation 7.2

Where;

R - Position along radius [m]

Z - Position along axis (along film length) [m]

7.2.1.3 Predictions of the Model

A large number of variables can be adjusted for the model, such as defect size, film thickness, ambient temperature and humidity, however it can is now sufficiently sophisticated to allow film crystallinity to be defined and initial water content of the film. Whilst the model compares reasonably well to real world data for larger pinholes, it breaks down for smaller defects (Figure 7.2).

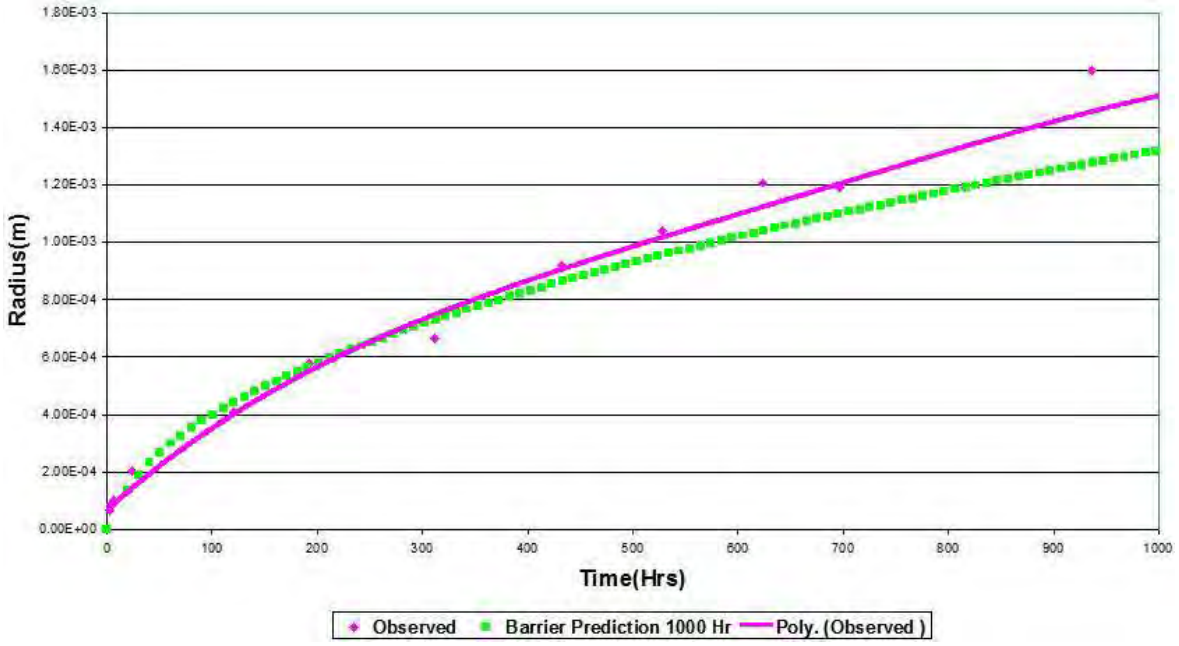

7.2 A: Defect radius = 10 µm

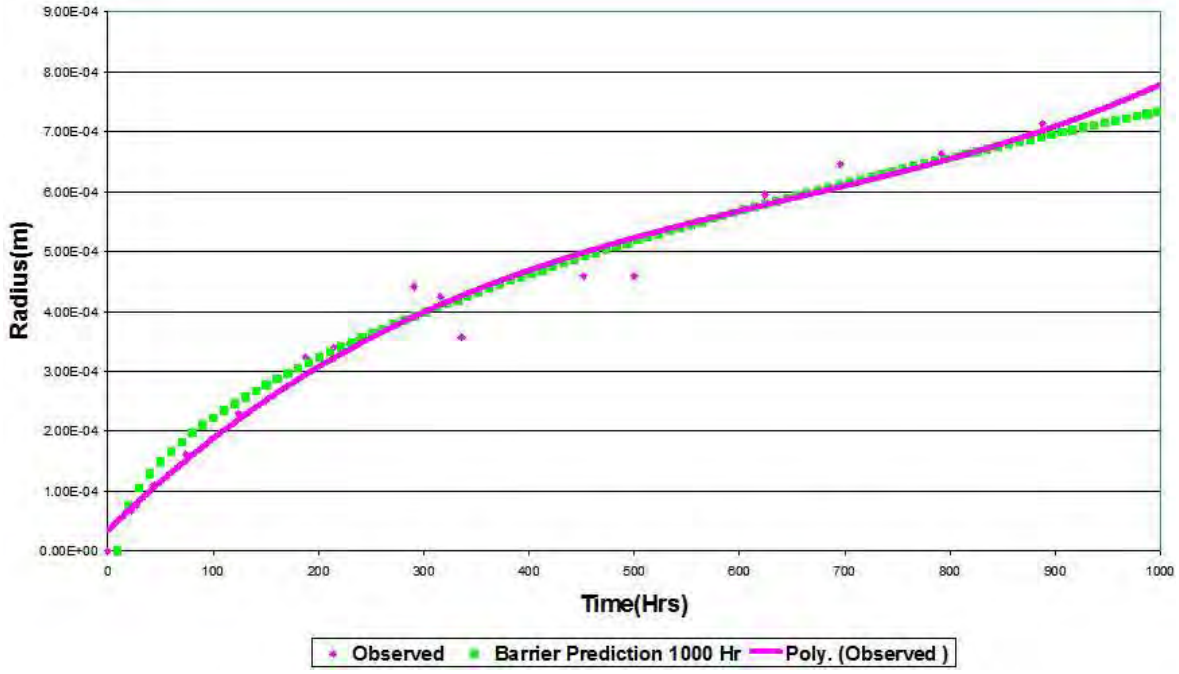

7.2 B: Defect radius = 4 µm

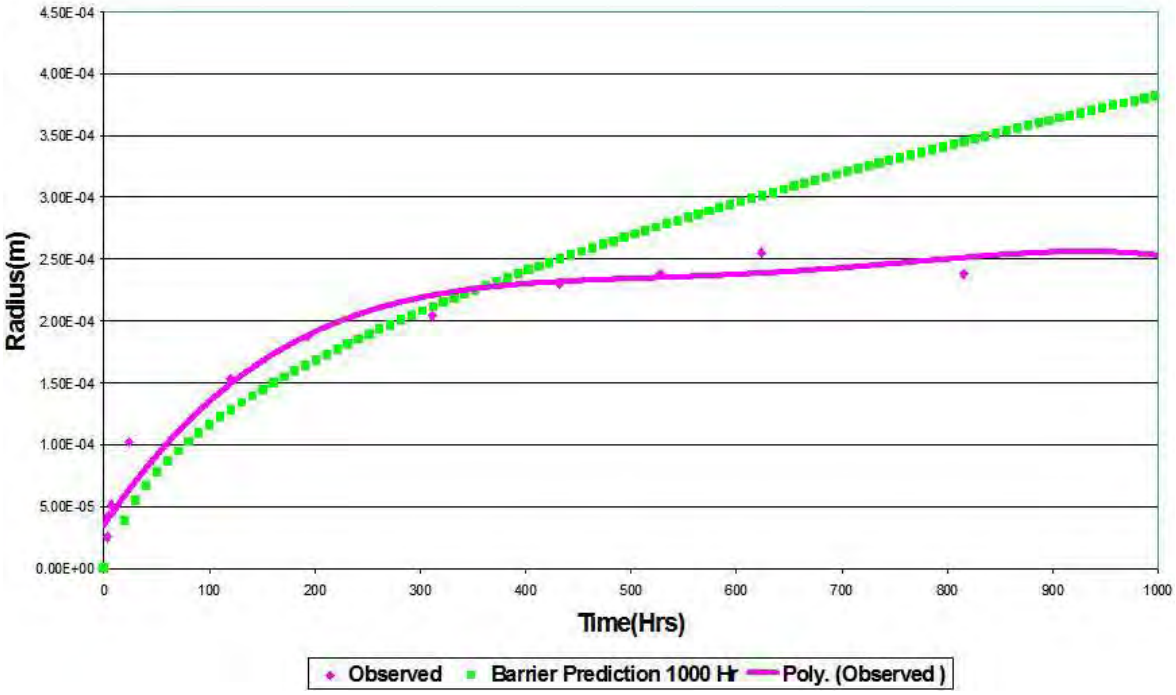

7.2 C: Defect radius = 1.7 µm

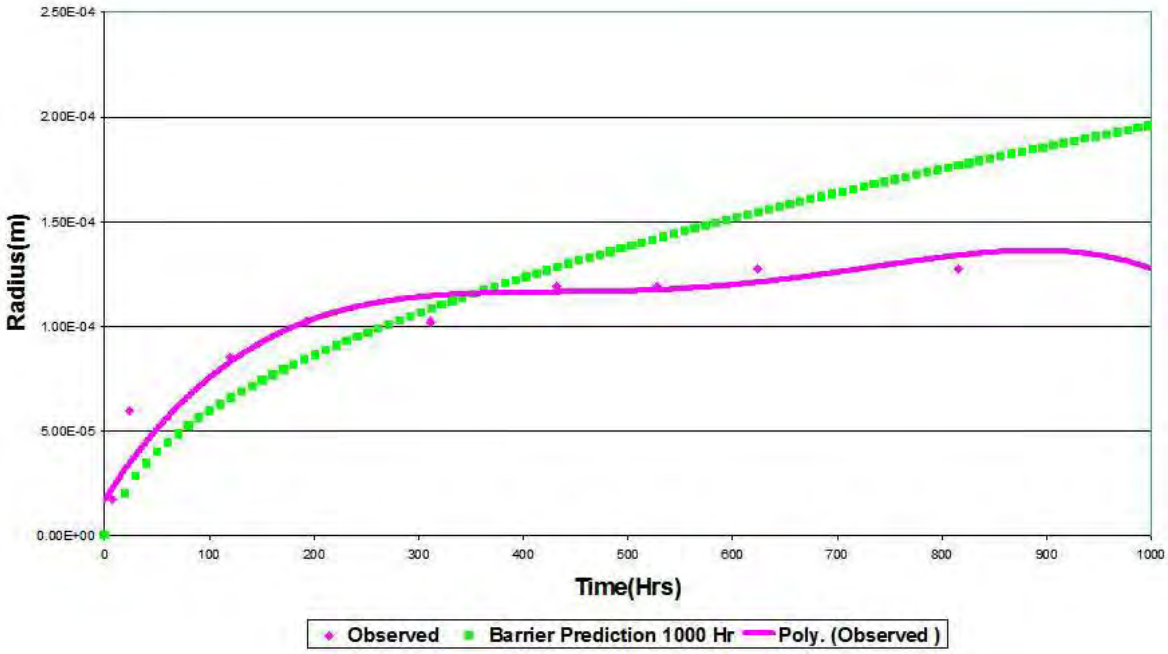

7,2 D: Defect radius = 0.8 µm

Figure 7.2: Four results showing the observed radius in the calcium test (pink) against the exposure time compared to the barrier theory prediction (green)

It is believed that the model fails when applied to smaller defects due to a number of possible reasons, such as the water permeating into the epoxy resin after a given time, or that the model itself could break down given that it is based on real world observations which could introduce experimental errors. It is also possible that the assumptions which allow the model to use Fickian diffusion may cause it to fail for smaller defects; as the diffusion path becomes narrower, the water is more likely to interact with the barrier material more, however this attraction is considered to be non-existent in the model.

It is clear that there are inconsistencies between existing knowledge and actual barrier permeation, despite the large amount of work dedicated to the model it is still insufficient to describe the whole system. This suggests other parameters exist which effect diffusion through thin films which have not yet been defined.

7.2.2 Film Defect Analysis

The desired objective for DTF was to eliminate pinholes, but the prevention of the largest failure sites was the priority. Analysing a calcium test sample by light microscopy illuminated with oblique lighting, it was determined that the largest pinholes were actually comprised of multiple smaller defects rather than single, catastrophic barrier flaws (Figure 7.3).

Figure 7.3: Oblique illumination light microscopy highlighting defect sites, water ingress areas are highlighted as light blue areas whilst calcium test pinholes with diffused calcium oxide areas can be viewed as dark circles within these regions

Whilst the presence of pinholes can be attributed to the existence of surface defects, it transpires that an upper limit exists for the size of any extrinsic debris present; hence there appears to be a finite limit to the size of the resulting defects. It is believed that there are two reasons for this; the first was revealed through discussions with researchers within DTF, specifically that the largest particles are removed during production from both the effects of film winding and from cleaning methods such as the application of air knives and tacky rollers (CAB Consulting, 2003) (Figure 7.4). Secondly, the display grade films are produced in very clean environments, the air filters in these production zones can filter out the majority of large particulates much easier than the smaller ones, resulting in a reduction of the average particle size to which films may be exposed. Any remaining particles below this threshold are sufficiently small enough to remain adhered to the film through

electrostatic and Van der Waals type forces (Hodgeson, 2010). However, results in Chapter 6 raise questions about the hygiene of the clean room environments and whether there is a source of debris introduced at another stage of film production.

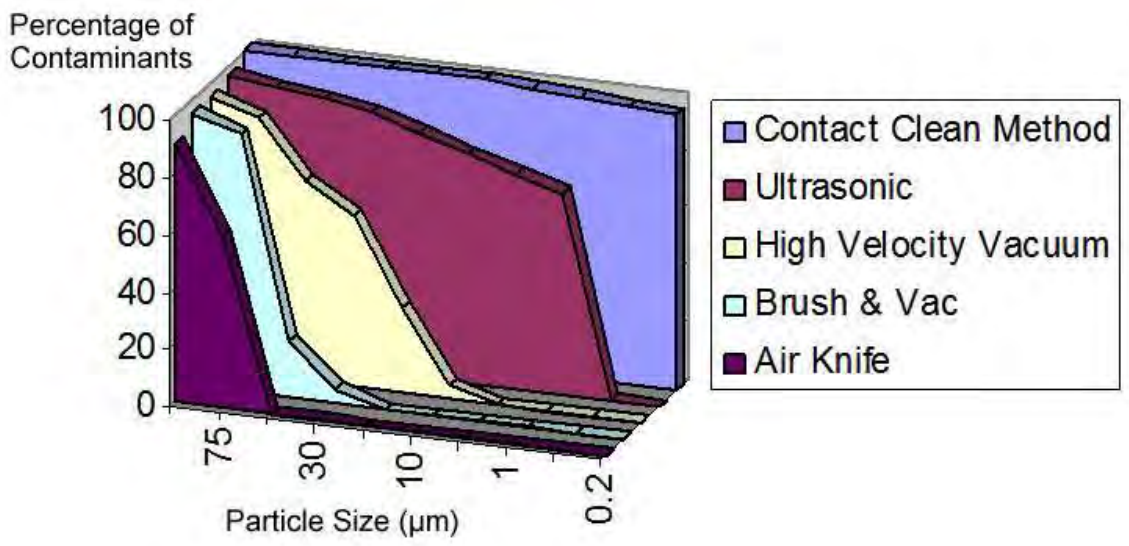

Figure 7.4: Graph to show the cleaning efficiency of multiple techniques on decreasing particle sizes (CAB Consulting, 2003)

This is supported by AFM data of defect sizes, which shows that the majority of defects are centred on a 2 µm diameter distribution (Figure 7.5). The large extrinsic contaminants discovered in Chapter 6

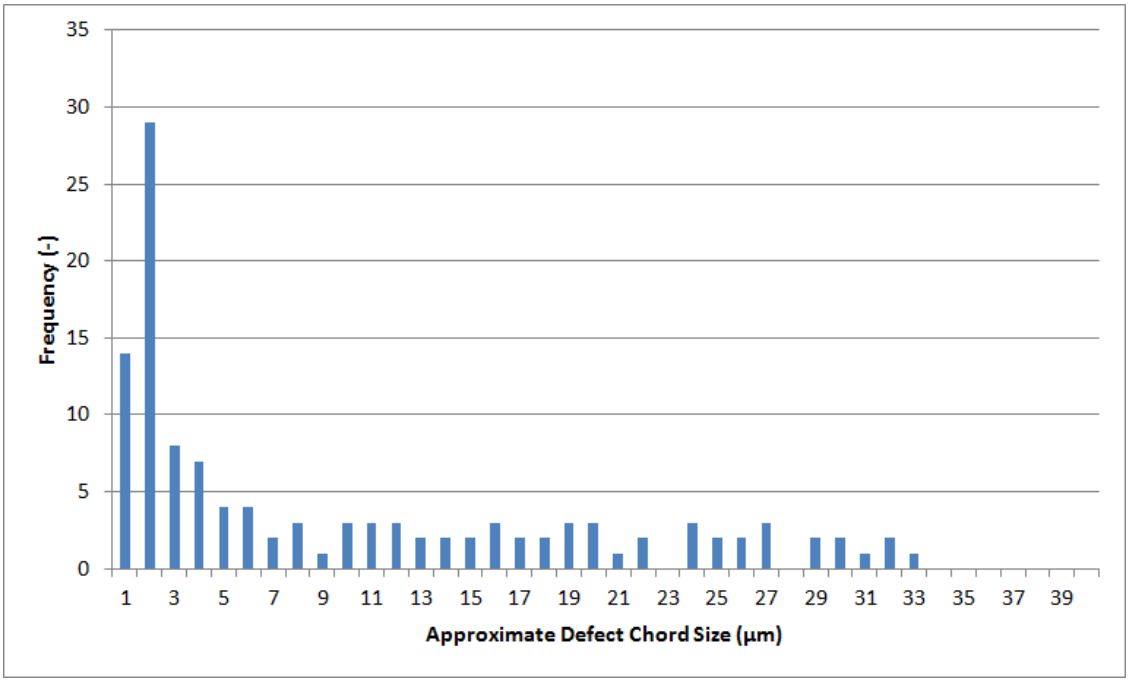

Figure 7.5: Distribution of defect sizes detected by AFM of 121 recorded defect sites

7.3 Defect - Pinhole Permeation Correlation

A wide range of data on defect dimensions against permeation contribution was collected using both AFM and WLI. As discussed in Section 6.1.2, application of the AFM allows much smaller defect sites to be examined than would be possible by SEM. Using the calcium test, locations of many pinholes was determined across a range of polymer samples. Subsequent AFM analysis found the most common were 'pit-like' defects (Figure 7.6), believed to be created when a coated extrinsic particle is removed during calcium test delamination; as demonstrated in Section 6.4.2. Their frequency made them ideal for statistical comparison.

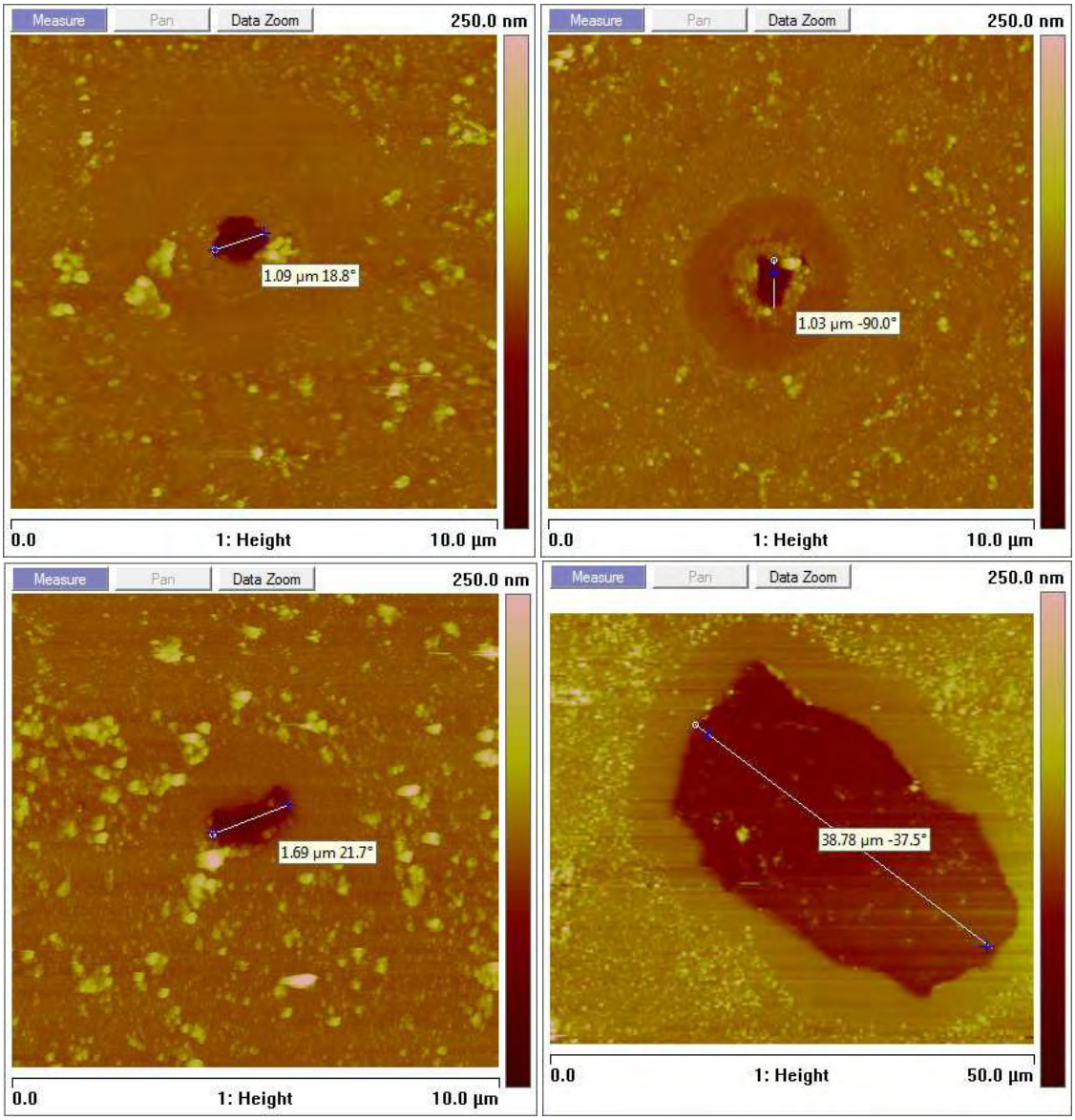

Figure 7.6: Examples of the non-linear relationship of barrier defect to pinhole size, defect dimensions with corresponding pinhole size in square brackets; 1.09 µm [34 µm2] (top left), 1.03 µm [84 µm2] (top right), 1.69 µm [158 µm2] (bottom left) and 38.78 µm [275 µm2] (bottom right)

The largest pinhole sites in calcium tests were expected to be the locations of the largest contaminants, however a linear relationship was not observed (Figure 7.6), similarly sized surface defects were capable of creating a large range of pinholes sizes.

Datasets for each calcium spot were plotted, featuring the defect area as a function of pinhole area (which can be interpreted as permeation) (Figure 7.7), they are plotted independently to remove any ambiguity resulting from fluctuations in sample exposure times. Attempting to fit a linear trend line to these plots allows us to apply a coefficient of determination (R^2) to determine the proportion of variability in each dataset compared to this line (Steel, 1960); the closer the value is to one, the more linear the relationship.

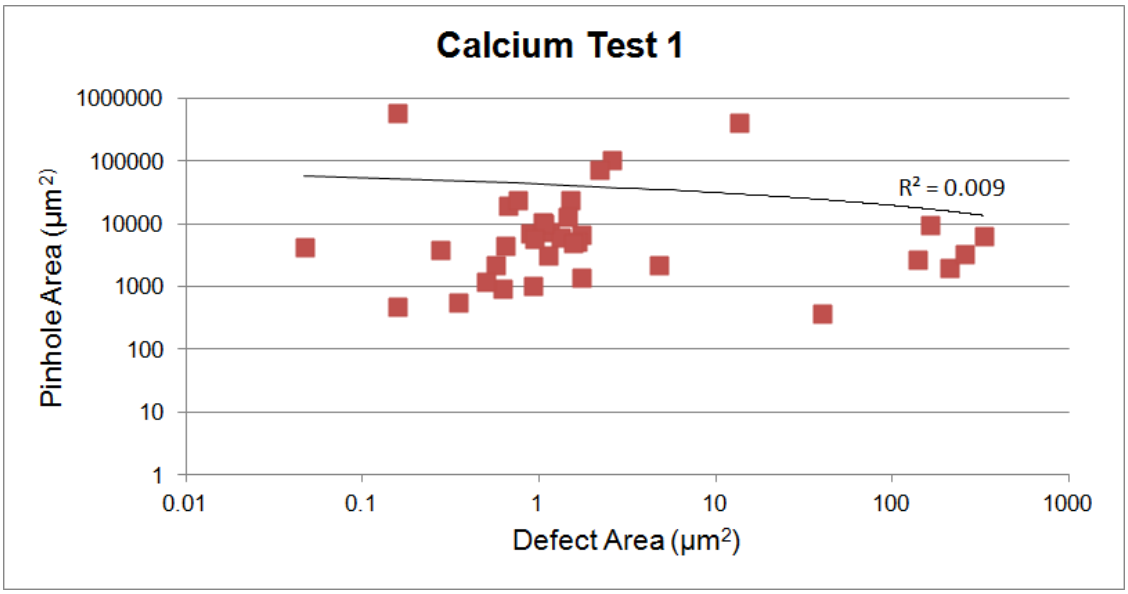

7.7 A: **Defect size versus pinhole diameter for Calcium Test 1, R^2 = 0.009**

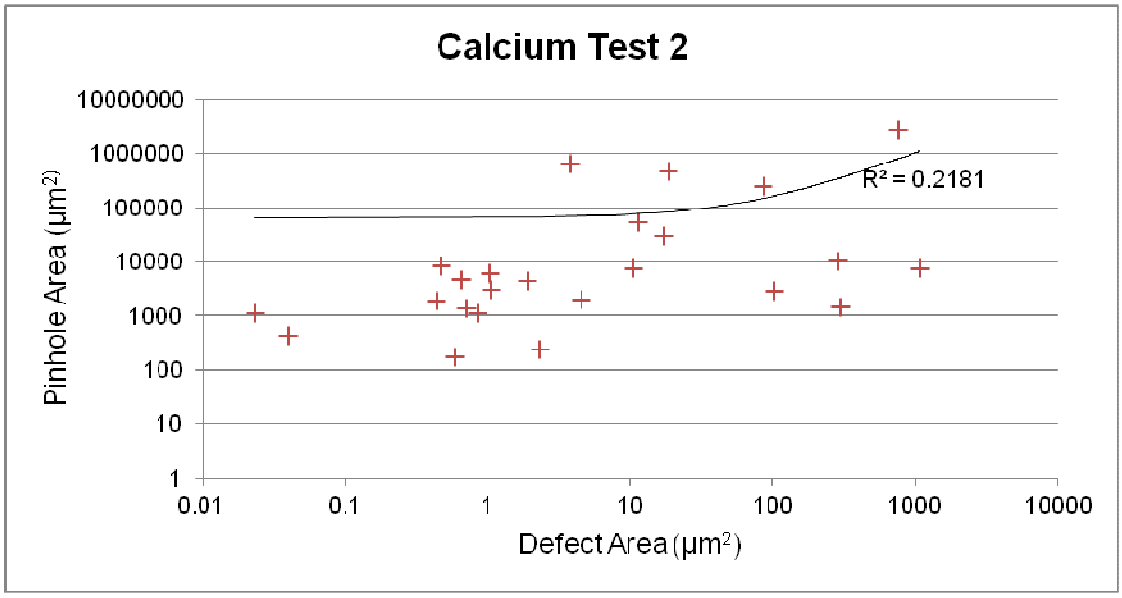

7.7B: Defect size versus pinhole diameter for Calcium Test 2, R^2 = 0.2181

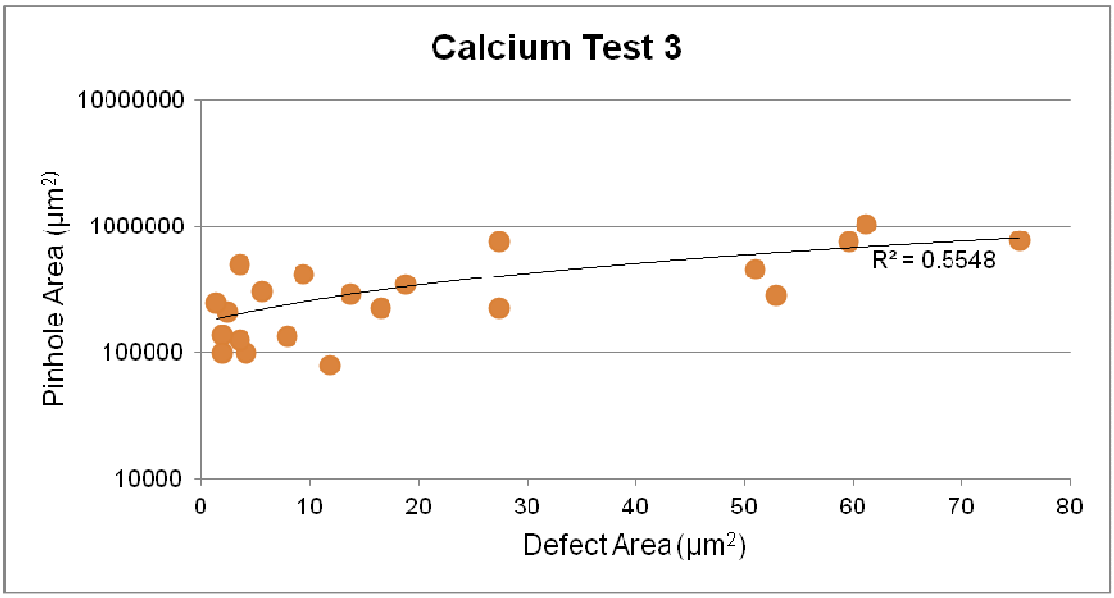

7.7 C: Defect size versus pinhole diameter for Calcium Test 3, R^2 = 0.5548

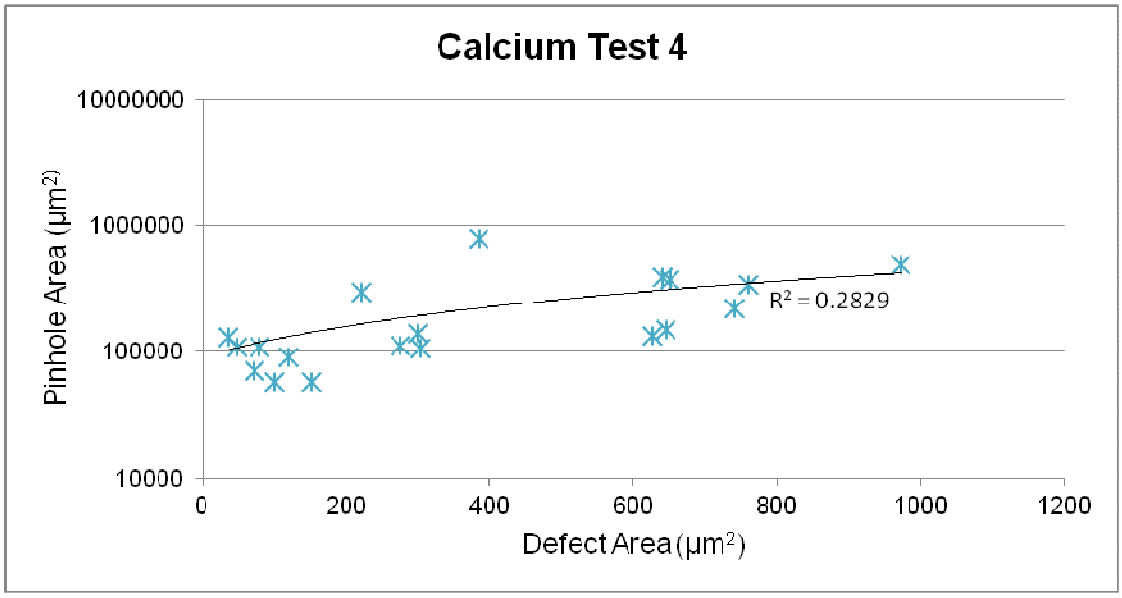

7.7 D: Defect size versus pinhole diameter for Calcium Test 4, R^2 = 0.2829

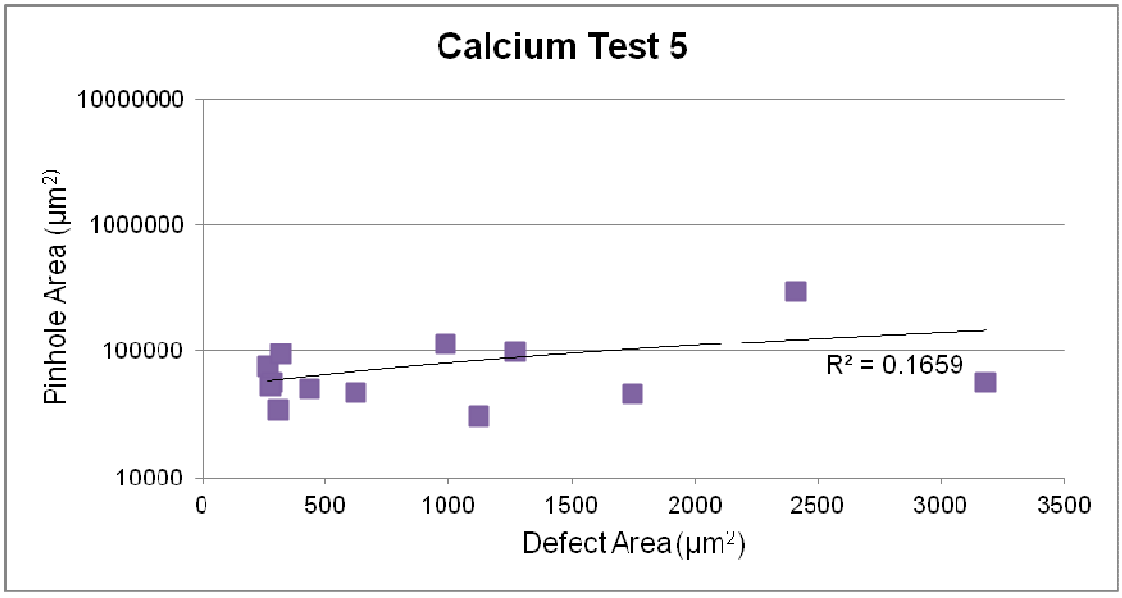

7.7 E:Defect size versus pinhole diameter for Calcium Test 5, R^2 = 0.1659

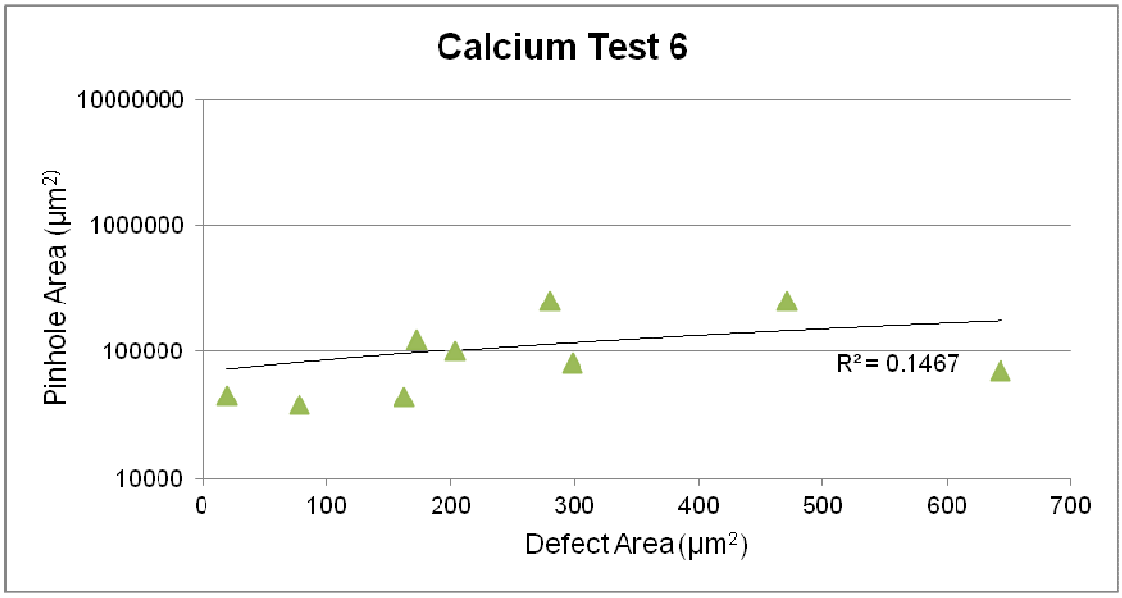

7.7 F: Defect size versus pinhole diameter for Calcium Test 6, R^2 = 0.1467

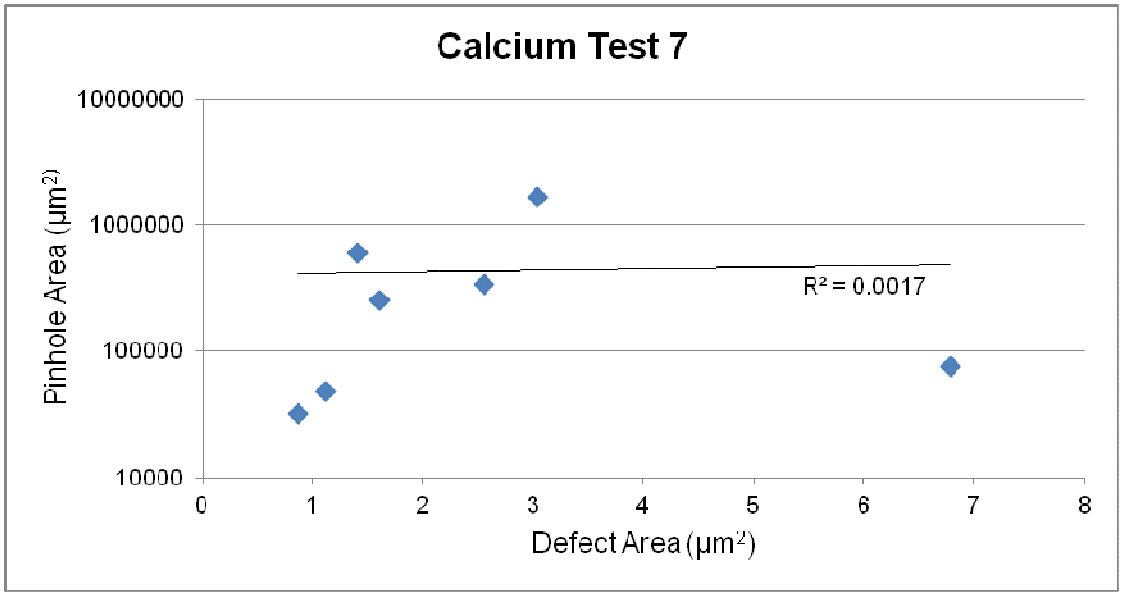

7.7 G: Defect size versus pinhole diameter for Calcium Test 7, R^2 = 0.0017

Figure 7.7: Seven plots showing pinhole degradation regions plotted against the corresponding defect areas

Examining these graphs, it seems clear even before the application of an R^2 value that none have a strong linear relationship, indeed, 'Ca-test 4' has the best fit from all the data but even at 0.55 this is in poor agreement. It can be stipulated from these data that even if the larger dust particles were

completely removed from the production process, the smaller particles are still capable of creating significant pinholes. So whilst efforts can be made to eliminate the largest contaminants from the working environment, this would not in fact solve the issue of the 'big hits'.

The data gathered in this thesis so far demonstrates that there is no simple scaling with the size of contaminant, this further supports the theory that the lateral dimensions of defects are not the sole determining factor in permeation; there must be other features not yet been determined which have a more significant contribution.

Clearly, the mechanism of permeation is not fully understood, current theories and models are based on existing observations, many of these are mathematically derived and have to make a number of assumptions about these systems. Existing experimental work has been based on spherical particles of well defined sizes and hence it is of little surprise that these linear relationships have been observed (Lim, 2001a; Lim, 2001b), in contrast to the data obtained here for irregularly shaped dust particles.

Whilst straight-line plots have not been observed for real world systems in this thesis, results this far support the theories that the majority of defect sites are the result of extrinsic contaminants. Concerns within DTF originally centred on the assumption that barrier failures were caused by intrinsic defects resulting from manufacturing defects rather than a result of extrinsic debris during post-processing. It was decided that the impact of both types of defect should be investigated so that studies could be targeted in the right area.

7.4 Surface Quality

Using artificially contaminated systems, it is possible to determine the effects of both intrinsic and extrinsic defects using very well characterised systems. Film cleanliness is considered to be a critical factor for maintaining high quality barriers. (DTF, 2007)

Flaws can be described as intrinsic or extrinsic. The former make up a part of the film surface, they are present throughout film manufacture and typically have much larger X & Y dimensions. The latter are those which settle on the film surface after production, they tend to be made up of debris created during the slitting processes or airborne dust and are held on the film via electrostatic forces (DTF, 2007). It is comparatively simple to add extrinsic flaws to a film with the addition or particles or dust, however generating well defined intrinsic flaws can be more challenging.

7.4.1 The effect of intrinsic defects

It was already known within DTF that intrinsic contaminants were capable of disrupting the barrier and measures are already undertaken to reduce their impact, primarily through planarisation (DTF, 2007).

7.4.1.1 Planarisation

Film roughness can have a highly detrimental effect on barrier performance, to reduce the detrimental effect which intrinsic have on barrier performance a planarising hard coat can be added to a film surface. It is deposited as a wet coat to the polyester during manufacture and acts to increase the smoothness of the surface by capturing existing extrinsic debris and filling scratches which may be present on the raw film after production (Figure 7.8).

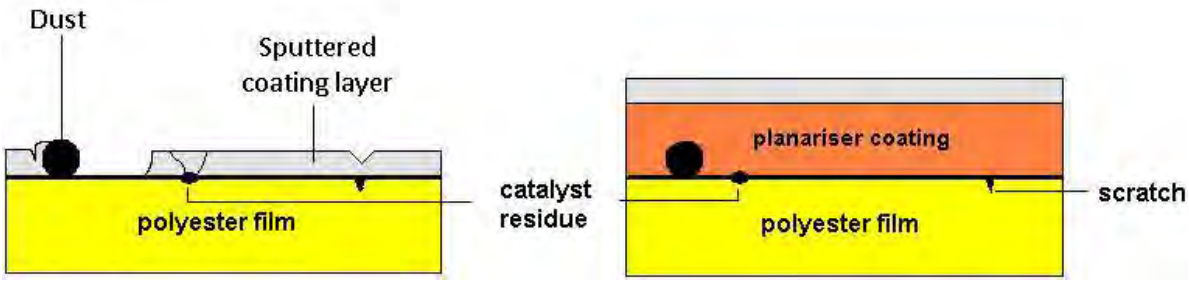

Figure 7.8: Schematic to demonstrate the effect of planarisation on polyester film, note that without a planarising layer the sputtered coating is disrupted by surface features and debris

7.4.1.2 Visualised Effect of Planariser on PEN

Permeation measurements for equivalent films, both with and without planarisation, show a dramatic difference in barrier performance (Figure 7.9). Planarisers reduce the surface roughness of the substrate and greatly increase the polymer scratch resistance, furthermore no morphological differences have been observed between transistors made on planarised PEN or on silicon (O'Rourke, 2007). This suggests that the surface smoothness of the planarised surface is a comparable quality to silicon wafers.

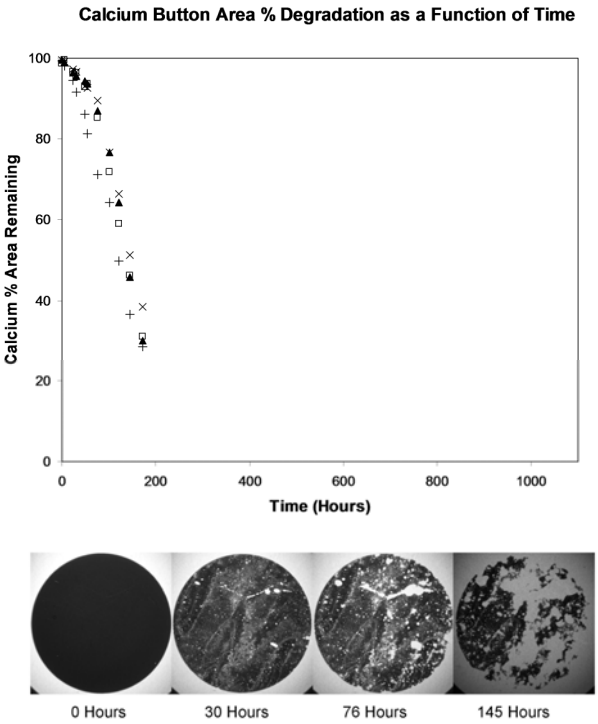

Aluminium oxide on unplanarised polyester

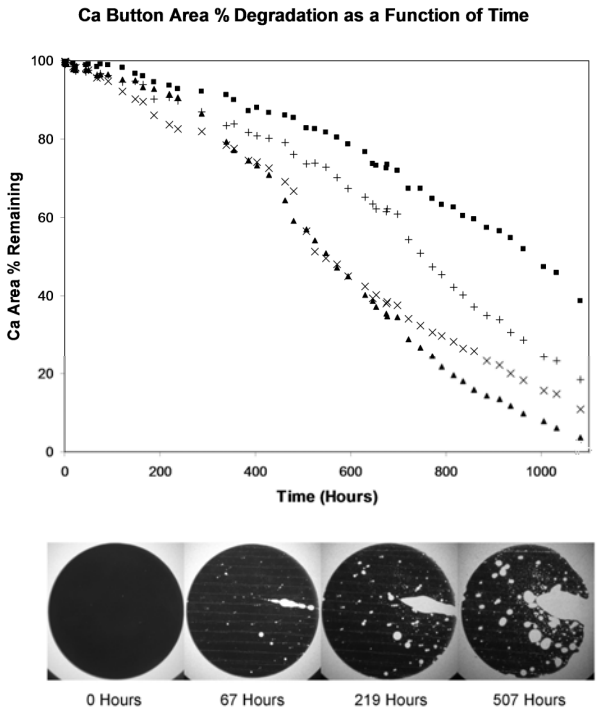

Aluminium oxide on planarised polyester

Figure 7.9: Barrier performance comparison of unplanarised (top) and planarised polyesters (bottom) showing the influence of increased surface

Similarly, OLED pixels printed on to both raw and planarised versions of the same film produce results which mirror those seen in the calcium test, the unplanarised film exhibits many pixel dropouts whereas the planarised version appears ideal (Figure 7.10).

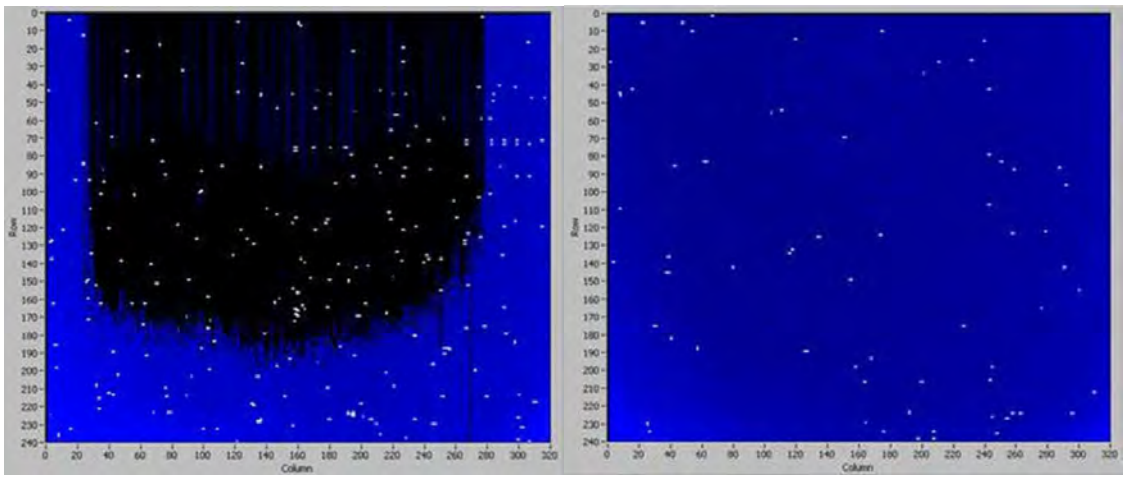

Figure 7.10: QVGA array test on non-planarised (left) and planarised PEN (Right), blue areas represent 'healthy' pixels (O'Rourke, 2007)

The surface smoothness of planarised substrates can be quantified using white light interferometry, an analysis which is routinely carried out within DTF.

7.4.2 Quantification of the Planarising Effect

Using WLI, large area stitched arrays of PEN can be captured to demonstrate the dramatic effect planarisers have in reducing the intrinsic peak count of industrial grade PEN (Figure 7.11).

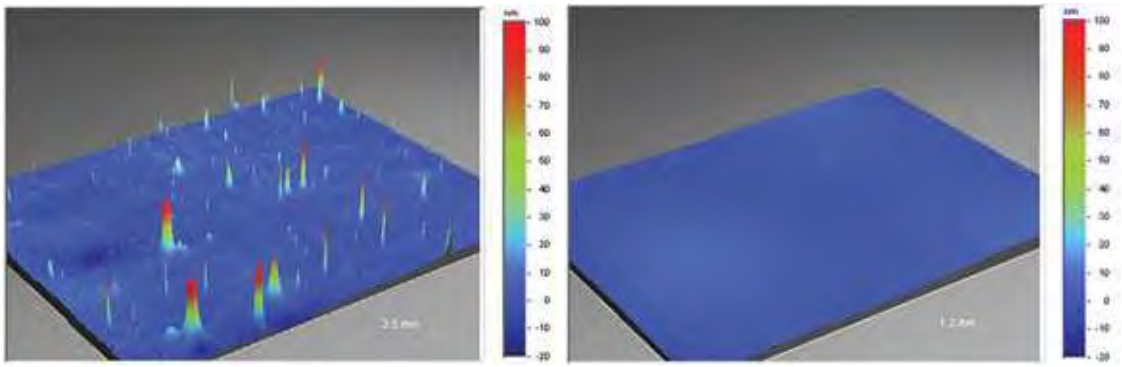

WLI topography images of industrial grade PEN (left) and planarised PEN (right)

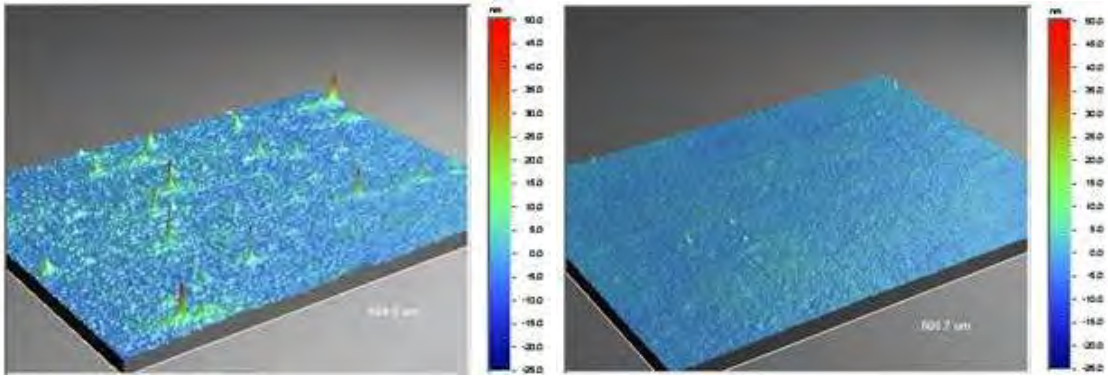

Pre-treat coating helps layer adhesion but at the expense of surface smoothness [Ra 1.53] (left) and Planarised PET, comparable to the surface of a polished mirror [Ra 0.6 nm] (Rakos, 2010b)

Figure 7.11; Four pictures showing how the planariser coating affects the surface smoothness

By varying the planariser depth on samples of identical base film, its ability to reduce surface roughness can be demonstrated. Figure 7.12 shows peak counts measured with a white light interferometer of industrial grade PEN and two coated analogues with different planariser thicknesses.

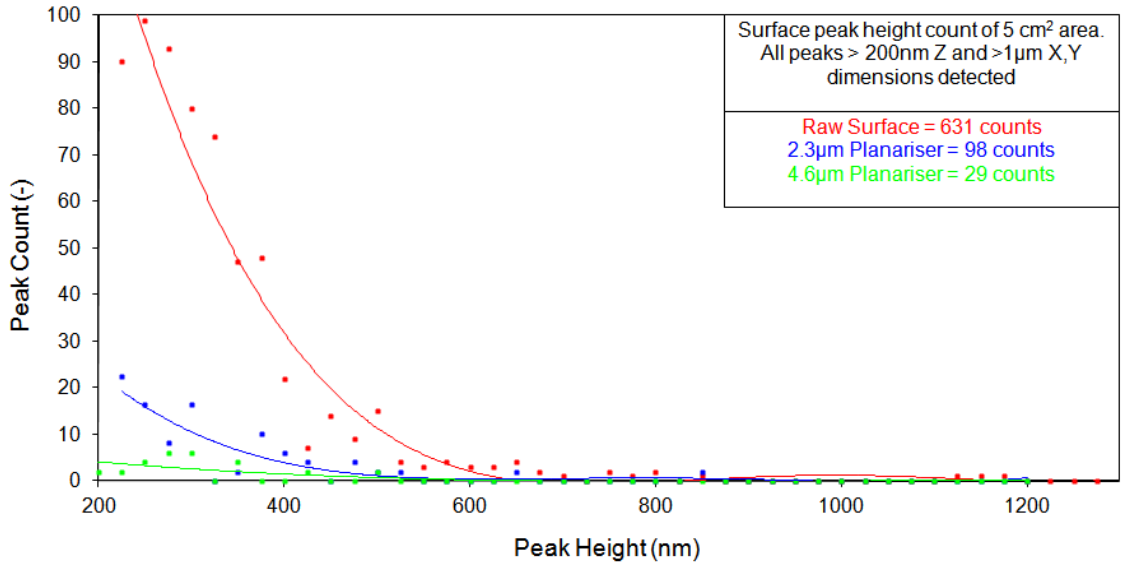

Figure 7.12: Extreme surface peak height count for PEN (Kaladex) and its equivalents with 2.3 µm and 4.6 µm planariser coat thicknesses

The data suggest that the base peaks (those lower than 0.45 µm) are planarised out by the thinner 2.3 µm layer, evidenced by a 6.4 times reduction in peak counts, the majority of peaks on the raw PEN lie in the lower height region of the graph. It is logical to assume that the lower peaks will be planarised out first, with the higher peaks still protruding through the layer. The 4.6 µm coating planarises out approximately all 0.6-0.7 µm surface peaks present on the other two samples.

The number of intrinsic defects detected over any large area of displays grade planarised PEN is very small, even when analysed with the higher resolving power of an AFM or SEM, however the number of pinholes which develop on calcium test cells occur at a frequency which if caused by intrinsic defects should make them much more easy to detect. This suggests that whilst intrinsics may contribute to barrier discontinuities, they are unlikely to be responsible for the majority of pinholes and supports recent conclusions within DTF (Rakos, 2010b).

7.5 Artificial Surface Features

7.5.1 Ultraclean Film

A good way of testing whether intrinsic flaws have any major significance would be to examine a film which is known to be free of extrinsic defects. To perform such a study a polyester film with guaranteed hygiene was required, this was found in the form of a development polyester; a co-extruded polymer featuring two layers, a base polyester and a thinner, sacrificial protective layer. The two are co-extruded immediately from the melt, in this way the primary polyester surface remains sheltered from any potential extrinsic contaminants up to the moment the protective layer is removed, moreover, any contaminants which may be introduced during production are captured in the sacrificial protective layer.

Depositing a layer of calcium directly on to the internal polyester surface immediately after manually peeling away the protective layer would highlight any major surface flaws, as the calcium layer is only 100 nm thick any significant intrinsic or extrinsic protrusions would be observable using transmitted light microscopy.

7.5.1.1 Visualisation of Intrinsic and Extrinsic Defects on Ultraclean Peelable

Samples of the peelable film were taken from the same source, half of which remained protected until the moment immediately before calcium deposition, whilst the other half were peeled and placed in an open office two weeks prior to testing to allow dust to accumulate on the surface. The resultant calcium tests are very revealing (Figure 7.13). A large number of contaminants were apparent on samples which had been exposed to the office environment, whereas those which remained covered remained almost defect free. Given the frequency of defects observed on displays grade PEN, a film which is considered to have an exceptionally smooth surface compared to the 'rough' ultraclean peelable, it is likely that extrinsic contaminants such as dust play a significant role in barrier disruption.

Figure 7.13: Calcium test buttons from samples of 'ultra-clean peelable', showing pinhole counts of 5 on the protected button (top) and 408 on the contaminated (bottom), both are 28 mm in diameter

Analysis of the calcium in Figure 7.13 reveals that 0.38% of the contaminated surface is covered with defects whereas on the clean surface they make up less than 0.002% of the total area. Whilst these are relatively small percentages the contaminated surface has 190 times greater number of surface peaks. It is important to note that these results are only comprised of defects greater than 100 nm in diameter, smaller particles which although visible in Figure 7.13, only cause a thinning of the barrier and were not significant enough to visualise a break without extended calcium testing. Clearly, the low count of intrinsic features suggests that this is not the major cause of the large number of barrier failures. If a calcium spot on a 'rough' development film in which we expect to see a large number of intrinsic defects reveals only 5 such flaws, then we can assume that barrier failure to the degree observed on calcium tests of displays grade PEN caused primarily by intrinsic flaws is highly unlikely.

7.5.2 The Effect of Intrinsic and Extrinsic Contaminants on Barrier Layers

The results in Section 7.4.1 demonstrated that high counts of dust can accumulate on a surface in a short space of time, the detrimental effects that dust can have are well known within the semiconductor industry (Zant, 2004).

To compare this effect, two samples of film were obtained; one was a section of coated PEN (also known as 'pre-treat') featuring a surface coating embedded with a mixture of both 40 & 100 nm silica particles, at 2 & 1 wt% respectively. The other was a section of the same PEN polymer without the binary silica coating, but was exposed to an open office for one week, followed by non-contact cleaning with compressed air. Using the calcium test we can compare permeation through both films, the contrast between the two is huge; room dust samples fail in a matter of hours at ambient conditions compared to a lifetime of weeks for the pre-treat sample (5.14).

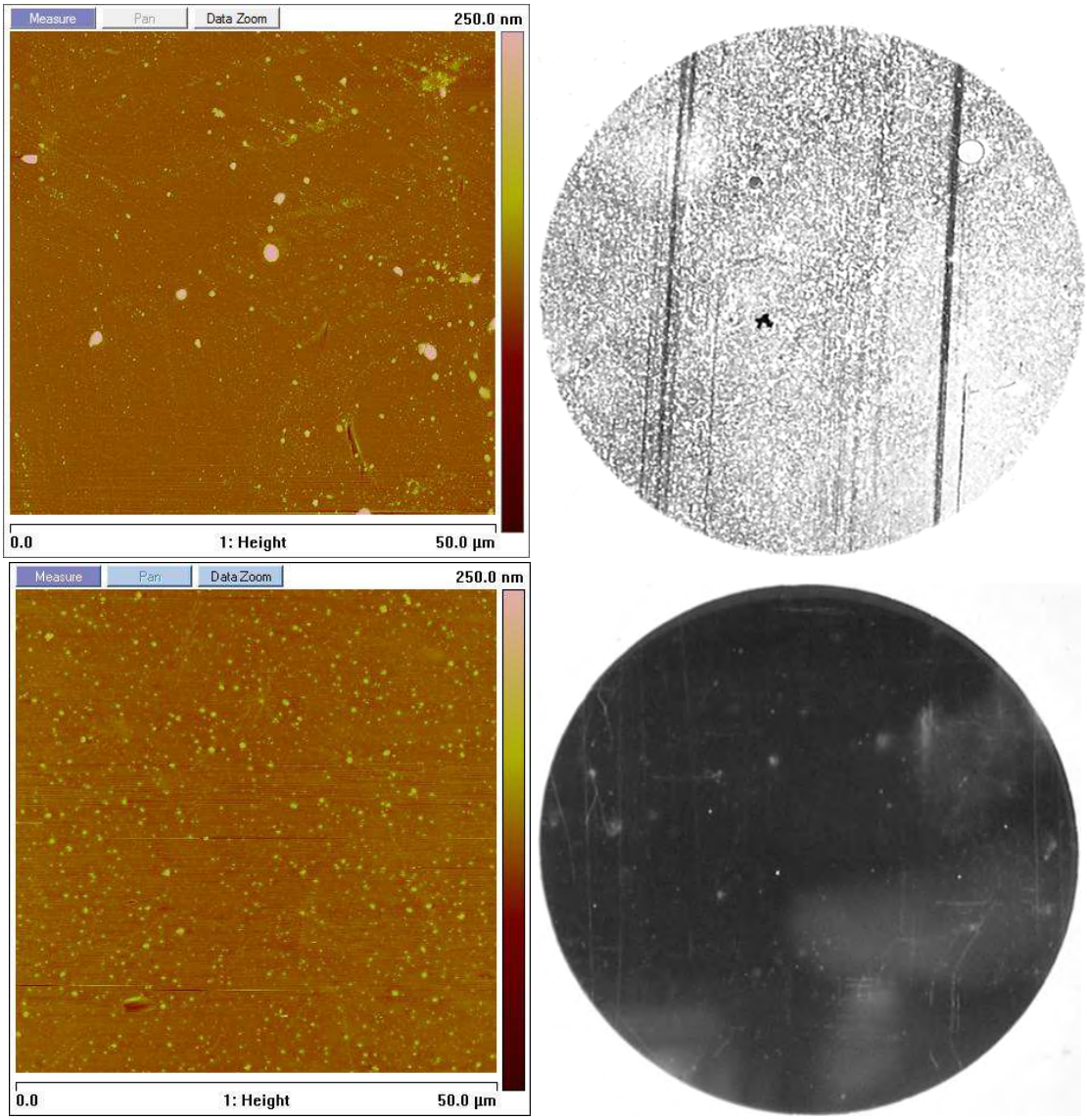

Figure 7.14: 50 µm AFM topography scans of both dust contaminated planarised PEN (top left) and pre-treat PEN (bottom left) with corresponding calcium tests after 24 hours (right)

Despite the large amount of surface texture, the pre-treat sample lasted for a much longer period. Analysis of the pinholes on the pre-treat sample actually revealed that degradation which did occur was a result of large flaws in the film surface (Figure 7.15) rather than as a direct result of the embedded silica particles.

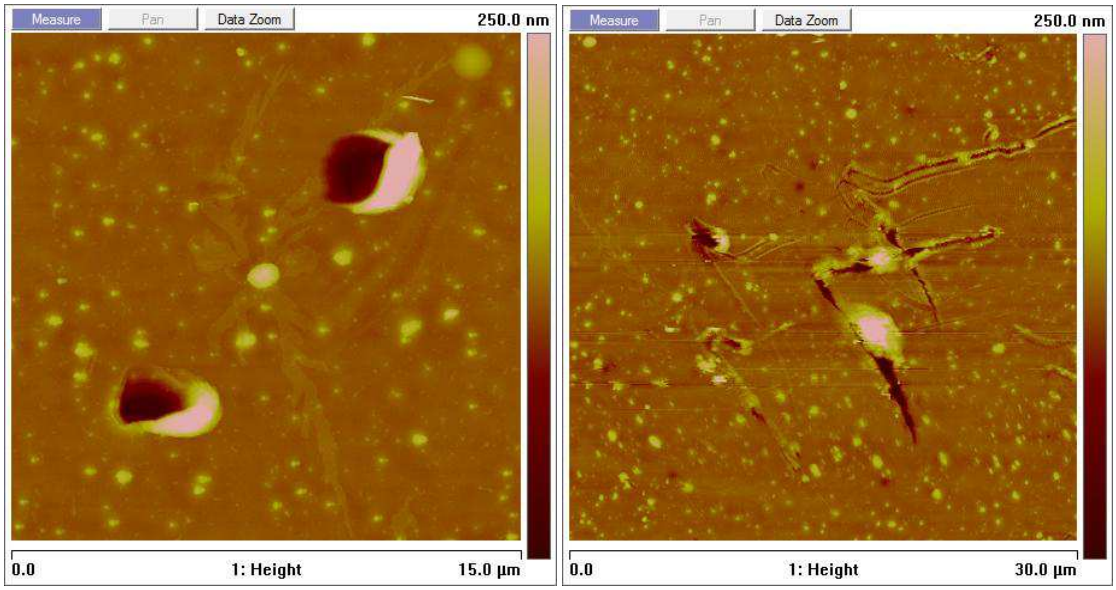

Figure 7.15: AFM topography images showing examples of typical flaws responsible for the major pinholes in pre-treat PEN calcium tests

It was decided that the test should be repeated, but with a well defined, comparable size of extrinsic particles.

7.5.3 Performance Comparison of Intrinsic and Extrinsic Contaminants

The experiment in Section 7.4.2 was repeated but instead of comparing dust to pre-treat, a clean sample of PEN was taken and dusted with 100 nm silica particles before barrier coating. As room dust consists of a range of particle sizes, the idea of this experiment was to make a direct comparison between features of comparable size.

Calcium testing was carried out on both samples, both performed better than expected (Figure 7.16), the pre-treat sample displayed superior performance and any pinholes again occurred at sites of major surface disruption, such as those displayed in Figure 7.15. Despite the large covering of silica particles the extrinsically contaminated sample performed better than the previous room dust sample (Figure 7.14), it is believed that an increased number of larger particles and particle shape in the latter are the main reasons for this.

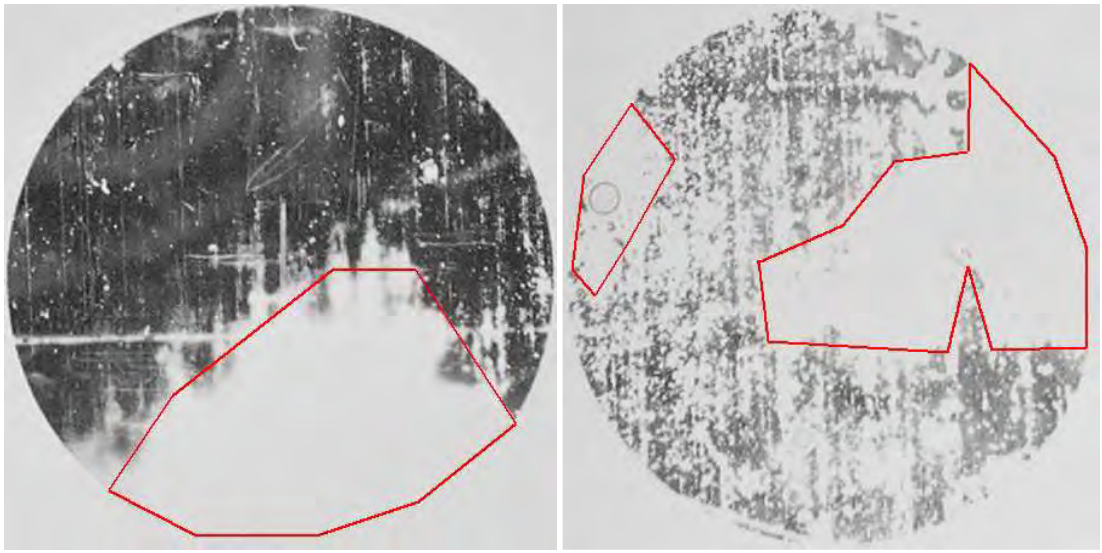

Figure 7.16: Results of calcium test after 216 hours at ambient conditions showing differences in performance between barrier coated pre-treat PEN (left) and planarised PEN contaminated with 100 nm silica particles (right). Red outlined regions are a result of over adhesion, not permeation

These results further support the argument that extrinsic debris, regardless of size is responsible for barrier disruption, with the major difference between the two samples being was the intrinsic and extrinsic nature of the contaminants.

7.5.3.1 Examination of Sample Barrier Coatings

Using the AFM to analyse the surface of the pre-treat before and after barrier coating helps rationalise results from Section 7.4.2. Surface topography is visible in all scans, at a 20 μm field of view there is no clear difference between images either visually or mathematically. When we look at a 2 μm field of view however, the granular structure of the aluminium oxide becomes apparent (Figure 7.17). This shows that despite the topography of the surface, all the small intrinsic features receive an even coating of aluminium oxide.

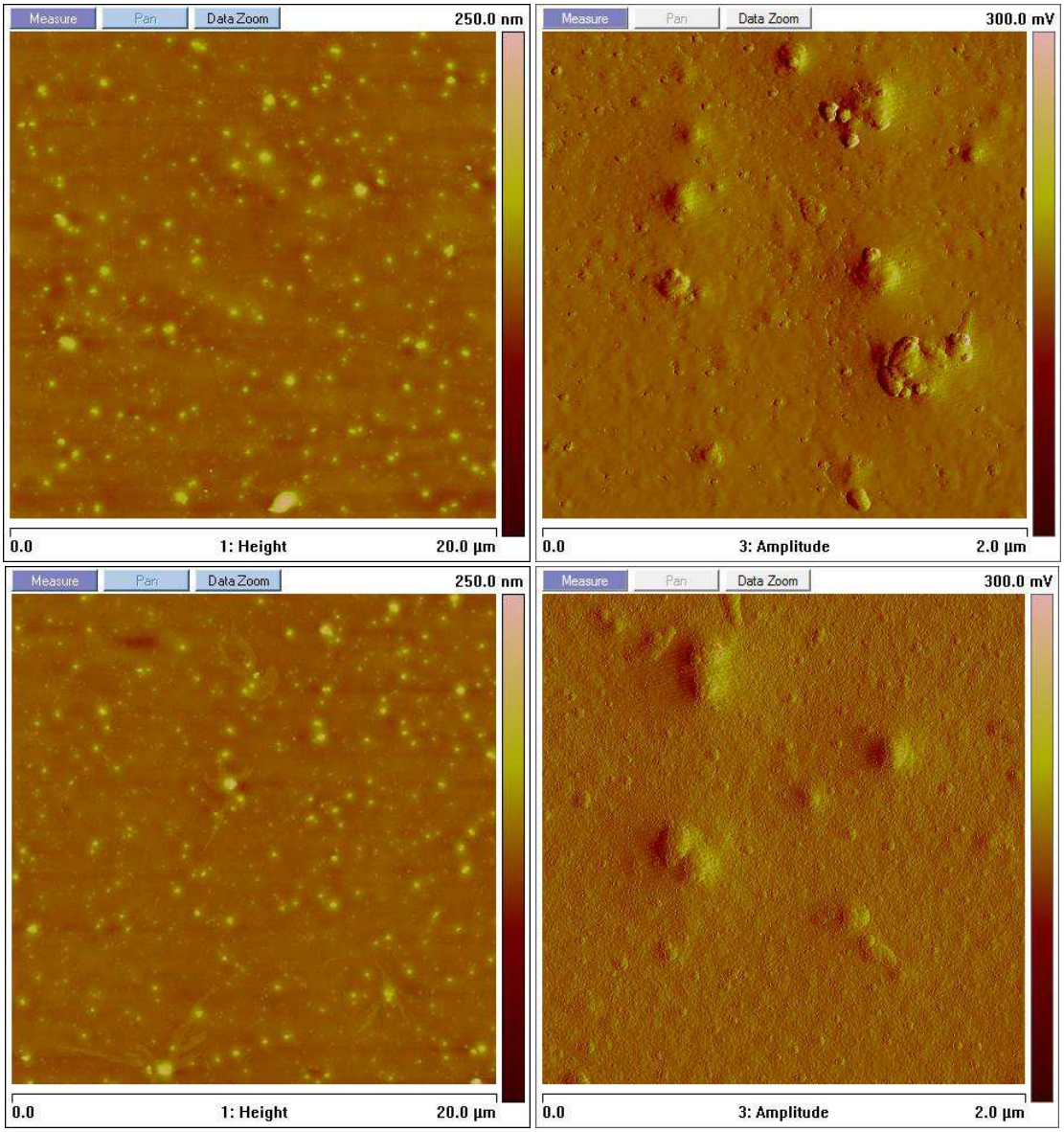

Figure 7.17: 20 µm AFM topography images of non-barrier coated pre-treat PEN (top left) and barrier coated pre-treat PEN (bottom left), 2 µm amplitude images of the non-barrier coated (top right) and barrier coated (bottom right) scans highlight the granular structure of the barrier coat

Comparing typical roughness parameters confirms that there is little difference between the two samples (Table 7.1). Whilst the barrier coated sample is measured as being slightly less rough at a 20 µm FOV, at 2 µm FOV it is measured to be marginally rougher; both of these differences are very

small however and cannot be attributed to the barrier coating alone, it is more likely that the differences are a result of the macro features present in each scan.

Table 7.1: Roughness parameters for barrier and non-barrier coated pre-treat PEN

	R_a (nm)	R_q (nm)	rsk	rku	R_{pm} (nm)	R_p (nm)
Pre-treat 20 µm	3.91	8.24	6.34	63.05	143.22	163.5
Barrier 20 µm	3.87	7.63	5.45	45.17	97.78	107.79
Pre-treat 2 µm	4.94	9.35	5.31	53.35	122.21	218.73
Barrier 2 µm	5.63	11.04	5.13	38.88	125.39	133.06

Performing the same analysis on the extrinsic silica particles, the measured height both before and after barrier application suggests all features received an even coating of aluminium (Figure 7.18).

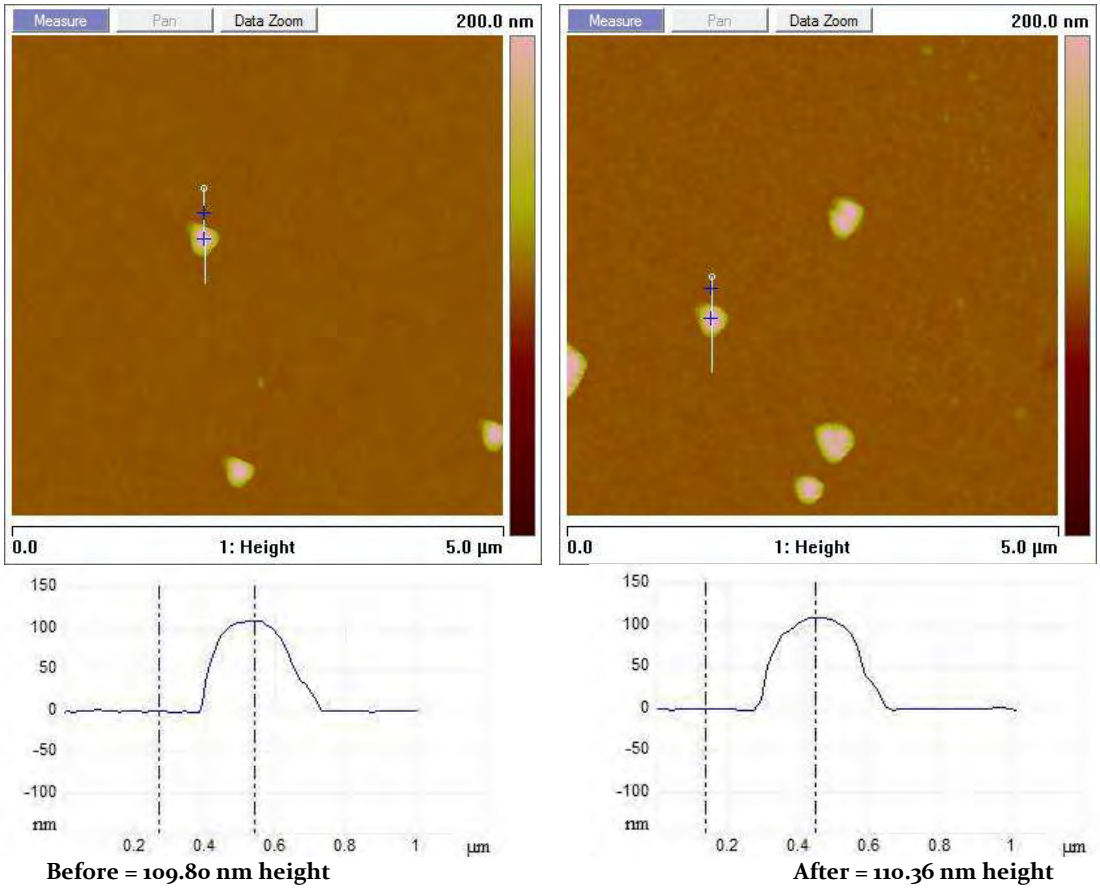

Figure 7.18: 100 nm spherical silica particles on a planarised PEN substrate, before barrier coating (left) and after (right). Note, non-spherical particle appearance is an artefact of the tetrahedral AFM tip shape

It is believed that the shadowing area created under any extrinsic particles (Lim, 2001a; Lim, 2001b) may be the key factor in determining the contribution to permeation; no intrinsic defects will have such features meaning the barrier layer can coat the entirety of the peak without leaving any voids, hence the much better calcium test performance.

According to existing theory, extrinsic particles will receive a coating of barrier but voids will be present, it is quite possible that the heights measured using AFM are actually peaks caused by barrier coating on top of particles and not the silica itself (Kim, 2002) (Figure 7.19).

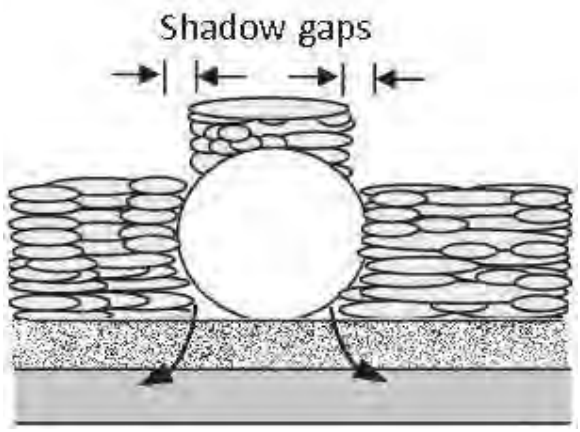

Figure 7.19: Schematic of an extrinsic particle on a barrier coated film showing the barrier 'cap', thought to be responsible for forcing diffusion to occur only around the defect perimeter (Kim, 2002)

It was decided that an attempt to determine whether the schematic displayed in (Figure 7.19) is the situation encountered in this section, as it would offer a simple explanation as to why extrinsic coatings do cause barrier failure.

7.6 Barrier Deposition Techniques

One of the strengths of the AFM is that it allows the manipulation of particles on the surface of the substrate under analysis, using this ability it is possible to move a particle which has been barrier coated.

7.6.1 The Shadowing Effect

Examples in the literature suggest that a shadowing effect is the reason for any observed permeation (Lim, 2001a; Lim, 2001b). This can be observed on both the micro- and macro-scale, such as underneath microscopic silica particles present during the barrier deposition process, or on the macro-scale, observed within a vacuum deposition chamber (Figure 7.20). This highlights the importance of line of sight when carrying out deposition using such techniques.

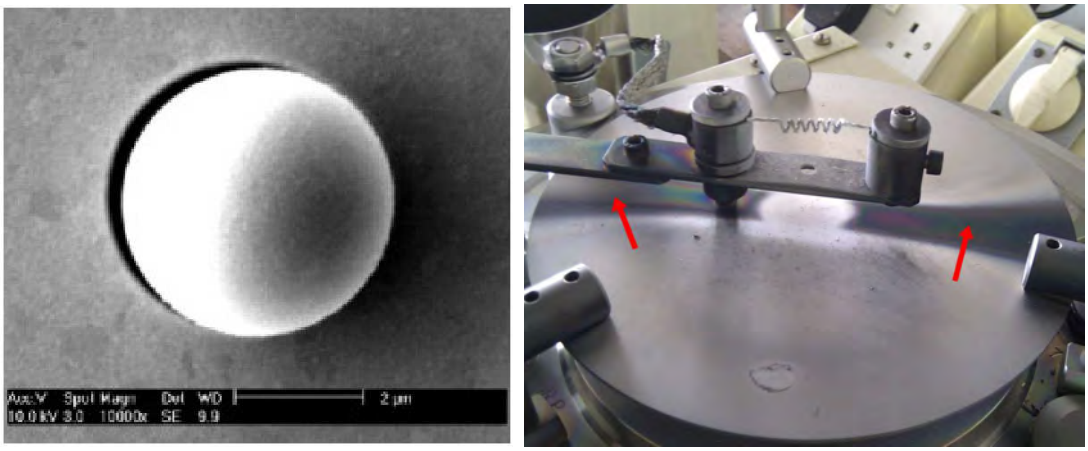

Figure 7.20: SEM image demonstrating the line of sight shadowing effect caused by a silica particle on a film surface (left) (Lim, 2001a; Lim, 2001b) and a photograph displaying the same effect on the macro-scale within an evaporative vacuum deposition chamber (right – red arrows)

Four different particle sizes were placed on to planarised PEN, a layer of aluminium was then deposited over these using a vacuum deposition chamber. The AFM was subsequently employed to remove a particle from each of these surfaces and record the topography. All cross sections show steep sided walls, an artefact of the line of sight nature expected from evaporative deposition and a result of the perpendicular incident angle of the aluminium coating.

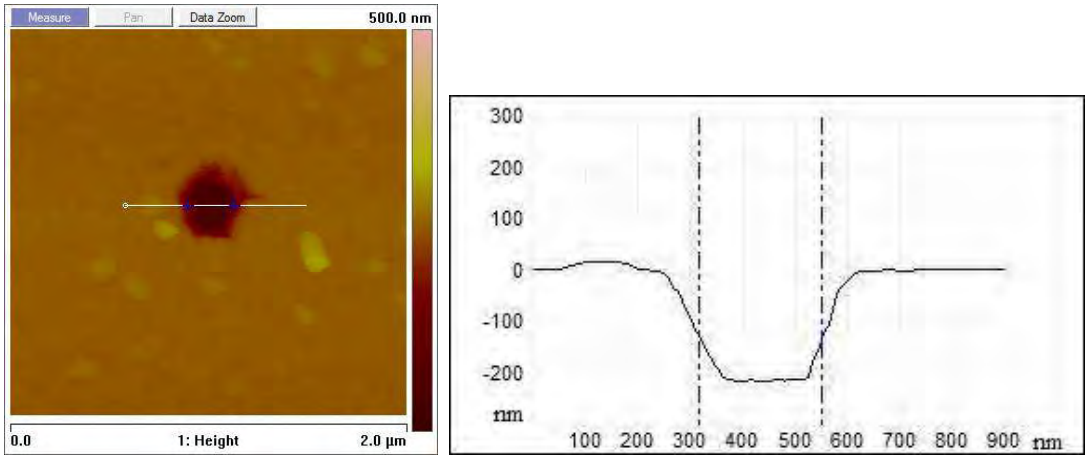

0.3 µm particle shadow

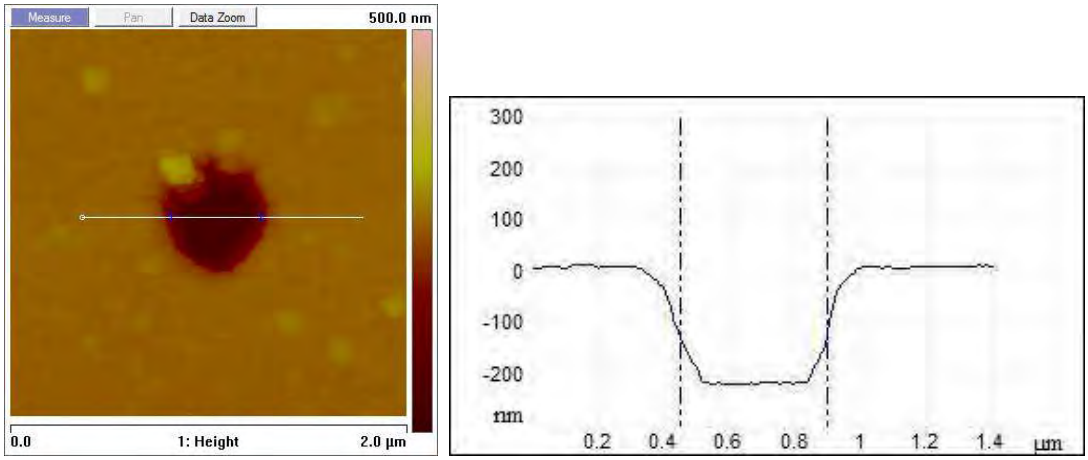

0.5 µm particle shadow

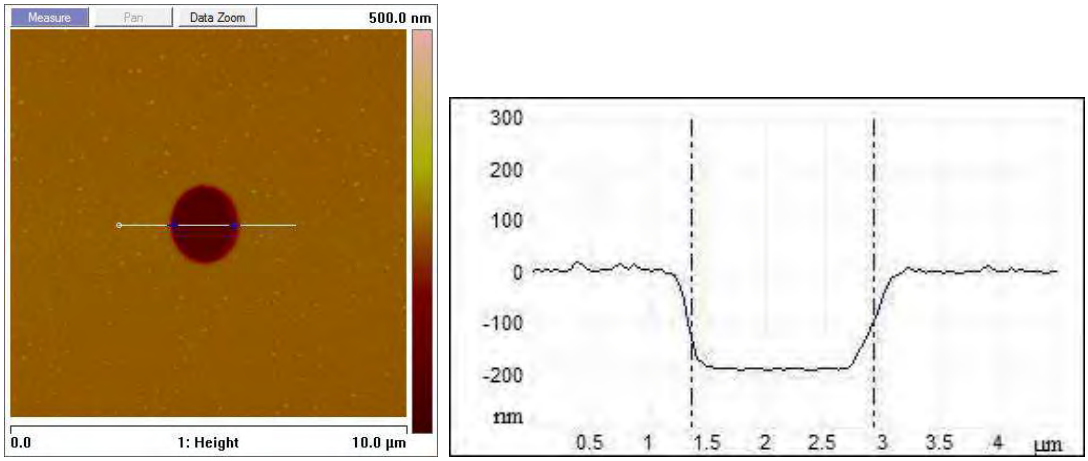

1.5 µm particle shadow

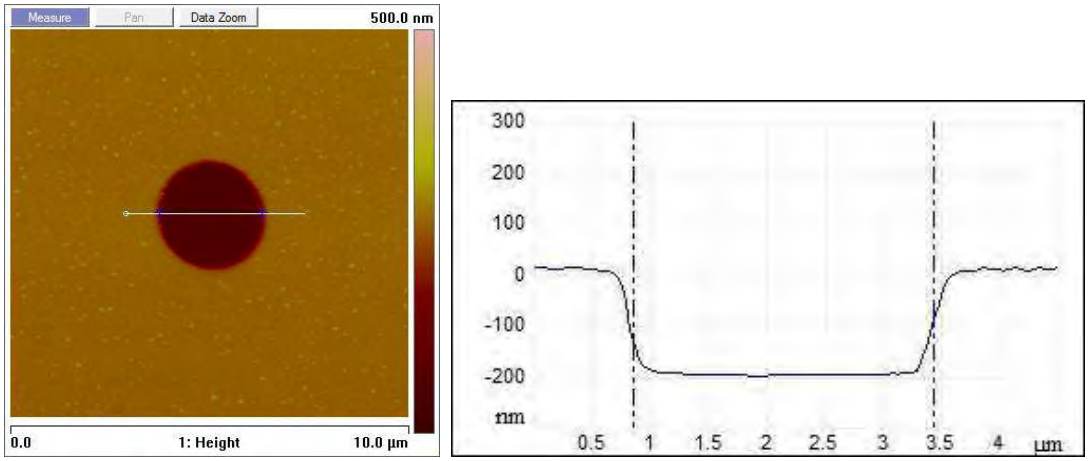

2.5 µm particle shadow

Figure 7.21: AFM Topography images of particle shadows created in vacuum deposited aluminium, determined using full width half maximum; edge gradients of pits area result of AFM tip convolution

The effect is clearly demonstrated if the aluminium approaches the surface at an extreme incident angle, when the aluminium approached at almost 90 º the long shadows created behind any surface particles are clear (Figure 7.22).

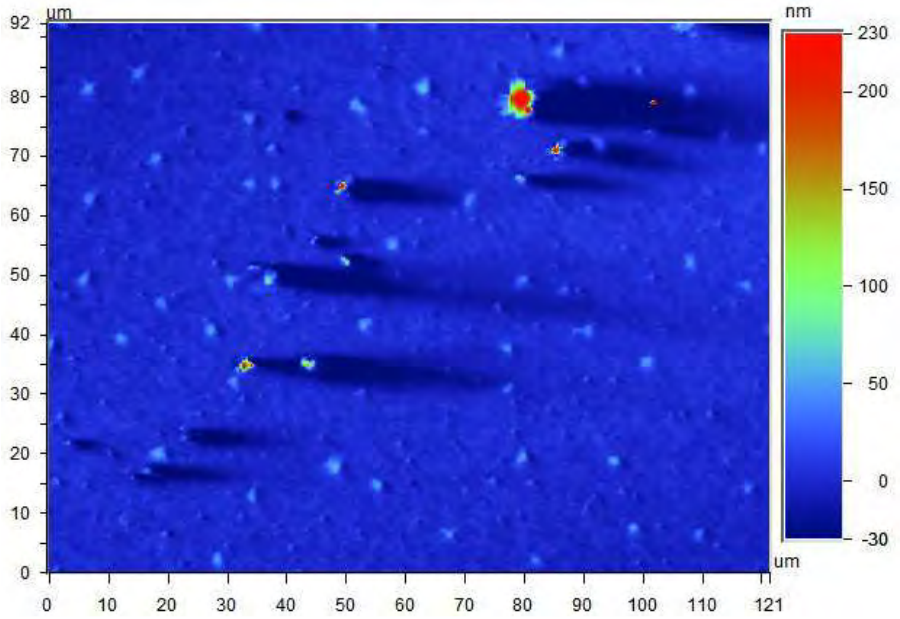

Figure 7.22: WLI topography image of the shadowing created behind silica particles using vacuum evaporative aluminium deposition incident from the left of the image

However, when the AFM is applied to remove the same particles which have been barrier coated using DTF's production deposition technique, a very different result is observed (Figure 7.23).

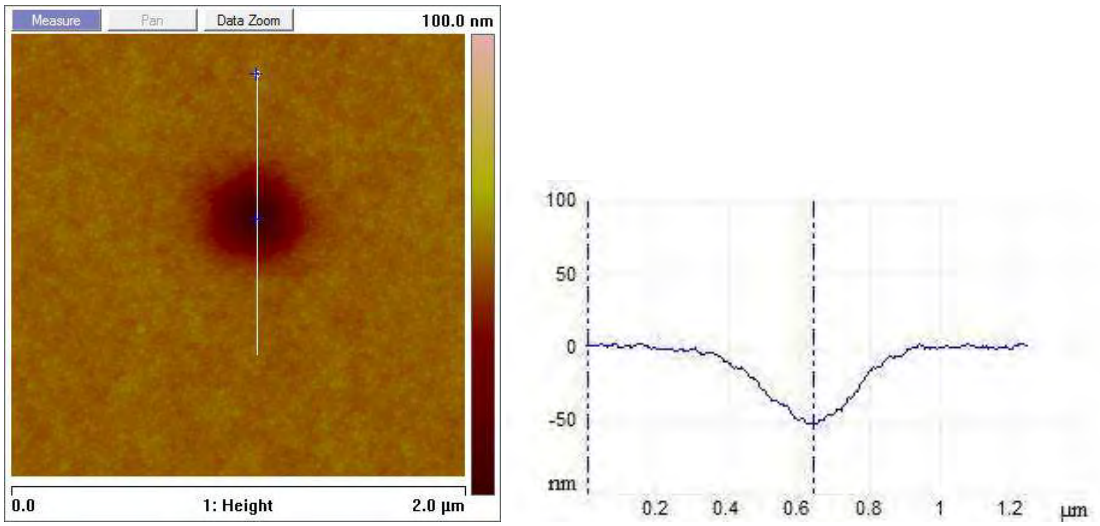

0.3 µm particle shadow

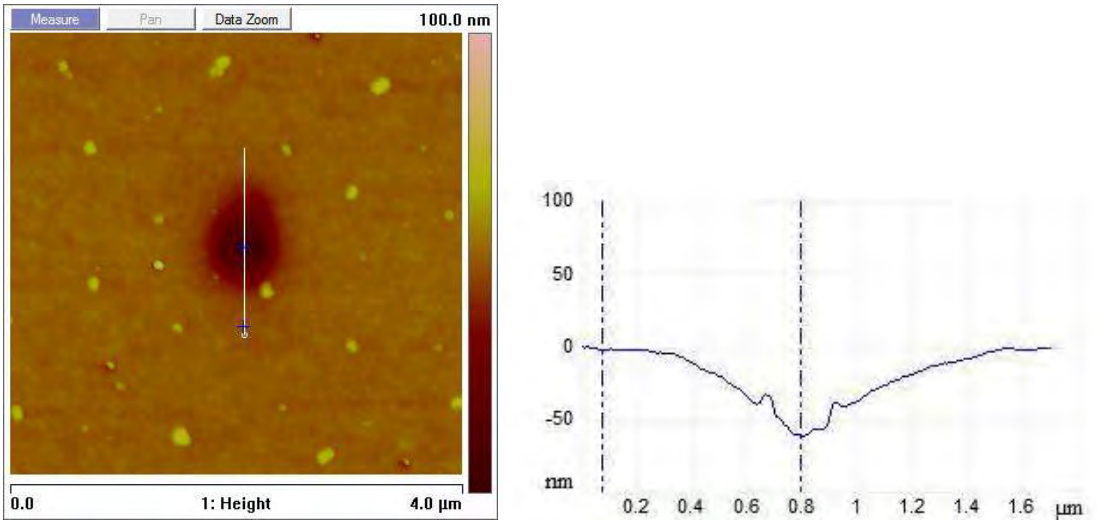

0.5 µm particle shadow

Figure 7.23: AFM topography images of particle shadows in a production barrier film surfaces after the removal of particles, with the corresponding cross-sections of these voids showing very gradual edge angles (right) compared to those in Figure 7.21

It becomes clear that there are huge differences between the barrier deposition techniques, the likes of which have not been considered in any literature. It is assumed by many that sample

preparation in is analogous to all manufacturing processes in this area, although literature utilised a range of barrier materials and thicknesses, it was the deposition technique which was felt required investigation.

7.6.2 Coating mechanics

As stated, many groups believe all barrier coating techniques to be comparable, however if we examine these in detail differences between published results and those in this thesis become apparent. Many studies into OLED devices utilise vacuum evaporative deposition, whereas DTFs manufacturing process utilises reactive magnetron sputtering (MacDonald, 2008b). With the former, metal atoms are blasted away from a source in all directions by rapidly heating the material beyond its boiling point. These then condense on to any surface with which they come into contact, if there is an overhang perpendicular to the incoming atoms, a shadow will be created.

During reactive magnetron sputtering, it is known that metal atoms are also removed from the target in many directions, but when these atoms encounter the film surface they migrate until they encounter a nucleating site (Chang, 2010). Furthermore, DTF's sputtering is a roll-to-roll process, meaning that moving the substrate underneath the target further ensures that incident particles are more likely to reach under any potential overhang (Figure 7.24)

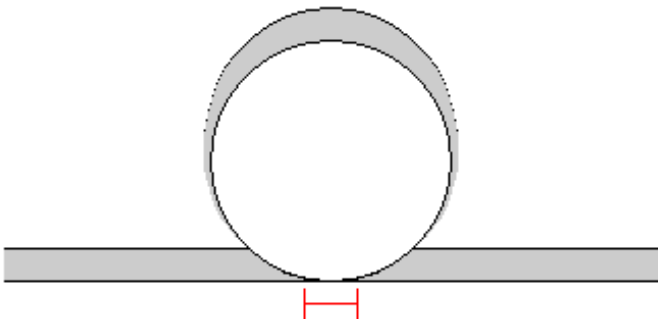

Figure 7.24: Diagram to show barrier undercoating through reactive magnetron sputtering

Although the sputtering process does make the potential hole underneath any contaminants somewhat smaller, there remains a contact point between the particle and film which would remain as a potential ingress point for water (Red highlight in Figure 7.24). This may explain why some large defects do not cause as significant barrier breaks as some smaller contaminants, simply because they have a smaller surface contact area. Considering these findings, it seems likely that the footprint of the particulate on the film surface is the factor which has the greatest influence on permeation. It was decided that a precisely controllable system to model this was then required and its development discussed in detail in Chapter 8.

7.7 Conclusions

In this chapter a large number of features and flaws have been examined to test the theories surrounding the causes of barrier permeation. Existing theories including DTFs barrier model have not tried to identify the defects which cause the permeation and have had to make numerous assumptions, hence their inability to accurately simulate these systems in all circumstances.

It was shown that the biggest degradation areas are a cumulative effect of many smaller defects rather than a few large ones, this is supported by both light microscopy and AFM finding the majority of defect sites are on the order of less than 2 μm, believed to be a result of the cleaning techniques applied during manufacturing which removes the largest contaminants.

Despite findings in existing literature, no linear relationship has been observed between defect size and permeation in this work. It is likely that the size of the extrinsic contaminant is not the factor which determines how severely the particle affects the barrier.

This chapter has also demonstrated that whilst the intrinsic textures can be highly detrimental to barrier quality, the use of planarisers greatly reduces this, effectively removing any intrinsic features thereby creating a very smooth surface for subsequent applications. The quality of planarised films has been demonstrated using WLI to be very high. Hence it is concluded that

intrinsic features are not responsible for the majority of barrier failures, supporting evidence from Chapter 6 that dust is the major cause. Film hygiene has been shown to be highly important for these materials. Taking two systems which utilise the same particle sizes but setting one to be intrinsic and the other as extrinsic, the latter has a much greater negative effect on barrier film performance. Dust has been shown to be even more damaging, likely to be a result of the large range of particle shapes and sizes.

Whilst existing work blames the shadowing effect, this is only applicable during one type of barrier deposition, DTFs barrier technique does not reproduce this effect. Findings from this chapter suggest that it is actually the contact area between the contaminant and surface which may be the most significant factor. This may reveal why some large defects do not cause barrier breaks as significant as some smaller contaminants; that is, they have a smaller total contact area.

Taking all the findings in this chapter, it was decided that creating a model system in which a range of known defects could be created on a film surface to test the theory of the contact area and its detrimental effect on barrier performance. The angle created by external contaminants was also though to play a part and so the creation of a model system to do this is discussed in detail in Chapter 8.

8. Modelling Film Defects

8.1 Introduction

Chapter 6 described the existing theories of defects in polymer films. It then showed results indicating that a new theory was required to explain the phenomena. This chapter develops a new model in an attempt to determine the effect of defect size on the barrier layer, making use of two methods for placing known standard defects on to films.

Indentation techniques were initially trialled to produce model defects of known dimensions, with the failure of this, standardised particles of known size were used to create defects. This was extended into a system where particles could be sunken into the film to known depths through extensive experimental work. The heights of these particles were confirmed using AFM and SEM with SEM-EDX applied to assure barrier covering of all particles.

8.2 Creation of a Model System

Evidence from Chapters 6 & 7 suggest that it is not simply the defect size which is the critical determining factor for the level of moisture permeation, but the area of the contaminant in contact with the film. As discussed in Chapter 7, the sputtering process effectively negates the shadowing effects reported elsewhere, however the actual contact area between the contaminant and film cannot be covered by barrier particles approaching from any angle and as such remain uncovered.

It is also true however, that intrinsic defects can cause disruption to the barrier layer as demonstrated in Chapter 7. Whilst they are often eliminated by the use of planariser, failure resulting from these is believed to be due to sharp edge angles and must also be understood, especially as intrinsic flaws examined thus far had relatively shallow edge angles. It is suspected that these may also play a key role in the effects observed with extrinsic defects, hence their effect was to be investigated.

8.3 Indenting

Whilst surveying calcium test defects on an industrial sample, it was found to be covered with a large number of very small pits, typically 100-300 nm across (Figure 8.1). Discussions with DTF researchers revealed that these features had been observed previously during SEM analysis and were a result of a manufacturing process. Despite their size and frequency, it transpired that these tiny pits had no noticeable effect on the barrier performance.

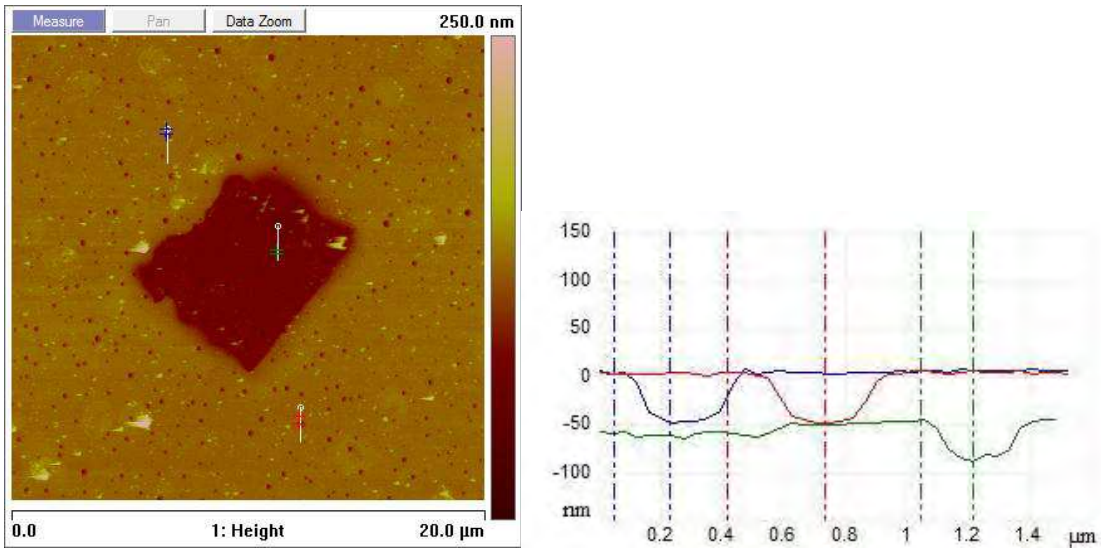

Figure 8.1 I: AFM topography scan of a defect on a section of planarised PEN with numerous sub-micron holes present (left) and cross sections of these flaws (right). Depths of features are 51.83 nm, 52.75 nm and 44.59 nm

It was hypothesised that if larger indents or more significant edge angles were created then an effect may become apparent. Having access to the AFM allowed for this line of enquiry to be pursued; specifically utilising the tool as a nano-indenter to create holes in the polymer surface. These additions can be created with a known edge angle ready for barrier coating. Performing indentations using a variety of AFM probes would allow the creation of pits with known edge gradients thus allowing the impact of specific angles on barrier coating to be investigated (Figure

8.2). Using the AFM to carry out the sample preparation also provides the means to image the area allowing visualisation and collection of exact dimensional data.

Figure 8.2: Schematic to show the creation of artificial pits in the surface of the polymer using a range of tips, note the increasing edge angle on each indent

It was found that the existing system with which the AFM was controlled was incapable of performing indentations due to limitations with the controlling computer and software. DTF were quick to rectify this through the purchase of a new computer system, however even with the new controller it rapidly became clear that the AFM was never designed to allow the kind of detailed indentations desired for this study. The realisation that the 'closed loop' piezo scanning head actually operated with an open loop in the Z-direction meant that any indenting required calibration for each surface to ensure that the correct amount of force was applied at each point, however even these were approximate at best.

Despite the hardware limitations, extended use of the indenter software revealed that it contained a number of bugs and flaws in the code which, after speaking with a Bruker applications scientist, revealed that which was first suspected; that the AFM was never meant to be used as a precise nano-indenter and the existing software was to create the functionality rather than allow precise measurements to be carried out (Armstrong, 2009).

8.3.1 Indenter Process Development

Regardless of these setbacks, work continued in an attempt to make the tool workable and the nano-indenter was brought into a useful state, whereby it could be used to create surface indentations of a required depth. The first attempts were carried out on gold, then polycarbonate, and ultimately moved on to PEN, however the work was not without further setbacks.

8.3.1.1 Double Indentations

The first issue arose during initial calibration indentations; whenever the machine was instructed to perform an indentation, it would perform the operation twice approximately in the same location (Figure 8.3).

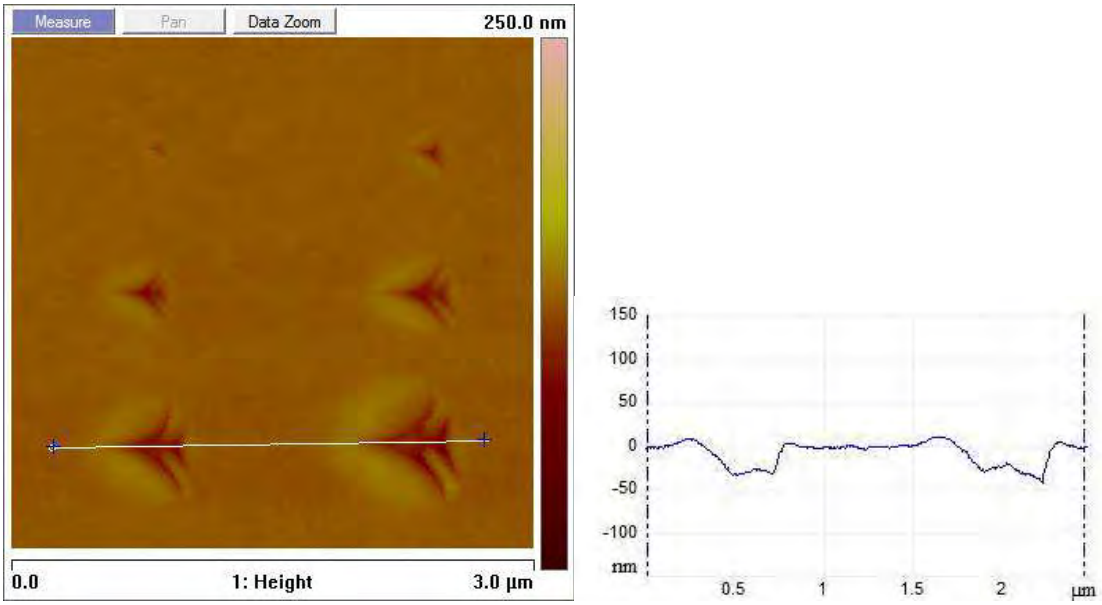

Figure 8.3: Unintentional double indentations created by the AFM during initial calibration

After speaking with one of the engineers at Bruker and confirmation of the machine settings, it was found that the fault was a result of the software, which was solved with a complete format of the machine followed by a fresh installation of the application.

8.3.1.2 Trenching

The next issue was noticed when carrying out particularly large indentations and scratches, whereby major 'trenching' was occurring, although this was expected, it needed to be eliminated. The effect is caused during nano-scratching, whereby the material which makes up the surface is pushed or pulled to the sides of the indentation, creating raised areas. This loose material creates unwanted surface peaks which can affect the permeation results (Figure 8.4).

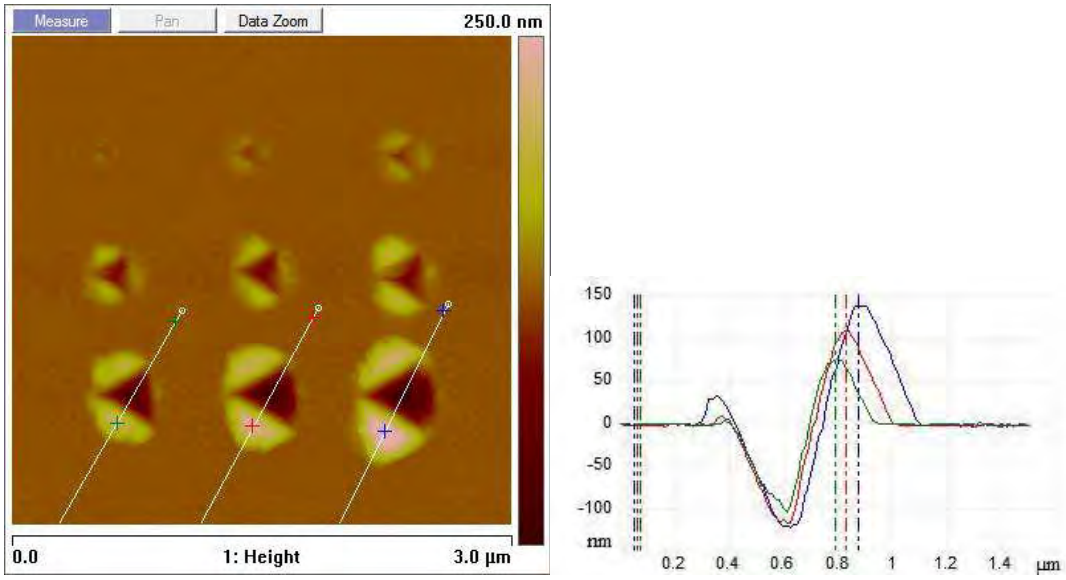

Figure 8.4: Example of the trenching effect on a gold substrate, chosen as an extreme case; sectioned indents are 121.5, 116.6 and 101.6 nm deep with corresponding peaks of 140.8, 111.1 and 75.5 nm

Attempts to carry out multiple small indentations in the same area was attempted, however similar problems as demonstrated in this section, were encountered. Reducing the depth of the defects to a minimum alleviated the issue to a degree, given that the edge angle was the main concern of the study it was felt that the depth of the flaw did not need to be particularly large and this workaround would be sufficient. While it is possible that the trenching effect could be analogous to scratches found on manufactured films, the extrinsic effect had already been considered, so measuring the edge angle of defects without the effects of protrusions was required.

8.3.1.3 Planariser Hardness

The process then moved on to the production material; displays grade planarised PEN, where the greatest problem so far was encountered. The planariser is coated on to the film surface not only to reduce surface roughness, but its physical properties also allow it to act as a protective hard coat. This coating proved to be too hard to indent using the AFM, beyond the maximum available force of the diamond-tipped probe (with a maximum cantilever spring constant of 300 N/m), it was not possible to mark the surface. The diamond tip was the hardest probe available, if it could not be used to indent on the surface then the relatively softer, higher aspect ratio silicon probes would certainly not work, however these probes were required to create the varied edge angles for this study. Despite this, even if a cantilever could be obtained which did not bend when driven into the surface of the sample, the angle at which the probe approaches the surface can cause the tip to slide before it indents.

8.3.1.3i Attempts on Standard PEN

As a result of the planariser hardness, the study proceeded on standard PEN; whilst it was possible to indent to a range of depths using probes with different edge angles and subsequently barrier coat them, the poor quality of the polymer surface meant that pinhole measurements could not be taken. The background permeation demonstrated in Chapter 6 was so great on the industrial grade film that it was not possible to distinguish the influence that individual indentations had on the overall permeation. Problems were further exacerbated by the poor calcium test results; the locations of the artificial defects could not be re-located and any attempts to use a non-calcium test based location method tended to affect the results of the calcium test.

8.3.1.3ii Application of a Standalone Indenter

As a result of these issues, discussions were opened with Agilent to investigate the use of a purpose built tool to create the required indentations in the surface. This machine was capable of indenting planarised PEN and was also able to quantify the modulus differences between that and the

uncoated material (Agilent, 2010) (Figure 8.5). However, carrying out this process required a great deal of handling and the resultant exposure to many non-clean environments introduced many extrinsic defects to the film surface. As a result, both the indented test and control samples which had been through all these handling processes failed rapidly, making conclusions impossible.

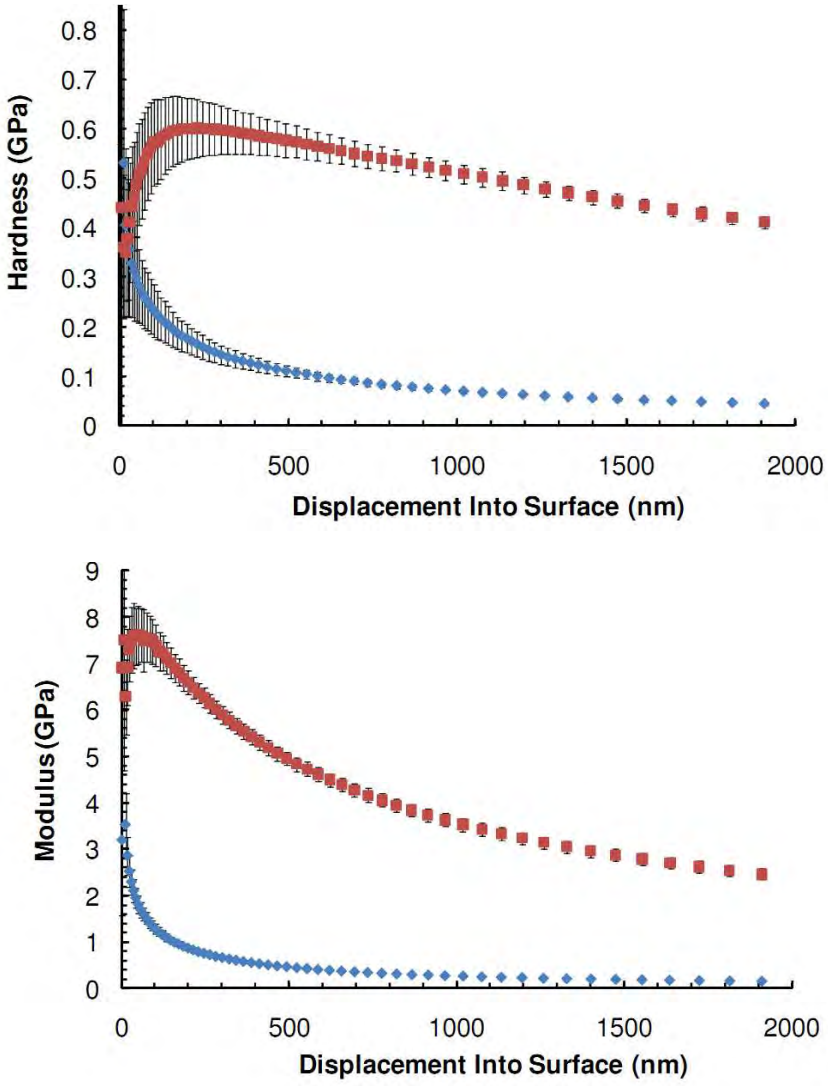

Figure 8.5: Agilient G200 indentation study demonstrating large differences in hardness (top) and modulus (bottom) for both Planarised (red) and raw PEN (blue) (Agilent, 2010)

It was decided that as this work required the application of a highly controllable technique to identify the differences in specific features of a known size, a new approach should be found.

8.4 Extrinsic Particles

From the limitations of the attempted indentation method, a new approach was sought; instead of creating intrinsic flaws, it was decided to apply extrinsic particles of a known diameter to the film and embed them into the surface. In theory this should allow for a wide degree of control over the particle depths and hence both the edge angle and contact areas for each particle size could be accurately controlled and tested (Figure 8.6). Whilst it was desirable to keep both variables isolated, embedding particles of different sizes to the same depths would allow the testing of different contact areas whilst maintaining the same edge angles allowing the two to be analysed individually.

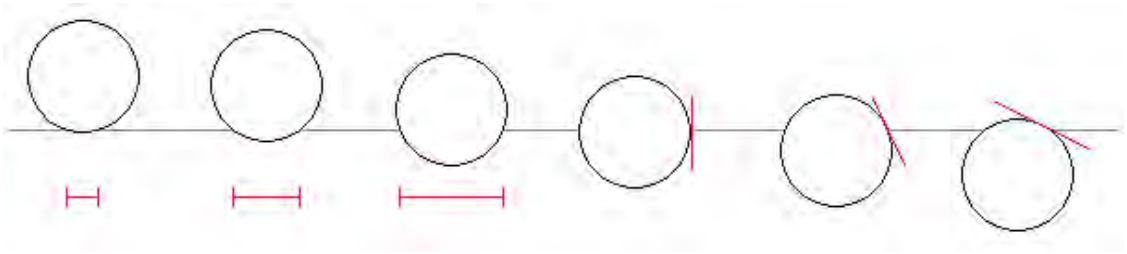

Figure 8.6: Schematic to illustrate the change in edge angle (red tangents) and particle footprint (red t-bars) at the particle-film interface with increasing particle depth

8.4.1 Particle Placement

The first stage of this process was to devise a reproducible method to prepare samples with which the particle depth could be precisely controlled.

8.4.1.1 Vacuum Particle Deposition

Initial attempts employed a vacuum deposition method to 'spray' a known mass of particles on to a discrete section of film; this involved placing the sample into a vacuum chamber then rapidly

introducing the silica particles via a valve. Custom glassware was produced and initial trials appeared promising (Figure 8.7), however the method was very messy, leaving vacuum sealant residues on the film surface and was incapable of the precise control needed for ultra-low concentration particle counts. Microscopy analysis also revealed that despite using high vacuum, the conditions were insufficient to break the inter-particle adhesion forces responsible for agglomeration (Figure 8.7).

Despite the initial success of this technique, during a later experimental trial, the failure of a vacuum seal caused irreparable damage to the customised glassware, signalling the end of this method.

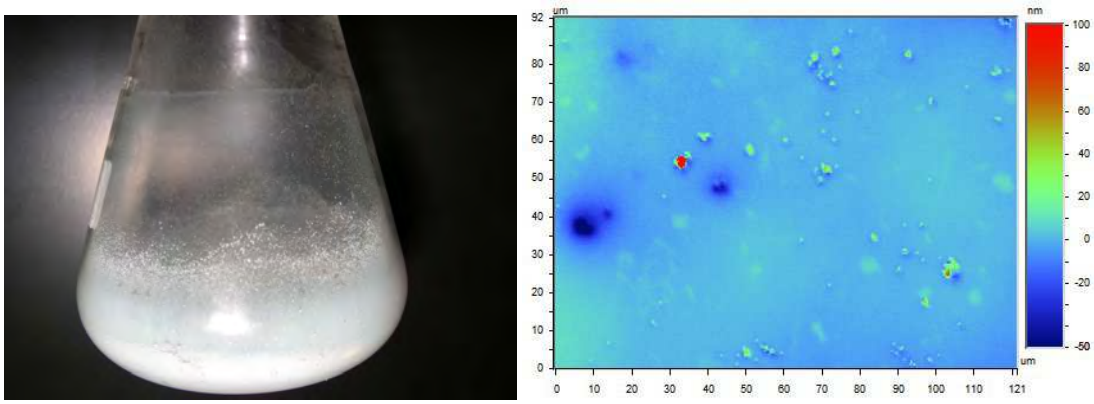

Figure 8.7: Example dispersion of vacuum deposition method inside flask (left) and WLI image showing agglomeration of particles deposited on to a film using this method (right)

8.4.1.2 Wet-coat Particle Deposition

Discussions with a coatings expert within DTF revealed a wet-coating method which had the potential to evenly deposit particles across a film surface in low concentrations (Robinson, 2009). With the addition of a suitable surfactant, as explained in Chapter 4, its reliability was tested on planarised PEN and demonstrated excellent uniform coverage of the silica particles (Figure 8.8).

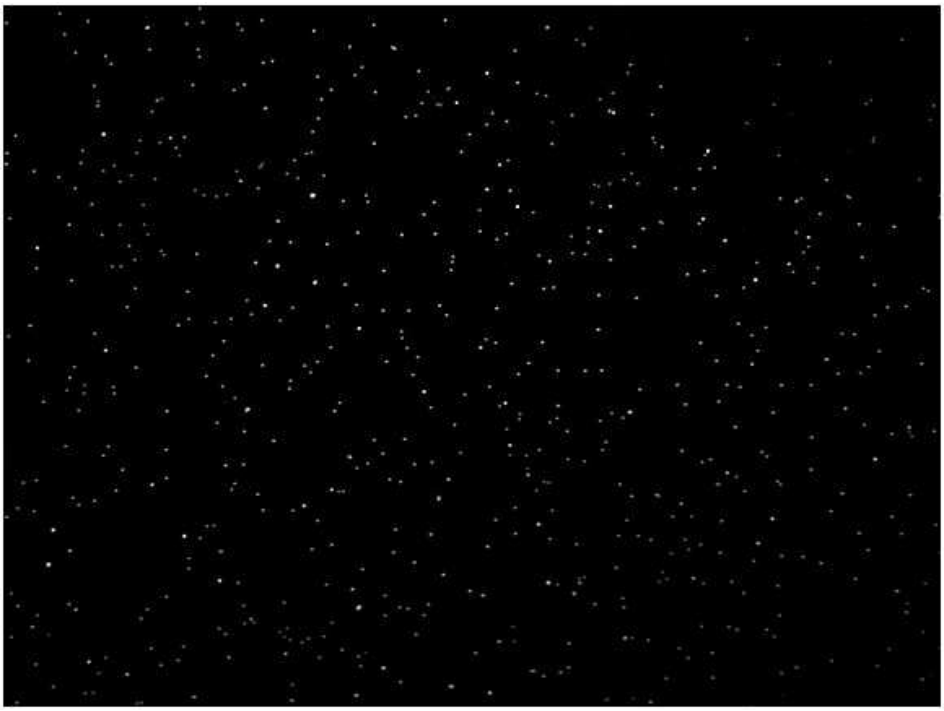

8.8 A: 200x cross polar optical microscopy image of a 0.001g solution of 0.5 µm silica particles

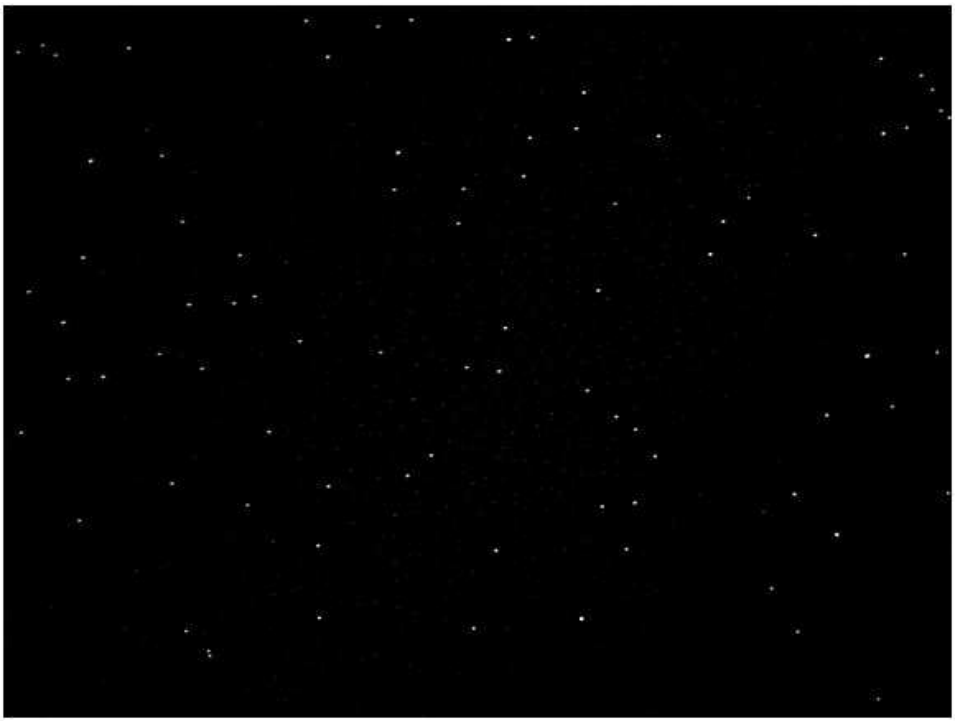

8.8 B: 200x cross polar optical microscopy image of a 0.0001g solution of 0.5 µm silica particles

8.8 C: 200x cross polar optical microscopy image of a 0.00001g solution of 0.5 µm silica particles

Figure 8.8: Three pictures showing dispersions of silica particleswet coated on to planarised PEN

Whilst a great deal of effort was required to create the required concentrations of the polymers, the technique was ideal for this study, even at low concentrations the particles could be evenly distributed across the film surface and hence, after further testing it was chosen as the preferred method for particle deposition.

8.4.2 Base Film Selection

With a technique to deposit particles on the film surface defined, a suitable material was required to allow these particles to be embedded, fortuitously DTF make a range of products which utilise a so called 'heatseal' coating, featuring a thermosetting polymer coating. This becomes soft when heated, polymerising and setting into a smooth, hard plastic surface when it cools.

8.4.2.1 Heatseal film 1

Initially, experiments were trialled on a 152 µm thick film with a 4 µm heatseal layer, chosen for its ease of handling. The first tests were carried out above 200 °C at exposure times of around 60 seconds, typical working conditions for this grade of film, to examine the performance of different Mayer bars. Interestingly, despite a range of temperatures from 200-240 °C, the particles were all enveloped to an average depth of around 70% of their total diameter (Figure 8.9). This was unexpected by researchers within DTF and is discussed in greater detail in Section 8.3.3. These initial temperatures were clearly too high but demonstrated the proof of concept that this system could be used to embed particles to different depths within the polymer surface.

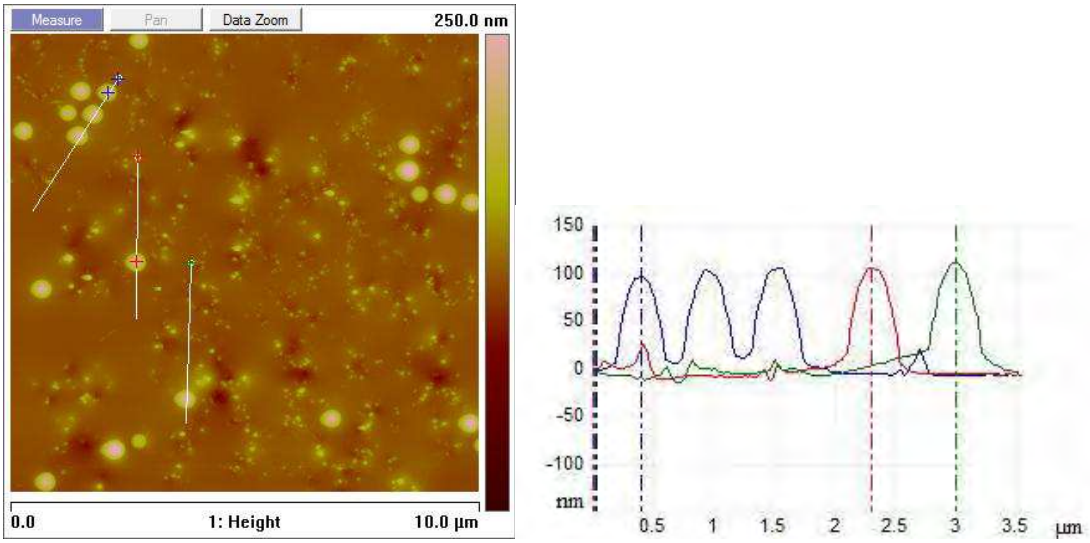

Figure 8.9: Example AFM topography image of 0.5 µm silica particles embedded into Core 1 with labelled cross sections (left) and a chart of these sections showing typical particle heights;98.81, 106.43 and 114.70 nm

Initial AFM results showed that whilst a good coverage of particles was achieved there was an issue cause by the prominent 'anti-block' surface coating added during production to prevent the polymer from adhering to itself during winding, but this additive also creates additional texture which could interfere with the barrier layer (Figures 8.10).

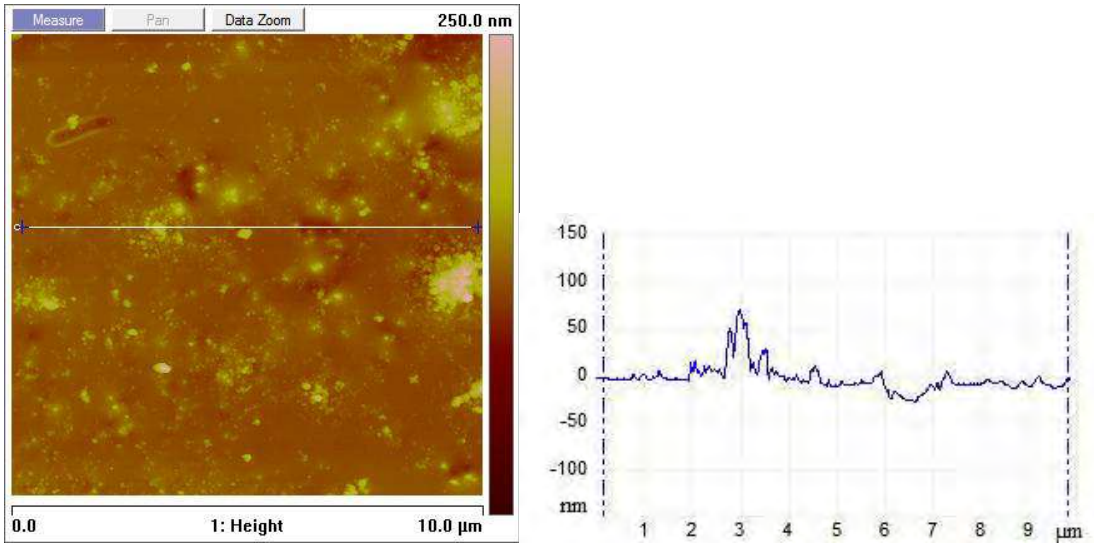

Figure 8.10: AFM topography image of a typical Heatseal Film 1 surface before heat treatment (left) and a cross section of this surface showing rough texture (right)

Original discussions with researchers in DTF suggested that these raised areas would be enveloped into the heatseal during the polymerisation stage, however this was clearly not the case. Despite this the early work revealed a great deal about particle concentration control which was carried through into the later stages.

8.4.2.2 Heatseal Film 2

Work was then moved on to a thinner 30 µm film also featuring a 4 µm heatseal layer. Whilst the film thickness was only 20% that of Heatseal Film 1 and hence more challenging to handle, it provided a smooth surface to work with (Figure 8.11). Multiple samples were produced using a 1% by weight 0.5 µm silica particle system of set concentrations, temperature and residence times to determine where the best working conditions lay. These films were then analysed using AFM, multiple areas were examined and the average heights of the silica particles were measured and recorded.

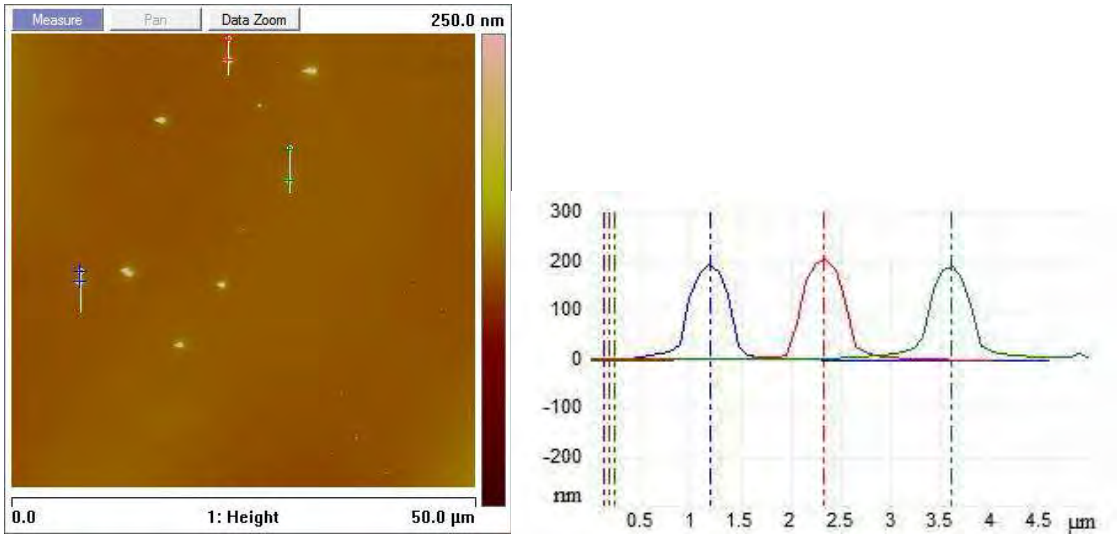

Figure 8.11: AFM topography image of 850 with embedded 0.5 µm silica particles (left) and corresponding height cross sections for three labelled particles; 193.6, 207.9 and 189.8 nm

8.4.3 Particle Depth Calibration

A series of samples of Heatseal Film 2 were produced at different temperatures between 70 - 170 °C with 10 °C increments using 1 wt.% 0.5 µm silica particles and a 20s residence time (Figure 8.12).

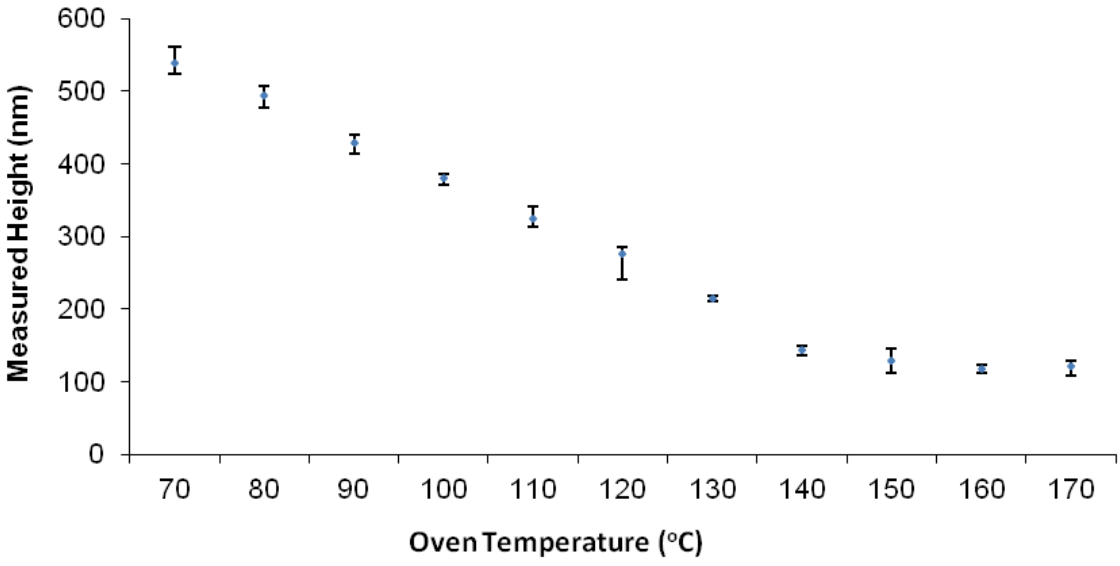

Figure 8.12: Average height of exposed particles set in heatseal after exposure to multiple temperatures

It is worth noting that whilst average particle heights appear large compared with manufacturer's specified diameter of 500 nm, the actual average particle size is in fact larger. The data sheet supplied with the material states an average diameter of around 540 nm, in house measurements using light scattering confirmed this figure and is presented in Appendix B.

These results showed that for the 0.5 μm particle system, the upper temperature limit observed with Heatseal Film 1, above which particle depth remains unchanged actually starts from 140 °C. It is postulated that the process is kinetically limited upto 140 °C. As all Heatseal Film 1 samples were prepared above 200 °C this explains why all particles depths were the same in the first set of experiments. It is believed that the effect observed where the particle heights remain constant above certain temperature is one of dynamic wetting. If more time were available, the experiment could be repeated using a variety of particles including glass, metals and other inorganic particles. As the silica system was required for the main experimental study and was operating as desired, no further work was carried out in this area within the scope of this thesis.

8.4.3.1 Confimation using SEM

The depth of the silica particles was also confirmed using SEM (Figure 8.13), the suggestion of a wetting effect can be seen clearly in the 60 °C and 80 °C images where a surface tension like effect associated with water, can be seen between the heatseal and particles.

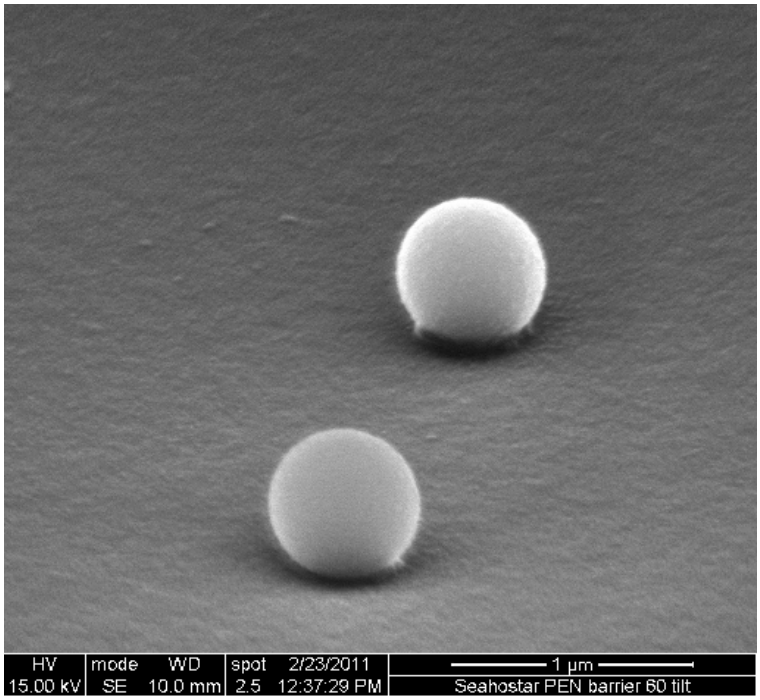

8.13 A: SEM image of 0.5 µm particles on healtseal film heated at 60 °C for 60 seconds

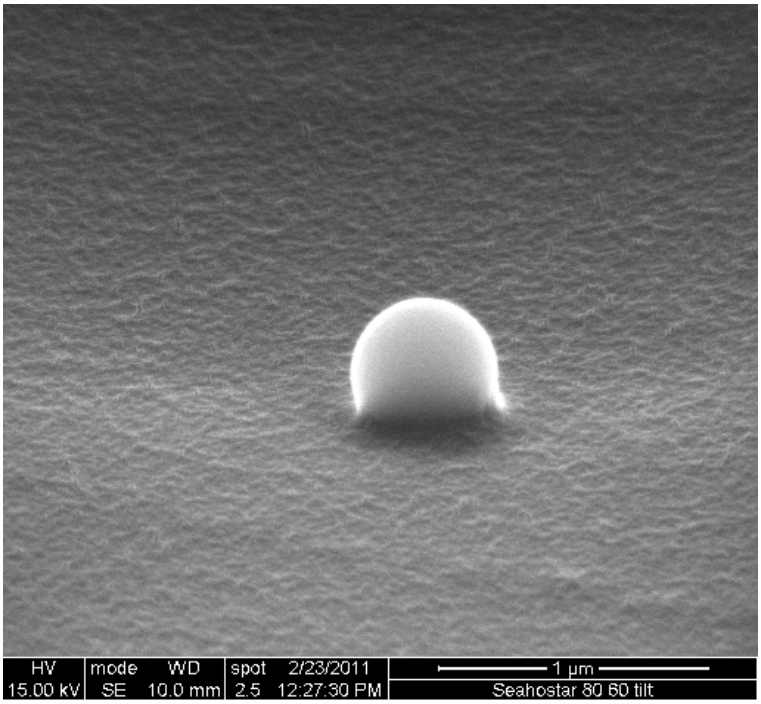

8.13 B: SEM image of a 0.5 µm particle on healtseal film heated at 80 °C for 60 seconds

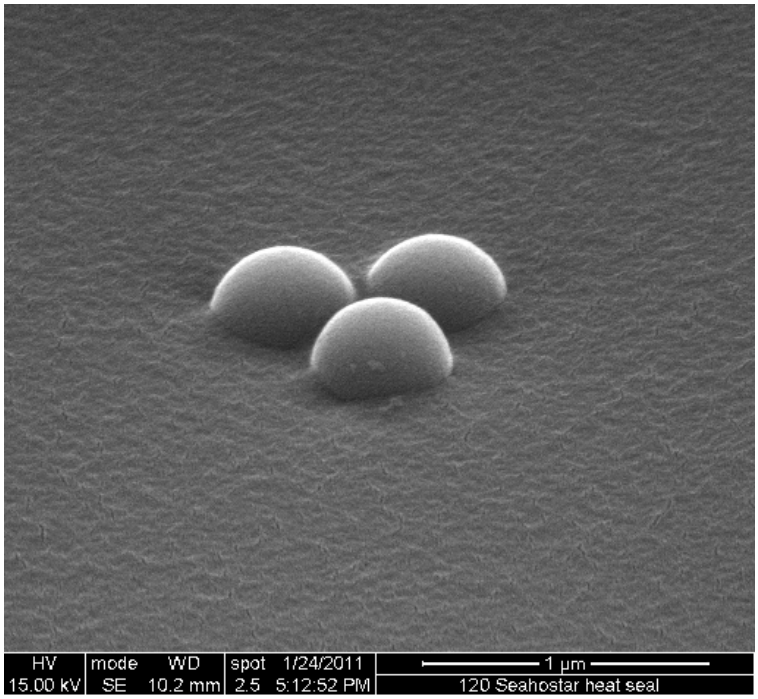

8.13 C: SEM image of 0.5 µm particles on healtseal film heated at 120 °C for 60 seconds

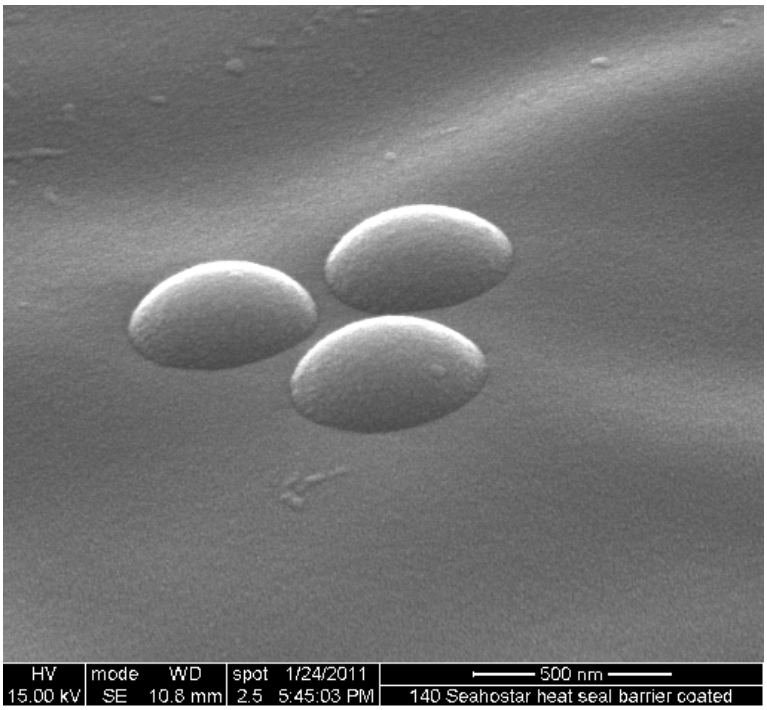

8.13 D: SEM image of 0.5 µm particles on healtseal film heated at 140 °C for 60 seconds

Figure 8.13: Four images showing the particles depths after heating at different temperatures

8.4.3.2 Confirmation Using AFM

The experiments were repeated for 0.1 and 0.3 µm silica particles (Figure 8.14), the results of which were comparable to those seen during the 0.5 µm series. This shows that the degree to which a particle protrudes from the surface remains the same at set conditions, regardless of particle size.

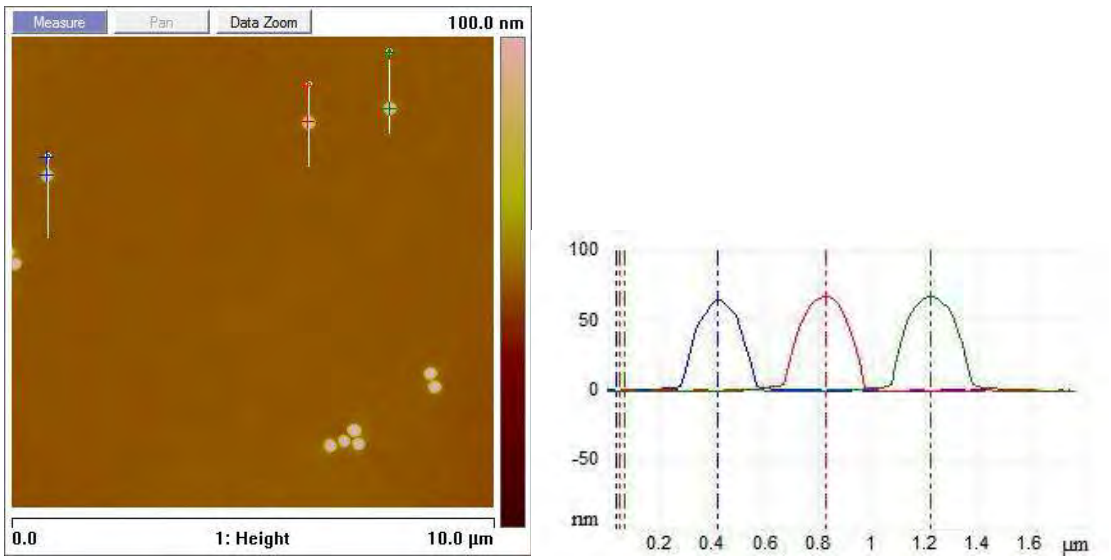

8.14 A: AFM topography image of 0.3 µm silica particles (left) and corresponding height cross sections for three labelled particles; 64.7, 67.5 and 66.8 nm. Sample was heated to 160 °C for 30 seconds

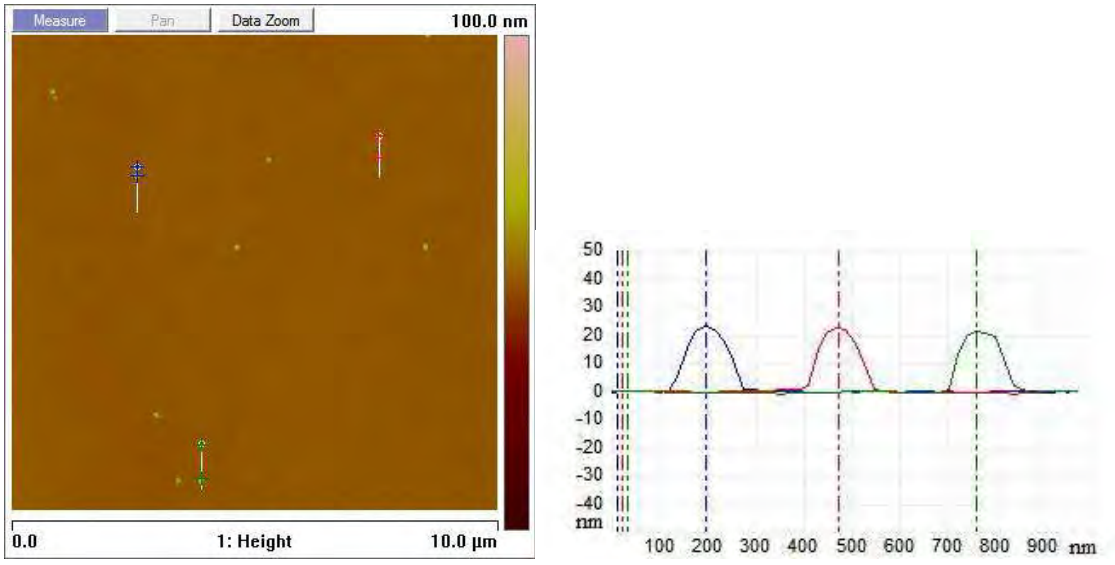

8.14 B: AFM topography image of 0.1 µm silica particles (left) and corresponding height cross sections for three labelled particles; 23.1, 22.6 and 21.5 nm. Sample was heated to 160 °C for 30 seconds

Figure 8.14: Two pictures showing AFM measurements of embedded silica particles on Heatseal Film 2

Comparing data for 0.1, 0.3 and 0.5 μm silica particles, we can see the percentages to which each particle size sinks and is comparable in every case (Figure 8.15).

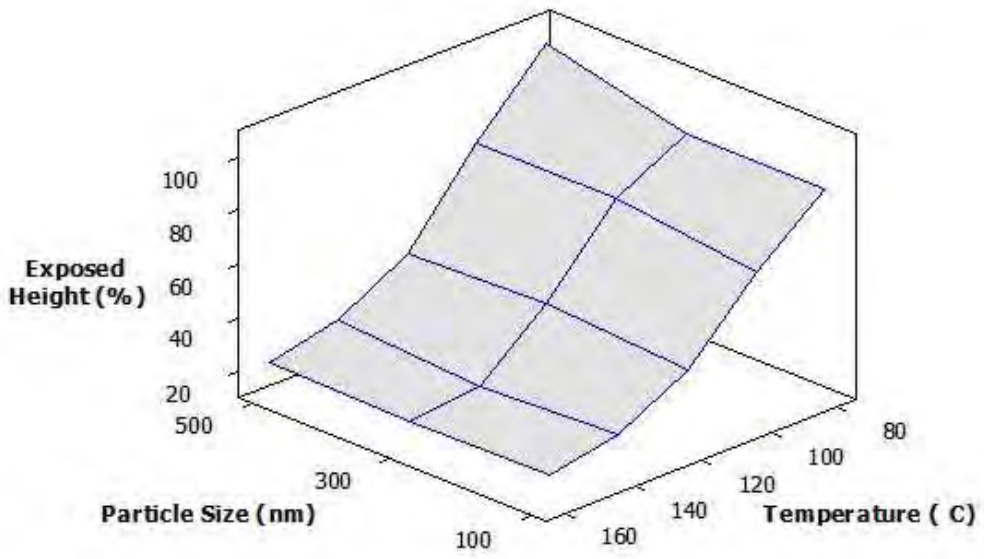

Figure 8.15: Three dimensional surface plot showing the relationship between the exposed height of a particle (expressed as a percentage of its total diameter) compared to oven temperature and particle size

8.4.3.3 Experimental Calibration

Knowing that particle depth was independent of size meant that protrusion heights determined for one set of particles could be applied to all. Further work was carried out to test the effect of different residence times at various temperatures using the 0.5 μm system. Whilst this work was very time consuming it allowed a three dimensional plot of these factors to be drawn, using which a desired particle protrusion height could be chosen and the required preparation parameters could be read (Figure 8.16).

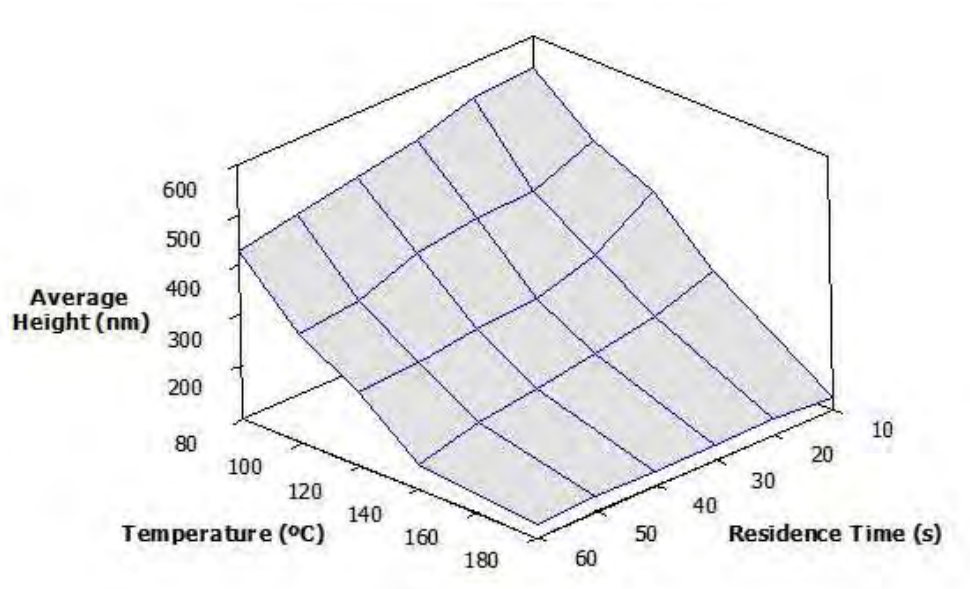

Figure 8.16: Three dimensional surface plot, demonstrating the dependence of temperature and oven residence time on particle depth

8.4.3.4 Occurrence in Industrial Work

During analysis work carried out for one of DTFs senior researchers on another heatseal film exhibited similar results. The researcher wished to know the effect that different heatseal layer thicknesses (1.0, 2.2 and 4.8 µm) would have on the eventual heights at which 1 µm silica particles would protrude from the film; the results mirror those observed above. All particles sank to around 70% of their total diameter regardless of heatseal thickness and heating conditions (Figure 8.17).

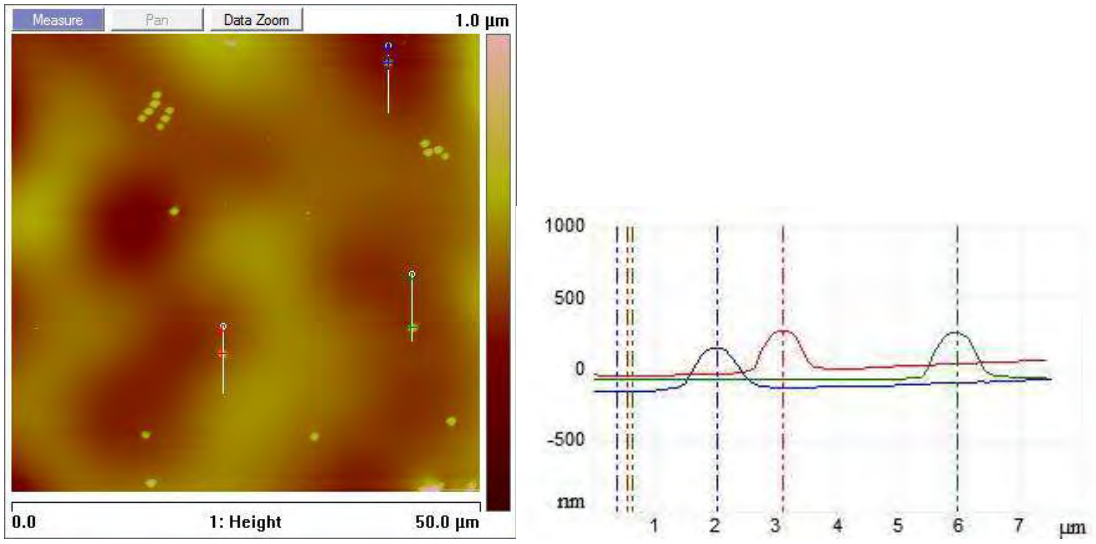

8.17 A: AFM topography image of 1 µm silica particles embedded in a 1.1 µm heatseal layer (left) and corresponding height cros sections for the three labelled particles; 310.7, 315.0 and 326.2 nm

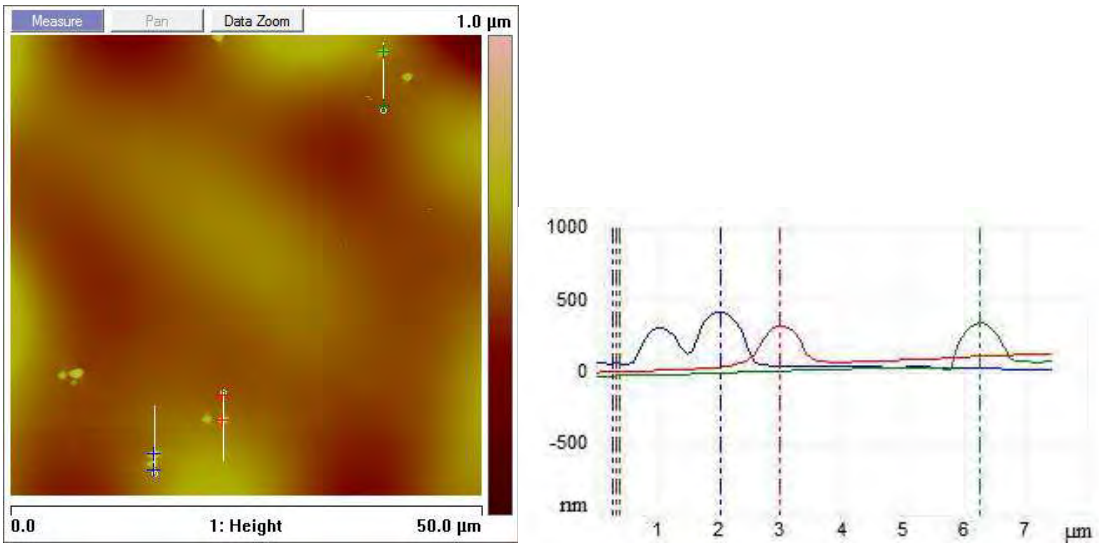

8.17 B: AFM topography image of 1 µm silica particles embedded in a 2.2 µm heatseal layer (left) and corresponding height cros sections for the three labelled particles; 319.0, 321.6 and 312.7 nm

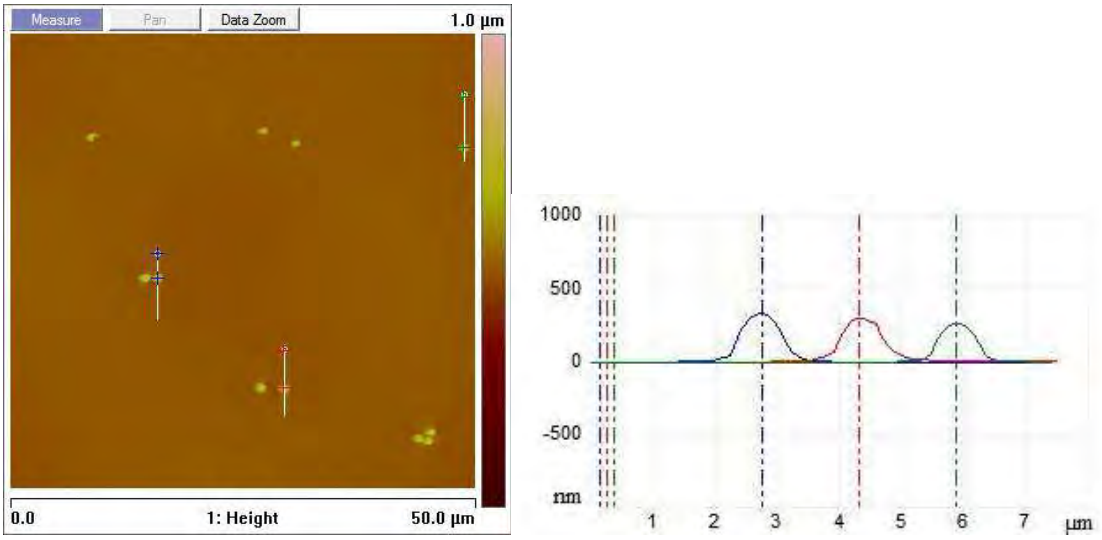

8.17 C: AFM topography image of 1 µm silica particles embedded in a 4.8 µm heatseal layer (left) and corresponding height cross sections for the three labelled particles; 332.3, 319.4 and 288.9 nm

Figure 8.17: Three pictures showing AFM results of silica particle heights embedded in a development heatseal film

8.5 Calcium Testing Model Systems

At this point the particle system was well understood and could be controlled to produce samples of heatseal film with particles sunk to precise depths. Model samples were produced using 0.1, 0.3 & 0.5 µm silica particles which were sunk to 25 and 75 % of their diameters into the heatseal film, these were then barrier coated and calcium tested to examine the effects on barrier performance. It is expected that when sunken to 25 %, the particles will have a sufficiently steep edge angle and an overhang large enough to hinder the sputtering process and giving a large contact area, whereas at 75 % depth there would be no opportunity for shadowing and the edge angle would be very gradual.

It was believed that both the 0.3 and 0.5 µm silica particles would cause significant disruptions to the barrier when only 25% sunken and much less impact at 75 %, but given the size of the 0.1 µm particles, it was thought that even at 25% of their depth they would still receive an adequate coating of aluminium oxide to produce a reasonable barrier. The results were proved similar to the

theory (Figure 8.18), however the 0.1 µm silica particles also affected the barrier in the same manner as the larger particles. It is worth noting that in all images, the particularly large white areas on the results for 75 % depths are a result of poor adhesion between the film and glass. If permeation was only a factor of the contact area between the contaminant and film, both sets of results would be similar, however this is not the case.

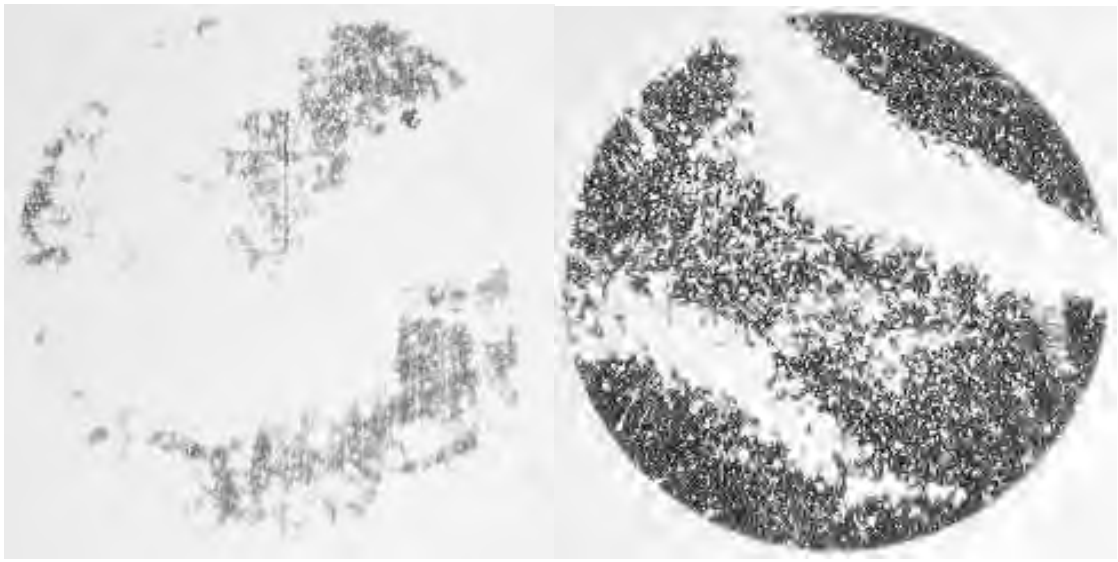

8.18 A: 0.1 µm silica sunken to depths of 25 % (left) and 75 % (right) of their total diameters

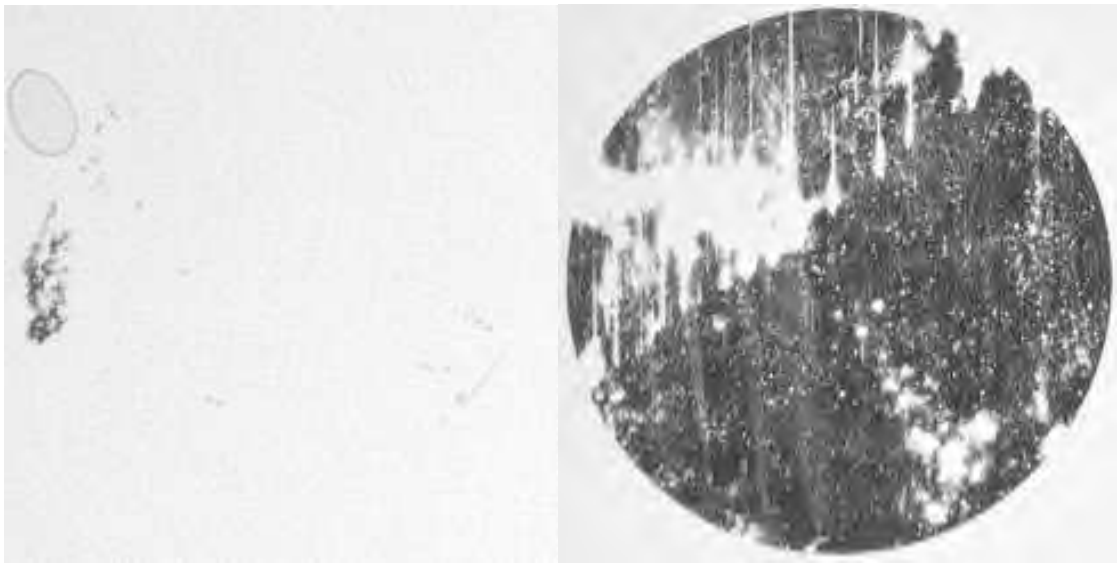

8.18 B: 0.3 µm silica sunken to depths of 25 % (left) and 75 % (right) of their total diameters

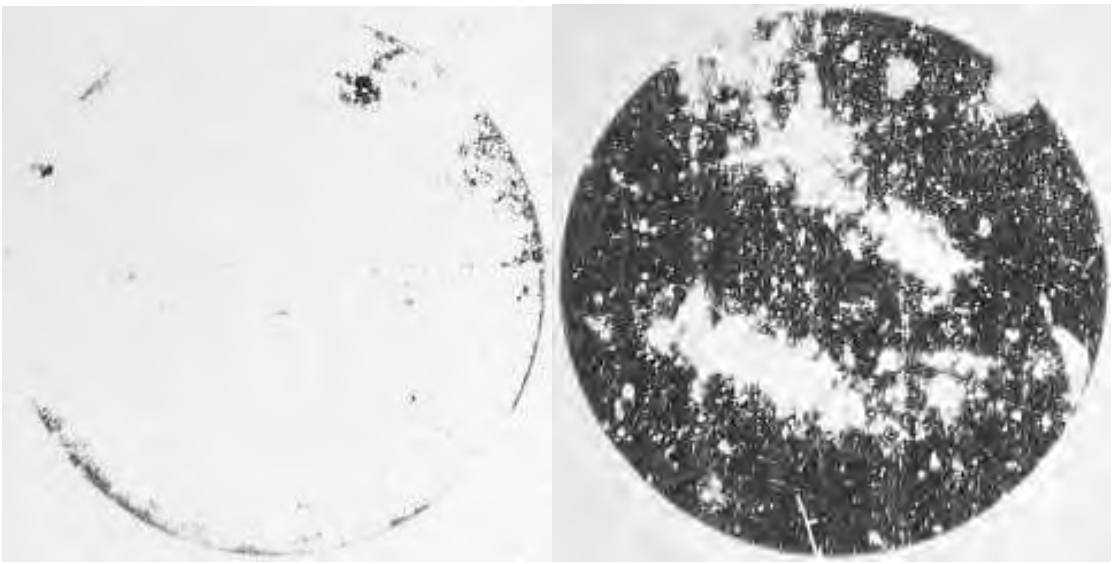

8.18 C: 0.5 µm silica sunken to depths of 25 % (left) and 75 % (right) of their total diameters

Figure 8.18: Three pictures showing calcium test results after 336 hours for silica particles sunken to different depths on heatseal film

8.5.1 Additional Particle Sizes and Depths

These results were extended to include a wider size range of particles to a greater range of depths including 0, 25 & 75 percent of their diameters, whilst not as striking, the results agree with those in (Figure 8.18). The samples which were heated to the lowest temperatures and hence with particles protruding further from the surface displayed more rapid calcium degradation and hence higher permeability (Figure 8.19).

8.19 A: 0.1 µm silica sunken to depths of 25 % (left), 50 % (centre) and 75 % (right) of their total diameters

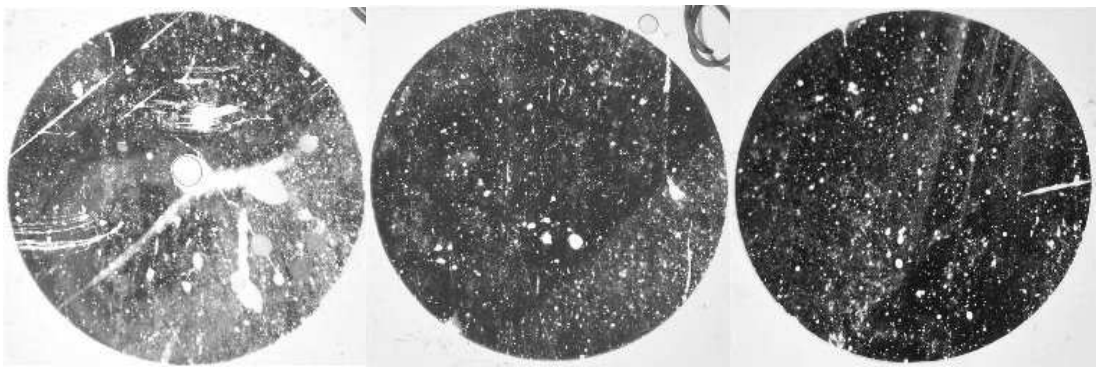

8.19 B: 0.5 µm silica sunken to depths of 25 % (left), 50 % (centre) and 75 % (right) of their total diameters

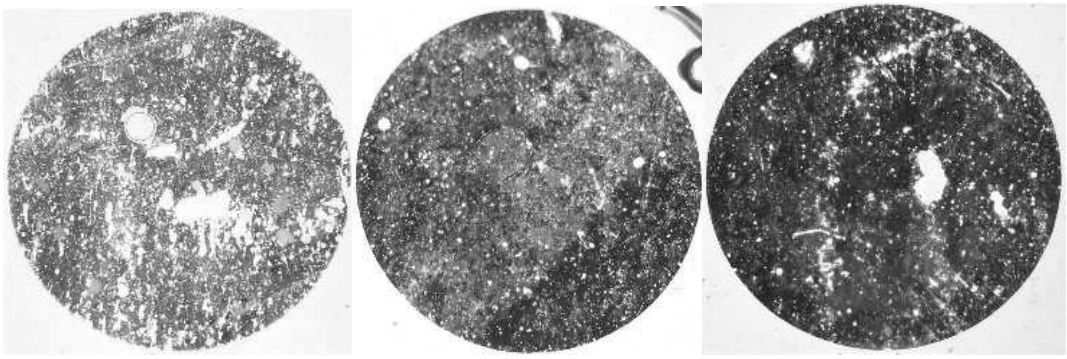

8.19 C: 2.5 µm silica sunken to depths of 25 % (left), 50 % (centre) and 75 % (right) of their total diameters

Figure 8.19: Three pictures showing calcium test results after 168 hours for silica particles sunken to different depths on heatseal film

It was not possible to age the samples in Figure 8.19 for as long as those in Figure 8.18, this is due to the removal of the testing equipment, ideally the samples would have been aged for the same

amount of time. Further testing on these systems would also have been preferred to examine the permeation as a function of pinhole size and particle depth on a per-defect basis.

8.5.2 SEM-EDX Analysis of Barrier Layer

The predications for these films were as expected, however there were concerns that the 0.1 µm silica particles may have been removed from the surface during the lower temperature tests, hence the similar results between samples, however SEM analysis revealed that this was not the case (Figure 8.20).

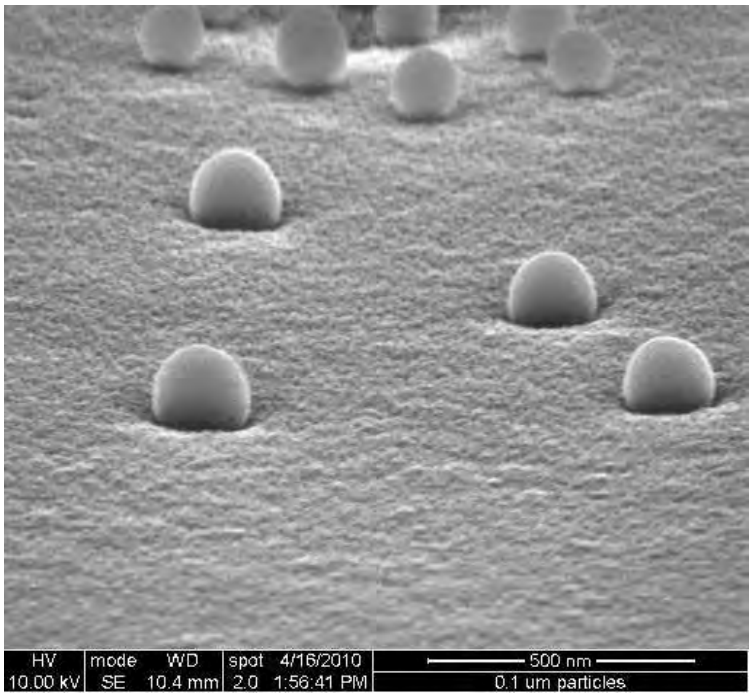

Figure 8.20: SEM Image of barrier coated 0.1 µm particles heated to 80 °C on heatseal film

The appearance of the silica was unexpected, it was assumed that the 0.1 µm particles would be buried under the barrier layer, however the SEM clearly shows this is not the case, in fact it appears that each particle has a complete uniform coating over its entirety. The size of each particle certainly appears to be larger compared to the scale bar on the SEM and the particles were held in

place relatively strongly, evidenced by the inability of the SEM electron stream to move them, a procedure which is easily possible when examining the non-barrier coated particles. It is worth noting that the scale bar on the SEM images are approximate and although attempted, AFM analysis was not possible on these smaller particles as the probe has the effect of removing them from the surface, making them especially difficult to image.

SEM-EDX was performed on the particles imaged in Figure 8.13, to compare the levels of aluminium (Figure 8.21). As one might expect the same elements are present in both scans, using a low beam acceleration voltage so that only the upper layers are examined, only aluminium and the polymer can be detected on the reference, whereas on the particle itself a large amount of silica is visible. It is possible that the steep edges of the particle are increasing the silicon counts, especially as the difference between the aluminium peaks is very small.

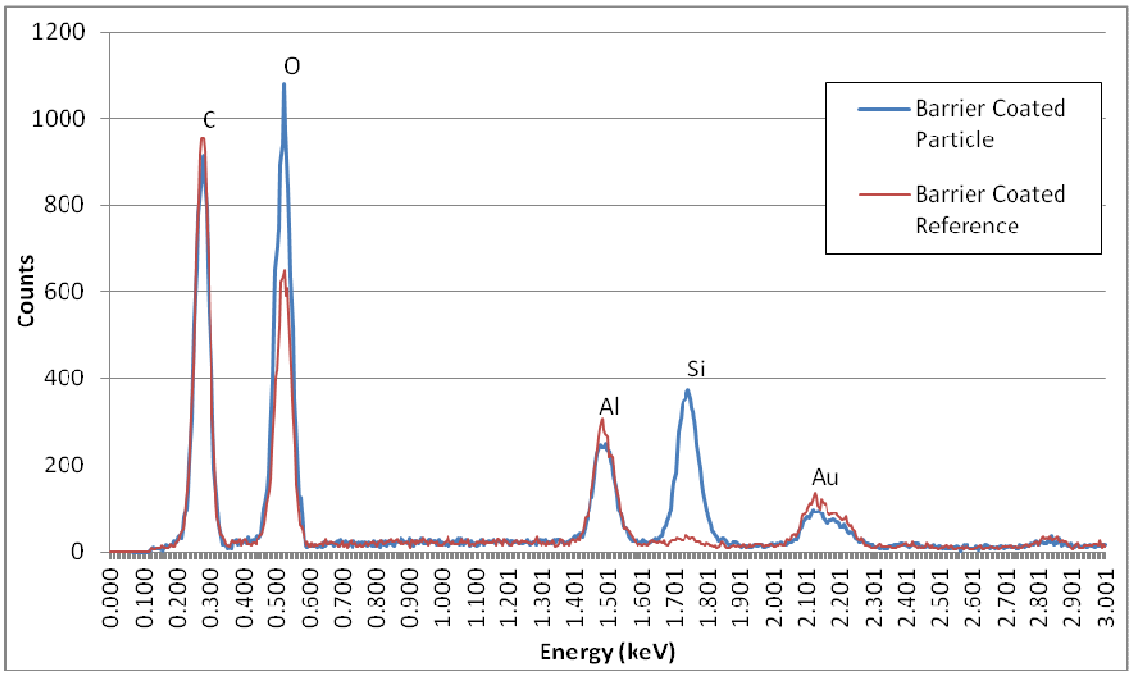

Figure 8.21: SEM-EDX of the surface of a barrier coated silica particle and reference area

8.5.3 SEM-EDX Study of Particle Depths around Particles

Using SEM-EDX we can obtain information for the relative amounts of material in different locations, it was predicted that the areas close to the base of particles which were only slightly submerged in the heatseal layer would have a lesser coating of barrier, although it would still be present. Measuring the counts associated with aluminium from an exposed area of film gives a strong Al-response (Figure 8.22, Purple Line), comparing this to the counts detected on top of any additional silica particles (Figure 8.22, Green Line) indicating that all exposed areas receive an even coating of aluminium oxide. Measuring the response close to the base of a particle (Figure 8.22, Red Line) still gives comparable counts to the reference, again indicating a uniform barrier. When SEM-EDX is performed in the particle shadowing area (Figure 8.22, Blue Line) reduced aluminium counts are observed which further decrease as we focus the EDX beam closer to the base of the particle.

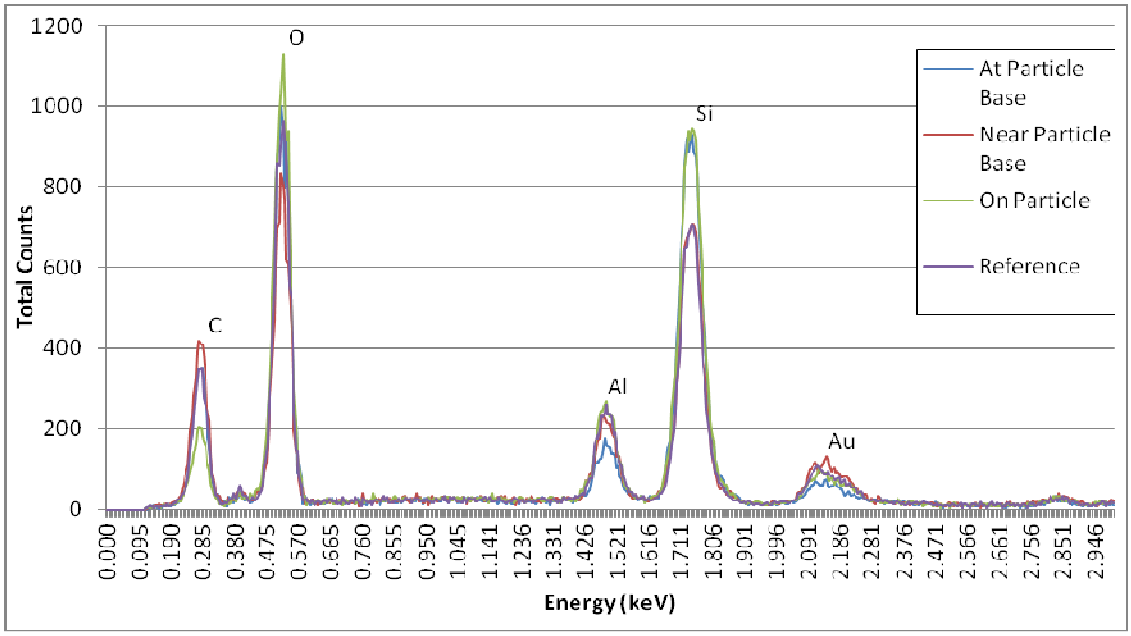

Figure 8.22: SEM-EDX data taken at different areas around a barrier coated silica particle

The results of the experiments in this chapter suggest a regime whereby it is believed that the path of water travels through the edge of the footprint region and around the contaminant particle

where it can escape through thinner areas of barrier (Figure 8.23). When a particle is set more deeply into a film there is a more complete barrier coating, hence the better performance.

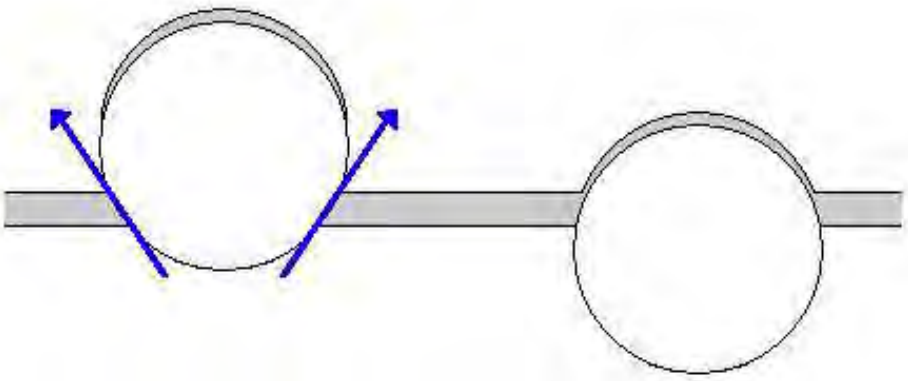

Figure 8.23: Schematic to show the permeation of water (blue arrows) through particles set at 25% of their total diameter (left) and the light barrier coating which prevents this in those set to 75% (right)

It is now believed that the contact area and edge angle both play a role in determining the degree of significance that a contaminant will have on barrier layer disruption. If a large intrinsic defect with gentle edge angles exists, although it effectively has a very large footprint the gentle edge angles mean it will receive a complete barrier covering. A small defect with sharp edge angles is most likely to disrupt the barrier, however having a small footprint usually means a small defect, and is sufficiently covered by the barrier layer or allows such a small quantity of water though that its contribution is dwarfed by other defects. A large defect which has a small contact area will result in a barrier break, but not as severe as one may expect, as the incident barrier coating is capable of getting under the defect overhang, making effective defect smaller. It is only with the combination of a relatively large contaminant with steep sides where the most significant damage occurs.

8.6 Conclusions

In this chapter a new model to explain the behaviour of defects in thin barrier films has been developed. By introducing flaws of known dimensions then observing their effects, it was possible to draw new conclusions about defect properties. Indentation was trialled for this application but ultimately the introduction of controlled particles was a better method. A wet coating method produced a good dispersion of particles which could be sunken to known depths, confirmed using AFM and SEM. Calcium testing of these samples showed that when they were protruding out of the surface by a large degree, barrier performance was poor, but as they were set to greater depths barrier performance improved. SEM data confirmed that particles were coated with aluminium layer, although not as thick as was expected with the barrier coating being thinner towards the base of particles and on the particle surfaces.

It is now believed that the contact area and edge angle both play a role in determining the degree of significance that a contaminant will have on barrier layer disruption rather than the particle size. If a large intrinsic defect with gradual edge angles is present on the surface, despite the large footprint, it will still receive a complete barrier covering and cause little disruption to the barrier. A small defect with sharp edge angles is capable of disrupting the barrier assuming it is of a height greater than the barrier depth, however the small footprint of these would mean that such a small quantity of water passes that its contribution to permeation is dwarfed by other defects. A large defect which has a small contact area will result in a barrier break, but not as severe as one may expect, as the incident barrier coating is capable of reaching under the defect overhang, making the contact area smaller. It was the combination of a relatively large contaminant with steep sides where the most significant damage occurred.

9. Final Conclusions and Future Work

This thesis set out to review the literature on film defects, identify and determine the source of these, characterise their features to establish the reasons for damage and model the results. This suggests future work which should allow the elimination of such defects from the production process.

9.1

In Chapter 3 it was determined that there was little existing work in the published literature in this field and that which did exist was not particularly detailed. While dust was assumed to be the reason for failures by some, other disagreed and no work existed to explicitly prove either case. Though there are likely to be multiple permeation mechanisms, the permeation of water though large pinholes was deemed to be the most significant.

9.2

A significant advance was the development of large scale AFM stitching to show that film defects could be mapped by AFM over large film areas. This technique was capable of extending the field of view of the instrument making it capable of analysing large areas like WLI, but with the detail afforded by AFM. No such application of the AFM has been attempted before without specialist modifications. The technique is currently being developed by the equipment manufacturer into a method to be integrated into their instruments. It also became used in DTF analysis studies, especially for new product development.

9.3

The calcium test was developed from a simple permeation technique into a reliable method to direct the application of AFM, allowing pinholes to be identified instantly without the need for a complete surface appraisal. With the addition of SEM, it was determined that these extrinsic contaminants were present before the barrier coating process and were mostly comprised of typical airborne dust.

9·4

A more rigorous AFM study of these defects showed that, permeation did not scale with defect size. The effect of intrinsic features was also examined and it was demonstrated that while they can contribute to permeation, the effect of extrinsic defects was far greater and more likely to be the cause of failure in DTF barrier films. Differences in barrier deposition techniques were noticed and the theory that the defect footprint was the major cause of failure rather than size alone was the major issue.

9·5

A model was then developed to account theoretically for the experimental results. Attempts to use the AFM as an indenter to make standard defects proved to be of limited success. Inserting known particles to act as artificial defects proved to be both more accurate and successful. Through the application of the calcium test to this system, it was demonstrated that the contact area between a defect and the surface does appear to produce a linear relationship with regards to permeation. Ultimately it was concluded that a large intrinsic defect with gradual edge angles will still receive a complete barrier covering and cause little disruption to the barrier. A small defect with sharp edge angles only has a small footprint and has a very small contribution to the overall permeation. A large defect which has a small contact area will result in a barrier break, but not as severe as one may expect. The combination of a large contaminant with steep sides was the most destructive kind of film defect for water permeation.

Potential Future Work

The main focus of any future work would be to eliminate defects from the production process. It has been demonstrated in this study that failures which exist on flexible OLED displays are a result of pinholes in the protective barrier layers, caused by airborne dust. This dust is present on the surface of the polymer before the application of the protective layer and has been shown to be capable of perforating the barrier. As the composition and size of the contaminants are now known, work to eliminate these from the production process can now be employed with the goal of removing them completely from the production process and allowing DTF to produce displays grade films with the required quality to allow OLED devices to be produced with long lifetimes.

The AFM stitching technique has also gathered a great deal of interest from the equipment manufacturer who are currently looking to extend the method into an analysis method for their instruments. This has already been introduced into DTF's research activities and with work from the manufacturer will see widespread application.

Application of non-silica particles to the model would have been interesting to determine whether the same sinking behaviour occurs with particles of a different composition. Furthermore, replacing the silica with non-spherical particles would have been very interesting to examine both their behaviour in the heat-seal film and their effect on the barrier performance. It would have also been preferable to carry out more calcium tests in Chapter 8, due to time constraints this was not possible during the timescale of this study. Such information would allow detailed mathematical modelling to be carried out.

References

(Agilent, 2010) Agilent Technologies Document, Issued for Joseph Bottomley "MECHANICAL CHARACTERIZATION OF TWO POLYMER FILM SURFACES", *Agilent Technologies*, 2010

(Aldrich, 2007) "Material Matters, Chemistry Driving Performance – Organic Electronics", Volume 2, Number 3, 2007

(Aquatran 2006) MOCON, Inc. Aquatran Data Sheet "High Sensitivity Coulometric Water Vapour Transmission Rate Test System – AQUATRAN Model 1" 2006

(Adam, 2007) R. Adam, W. A. MacDonald, M. K. Looney, R. Eveson, C. Thomson, R. Kelly, L. Allen, S. Louch, "The Calcium Test as a Tool for Water-vapor Barrier Evaluation of Flexible Barrier Substrates", *Proceedings of Asia Display*, Volume 1, 33-6, p.894-898 (2007)

(Armstrong, 2009) Discussions with Veeco Metrology Applications Engineer, Ian Armstrong, 2009

(Armstrong, 2011) Discussions with Veeco Metrology Applications Engineer, Ian Armstrong, 2011

(Aziz, 1996) H. Aziz, G. Xu, "A degradation mechanism of organic light-emitting devices", *Synthetic Metals*, Volume 80, Issue 1, p.7-10, 1996

(Aziz, 1998 a) H. Aziz, Z. Popovic, C. P. Tripp, N-X. Hu, A-M. Hor, G. Xu, "Degradation processes at the cathode/organic interface in organic light emitting devices with Mg:Ag cathodes", *Appl. Phys. Lett.*, 72, p.2642, 1998

(Aziz, 1998 b) H. Aziz, Z. Popovic, S. Xie, A-M. Hor, N-X. Hu, C. Tripp, G. Xu, "Humidity-induced crystallization of tris (8-hydroxyquinoline) aluminum layers in organic light-emitting devices", *Appl. Phys. Lett.*, 72, p.756, 1998

(Aziz, 2004) H. Aziz, Z. Popovic "Degradation Phenomena in Small-Molecule Organic Light-Emitting Devices", *Chemistry of Materials*, 16, 23, p.4522-4532, 2004

(Barrer, 1941) R. M. Barrer, "Diffusion In and Through Solids." *New York: Cambridge University Press*, 1941

(Bergh, 1972) A. A. Bergh, P. J. Dean, "Light-Emitting Diodes" *Proceedings of IEEE*, 60, 156, 1972

(Berntsen, 1998) A.J.M. Berntsen, P. van de Weijer, Y. Croonen, C.T.H.F. Liedenbaum, J.J.M. Vleggaar, "Stability of polymer light-emitting diodes", *Philips Journal of Research*, Volume 51, Issue 4, p.511-525, 1998

(Bobst, 2012) Information access from "http://www.bobst.com/uken/products/vacuum-coating-metallizing/vacuum-coaters/overview/machine/general-optilab/", 2012

(Bouten, 2002) P. C. P. Bouten, G. Nisato, P. J. Slikkerveer, H. F. J. J. Van Tongeren, E. I. Haskal, P. Van Der Sluis, "Method for measuring a permeation rate, a test and an apparatus for measuring and testing", *United States patent application* 0152800 A1, 24th October 2002

(Bruker, 2011) "Dimension FastScan" *Bruker Corporation Sales Brochure*, Revision A2, 2011

(Bryan, 2005) B. D. Vogt, H-J. Lee, V. M. Prabhu, D. M. DeLongchamp, E. K. Lin, W-l. Wu, S. K. Satija, "X-ray and neutron reflectivity measurements of moisture transport through model multilayered barrier films for flexible displays", *Jour. App. Phys.* 97, 114509, 2005

(Burroughes, 1990) J. H. Burroughes, D. D. C. Bradley, A. R. Brown, R. N. Marks, K. Mackay, R. H. Friend, P. L. Burns, A. B.Holmes, "Light-emitting diodes based on conjugated polymers" *Nature*, 347, 6293, p.539-541, 1990

(Burrows, 1994) P. E. Burrows, V. Bulovic, S. R. Forrest, L. S. Sapochak, D. M. McCarty, and M. E. Thompson, "Reliability and degradation of organic light emitting devices", *Appl. Phys. Lett.*, 65, 2922, 1994

(Burrows, 2001) P.E Burrows, G.L Graff, M.E Gross, P.M Martin, M.K Shi, M Hall, E Mast, C Bonham, W Bennett, M.B Sullivan, "Ultra barrier flexible substrates for flat panel displays", *Displays*, 22, 2, P.65-69, 2001

(CAB Consulting, 2003) "Planarised polyester films for Flexible Electronics" *CAB Consulting Ltd, 2003, via DTF internal document*, 2007

(Carcia, 2006) P. F. Carcia, R. S. McLean, M. H. Reilly, M. D. Groner, and S. M. George, "Ca test of Al_2O_3 gas diffusion barriers grown by atomic layer deposition on polymers", *Appl. Phys. Lett*., 89, 031915, 2006

(Carcia, 2009) P. F. Carcia, R. S. McLean, M. D. Groner, A. A. Dameron, and S. M. George, "Gas diffusion ultrabarriers on polymer substrates using Al_2O_3 atomic layer deposition and SiN plasma-enhanced chemical vapor deposition", *J. Appl. Phys.*, 106, 023533, 2009

(Chang, 2010) C. D. Chang, J. J. Yeh, R. J. Weng, W. S. Hwang, "Simulation of nucleation and growth stages for sputtered films", *Modelling Simul. Mater. Sci. Eng.*, 18, 2, 025010, 2010

(Chiu, 2009) Y. L. Chiu, "Chemical Analysis in the SEM", *University of Birmingham Centre of Electron Microscopy*, Deparment of Mechanical and Metallugical Engineering; short course lecture notes (2009)

(Charton, 2006) C. Charton, N. Schiller, M. Fahland, A. Holländer, A. Wedel, K. Noller, "Development of high barrier films on flexible polymer substrates" *Thin Solid Films*, 502, 1–2, P. 99-103, 2006

(Chatham, 1996) H. Chatham, "Oxygen diffusion barrier properties of transparent oxide coatings on polymeric substrates," *Surf. Coat. Technol.*., 78, p.1–9, 1996

(Choi, 2007) J. H. Choi, Y. M. Kim, Y. W. Park, J. W. Huh, B. K. Ju, I. S. Kim, H. N. Hwang, "Evaluation of gas permeation barrier properties using electrical measurements of calcium degradation", *Rev. Sci. Instrum.*, 78, 064701, 2007

(Choi, 2008) M-C. Choi, Y. Kim, C-S. Ha, "Polymers for flexible displays: From material selection to device applications", *Progress in Polymer Science*, 33, 6, p.581-630, 2008

(Chwang, 2003) A. B. Chwang, M. A. Rothman, S. Y. Mao, R. H. Hewitt, M. S. Weaver, J. A. Silvernail, K. Rajan, M. Hack, J. J. Brown, X. Chu, L. Moro, T. Krajewski, N. Rutherford, "Thin film encapsulated flexible organic electroluminescent displays" *Appl. Phys. Lett.*, 83, 413, 2003

(CNET, 2008) "GE demonstrates printed OLEDs for flexible lighting" 12 March 2008, "http://news.cnet.com/8301-11128_3-9891842-54.html?part=rss&subj=news&tag=2547-1_3-0-20" Retrieved 29/3/12

(CNET, 2012) “LG's 55-inch 55EM9600 OLED TV wins Best of CES” 12 January 2012, “http://ces.cnet.com/8301-33379_1-57358177/lgs-55-inch-55em9600-oled-tv-wins-best-of-ces/” Retrieved 29/3/12

(Crawford, 2005) Gregory P. Crawford (2005). *Flexible Flat Panel Displays*. New York: John Wiley & Sons. p1-35, 2005

(Cubicciotti, 1952) D. Cubicciotti, “The oxidation of calcium at elevated temperatures”, *J. Am. Chem. Soc.*, 74, p.557, 1952

(Cullen, 2007) John Cullen, “Advances made in the field of barrier films”, *Dupont Teijin Films/University of Strathclyde internal document*, 2007

(Dameron, 2008) A.A. Dameron, S.D. Davidson, B.B. Burton, P.F. Carcia, R.S. McLean and S.M. George, "Gas Diffusion Barriers on Polymers Using Multilayers Fabricated by Al2O3 and Rapid SiO2 Atomic Layer Deposition", *J. Phys. Chem. 112*, p.4573-4580, 2008

(Decker, 2002) W. Decker, B. M. Henry, “Basic Principles of Thin Film Barrier Coatings” *Proc. Soc. Vac. Coat.*, 45 492-502, 2002

(Dennler, 2001) G. Dennler, A. Houdayer, Y. Segui, and M. R. Wertheimer, “Growth and structure of hyperthin SiO_2 coatings on polymers”, *J. Vac. Sci. Technol.*., A 19, 2320 (2001)

(Do, 1999) L-M. Do, D-H. Hwang, H-Y. Chu, T. Zyung, “Progress of dark spot and blister formation in polymeric lighting-emitting diodes”, *Synthetic Metals*, 102, 1–3, P. 1006-1007, 1999

(Do, 2000) Lee-Mi Do, Do-Hoon Hwang, Hye-Yong Chu, Seong Hyun Kim, Jeong-Ik Lee, Heuk Park, Taehyoung Zyung, “The initial state of dark spots in degradation of polymer lighting-emitting diodes”, *Synthetic Metals*, 111–112, P.249-251, 2000

(Dodabalapur, 1997) A. Dodabalapur, “Organic light emitting diodes”, *Solid State Communications*, 102, 2–3, P.259-267, 1997

(DTF, 2007) “Planarised polyester films for Flexible Electronics”, *Dupont Teijin Films Internal Document*, 2007

(DTF, 2008) “Teonex Q65a Star Diagram”, “http://usa.dupontteijinfilms.com/marketspaces/construction/pvcells.aspx”, Accessed on 29/3/12

(Dunkel, 2005) R. Dunkel, R. Bujas, A. Klein, V. Horndt, "Method of Measuring Ultralow Water Vapor Permeation for OLED Displays," *Proc. IEEE*, 93, 8, p.1478-1482, 2005

(DuPont, 2010) “DuPont Delivers OLED Technology Scalable for Television”, May 12, 2010 ”http://www2.dupont.com/Displays/en_US/news_events/article20100512.html, retrieved on 28/3/12

(Edge, 2009) Discussions with Steven Edge, CPI calcium test scientist (2009)

(Engadget, 2008) “Samsung titillates with transparent and 0.05mm 'flapping' OLED panels” 29 October 2008 “http://www.engadget.com/2008/10/29/samsung-titillates-with-transparent-and-0-05mm-flapping-oled-p/” Retrieved 29/3/12

(Engadget, 2010) "Universal Display ships eight wrist-worn OLED displays to military, too late to help Noble Team" October 2010 "http://www.engadget.com/2010/10/07/universal-display-ships-eight-wrist-worn-oled-displays-to-milita/", Retrieved on 29/3/12

(Erlat, 1999) A. G. Erlat, R. J. Spontak, R. P. Clarke, T. C. Robinson, P. D. Haaland, Y. Tropsha, N. G. Harvey, and E. A. Vogler, "SiOx gas barrier coatings on polymer substrates: morphology and gas transport considerations," *J. Phys. Chem. B*, 103, p.6047–6055, 1999

(Erlat, 2001) A.G. Erlat, B.M. Henry, J.J. Ingram, D.B. Mountain, A. McGuigan, R.P. Howson and C.R.M. Grovenor, G.A.D. Briggs, Y. Tsukahara, "Characterisation of aluminium oxynitride gas barrier films" *Thin Solid Films*, 388, 1, p.78-86, 2001

(Erlat, 2004) A. G. Erlat, B. M. Henry, C. R. M. Grovenor, A. G. D. Briggs, R. J. Chater, Y. Tsukahara, "Mechanism of Water Vapor Transport through PET/AlOxNy Gas Barrier Films" *J. Phys. Chem. B*, 108, 3, p.883-890, 2004

(Ettedgui, 1997) E. Ettedgui, G.T. Davis, B. Hu, F.E. Karasz, Degradation of polymer-based light-emitting diodes during operation", *Synthetic Metals*, 90, 1, P.73-76, 1997

(Fergason, 1969) J. Fergason, U. S. Patent, 3 731 986, 1969

(Ferns, 2007) S. Ferns, "Time to get with the programme?" Financial Times Online, February 24, 2007 2:00 am http://www.ft.com/cms/s/0/082fb8c2-c3ac-11db-9047-000b5df10621.html, retrieved 28/3/12

(Forge, 2009) Simon Forge, Colin Blackman, Sven Lindmark, "OLEDs and E-PAPER: Their Disruptive Potential for the European Display Industry" *JRC-IPTS Report*, EUR 23989 EN, 2009

(Garcia-Ayuso, 1996) G. Garcia-Ayuso, L. Vazquez, and J. M. Martinez-Duart, "Atomic force microscopy (AFM) morphological surface characterization of transparent gas barrier coatings on plastic films," *Surf. Coat. Technol.*,. 80, p.203–206, 1996

(Gardonio, 2007) S. Gardonio, L. Gregoratti, P. Melpignano, L. Aballe, V. Biondo, R. Zamboni, M. Murgia, S. Caria, M. Kiskinova, "Degradation of organic light-emitting diodes under different environment at high drive conditions", *Organic Electronics*, 8, 1, P.37-43, 2007

(Ghosh, 2005) A. P. Ghosh, L. J. Gerenser, C. M. Jarman, and J. E. Fornalik, "Thin-film encapsulation of organic light-emitting devices", *Appl. Phys. Lett.*, 86, 223503, 2005

(Gibbs, 1953) D. S. Gibbs, H. J. Svec, "Metal-Water Reactions. I. The Reaction between Calcium and Water Vapor", *J. Am. Chem. Soc.*, 75, 23, p.6052-6054, 1953

(Glyn, 2012) Glyn High Tech Distribution web page "http://www.glyn.com.au/Displays_CMEL.htm" retrieved on 3/4/12

(Graff, 2004) G. L. Graff, R. E. Williford, and P. E. Burrows, "Mechanisms of vapor permeation through multilayer barrier films: Lag time versus equilibrium permeation", *J. Appl. Phys.*, 96, 1840, 2004

(Greener, 2007) J. Greener, K. C. Ng, K. M. Vaeth, T. M. Smith, "Moisture Permeability Through Multilayered Barrier Films as Applied to Flexible OLED Display", *J. Appl. Polym. Sci.*, 106, p.3534–3542, 2007

(Groner, 2006) M. D. Groner, S. M. George, R. S. McLean, and P. F. Carcia, "Gas diffusion barriers on polymers using Al_2O_3 atomic layer deposition", *Appl. Phys. Lett.*, 88, 051907, 2006

(Gross, 2009) L. Gross, F. Mohn, N. Moll, P. Liljeroth, G. Meyer, "The Chemical Structure of a Molecule Resolved by Atomic Force Microscopy " *Science*, 325, 5944, p.1110-1114, 2009

(Hairston, 2009) N. Hairston, "The standard TV set" *LCD TV Association, LCD TV Matters*, 2, 4, p.39-42, 2009

(Hanika, 2003) M. Hanika, H. C. Langowski, U. Moosheimer, W. Peukert, "Inorganic Layers on Polymeric Films – Influence of Defects and Morphology on Barrier Properties", *Chem. Eng. Tech.*, 26, p.605-614, 2003

(Hariharan, 2003) P. Hariharan, "Optical interferometry", 2nd ed. *Amsterdam ; Boston: Elsevier/Academic Press*,p. 1-28, 2003

(Henry, 1999) B. M. Henry, F. Dinelli, K.-Y. Zhao, C. R. M. Grovenor, O. V. Kolosov, G. A. D. Briggs, A. P. Roberts, R. S. Kumar, and R. P. Howson, "A microstructural study of transparent metal oxide gas barrier films," *Thin Solid Films*, 355–356, p.500–505, 1999

(Henry, 2001) B.M Henry, A.G Erlat, A McGuigan, C.R.M Grovenor, G.A.D Briggs, Y Tsukahara, T Miyamoto, N Noguchi, T Niijima, "Characterization of transparent aluminium oxide and indium tin oxide layers on polymer substrates", *Thin Solid Films*, 382, 1–2, P.194-201, 2001

(Hodgeson, 2010) Discussions with M. Hodgeson, DTF barrier specialist, 2010

(Hollands, 2002) J. G. Hollands, H. A. Parker, S. McFadden, R. Boothby, "LCD versus CRT Displays: A Comparison of Visual Search Performance for Colored Symbols", *Human Factors: The Journal of the Human Factors and Ergonomics Society*, 44, 2, p.210-221, 2002

(Hoogboom, 2006) J. Hoogboom, T. Rasing, A. E. Rowan, R. J. M. Nolte, "LCD alignment layers. Controlling nematic domain properties", *Jour. Mat. Chem.*, 16, 1305, 2006

(Hsu, 2009) C.M. Hsu, C.S. Kuo, W.C. Hsu, W.T. Wu, "Nickel doped indium tin oxide anode and effect on dark spot development of organic light-emitting devices", *Applied Surface Science*, 255, 6, P.3759-3763, 2009

(Invitrogen, 2009) "Fluorescent Tags for Detecting ALD Coating Defects" *ALD defect tag protocol document*, Invitrogen, 2009

(IRTS-Lithography, 2011) "The International Technology Roadmap for Semi-conductors, 2011 Edition – Test and Test Equipment" *IRTS*, Obtained from "http://www.itrs.net/Links/2011ITRS/Home2011.htm", 29/3/12

(IRTS-Test, 2011) "The International Technology Roadmap for Semi-conductors, 2011 Edition – Test and Test Equipment", *IRTS*, Obtained from "http://www.itrs.net/Links/2011ITRS/Home2011.htm", 29/3/12

(Jakhanwal, 2011) V. Jakhanwal, *IHS iSuppli OLED Market Tracker Abstract*, 2011, "http://www.isuppli.com/Display-Materials-and-Systems/Pages/LED-TV-Continues-to-Grow-in-US-TV-Market.aspx", Accessed on 29/3/12

(Jamieson, 1983) E. H. H. Jamieson, A. H. Windle, "Primary Title: Structure and oxygen-barrier properties of metallized polymer film", *J. Mat Sci.*, 18, 1, p.64-80, 1983

(Jia, 2011) Zheng Jia, Matthew B. Tucker, Teng Li, "Failure mechanics of organic–inorganic multilayer permeation barriers in flexible electronics", *Composites Science and Technology*, 71, 3, P.365-372, 2011

(Jin, 2003) C. S. Jin and K. Lin, "Study to minimise OLED device degradation and failure using a parylene layer", *Inst. Mat. Eng.*, 2003
http://www.imre.a-star.edu.sg/rGallery/OLE_Degrade.asp, Retrieved on 16/04/12
(Jones, 2009) I. P. Jones, 2009 "Chemical Analysis in the SEM", *University of Birmingham Centre of Electron Microscopy*, Deparment of Mechanical and Metallugical Engineering; short course lecture notes (2009)

(Kawamoto, 2002) H. Kawamoto, "The history of liquid-crystal displays", *Proceedings of the IEEE* , 90, 4, p.460-500, 2002

(Ke, 2002) L. Ke, S-J. Chua, K. Zhang, N. Yakovlev, "Degradation and failure of organic light-emitting devices", *Appl. Phys. Lett.*, 80, 2195, 2002

(Kim, 2002) J.S. Kim, P.K.H. Ho, C.E. Murphy, N. Baynes, R.H. Friend, "Nature of Non-emissive Black Spots in Polymer Light-Emitting Diodes by In-Situ Micro-Raman Spectroscopy" *Adv. Mater.*, 14, 3, p.206-209, 2002

(Kolosov, 2001) D. Kolosov, D. S. English, V. Bulovic, P. F. Barbara, S. R. Forrest, M. E. Thompson, "Direct observation of structural changes in organic light emitting devices during degradation", *J. Appl. Phys.*, 90, 3242, 2001

(Kotova, 2004) O. V. Kotova, S. V. Eliseeva, E. V. Perevedentseva, T. F. Limonova, R. A. Baigeldieva, A. G. Vitukhnovsky, N. P. Kuzmina, "The topography of organic light-emitting diode-component functional layers as studied by atomic force microscopy", *Mendeleev Communications*, 14, 4, P.155-157, 2004

(Lewis, 2004) J.S. Lewis, M.S. Weaver, "Thin-film permeation-barrier technology for flexible organic light-emitting devices", *Selected Topics in IEEE Journal of Quantum Electronics*, 10, 1, p.45- 57, 2004

(Liew, 2000) Yoon-Fei Liew, Hany Aziz, Nan-Xing Hu, Hardy Sze-On Chan, Gu Xu, Zoran Popovic, "Investigation of the sites of dark spots in organic light-emitting devices", *Appl. Phys. Lett.*, 77, 17, p.2650-2652, 2000

(Lim, 2001a) S. Lim, W. Wang, S. Chua, "Degradation of organic light-emitting devices due to formation and growth of dark spots" *Materials Science and Engineering B*, 85, 2-3, p.154-159, 2001

(Lim, 2001b) S. Lim, L. Ke, W. Wang, S. J. Chua, "Correlation between dark spot growth and pinhole size in organic light-emitting diodes," *Appl. Phys. Lett.*, 78, 15, p.2116-2118, 2001

(Lim, 2002) S.F. Lim, W. Wang, S.J. Chua, "Understanding Dark Spot Formation and Growth in Organic Light-Emitting Devices by Controlling Pinhole Size and Shape", *Adv. Funct. Mater.*, 12, 8, p.513-518, 2002

(Looney, 2010) K. Looney, R. Blissett & H. Davies, "Barrier Model User Documentation" *DTF Internal Document*, 2010

(MacDonald, 2004) W. A. MacDonald, "Engineered films for display technologies", *J. Mater. Chem.*, 14, 1, p.4-10, 2004

(MacDonald, 2008a) W. A. MacDonald, M. K. Looney, D. MacKerron, R. Eveson, K. Rakos, "Designing and manufacturing substrates for flexible electronics" *Plastics, Rubber and Composites*, 37, 2-4, p.41-45, 2008

(MacDonald, 2008b) W. A. MacDonald, F. Placido, R. W. Eveson, August 2008, *Composite Films Suitable For Use In Opto-Electronic And Electronic Devices*, US Patent 20080193747

(Magonov, 2000) S.N. Magonov; Atomic Force Microscopy in Analysis of Polymers - Encyclopedia of Analytical Chemistry, R.A. Meyers (Ed.), p.7432–7491, *John Wiley & Sons Ltd, Chichester*, 2000

(Mao, 2007) S. S. Mao, "Organic Light Emitting Diodes With Structured Electrodes", International patent application 067548, 26th April 2007

(Marsh, 2011) Discussions with Paul Marsh, Intertek Senior Research Scientist, 2011

(McElvain, 1996) J. McElvain, H. Antoniadis, M. R. Hueschen, J. N. Miller, D. M. Roitman, J. R. Sheats, and R. L. Moon, "Formation and growth of black spots in organic light-emitting diodes", *J. Appl. Phys.*, 80, 6002, 1996

(McKenzie, 2006) P. McKenzie, S. Kiang, J. Tom, E. A. Rubin, M. Futran, "Can pharmaceutical process development become high tech?" *J. AlChE*, 52, 12, p.3990-3994, 2006

(Merck, 2007) Merck Brochure "Liquid Crystals, Merck Makes Communication Visible", acquired March 2007

(Millard, 2000) I.S Millard, High-efficiency polyfluorene polymers suitable for RGB applications, *Synthetic Metals*, 111–112, P.119-123, 2000

(Minoni, 2000) U. Minoni, L. Rovati, F. Docchio "Interferometric distance sensors" (S. Martellucci, N. A. Chester, A.G. Mignani - O*ptical Sensors and Microsystems: New concepts, Materials and Technologies* - Springer - Verlag Milano (ITA)) – p.15-31, 2000

(MOCON Pres. 2010) Joel Fischer - Different Test Methods for High Barrier WVTR Testing – *MOCON Webinar Series*, 2010

(Mori, 2006) Y. Mori, S. Kinoshita, *Display Method and Display Apparatus*, 7139008 B2, 2006

(Nagai, 2007) M. Nagai, "Defects of Passivation Films for Color-Filter-Based OLED Devices", *J. Electrochem. Soc.*, 154, J65, 2007

(Nisato, 2002) G. Nisato, P. Bouten "Permeation Methods, Public Report", September 2002

(Nisato, 2003) G. Nisato, M. Kuilder, P. Bouten, L. Moro, O. Philips, and N. Rutherford, "P-88: Thin Film Encapsulation for OLEDs: Evaluation of Multi-layer Barriers using the Ca Test", *SID Symposium Digest*, 34, 550, 2003

(Norenberg, 1999) H. Norenberg, T. Miyamoto, Y. Tsukahara, G. D. W. Smith, and G. A. D. Briggs, "Mass spectrometric estimation of gas permeation coefficients for thin polymer membranes", *Rev. Sci. Instrum.*, 70, 2414, 1999

(Nguyen, 1999) T.P Nguyen, M Spiesser, A Garnier, M de Kok, V.H Tran, "A degradation study of poly(p-phenylene vinylene) based light emitting diodes", *Mat. Sci. Eng. B*, 60, 1, P.76-81, 1999

(O'Rourke, 2007) S. O'Rourke "Planarised polyester films for Flexible Electronics", *DTF internal document*, 2007

(OLED-Info, 2012) OLED-Info.com "http://www.oled-info.com/companies/chemical_companies", accessed 28/1/12

(Paetzold, 2003) R. Paetzold, A. Winnacker, D. Henseler, V. Cesari, and K. Heuser, "Permeation rate measurements by electrical analysis of calcium corrosion", *Rev. Sci. Instrum.*, 74, 5147, 2003

(Park, 2005a) S. K. Park, J. Oh, C. Hwang, & J. Lee, "Ultra Thin Film Encapsulation of Organic Light Emitting Diode on a Plastic Substrate", *Electronics Telecommunications Research Inst.*, 27, 5, p.545-550, 2005

(Park, 2005b) S. K Park, J. Oh, C. Hwang, J. Lee, Y. Yang, H. Y. Chu, "Ultrathin Film Encapsulation of an OLED by ALD" *Electrochem. Solid-State Lett.*, 8, H21, 2005

(Park, 2009) O. K Park, J. H. Ka, "Flat Panel Display Device Method of Aging the Same and Method of Testing Lighting of the Same." *United States Patent Application* 0262048 A1, 2009

(Phillips, 1994) R. W. Phillips, "Atomic force microscopy for thin film analysis", *Surface and Coatings Technology*, 68–69, p.770-775, 1994

(Plumb, 2005) K. Plumb, "Continuous Processing in the Pharmaceutical Industry: Changing the Mind Set", *Chemical Engineering Research and Design*, 83, 6, p.730-738, 2005

(Prins, 1959) W. Prins, J. J. Hermans, "Theory of Permeation through Metal Coated Polymer Films", *J. Phys. Chem.*63, 5, 716-720, 1959

(Qi, 2011) Y. Qi, "Investigation of organic films by atomic force microscopy: Structural, nanotribological and electrical properties", *Surface Science Reports*, 66, 11–12, p.379-393, 2011

(Rakos, 2010a) Discussion with Karl Rakos, Senior Experimental Scientist at Dupont Teijin Films, 2010

(Rakos, 2010b) K. Rakos, "Large Area Metrology (LAM) Data for peelable film (PF0239)", *Dupont Teijin Films Internal Document*, 2010

(Rakos, 2012) Discussion with Karl Rakos, Senior Experimental Scientist at Dupont Teijin Films, 2012

(Reinitzer, 1888) F. Reinitzer, "Beiträge zur Kenntniss des Cholesterins," *Wiener Monatschr, Für Chem.*, 9, p.421–441, 1888

(Reuters, 2011) "Japan backs Sony, Toshiba, Hitachi LCD merger" August 2011 "http://www.reuters.com/article/2011/08/31/us-japan-displays-idUSTRE77U0VL20110831", Retrieved on 29/3/12

(Roberts, 2002) A.P. Roberts, B.M. Henry, A.P. Sutton, C.R.M. Grovenor, G.A.D. Briggs, T. Miyamoto, M. Kano, Y. Tsukahara, M. Yanaka, "Gas permeation in silicon-oxide/polymer (SiOx/PET) barrier films: role of the oxide lattice, nano-defects and macro-defects", *Journal of Membrane Science*, 208, 1–2, p.75-88, 2002

(Robinson, 2009) Discussions with Julian Robinson, Business Research Associate within Dupont Teijin Films, 2010

(Rollings, 2010) "Nexus one screen microscope image - Photo taken with a 200x digital microscope" Matthew Rollings at en.wikipedia, Accessed 29/3/12

(Rossi, 1993) Giuseppe Rossi, Mark Nulman, "Effect of local flaws in polymeric permeation reducing barriers", *J. App. Phys.*, 74, 9, p.5471-5475, 1993

(Samsung, 2012a) Samsung Galaxy S2 Phone Specifications, "http://www.samsung.com/global/microsite/galaxys2/html/specification.html", retrieved on 28/3/12

(Samsung, 2012b) "SAMSUNG Unveils the Super OLED TV – The Ultimate in Picture Quality", http://www.samsung.com/us/news/newsRead.do?news_group=productnews=consumerproduct=tv&news_seq=20077, Retrieved on 29/3/12

(Sarkar, 2001) S. L. Sarkar, X. Aimin and D. Jana; Scanning Electron Microscopy, X-Ray Microanalysis of concretes, 7, p.231-236, 2001

(Sauerbrey, 1959) G. Sauerbrey, "The use of quartz oscillators for weighing thin layers and for microweighing" *Zeitschrift Für Physik*, 155, p.206-222, 1959

(Savvate'ev, 1997) V. N. Savvate'ev, A. V. Yakimov, D. Davidov, R. M. Pogreb, R. Neumann, Y. Avny, "Degradation of nonencapsulated polymer-based light-emitting diodes: Noise and morphology", *Appl. Phys. Lett.*, 71, 3344, 1997

(Schaer, 2001) M. Schaer, F. Nüesch, D. Berner, W. Leo, L. Zuppiroli, "Water Vapor and Oxygen Degradation Mechanisms in Organic Light Emitting Diodes", *Adv. Funct. Mater.*, 11, 2, p.116–121, 2001

(Scott, 1996) J. C. Scott, J. H. Kaufman, P. J. Brock, R. DiPietro, J. Salem, J. A. Goitia, "Degradation and failure of MEH-PPV light-emitting diodes", *J. App. Phys.*, 79, 5, p.2745-2751, 1996

(Sheats, 1998) James R. Sheats, Daniel B. Roitman "Failure modes in polymer-based light-emitting diodes" *Synthetic Metals*, 95, 2, p.79-85, 1998

(Sheats, 2007) J. R. Sheats, "Organic LEDs Look Forward to a Bright , White Future", *Science,* 273, p.1762-1763, 2007

(Shen, 2000) J Shen, D Wang, E Langlois, W.A Barrow, P.J Green, C.W Tang, J Shi, "Degradation mechanisms in organic light emitting diodes", *Synthetic Metals*, 111–112, p.233-236, 2000

(da Silva Sobrinho, 1998) A. S. da Silva Sobrinho, M. Latreche, G. Czeremuszkin, J. E. Klemberg-Sapieha, and M. R. Wertheimer, "Transparent barrier coatings on polyethylene terephthalate by single- and dual-frequency plasma-enhanced chemical vapor deposition", *J. Vac. Sci. Technol. A*, 16, 3190, 1998

(da Silva Sobrinho, 1999) A.S. da Silva Sobrinho, G. Czeremuszkin, M. Latrèche, G. Dennler, M.R. Wertheimer, "A study of defects in ultra-thin transparent coatings on polymers" *Surface and Coatings Technology*, 116–119, p.1204-1210, 1999

(da Silva Sobrinho, 2000) A. S. da Silva Sobrinho, G. Czeremuszkin, M. Latreche, M. R. Wertheimer, "Defect-permeation correlation for ultrathin transparent barrier coatings on polymers", *J. Vac. Sci. Technol. A*, 18, 1, p.149-157, 2000

(Sony, 2008) Sony XEL-1 OLED Digital TV Operating Instructions, p.6, 2008

(Sony, 2012) Images retrieved from "http://www.sony.co.uk/product/tv-28-11-oled/XEL-1", retrieved on 28/3/12

(Steel, 1960) Steel, R. G. D. and Torrie, J. H., *Principles and Procedures of Statistics,* New York: McGraw-Hill, 1960, pp. 187, 287

(Stevens, 2009) M. Stevens, S. Tuomela, D. Mayer, "Water Vapor Permeation Testing of Ultra-Barriers: Limitations of Current Methods and Advancements Resulting in Increased Sensitivity", *MOCON, Inc.*, 2009

(Tamagaki, 2010) H. Tamagaki, T. Okimoto, T. Segawa, "Transparent High Barrier Coating on Flexible Film Substrate by Roll to Roll PECVD System", *ITE and SID*, IDW December 2010, FLX7/FMC6–1, p.1709-1712, 2010

(Tang, 1987) C. W. Tang and S. A. VanSlyke, "Organic electroluminescent diodes", *Appl. Phys. Lett.*, 51, 913, 1987

(Telegraph, 2009) "Japanese develop 'television wallpaper'" 23 February 2009 "http://www.telegraph.co.uk/news/worldnews/asia/japan/4786367/Japanese-develop-television-wallpaper.html", Retrieved 29/3/12

(Telegraph, 2012) "'The future of television': LG reveals 4mm-thick OLED TV" http://www.telegraph.co.uk/technology/ces/8989445/The-future-of-television-LG-reveals-4mm-thick-OLED-TV.html, Retrieved on 29/3/12

(Tropsha, 1997) Y. G. Tropsha and N. G. Harvey, "Activated rate theory treatment of oxygen and water transport through silicon oxide/ poly(ethylene terephthalate) composite barrier structures," *J. Phys. Chem. B*, 101, p.2259–2266, 1997

(Tse, 2009) Y. Y. Tse, "Electron Microscopes, an overview", *University of Birmingham Centre of Electron Microscopy*, Deparment of Mechanical and Metallugical Engineering; short course lecture notes, 2009

(Veeco, 1999) "WYKO Surface Profilers Technical Reference Manual", *Veeco Metrology Group*, Version 2.2.1, 1999

(Veeco, 2000) "Scanning Probe Microscopy Training Notebook", *Veeco Metrology Group*, Version 3.0, 2000

(Veeco, 2001) Veeco Dimension 3100 SPM Specifications Sheet, 2001

(Veeco, 2008) Veeco Instruments "A Practical Guide to SPM, Scanning Probe Microscopy" 2008, "www.veeco.com/pdfs/library/SPM_Guide_0829_05_166.pdf", Accessed 29/3/12

(Veeco, 2009) "Wyko NT Series Optical Profilometers" Veeco Sales Brochure (2009)

(Weaver, 2002) M. S. Weaver, L. A. Michalski, K. Rajan, M. A. Rothman, J. A. Silvernail, J. J. Brown, P. E. Burrows, G. L. Graff, M. E. Gross, P. M. Martin, M. Hall, E. Mast, C. Bonham, W. Bennett, M. Zumhoff "Organic light-emitting devices with extended operating lifetimes on plastic substrates", *Appl. Phys. Lett.*, 81, 2929, 2002

(Weiss, 1989) J. Weiss, Ch. Leppin, W. Mader, U. Salzberger, "Aluminium metallization of polyester and polypropylene films: Properties and transmission electron microscopy microstructure investigations", *Thin Solid Films*, 174, 1, p.155-158, 1989

(Williams, 1963a) R. Williams, "Liquid Crystals in an Electric Field", *Nature*, 199, 4890, 273, 1963

(Williams, 1963b) R. Williams, "Domains in Liquid Crystals" *J. Chem. Phys.*, 39, 2, 384, 1963

(Wyant, 2002) James C. Wyant, "White Light Interferometry", *Proc. SPIE*, 2002

(Xu, 2004) M. S. Xu, J. B. Xu, H. Z. Chen and M. Wang, "Nanoscale investigation of moisture-induced degradation mechanisms of tris(8-hydroxyquinoline) aluminium-based organic light-emitting diodes", *J. Phys. D: Appl. Phys*., 37 2618, 2004

(Yonekura, 2010) D. Yonekura, K. Fujikawa, R. Murakami, "Influence of film structure on gas barrier properties of SiOxNy films" *Surface and Coatings Technology*, 205, 1, p.168-173, 2010

(Zant, 2004) Peter Van Zant: *Microchip Fabrication - A Practical Guide to Semiconductor Processing*. 5th Ed. New York : McGraw-Hill, p91-137, 2004

(Zhang, 2008) Y. Zhang, D. C. Miller, J. A. Bertrand, S-H. Jen, R. Yang, M. L. Dunn, S. M. George, Y. C. Lee, and Y-Z. Zhang, "12.3: Defect Visualization of Atomic Layer Deposition Enabled Polymer Barriers Using Fluorescent Tags" *SID Symposium Digest* 39, 143 (2008)

(Zhang, 2009) Yadong Zhang, Yu-Zhong Zhang, David C. Miller, Jacob A. Bertrand, Shih-Hui Jen, Ronggui Yang, Martin L. Dunn, Steven M. George, Y.C. Lee, Fluorescent tags to visualize defects in Al2O3 thin films grown using atomic layer deposition", *Thin Solid Films*, 517, 24, p.6794-6797, 2009

(Zhdan, 2009) Peter Zhdan, Jim Castle, University of Surrey Intensive Short Course, Scanning Probe Microscopy, Course Notes, 2009

(Zhu, 2009) Furong Zhu, "OLED Activity and Technology Development", *Singapore Institute of Materials Research and Engineering*, Symposium on Sustainability Driven Innovative Technologies, 2009

(Zou, 1997) Dechun Zou, Masayuki Yahiro, Tetsuo Tsutsui, Study on the degradation mechanism of organic light-emitting diodes (OLEDs)", *Synthetic Metals*, 91, 1–3, p.191-193, 1997

Appendix

The appendix gives experimental information on cleaning and analysis techniques.

Appendix 1: Developing cleaning regime for post calcium test samples

As described in Section 6.3.4.2, a cleaning method was investigated on post calcium test samples, different methods of cleaning were trialled on samples of PEN which had undergone calcium testing and the surfaces were analysed using AFM. The results of that work is displayed in Appendix 1. Whilst none of the methods return the surface back to the original levels of roughness, the best results are achieved using a brief ultrasonic clean with distilled water (Figure App.1).

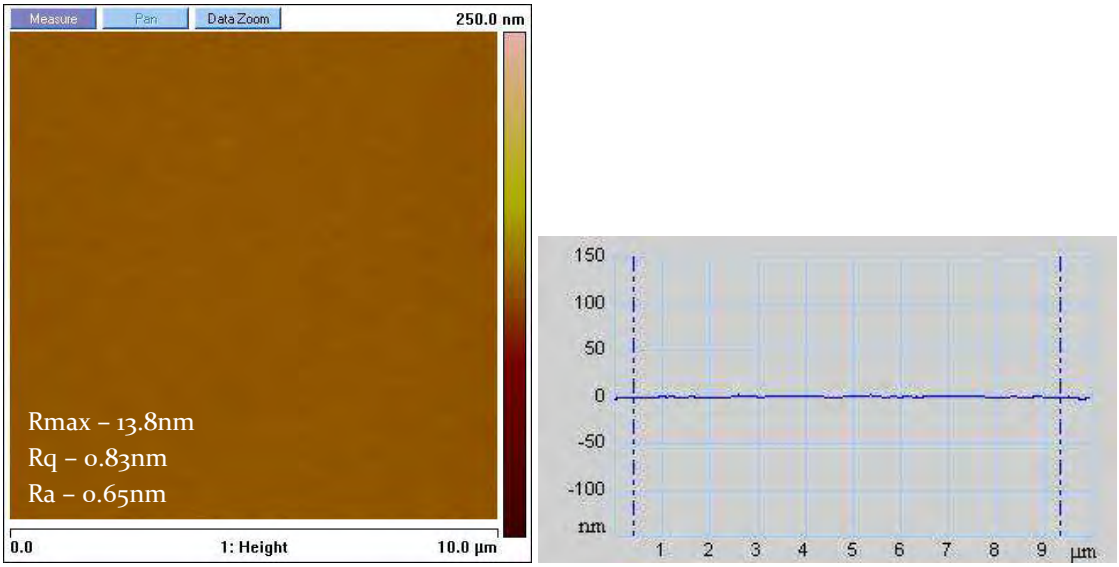

Planarised PEN

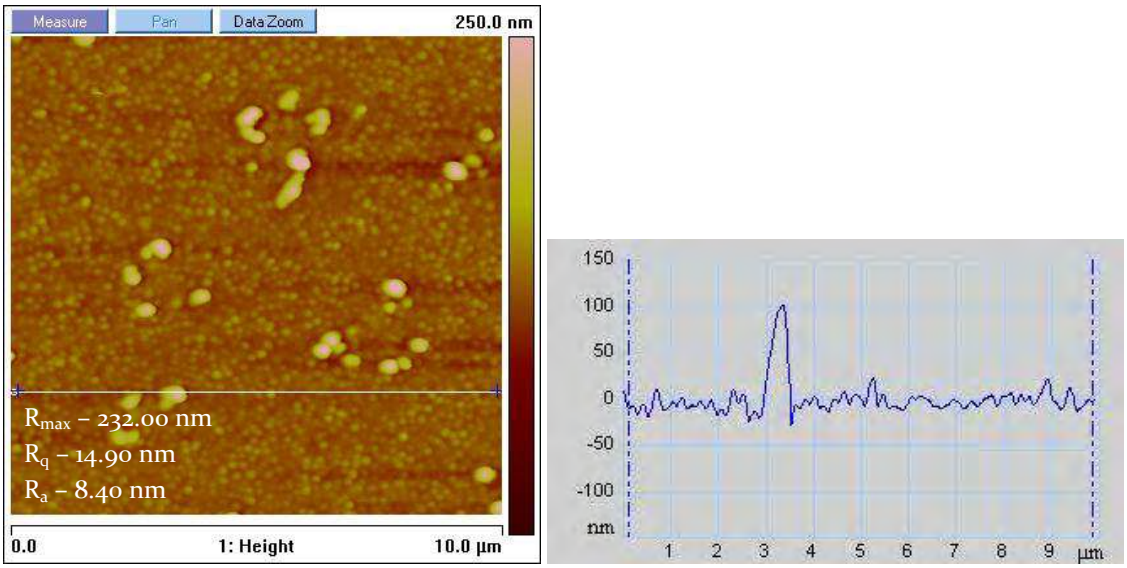

Calcium Oxide on post-calcium test planarised PEN

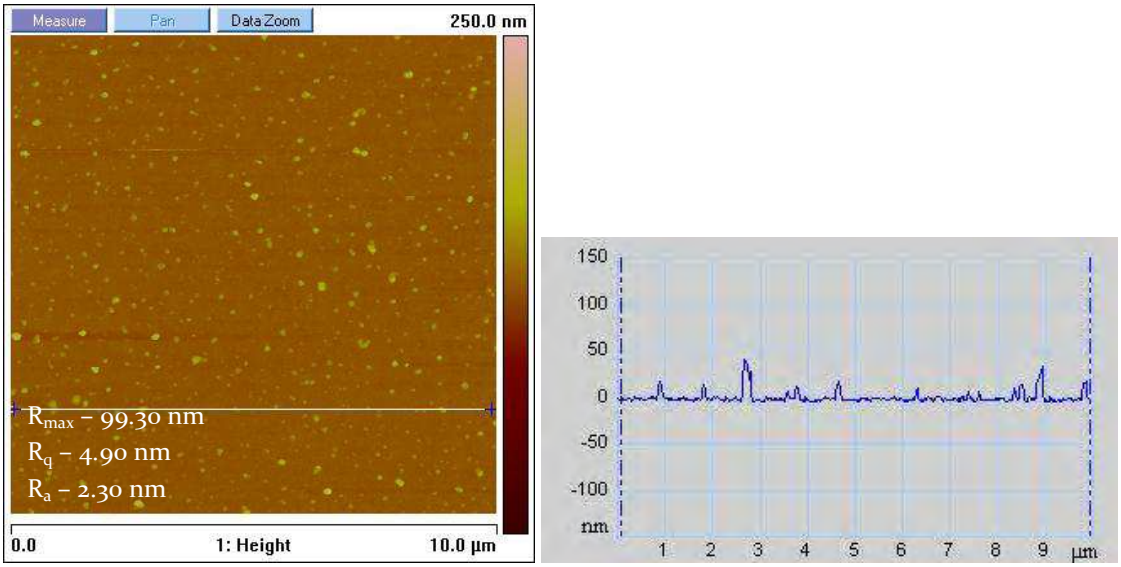

Post calcium test planarised PEN after rinse with deionised water

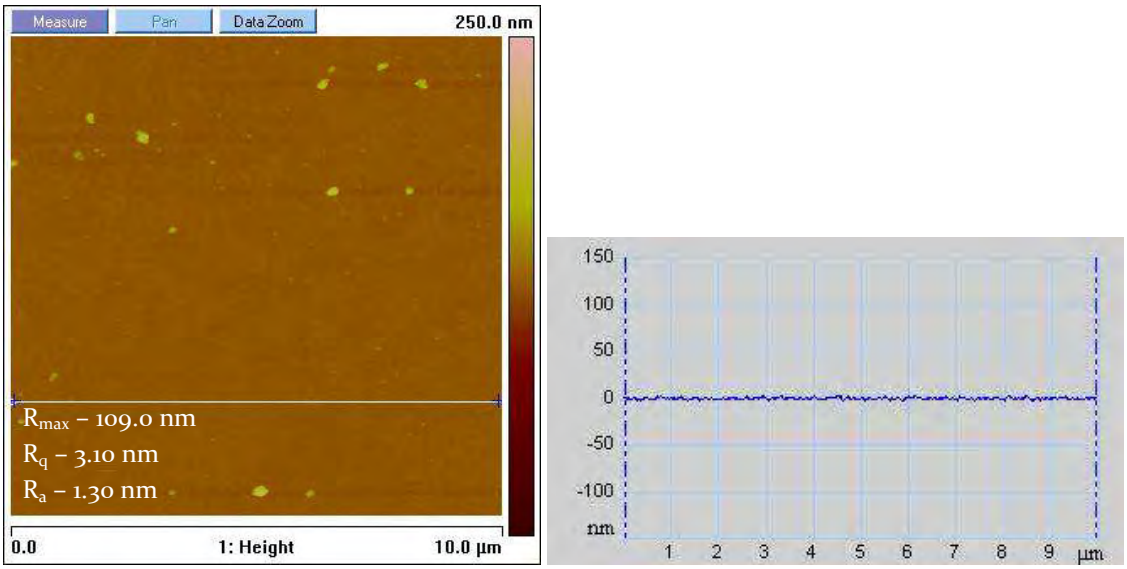

Post calcium test planarised PEN after rinse with mild hydrochloric acid

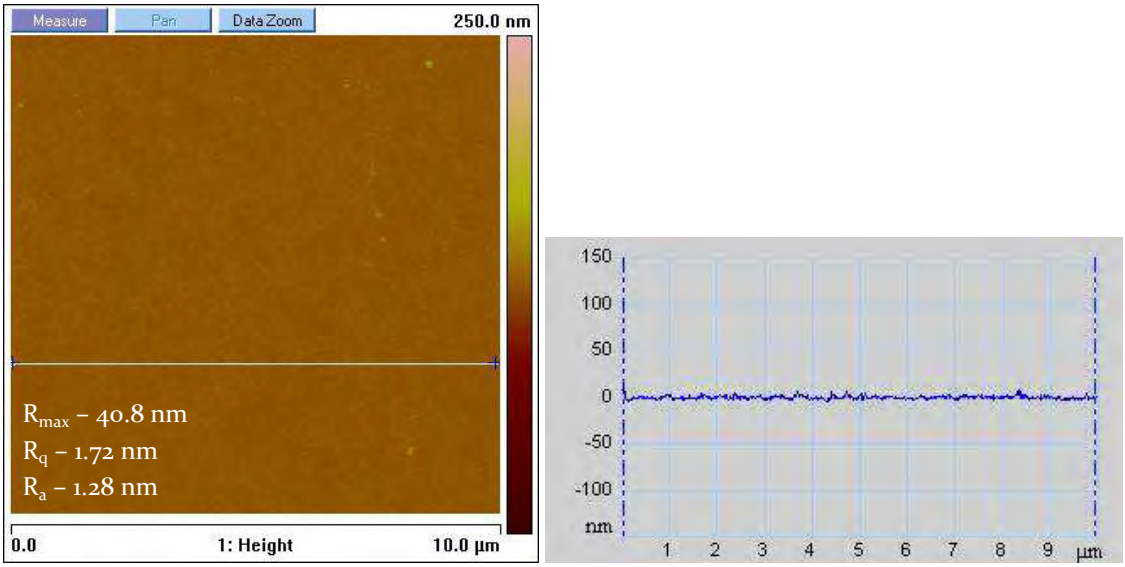

Post calcium test planarised PEN after ultrasonic treatment in deionised water

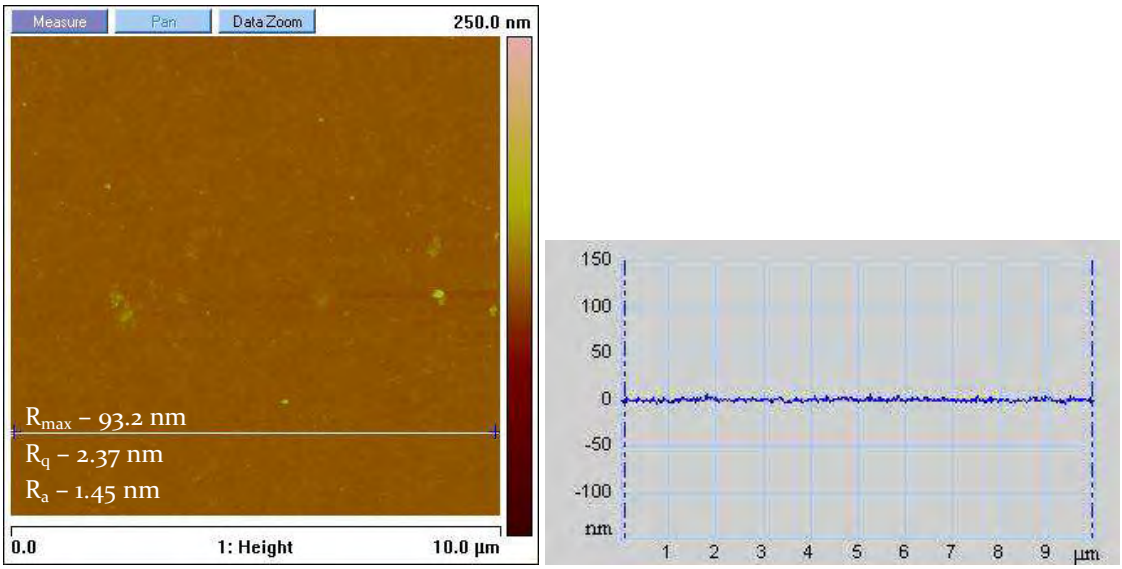

Post calcium test planarised PEN after ultrasonic treatment in deionised water and EDTA

Figure App.1: AFM Topography images to show the change in surface roughness after numerous post-calcium test cleaning methods, roughness inset over AFM images

Appendix 2: Confirmation of Seahostar particle diameters

As discussed in Section 8.3.3, the Seahostar particles obtained from Nippon Shokubai were supplied with information to confirm the exact particle sized. Regardless, the diameters of these were tested again at DTF to confirm the manufacturer specification (Figure App.3) using a Beckman Coulter NP-4 particle sizer.

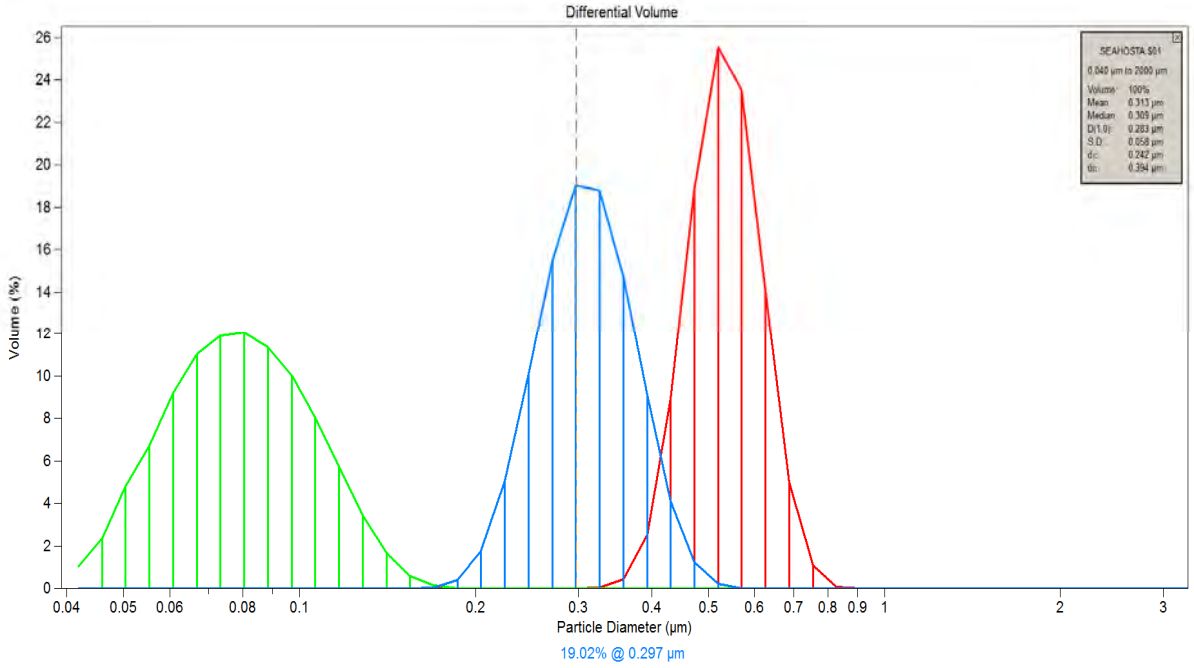

Figure App.2: Confirmation of particle size distribution of a range of Seahostar particles

Appendix 3: An alternative method to locate barrier defects

Fluorescent Tag with Confocal Microscopy

A presentation in 2008 (Zhang, 2008) which was published the following year (Zhang, 2009) described the use of a novel fluorescent tag reported to be capable of highlighting barrier defects on polyester films. A dye such as this has the potential to allow flaws in the surface of barrier film to be rapidly identified, it is described in the paper as a pre-cursor to allow direct defect analysis. The method of operation is relatively simple (Invitrogen, 2009), the barrier substrate under test is soaked in a solution containing the fluorescent tag for a number of minutes, during which the hydrophobic chains preferentially bind to the hydrophobic polymer surface exposed by flaws in the barrier layer (Figure 3.8), excess tag is then rinsed from the remainder of the surface. Subsequent exposure to laser light at 488 nm results in a strong fluorescence signal at 515 nm which can be isolated using a confocal microscope equipped with a band pass filter.

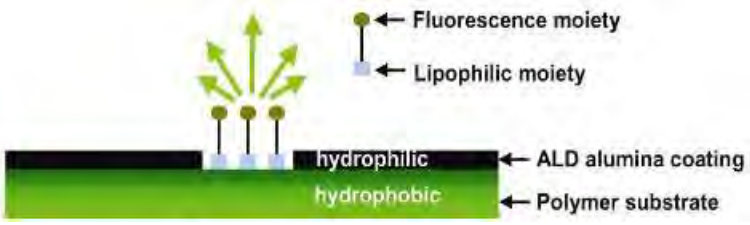

Figure 3.8: Schematic to represent the operation of the fluorescent tag which preferentially binds to the exposed polymer (Zhang, 2008)

The publication examined standard PEN, clean Al_2O_3 coated PEN and intentionally scratched Al_2O_3 coated PEN. Results demonstrated that the tag will associate with the entire surface of standard PEN, none of the surface of an undamaged barrier layer and only the scratches in the purposefully damaged sample. In this way the authors used the tag as a non-destructive way of rapidly locating

barrier breaks which could then be examined using SEM; it is stated that the tag can highlight areas as small as tens of nanometres.

Whilst this technique is promising as a labelling stage directing analysis with other microscopic techniques, it has a number of flaws;

Not all defects manifest as holes in the barrier, some particulates remain covered by the aluminium until they are dislodged (Jamieson, 1983), the tag will be incapable of highlighting these. Furthermore confocal microscopy is required to detect barrier breaks, without which the process cannot be used, whilst this is an improvement over standard optical microscopy the size of these defects are still on the limits of optical inspection. The authors also noted that if the PEN substrate is replaced with polyimide it becomes ineffective as the tag relies on a large difference in hydrophobicity between the coating and the substrate, although they suggest that continued research to produce more sensitive tags may provide a solution. As many polymers for OLED applications have surface treatments such as inorganic/organic hybrid planarisers, this brings into question how effective the tag may prove to be on 'real' samples; scoping work carried out for this thesis suggests it is indeed unsuitable. Finally, this method is solely a defect locating technique, whilst oxygen etching or the calcium test can locate defects, they can also provide additional permeation data. This technique may be used to locate barrier flaws, but there is no way to determine how substantial their role is in the overall film permeation.